UNIVERSITY OF CALIFORNIA, SAN DIEGO

Sloped Connections and Connections with Fillet Welded Continuity Plates for Seismic Design of Special Moment Frames

A dissertation submitted in partial satisfaction of the requirements for the degree Doctor of Philosophy

in

Structural Engineering

by

Adel Mashayekh

Committee in charge:

Professor Chia-Ming Uang, Chair
Professor Joel Conte
Professor Juan Carlos Del Alamo
Professor Juan C. Lasheras
Professor Benson Shing

2017

The Dissertation of Adel Mashayekh is approved, and it is acceptable in quality and form for publication on microfilm and electronically:

Chair

University of California, San Diego

2017

DEDICATION

To my loving and supportive family members:

my parents, Mohammad and Zohre Mashayekh

my brother, Abed Mashayekh

my lovely niece (Nika Mashayekh)

and my sister-in-law (Somaye Mashayekh)

EPIGRAPH

If you can’t explain it simply, you don’t understand it well enough.

Albert Einstein

TABLE OF CONTENTS

LIST OF TABLES

LIST OF FIGURES

ACKNOWLEDGEMENTS

This project was sponsored by the American Institute of Steel Construction (AISC). Mr. Tom Schlafly served as the project manager for this research. Schuff Steel Company donated the test specimens. AMEC Foster Wheeler donated weld inspection services to this project. Mr. Patrick M. Hassett of Hassett Engineering, Inc. reviewed the design of the test specimens on continuity plate welding. Mr. Steven Ball of John A. Martin & Associates, Inc. reviewed the design of sloped connection specimens.

Experimental testing was performed in the Powell Structural Laboratories and would not have been possible without the help of the expert staff members: Dr. Christopher Latham, Mr. Darren Mckay. I appreciate their assistance and technical guidance throughout the program.

I would like to send my deepest respect and appreciation to my PhD advisor, Professor Chia-Ming Uang. He has been an outstanding support, advocate and mentor for me. Not only has he provided me with fantastic training in conducting research, but he has also taught me several life lessons which will be crucial in my entire life. Serving as his teaching assistant provided me the opportunities to learn how to become an effective instructor; I treasured very much the opportunity to exercise the teaching skills while serving as an instructor in a summer session steel design course. In terms of research, he paved the path for me to work on a variety of topics. A unique opportunity of experimental, analytical, and numerical research works became a possibility for me to work on only through him. I could never be at this position if it was not due to his kind and unconditional supports.

Parts of chapters 2, 3 and 4, have been accepted for publication of the material as it may appear in *Engineering Journal*, 2017, Mashayekh, A., and Uang, C.M. The dissertation author was the primary researcher and author of this material.

VITA

2011 B.S. Civil Engineering, Sharif University of Technology

2013 M.S. Structural Engineering, University of California, San Diego

2017 Ph.D. Structural Engineering, University of California, San Diego

PUBLICATIONS

Refereed Journal Articles

Mashayekh, A., and Uang, C.M. (2017). "Experimental verification of a procedure for SMF continuity plate weld design." *Eng. J.*, AISC. (accepted)

Peng, Z., Mashayekh, A. and Zhu, Q. (2014). "Erythrocyte responses in low-shear-rate flows: effects of non-biconcave stress-free state in the cytoskeleton." *JFM*, 742, 96-118.

Technical Reports

Mashayekh, A., and Uang, C.M. (2016). "On establishing ASCE 41 m-Factor for flexural members of metal buildings." *Rep. No. SSRP16-03*, Dept. of Structural Engineering, University of California, San Diego, La Jolla, CA.

Mashayekh, A., and Uang, C.M. (2016). "Cyclic testing of bolted SidePlate steel moment frame connections for SMF applications: H and U series." *Rep. No. TR 16-01*, Dept. of Structural Engineering, University of California, San Diego, La Jolla, CA.

Mashayekh, A., and Uang, C.M. (2017). "Experimental verification of a procedure for SMF continuity plate weld design." *Rep. No. SSRP 16-10*, Dept. of Structural Engineering, University of California, San Diego, La Jolla, CA.

Mashayekh, A., and Uang, C.M. (2017). "Cyclic response of sloped steel moment connections." *Rep. No. SSRP 16-11*, Dept. of Structural Engineering, University of California, San Diego, La Jolla, CA.

Honors and Award

Recipient of Department of Structural Engineering Best Research Poster Awarded By: *Professor Albert Pisano; Dean of Jacobs School of Engineering, UCSD*, April 2017.

Exemplary Summer Graduate Teaching Scholar Award, *UCSD*, September 2016.

ABSTRACT OF THE DISSERTATION

Sloped Connections and Connections with Fillet Welded Continuity Plates for Seismic Design of Special Moment Frames

by

Adel Mashayekh

Doctor of Philosophy in Structural Engineering

University of California, San Diego, 2017

Professor Chia-Ming Uang, Chair

Steel Special Moment Frames (SMF) are one of the most popular lateral force-resisting systems for multistory building construction in high seismic regions due to their architectural versatility. With a significant amount of research that was conducted after the 1994 Northridge, California earthquake, AISC has published design guidelines (AISC 341 and AISC 358) to avoid brittle fracture of beam-to-column welded moment connections that occurred in more than 100 steel buildings. This dissertation addresses two issues related to the moment connection design of SMF.

Unless the column flanges are sufficiently thick, AISC 341 requires that continuity plates be installed, and that expensive complete-joint-penetration (CJP) groove welds be

used to connect the continuity plates to the column flanges; the conservative nature of this requirement stems from a lack of procedure that the designer can use to quantify the required seismic forces in the continuity plates such that more economical welds (e.g., fillet welds) can be used. The first objective of this research was to investigate a design procedure and to verify it with full-scale testing of two Reduced Beam Section (RBS) moment connections. It was shown that the proposed design procedure could result in a more economical weld design while developing the ductile response of the moment connection.

AISC seismic design codes implicitly assume that beams are orthogonal to the columns in elevation, but in real-life construction beams are sometimes connected to the columns with a slope. To fill this knowledge gap, both experimental and analytical studies were conducted. Full-scale testing of two additional moment connections with a 25° angle of inclination showed that sloped connections are vulnerable to brittle fracture at the "heel" location, where the beam flange and column form an acute angle. Fracture would initiate from the end of beam web CJP weld and the weld access hole. Guided by finite element simulation, a truss analogy model was proposed to predict the force concentration at the heel location. A Force Concentration Factor was introduced to evaluate when the effect of inclination can be ignored. When such effect needs to be addressed, a solution that introduces a curved slot in the beam web was proposed. The effectiveness of this solution was verified by nonlinear finite element analysis.

1 INTRODUCTION

1.1 Statement of Problems

The beam-to-column moment connections play a critical role in special moment frame (SMF) performance since they transfer bending moments. The resulting concentrated beam flange forces at column face are very high. These forces can cause column local flange bending (LFB), column web local yielding (WLY), and beam flange complete-joint-penetration (CJP) weld fracture due to stress concentration. To meet the requirements of these limit states, column transverse stiffeners (or continuity plates) at the beam flange levels are often required in accordance with AISC 341, *Seismic Provisions for Structural Steel Buildings* (AISC 2010a). Continuity plates, when required, add a significant amount of fabrication cost because a total of four continuity plates are required at each connection and CJP welds are required by AISC 341 to connect these plates to the column flanges.

The stringent welding requirements for continuity plates were established primarily to reflect how moment connection specimens tested in the past were fabricated. Another reason for having this conservative requirement is that no mechanics-based procedure that allows the designer to calculate the required forces in the continuity plate is available. Recently, Tran et al. (2013) proposed a flexibility-based procedure to fill this gap. This procedure opens the door for using non-CJP welds (i.e., fillet welds or partial-joint-penetration groove welds) to connect continuity plates to the column.

AISC 358 (AISC 2016b) provides a number of prequalified connections for seismic applications in Special and Intermediate Steel Moment Frames (SMF and IMF). This

design standard implicitly assumes that the beam frames orthogonally into the column in the elevation of the frame and also in plan view. In real-life construction, however, it is not uncommon that this orthogonal condition is violated. While these prequalified connections appear applicable when the slope angle does not deviate too much from orthogonal, it is not clear if these connections can be applied to cases when the angle is large.

1.2 Research Objectives

This research has two objectives. The first objective was to evaluate if alternative weld joints can be used for welding continuity plates to the columns. The second objective was to evaluate the cyclic performance of sloped connections.

1.3 Scope

The two topics investigated in this research are for the design of Special Moment Frames in high seismic regions. Full-scale testing of beam-column subassemblages with the Reduced Beam Section (RBS) connection were conducted. In addition, analytical studies including finite element simulation were also performed for the development of design guidelines for potential adoption by the AISC seismic design codes.

2 DESIGN OF CONTINUITY PLATES AND WELDS

2.1 General

This chapter starts with a review of the current design practice of designing continuity plates and their welds to the column for Special Moment Frames. An alternative design procedure recently proposed by UCSD researchers (Tran et al. 2013) was then described. This procedure was critically reviewed and some modifications were made before this revised procedure was used for the design of test specimens for experimental verification in Chapter 3.

2.2 AISC Design Requirement for SMF Continuity Plates and Welds

Section E3.6f of AISC 341 (2010) stipulates that continuity plates are not required when the column flange thickness meets the following two requirements:

$$t_{cf} \geq 0.4\sqrt{1.8 b_{bf} t_{bf} \frac{R_{yb} F_{yb}}{R_{yc} F_{yc}}} \tag{2.1}$$

$$t_{cf} \geq \frac{b_{bf}}{6} \tag{2.2}$$

where

F_{yb} = specified minimum yield stress of the beam flange,

F_{yc} = specified minimum yield stress of the column flange,

R_{yb} = ratio of the expected yield stress to the specified minimum yield stress of the beam,

R_{yc} = ratio of the expected yield stress to the specified minimum yield stress of the column,

b_{bf} = beam flange width,

t_{bf} = beam flange thickness, and

t_{cf} = column flange thickness.

Where continuity plates are required, the thickness of the plates shall be determined as following:

(a) for one-sided connections, continuity plate thickness shall be at least one-half of the thickness of the beam flange, and

(b) for two-sided connections, the continuity plate thickness shall be at least equal to the thicker of the two beam flanges on either side of the column.

AISC 341 requires that continuity plates be welded to the column flanges using CJP groove welds. Continuity plates can be welded to the column web using either groove welds or fillet welds. The required strength of the sum of the welded joints of the continuity plates to the column web shall be the smallest of the following:

(a) the sum of the design strengths in tension of the contact areas of the continuity plates to the column flanges that have attached beam flanges,

(b) the design strength in shear of the contact area of the plate with the column web,

(c) the design strength in shear of the column panel zone, and

(d) the sum of the expected yield strengths of the beam flanges transmitting force to the continuity plates.

Note in the 2016 edition of AISC 341 that items (c) and (d) have been replaced by the design shear strength of the column web when the continuity plate is welded to the column web, or the design shear strength of the doubler plate when the continuity plate is welded to an extended doubler plate.

In this dissertation, welds between the continuity plate and the column flanges are defined as the *flange welds*, and the weld between the continuity plate and the column web is defined as the *web weld*.

Equation (2.1) can be obtained by equating the design strength associated with the local flange bending (LFB) limit state ($R_n = 6.25t_{cf}^2F_{yc}$, Graham et al. (1960)) to an approximate beam flange force of $P_{uf} = 1.8b_{bf}t_{bf}F_{yb}$ and solving for t_{cf}; F_{yb} and F_{yc} are replaced by the expected yield stresses $R_{yb}F_{yb}$ and $R_{yc}F_{yc}$, respectively, in the above derivation. Equation (2.2) is based on the deformation of the column flange and is related to low-cycle fatigue failure (Ricles et al. 2000).

2.2.1 Basis of Eq. (2.1)

The design equation for LFB contained in AISC 360 (2010) was based on the research work of Graham et al. (1960) in conjunction with limit load and buckling analyses of Parkes (1952) and Wood (1955). The equation was derived using a plastic yield line analysis to fit the experimental results from local flange bending tests and lower bound approximations of dimensions of common girder and column combinations of the time.

To develop the LFB equation, one can divide the strength of the column flange into two parts when the column flange is loaded by the beam flange in tension. One part is the middle portion of the column flange (web and fillet area) and the other part is the column flange outside the fillet area. The strength of the column flange outside the fillet area was computed by Graham et al. (1960) based on the yield line theory in which they modeled the column flange as shown in Figure 2.1(a). Assuming each plate on either side of the fillet area has a height p and width q, the yield line theory gives the total strength from these two plates:

$$P_{cf1} = 2c_1F_{yc}t_{cf}^2 \tag{2.3}$$

where

$$c_1 = \frac{\frac{4}{\beta} + \frac{\beta}{\eta}}{2 - \frac{\eta}{\lambda}}$$

$$\eta = \frac{\beta\left(\left(\sqrt{\beta^2 + 8}\lambda\right) - \beta\right)}{4}$$

$$\lambda = \frac{h}{q}$$

$$p = 12t_{cf}$$

$$q = \frac{b_{cf}}{2} - k_{1c}$$

$$h = \frac{b_{bf}}{2} - k_{1c}$$

$k_{1c} = k_1$ of column section (AISC. (2011). Steel Constructional Manual, 14th Edition)

Based on approximations of dimensions of common beam and column combinations of the time, Graham et al. (1960) assumed a lower bound value of 3.5 for c_1.

Hajjar et al. (2000) introduced a different yield line pattern based on observations made from several pull-plate testing. Figure 2.1(b) shows their proposed yield lines on the plate. Figure 2.2 shows the failure mode of the column flange under the assumed yield line pattern. Δ is the out-of-plane deformation at the edge of the column flange. Using the principal of virtual work, the ultimate load can be computed as following:

Considering the linear tension load from the beam flange on the plate to be P_{cf1}/h, the external work, W_E, is:

$$W_E = \int_0^h \frac{P_{cf1}}{h}\frac{x}{q}\Delta d_x = \frac{P_{cf1}h\Delta}{2q} \tag{2.4}$$

The internal work, W_I, is equal to:

$$W_I = M_p\theta_n\sqrt{p^2 + 4q^2} + 2M_p\theta_x q \tag{2.5}$$

where

$$\theta_n = \frac{\Delta}{x} \tag{2.6a}$$

$$\theta_x = \frac{2\Delta}{p} \tag{2.6b}$$

$$x = \frac{pq}{\sqrt{p^2 + 4q^2}} \tag{2.6c}$$

$$M_p = \frac{t_{cf}^2 F_{yc}}{4} \tag{2.6d}$$

Substituting θ_n, θ_x, x, and M_p into Eq. (2.5):

$$W_I = t_{cf}^2 F_{yc} \left(\frac{p}{4q} + \frac{2q}{p}\right) \tag{2.7}$$

P_{cf1} then can be derived by equating W_E and W_I:

$$P_{cf1} = t_{cf}^2 F_{yc} \left(\frac{p}{2h} + \frac{4q^2}{ph}\right) \tag{2.8}$$

For the terms in the parentheses above, Hajjar et al. (2000) introduced a parameter which is similar to c_1 introduced by Graham et al. (1960). This parameter is defined as S_1:

$$S_1 = \frac{\left(\frac{4}{\beta} + \frac{\beta}{2}\right)}{\lambda}$$

where β and λ have been derived previously.

Following Salmon et al. (2009), the strength of the column flange for the local flange bending limit state, R_n, can be obtained as following:

$$R_n = 7t_{cf}^2 F_{yc} + 2k_{1c} t_{bf} F_{yc} \tag{2.9}$$

where the first terms is P_{cf1} when $c_1 = 3.5$ is substituted into Eq. (2.3), and the second term represents the portion of the load that goes directly into the column web and the fillet area. Conservatively using 80% of the R_n in Eq. (2.9) then solving for t_{cf} gives:

$$t_{cf} = \sqrt{\frac{R_n}{7F_{yc}}\left(1.25 - \frac{t_{bf}k_1F_{yc}}{R_n}\right)} \tag{2.10}$$

From tests conducted by Graham et al. (1960), the minimum value of $t_{bf}k_1F_{yc}/R_n$ was determined to be 0.15. Thus, using 0.15 for the second term in the bracket of Eq. (2.10) gives the conservative expression adopted by AISC for the minimum column flange thickness to avoid the need for continuity plates:

$$t_{cf} \geq 0.4\sqrt{\frac{R_n}{F_{yc}}} \tag{2.11}$$

Re-writing the above equation gives the nominal strength for LFB:

$$R_n = 6.25t_{cf}^2F_{yc} \tag{2.12}$$

Based on their pull plate test results, Hajjar et al. (2003) concluded that the equation above is reasonable and conservative.

2.2.2 Basis of Eq. (2.2)

Ricles et al. (2000) tested eleven Welded Unreinforced Flange-Welded Web (WUF-W) moment connection specimens with and without continuity plates, with four tested to investigate the effect of continuity plates on the cyclic performance. The beam size for all specimens was W36×150, while three different column sizes (W14×311, W14×398, W27×258) were used. They then performed a low-cycle fatigue analysis to establish a criterion which forms the basis for Eq. (2.2).

The low-cycle fatigue life prediction can be made using a ductile crack propagation model similar to the one proposed by Krawinkler and Zohrei (1983). The rate of increase of the crack size a is related to the plastic strain range $\Delta\varepsilon_p$, where

$$\frac{da}{dn} = Ca\left(\Delta\varepsilon_p\right)^{\beta} \tag{2.13}$$

in which the parameters C and β depend on the material properties, the geometry of the structural components, the shape of the crack, and the triaxiality condition. Triaxiality is the ratio between the hydrostatic pressure (σ_m) and the von Mises stress (σ_{eff}). The definition of σ_m and σ_{eff} are:

$$\sigma_m = -\frac{1}{3}\text{trace}\left(\sigma_{ij}\right) \tag{2.14}$$

$$\sigma_{eff} = \sqrt{\frac{2}{3}S_{ij}S_{ij}} \tag{2.15}$$

where σ_{ij} are the Cauchy stress components, and i, j represent the global directions, $i = 1, 2, 3$ and $j = 1, 2, 3$. S_{ij} are the deviatoric stress components such that $S_{ij} = \sigma_{ij} + \sigma_m\delta_{ij}$. Triaxiality is an important quantity when considering ductile rupture of metals because high triaxiality can cause a large reduction in the rupture strain, thereby limiting ductility (Barsom and Rolfe 1987; Lemaitre 1996). C can be evaluated by

$$C = \frac{\ln\left(\frac{a_f}{a_0}\right)}{\left(\varepsilon_{f,p}\right)^{\beta}} \tag{2.16}$$

in which a_0 is the initial flaw size, and a_f is the crack size at which ductile crack extension occurs under the engineering plastic strain $\varepsilon_{f,p}$. A mean value of a_0 equal to 0.0012 inch (about twice the average grain size) has been used by Krawinkler and Zohrei (1983), and is the order of magnitude of surface discontinuities observed at weld toes in high cycle fatigue studies by Signes et al. (1967). For a plate element, a_f (through-thickness crack) can be found by considering the net section fracture:

$$a_f = \left(1 - \frac{\sigma_y}{\sigma_u}\right)(t - a_0) \tag{2.17}$$

where σ_y and σ_u are the yield stress and tensile strength, respectively, and t and a_0 are the thickness of the plate and initial flaw size, respectively.

The relationship of strain range and cycles to failure under constant strain range can be presented as a log-log function (Bannantine et al. 1990), where

$$\ln(\Delta\varepsilon_p) = \ln(\varepsilon_f) - \frac{1}{k}\ln(n) \tag{2.18}$$

In Eq. (2.18) $\Delta\varepsilon_p$ is the plastic strain range, ε_f is the engineering strain of the tensile coupon at fracture, n is the number of cycles to failure, and k is a material constant. For $n = 356$ and $\Delta\varepsilon_p = 0.02$, k is equal to

$$k = \frac{\ln(356)}{\ln\left(\frac{\varepsilon_f}{0.02}\right)} \tag{2.19}$$

The engineering fracture strain ε_f can be determined from the logarithmic strain $\varepsilon_{p,f}$ considering necking effects using the approach proposed by Bridgman (1952). The value of k then can be obtained from Eq. (2.19). By integrating Eq. (2.13), one can show that β is equal to k in Eq. (2.19) for a constant amplitude strain range.

Low cycle fatigue loading may occur either under a constant amplitude strain range or variable amplitude strain range. For low-cycle fatigue under a constant amplitude of plastic strain range, $\Delta\varepsilon_p$, the number of stress cycles to failure, N_f, can be predicted by (Coffin 1954):

$$N_f = \left(\frac{\varepsilon_f}{\Delta\varepsilon_p}\right)^{\beta} \tag{2.20}$$

Given the initial flaw size a_0 and the constant plastic strain range of $\Delta\varepsilon_p$, the corresponding crack size a_c after n cycles can be predicted by solving Eq. (2.13), resulting in:

$$a_c = a_0 \exp\left[C\left(\Delta\varepsilon_p\right)^{\beta} n\right] \tag{2.21}$$

for a variable amplitude strain range, the strain range history is integrated by using the initial flaw size a_0, or crack size a_i at the last displacement amplitude, and the following equation to determine the crack size a_j due to a sequence of cycles in the strain history with the same strain range:

$$a_j = a_i \exp\left[C\left(\Delta\varepsilon_p\right)^{\beta} \Delta N\right] \tag{2.22}$$

The process is repeated for the next sequence of cycles having a constant strain range until the loading history is either completely accounted for, or until the crack size a_j reaches the critical value when fracture occurs. The number of cycles of failure N_f is thus determined if the crack size reaches the critical size at which net section fracture occurs before the loading history is completed.

Referring to Figure 2.3, Ricles et al. (2000) assumed the deflection at point A to be:

$$\Delta_A = \frac{q l^4}{8 E I_f} \tag{2.23}$$

where, q is the average tension force at the column face per unit length (i.e., $q = P_{uf}/b_{bf}$), l is the width of the column flange from the face of the column doubler plate to point A, E is the Young's modulus, and I_f is the moment of inertia of the column flange. Based on the test results, the equivalent width of the cantilever beam model is taken to be equal to 9 times the thickness of the column flange, t_{cf}.

Performing a low-cycle fatigue analysis on the three aforementioned column sections attached to the W36×150 beam without continuity plates revealed that a story drift of 3% radians or more could be achieved in a connection with l/Δ_A larger than or equal to

520, which corresponded to the W14×311 column section. The ratio between b_{bf} to t_{cf} for this section is close to 5.2. FEMA-350 (2000) then simplified this condition and set the additional continuity plate requirement to be as shown in Eq. (2.2).

2.3 Flexibility-Based Formulation

The procedure originally proposed by Tran et al. (2013) and subsequently modified slightly in this study is summarized below. Representing the beam flange force as

$$P_{uf} = C_{pf} R_{yb} b_{bf} t_{bf} F_{yb} \tag{2.24}$$

AISC 341 assumes the beam flange force adjustment factor, C_{pf}, is equal to 1.8 to establish the minimum column flange thickness requirement in Eq. (2.1) when continuity plates are not required. While this assumed value is reasonable for the pre-Northridge type welded flange-bolted web moment connections, where the bolted web is ineffective in contributing to the moment resistance, Tran et al. (2013) showed that this assumption, and hence Eq. (2.1), is conservative for some post-Northridge moment connections like the Reduced Beam Section (RBS) or Welded Unreinforced Flange-Welded Web (WUF-W) moment connections; the beam web of these connections is directly welded to the column flange with a CJP weld. Based on finite element analysis, the following C_{pf} values were recommended by Tran et al. (2013) for use in Eqs. (2.1) and (2.24):

(a) for RBS connection: $C_{pf} = 1.25$ (2.25)

(b) for WUF-W connection: $C_{pf} = 1.75$ (2.26)

With a significantly lower C_{pf} value for the RBS connection, continuity plates that are required per AISC 341 may be unnecessary.

When continuity plates are required, the beam flange axial force, P_{uf}, is apportioned to each continuity plate based on the following equation (Tran. et al. 2013):

$$P_{cp} = \frac{P_{uf}}{2}\left(\frac{b_{bf} - t_{pz} - 2t_{cf}}{b_{bf}}\right)\left(\frac{B_{cf}}{B_{cf} + B_{cp}}\right) \tag{2.27}$$

Where

b_{bf} = beam flange width,

t_{pz} = panel zone thickness,

t_{cf} = column flange thickness,

B_{cf} = column flange out-of-plane flexibility coefficient

$$= 0.26\frac{b^2}{Et_{cf}^3} + \frac{0.4\left[1 + 0.09\ln\left(\frac{b}{t_{cf}}\right)\right]}{Gt_{cf}}$$

E = Modulus of elasticity of steel = 29,000 ksi,

G = Shear modulus of elasticity of steel = 11,200 ksi,

b = $b_{clip} + b_n$ (total width of continuity plate),

b_{clip} = corner clip size,

b_n = net width of continuity plate,

B_{cp} = continuity plate in-plane flexibility coefficient

$$= \frac{0.42 - C}{Gt} + \frac{b^3}{Ed^3t}$$

C = 0 for interior connections, and for exterior connections:

$$= 0.6\left(\frac{b}{d}\right) - 0.14 \geq 0$$

See Tran et al. (2013) for the derivation of Eq. (2.27). Following the procedure, one can compute the required forces along three edges of the continuity plate (Figure 2.4). To ensure that the continuity plates have a sufficient in-plane stiffness, the designer then

checks the local flange bending and web local yielding limit states (AISC 2010c) of the column for the portion of the beam flange force that will be transmitted from the beam flange to the column web directly:

$$P_{uf} - 2P_{cf} \leq \phi R_n \tag{2.28}$$

Figure 2.4 shows that the edges of the continuity plate next to the loaded column flanges are subjected to both normal and shear forces; the shear force is needed to satisfy moment equilibrium. The Von-Mises yield criterion is then used by Tran et al. to check the strength of the continuity plates:

$$\left(\frac{P_{cp}}{F_{ycp}A_n}\right)^2 + \left(\frac{V_{cp}}{\frac{F_{ycp}}{\sqrt{3}}A_n}\right)^2 \leq 1.0 \tag{2.29}$$

where from moment equilibrium the shear force is

$$V_{cp} = \left(\frac{0.6b}{d}\right)\sum P_{cp} \tag{2.30}$$

F_{ycp} = yield stress of continuity plate,

d = depth of continuity plate,

t_{cp} = thickness of continuity plate, and

A_n = $b_n t_{cp}$.

When Eq. (2.29) is satisfied, either fillet welds or partial-joint-penetration groove welds can be used to connect the continuity plates to the column flanges. If not, Tran et al. suggested that complete-joint-penetration (CJP) groove welds still be used because continuity plates are expected to yield. To avoid the use of CJP welds, however, an alternative is to increase the thickness of the continuity plates such that Eq. (2.29) is satisfied.

In designing the specimens for this test program, some modifications were made to Eq. (2.29). By ignoring the corner clips in the continuity plates, Tran et al. (2013) suggested that the normal force, P_{cp}, be located at a distance 0.6*b* from the column web (Figure 2.4), and the moment produced by this force with an eccentricity with respect to the center of the net width of the continuity plate was ignored in checking the strength in Eq. (2.29). Reviewing the work of Neal (1961) and Astaneh-Asl (1998), Dowswell (2015) suggested an *M-V-P* yield criterion, which can be re-written for checking the continuity plate strength as the following:

$$\left(\frac{P_{cp}e}{Z_{xn}F_{ycp}}\right)+\left(\frac{P_{cp}}{F_{ycp}A_n}\right)^2+\left(\frac{V_{cp}}{\frac{F_{ycp}}{\sqrt{3}}A_n}\right)^4 \leq 1.0 \tag{2.31}$$

where Z_{xn} is the plastic section modulus of the net section:

$$Z_{xn}=\frac{t_{cp}b_n^2}{4} \tag{2.32}$$

Refer to Figure 2.5(a) for a continuity plate in a two-sided (i.e., interior) moment connection, where corners are clipped to clear the k-area of the column section. Freebody 3 in Figure 2.5(c) shows that the normal force P_{cp} acts at a distance 0.6*b* from the column web. Moment equilibrium requires that

$$V_{cp}=\left(\frac{0.6b}{d-2b_{clip}}\right)\sum P_{cp} \tag{2.33}$$

Next consider Freebody 1 or 2. The corner clip causes the normal force at the edge of the net width to shift by an amount e^* to satisfy moment equilibrium:

$$e^*=\frac{b_{clip}V_{cp}}{P_{cp}} \tag{2.34}$$

Therefore, the moment produced by the eccentrically loaded P_{cp} at the center of the net width equals eP_{cp}, where

$$e = 0.6b + e^* - (b_{clip} + 0.5b_n) \tag{2.35}$$

The same approach can be applied to the continuity plate in a one-sided (i.e., exterior) moment connection. But the shear force calculation needs to be modified. As shown in Figure 2.6, it is assumed that the normal force at the non-loaded column flange side of the continuity plate equals zero. Therefore, the shear force is

$$V_{cp} = \left(\frac{0.6b}{d - b_{clip}}\right) P_{cp} \tag{2.36}$$

Equation (2.31), not Eq. (2.29), was used to design the continuity plates in this test program.

The procedure to design the fillet welds follows.

(a) Design the flange weld for the required resultant force, R_{cp}:

$$\phi R_n \geq R_{cp} \tag{2.37}$$

where

$$R_{cp} = \sqrt{P_{cp}^2 + V_{cp}^2} \tag{2.38}$$

The design strength for 2-sided fillet welds is:

$$\phi R_n = 2(\phi)(0.6)t_e b_n F_{EXX}(1.0 + 0.5\sin^{1.5}\theta) \tag{2.39}$$

Where

ϕ $= 0.75$,

t_e $=$ effective throat of the fillet weld,

F_{EXX} = minimum specified ultimate strength of the weld,

θ = angle of the resultant force, R_{cp}, measured from the weld longitudinal axis:

$$= \tan^{-1}\frac{P_{cp}}{V_{cp}}$$

(b) Check the flange weld at the location of maximum tensile stress, q_{max}:

$$q_{max} = \frac{1.6P_{cp}}{b_n} \tag{2.40}$$

When 2-sided fillet welds are used, the value of q_{max} cannot exceed the unit-length design strength, which can be computed by using Eq. (2.39) with $b_n = 1.0$.

(c) Check maximum shear stress in the flange weld, τ_{max}:

$$\tau_{max} = \frac{2V_{cp}}{b_n} \tag{2.41}$$

(d) Design the web weld for a required shear force equal to the summation of force allocated to the continuity plate, $\sum P_{cp}$, as shown in Figure 2.4(a). For exterior moment connections [Figure 2.4(b)], the required shear force equals P_{cp}.

$$\phi R_n \geq \sum P_{cp} \tag{2.42}$$

For 2-sided fillet welds, the design strength is computed as:

$$\phi R_n = 2(\phi)(0.6)t_e l_w F_{EXX} \tag{2.43}$$

where

l_w = length of the web weld.

Tran et al. proposed that a ϕ value of 0.9 be used for designing the fillet welds. In this test program, however, it was decided to use the ϕ value (= 0.75) per AISC 360. Also, it was judged that using Eqs. (2.40) and (2.41) to check the local stresses are too stringent and

conservative. Test results to be presented later showed that no damage was observed in the fillet welds even though these two equations were not used in design.

Parts of chapters 2 have been accepted for publication of the material as it may appear in *Engineering Journal*, 2017, Mashayekh, A., and Uang, C.M. The dissertation author was the primary researcher and author of this material.

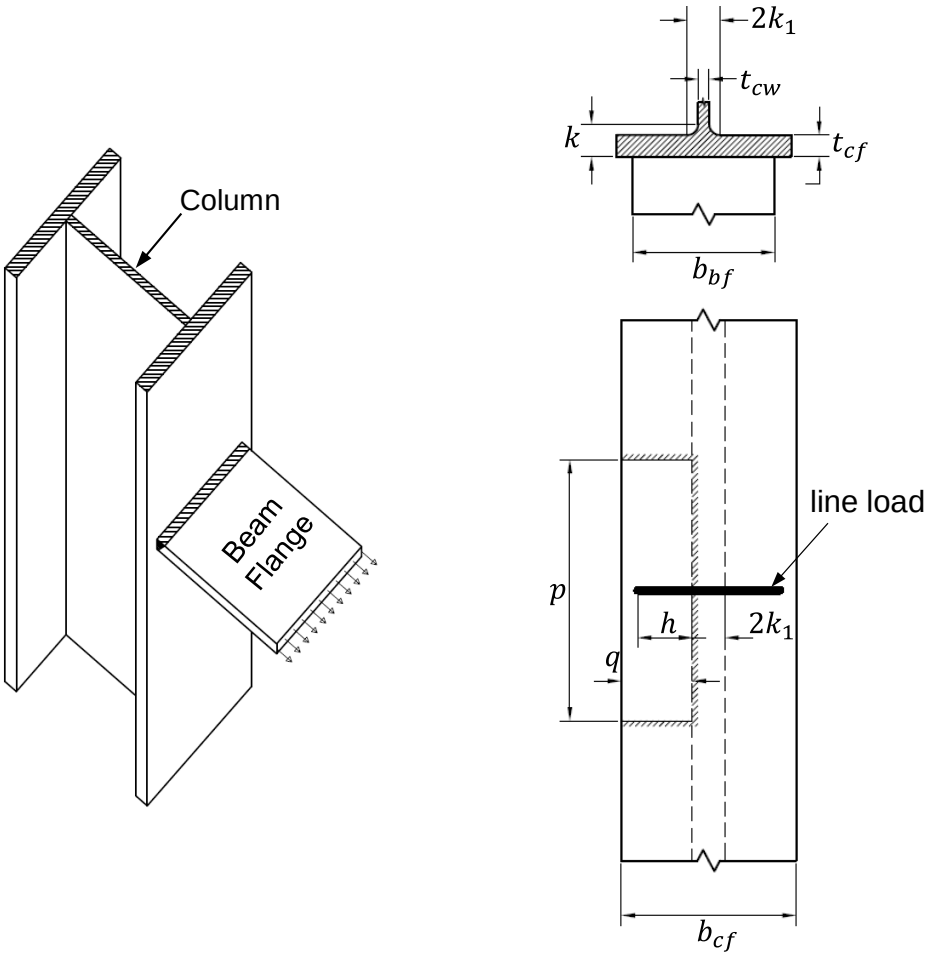

(a) Column Flange Model (Graham et al., 1960)

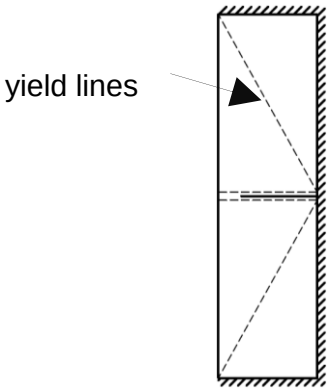

(b) Assumed Yield Line Pattern of Column Flange Due to LFB (Hajjar et al., 2000)

Figure 2.1 Column Flange Model and Yield Line Pattern for LFB Limit State

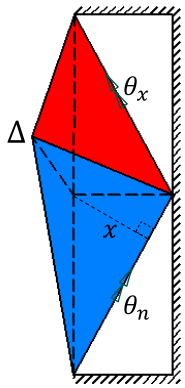

Figure 2.2 Column Flange Failure Under Proposed Yield Line by Hajjar et al. (2000)

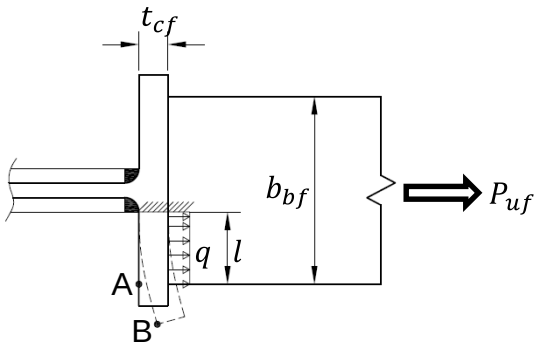

Figure 2.3 Column Flange Local Deformation Model (Ricles et al. 2000)

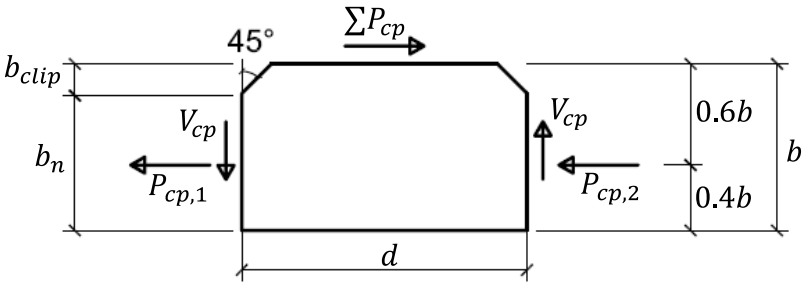

(a) Interior Connection

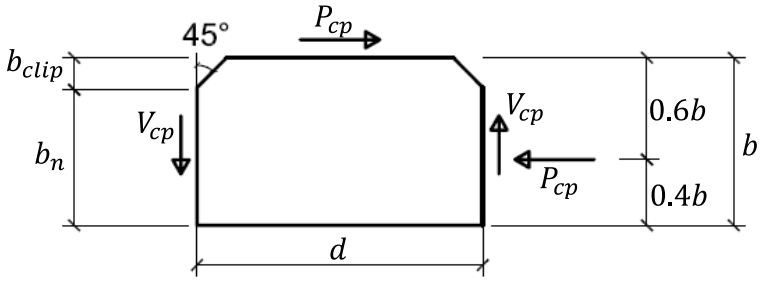

(b) Exterior Connection

Figure 2.4 Freebody Diagram of a Continuity Plate
(Adopted from Tran et al. 2013)

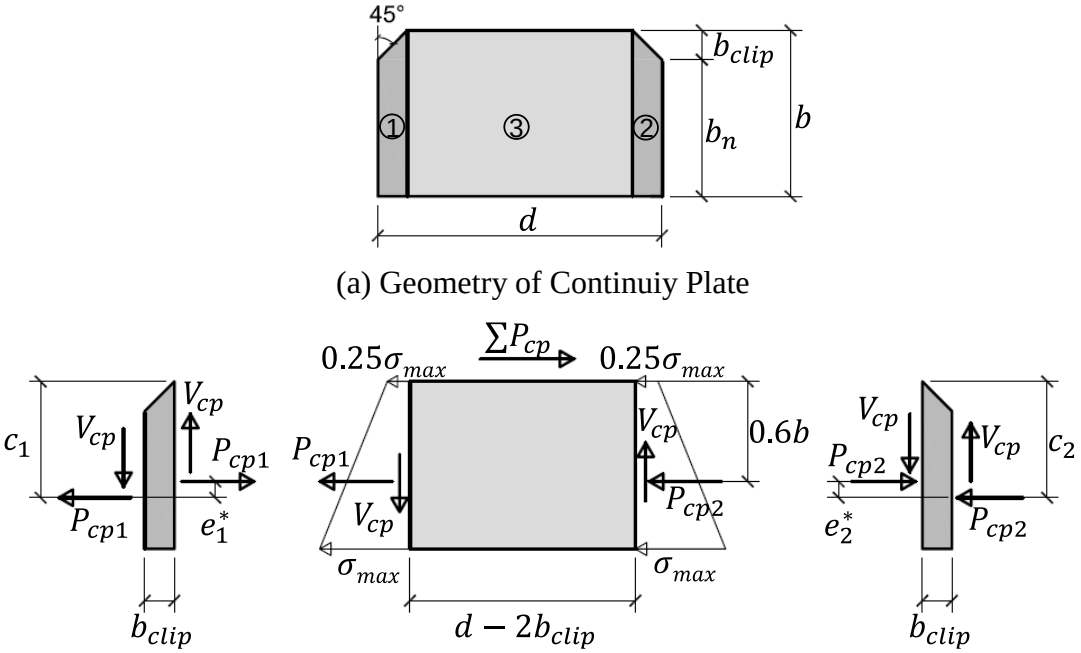

(a) Geometry of Continuiy Plate

(b) Freebody 1 (c) Freebody 3 (d) Freebody 2

Figure 2.5 Continuity Plate Freebody Diagrams (Interior Connection)

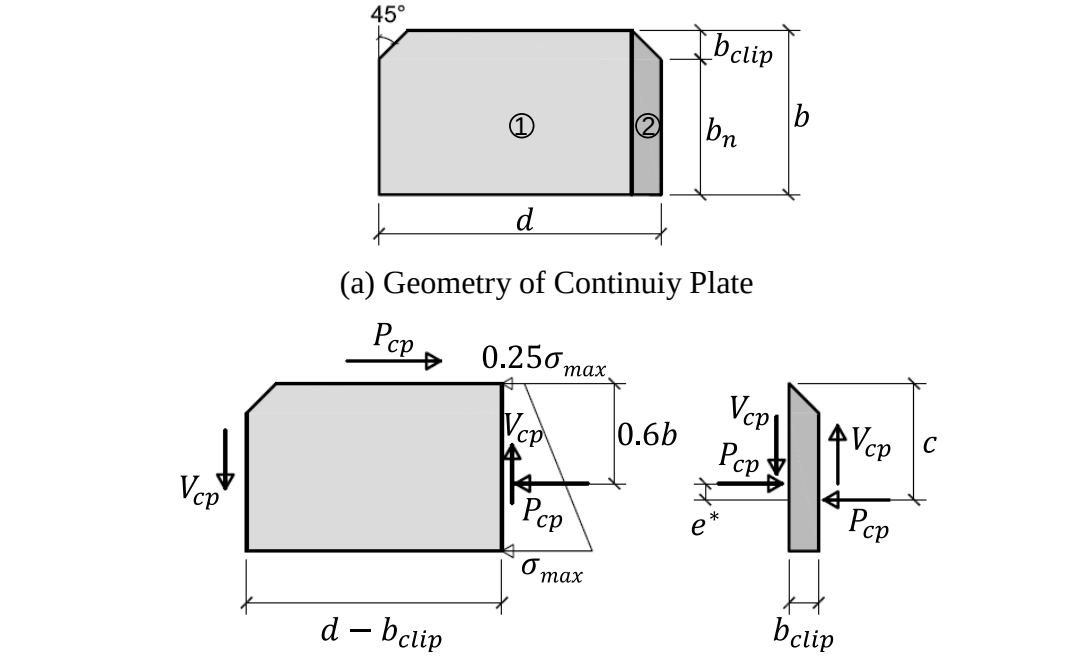

(a) Geometry of Continuiy Plate

(b) Freebody 1 (c) Freebody 2

Figure 2.6 Continuity Plate Freebody Diagrams (Exterior Connection)

3 TEST PROGRAM FOR CONTINUITY PLATE WELDING STUDY

3.1 Design of Test Specimens

3.1.1 Specimens Sizes

A W30×116 beam connected to a W24×176 "deep" column was selected for Specimen C1, whereas a W36×150 beam connected to a W14×257 "shallow" column was chosen for Specimen C2. Column height, h, was 16 ft and the beam span, L, was 15 ft. Table 3.1 shows the cross-sectional dimensions of the beams and the columns.

3.1.2 Moment Connection Design

The reduced beam section (RBS) connection was used for both specimens. The RBS design was carried out per AISC 358 (AISC 2010b); strong-column/weak-beam condition and panel zone strength satisfied the AISC 341 requirements. But continuity plates and welds were designed per the proposed flexibility-based procedure. Figure 3.1 and Figure 3.2 show the connection detail of both specimens.

A summary of key design parameters of each specimen is listed in Table 3.2. While satisfying the panel zone strength requirement in AISC 341, note the demand-capacity ratios (DCR) were high (0.9 and 0.95 for Specimens C1 and C2, respectively) so column flange kinking due to panel zone shear yielding would "challenge" the fillet welds connecting the continuity plates to the column flanges. For Specimen C2 with a shallow (W14) column, note the required shear force, V_{cp} (= 62.8 kips), acting on the continuity plate and flange weld is significant.

A comparison of the continuity plate and weld design based on the flexibility-based procedure and AISC 341 is summarized in Table 3.3. The proposed design called for a

continuity plate thickness of 7/8 in. for Specimen C2. AISC 341 implicitly assumes that continuity plates should remain essentially elastic. Since the effect of yielded continuity plates has never been reported in the literature, it was decided to use 5/8 in. thick continuity plates instead. A comparison of the welds for the continuity plates based on both procedures is also provided in the table. Although the proposed procedure called for thicker continuity plates, fillet welds, not CJP welds, were used for the flange welds.

Table 3.4 summarizes the components of Eq. (2.31) for the continuity plate design of both specimens. The continuity plates of Specimen C2 were significantly under-sized; the demand-capacity ratio was 1.31. The shear force component was minimal for the deep-column Specimen C1, mainly because the depth of the continuity plates was larger [Eq. (2.36)]. For the shallow-column Specimen C2, both shear and moment components were significant. Also, note that the moment component played a more significant role than the shear component in checking the plate strength for both specimens. Therefore, it is not appropriate to ignore the moment component and use Eq. (2.29) to check the strength of continuity plates.

3.2 Test Setup

The overall geometry of each test setup is shown in Figure 3.3. The inflection points were assumed to be at the mid-height of each story. Inflection points were simulated by mounting the column ends to two W14×257 hinge sections on its back side and a W14×342 on its bottom positioned to experience weak-axis bending (see Figure 3.4 for the hinges used in the testing of Specimen C2 which were identical for both Specimens). A corbel was bolted to the free end of the beam and attached to two 500-kip hydraulic actuators. Lateral restraint was provided on both sides of the specimens at two locations, one at corbel

location and one at 10 ft-3¼ in. from the centerline of the column. For Specimen C1, which utilized a deep column, two extra lateral restraints were provided. One was a bracing provided for the beam top flange near RBS location to simulate the slab restraining effect and the second was at the top end of the column. The second lateral restraint was a 2L3×2×1/2 strut to provide lateral support against twisting at the top end of the column; a deep column without the presence of a concrete slab was shown to prone to twisting (Chi and Uang 2002). The lateral restraint assembly is illustrated in Figure 3.5 for both specimens. Figure 3.6 shows the beam bracing and column top bracing for Specimen C1.

3.3 Material Properties

ASTM A992 steel was specified for the beams and columns. The continuity plates were fabricated from ASTM A572 Gr. 50 steel. Table 3.5 summarizes the steel mechanical characteristics obtained from tensile coupon tests conducted at UCSD (APPENDIX A).

3.4 Instrumentation

A combination of displacement transducers, strain gage rosettes, and uniaxial strain gages were used to measure the global and local responses. Figure 3.7 shows the location of displacement transducers. Displacement transducer L1 was used to control the stroke of the hydraulic actuators and at the same time used to monitor the beam end displacement. L2 was used to detect any slippage between the corbel and the beam end plate. L3 and L4 were used to monitor the panel zone shear deformation. L5 and L6 were used to monitor the column deformation. L7, L8, and L9 were used to monitor displacements at the column end supports, which were anticipated to be negligible.

Rosettes and uni-axial strain gages were used to measure the strains in the connection region (see Figure 3.8 and Figure 3.9).

3.5 Data Reduction

The total Inelastic Rotation (θ_p) of the specimen was calculated by dividing the inelastic component of the beam tip displacement (δ_p), measured at the actuator line of action, by the beam span length from the column centerline to the actuator line of action:

$$\theta_p = \frac{\delta_p}{L} = \frac{1}{L}(\delta_{total} - \delta_e) = \frac{1}{L}\left(\delta_{total} - \frac{P}{K}\right) \tag{3.1}$$

where δ_{total} is the total beam tip deflection measured by displacement transducer L1, P is the applied load, and K is the elastic stiffness determined from the initial low-amplitude test results. The panel zone component was determined from displacement transducers L3 and L4. Together with the measurement of transducers L5 and L6, the component of the total beam tip deflection due to the column deformation can also be established (Uang and Bondad, 1996).

3.6 AISC Acceptance Criteria

Per Section E3.6b of AISC 341, beam-to-column connections used in Special Moment Frames shall satisfy the following requirements:

(1) The connection shall be capable of accommodating a story drift angle of at least 0.04 rad.

(2) The measured flexural resistance of the connection, determined at the column face, shall equal at least $0.8M_p$ of the connected beam at a story drift angle of 0.04 rad, where M_p is the nominal plastic moment of the beam.

3.7 Loading Sequence

Testing was conducted in a displacement control mode. The loading sequence used for all specimens was the standard AISC loading sequence specified in Section K2 of AISC

341. This loading sequence specifies a series of load cycles at different Story Drift Angles (hereinafter referred to as "drift"), with the distance from the column centerline to actuator line of action being used in calculating the drift angle. The loading history begins with six cycles each at 0.00375, 0.005, and 0.0075 rad drifts. These are followed by four cycles at 0.01 rad drifts, two cycles at 0.015 rad drifts, two cycles at 0.02, 0.03, 0.04 rad drifts, etc. up until failure. It should be noted that in testing of Specimen C2, after successful completion of 0.05 rad drift cycles, it was decided to skip the 0.06 rad drift cycles before one cycle at 0.07 rad drift was applied.

3.8 Test Results of Specimen C1

3.8.1 Observed Performance

Figure 3.11 shows the specimen prior to testing. At 0.01 rad drift, minor yielding of beam top and bottom flanges was observed (Figure 3.12). At the end of the second cycle of -0.015 rad drift, panel zone yielding was observed and yielding in the beam flanges extended into the web [Figure 3.13(b) and (c)]. However, no damage to any of the continuity plates fillet welds was observed, [Figure 3.13(d) and (e)].

Both beam flange local buckling and lateral-torsional buckling were observed at 0.03 rad drift. The specimen reached its peak strength at this drift level, but the fillet welds remained intact (Figure 3.14). At 0.04 rad drift, yielding in the beam and panel zone as well as beam buckling became more severe (Figure 3.15). Figure 3.16 shows the global view of the specimen after completing one cycle at 0.05 rad drift. The beam flexural strength at the face of the column had degraded below 80% of the beam nominal plastic moment, and the test was stopped. Figure 3.17 shows the fillet welds of the continuity

plates after completing the test, showing no sign of damage. Figure 3.18 depicts lateral-torsional buckling of the beam at 0.03, 0.04, and 0.05 rad drifts.

3.8.2 Recorded Response

3.8.2.1 Global Response

A plot of the load versus beam tip displacement is shown in Figure 3.19. The relationship between the moment at the column face and the story drift angle is shown in Figure 3.20; the vertical axis on the right shows the moment normalized by the nominal plastic moment (M_{pn}) of the beam. Vertical dotted lines indicate 0.04 rad drift as required by AISC 341 for Special Moment Frame. The specimen completed two cycles at a story drift angle of 0.04 rad before the moment at the column face degraded below $0.8M_{pn}$.

Figure 3.21 shows the relationship between the moment at the column face and the total plastic rotation. Figure 3.22 shows that the panel zone yielded in shear. The "unusual" nonlinear response in the figure was due to twisting of the deep column (Chi and Uang 2002).

3.8.2.2 Local Response

Figure 3.23 shows the flexural strain profiles of the beam top and bottom flanges at a section 3 in. away from the column face. Buckling in the beam skewed the strain profiles at higher drift levels. Figure 3.24 and Figure 3.25 show the strain profiles on the top and bottom continuity plates, respectively. The continuity plates remained essentially elastic. Figure 3.26(a) and (c) show the normal strain profiles at Sections G and H, respectively. The strain near the non-loading column flange was lower than that near the loaded column flange. Figure 3.26(b) shows the normal strains on both surfaces of the top

continuity plate were very similar. Figure 3.26(d) compares the normal strains of the top and bottom continuity plates at a section 1½ in. away from the non-loaded column flange.

Figure 3.27 shows the flexural strain response of two pairs of strain gages located 30 in. above and below the top and the bottom beam flanges, respectively. The response of each pair is expected to be similar such that the plot lies on a 45° line. However, warping stresses created by column twisting when the drift 1.5% caused the response to deviate from a line of 45°. Figure 3.28 shows that shear yielding occurred near the top and bottom portions of the beam web.

3.9 Test Results of Specimen C2

3.9.1 Observed Performance

Significant panel zone yielding with column flange kinking was expected because Specimen C2 was designed with a demand-capacity ratio of 0.95 for the panel zone. Figure 3.29 shows the specimen prior to testing. The specimen remained essentially elastic until 0.0075 rad drift cycles. At the end of 0.0075 rad drift, yielding of the panel zone started (Figure 3.30). At the completion of 0.01 rad drift cycles, yielding at the top and the bottom beam flanges was also visible (Figure 3.31). Figure 3.32 shows the connection at the end of second cycle of -0.015 rad drift; the fillet welds connecting the continuity plates to the column flanges were intact. Yielding extended to the beam web at 0.03 rad drift [Figure 3.33(a)]. Panel zone yielding was significant, and yielding of the column flange at the column flange kink locations was observed [Figure 3.33(b) and (c)]. Figure 3.34 shows the specimen at 0.04 rad drift. All the fillet welds were intact [Figure 3.34(c) and (d)]. Although the $b_f/2t_f$ and h/t_w ratios of Specimens C2 were somewhat larger than those of Specimen C1 (Table 3.1), local buckling was less severe in C2 because the weaker panel zone

accommodated more inelastic deformation at the same drift level. As can be seen in Figure 3.34(f), panel zone yielding was very significant.

Figure 3.35 shows the specimen after completing two cycles at 0.05 rad drift. It was then decided to displace the specimen to 0.07 rad drift directly. Testing was stopped after completing one cycle at 0.07 rad drift because the beam flexural strength at the face of the column had degraded below 80% of the beam nominal plastic moment. Figure 3.36 and Figure 3.37 show the connection at the end of +0.07 and -0.07 rad drifts, respectively. Figure 3.38 shows lateral-torsional buckling of the beam at -0.05 and -0.07 rad drift. At 5% drift, note that lateral-torsional buckling was much less severe in Specimen C2 than in C1 [Figure 3.18(c)] because the latter had a deep column and was more prone to column twisting. On the way to return the specimen to its zero beam tip displacement, the beam bottom flange completely fractured (Figure 3.39).

It was observed after testing that continuity plates had yielded [Figure 3.40(a)] and column flange yielding at the kink locations was more pronounced [Figure 3.40(b) and (c)]. No damage in the fillet welds was observed, which was confirmed from magnetic particle inspection conducted after the test.

3.9.2 Recorded Response

3.9.2.1 Global Response

A plot of the load versus the beam tip displacement is shown in Figure 3.41. The relationship between the moment at the face of the column and story drift angle is shown in Figure 3.42. The specimen completed two cycles at a story drift angle of 0.05 rad before the moment at the column face degraded below $0.8M_{pn}$.

Figure 3.43 shows the relationship between the moment at the column face and the total plastic rotation. Figure 3.44 shows the panel zone experienced significant shear yielding and reached 8.5 times the shear yield strain. The column remained essentially elastic throughout the test.

3.9.2.2 Local Response

Figure 3.45 shows the flexural strain profiles on the beam top and bottom flanges at a distance 3 in. away from the column face. (Strain gage S14 malfunctioned.) The strain profiles were more uniform across the flange width when compared with those of Specimen C1 (Figure 3.23), mainly because a shallow (W14) column that was less prone to column twisting was used. The recorded strains in the top and bottom continuity plates (Figure 3.46 and Figure 3.47) showed that yielding had occurred. (Recall that the continuity plates were intentionally undersized by 1/4 in.) The maximum normal strain was about three times the yield strain. Despite the significant yielding in the continuity plates, the connection performance was not affected.

Figure 3.48 compares the normal strain profiles in the top and the bottom continuity plates. (The reading from rosette R01 seems unreliable since it almost read zero strains.) As comparison of Figure 3.48(d) with Figure 3.26(c) of Specimen C1 shows that more force in the continuity plate was transmitted to the unloaded column flange when a shallow column was used. Figure 3.49 indicates significant shear yielding on the beam web close to the column flange.

Parts of chapters 3, have been accepted for publication of the material as it may appear in *Engineering Journal*, 2017, Mashayekh, A., and Uang, C.M. The dissertation author was the primary researcher and author of this material.

Table 3.1 Member Sizes and Cross Sectional Dimensions

Spec. No.	Member	d (in)	t_w (in)	h/t_w	b_f (in)	t_f (in)	$b_f/2t_f$
C1	Beam (W30×116)	30.0	0.565	47.8	10.5	0.85	6.17
	Column (W24×176)	25.2	0.75	28.7	12.9	1.34	4.81
C2	Beam (W36×150)	35.9	0.625	51.9	12.0	0.94	6.37
	Column (W14×257)	16.4	1.18	9.71	16.0	1.89	4.23

Table 3.2 RBS Connection Key Design Parameters

(a) Specimen C1: W30×116 Beam Connected to a W24×176 Column

RBS Dimensions: $a = 7$ in., $b = 25$ in., $c = 2$ in.
Plastic Section Modulus of RBS Section, $Z_{RBS} = 278.9$ in^3; $\frac{Z_{RBS}}{Z_{beam}} = 0.74$
Probable maximum moment, $M_{pr} = 1470$ kip-ft
Shear force at the center of the RBS, $V_{RBS} = 119.3$ kips
Probable maximum moment at the face of the column, $M_f = 1664$ kip-ft
Plastic moment of the beam based on the expected yield stress, $M_{pe} = 1732.5$ kip-ft
$\phi_d M_{pe} = 1732.5 \geq M_f = 1664$ kip-ft (OK)
Strong-Column/Weak-Beam Check: $\frac{\sum M_{pc}^*}{\sum M_{pb}^*} = 2.38 \geq 1.0$ (OK)
Panel Zone Demand-Capacity Ratio (DCR) = $\frac{573.11}{636.5} = 0.9 \leq 1.0$ (OK)
No Doubler Plates Required
Continuity Plate Flange Weld Forces (Normal, Shear, and Resultant): $P_{cp} = 157.6$ kips, $V_{cp} = 26.7$ kips, $R_{cp} = \sqrt{P_{cp}^2 + V_{cp}^2} = 159.8$ kips
Continuity Plate Web Weld Force (Shear): $\sum P_{cp} = 157.6$ kips
Continuity plate thickness,$t_{cp} = 3/4$ in.
Continuity Plate-to-Column Flange Weld: $9/16$ in. (Fillet Welds)
Continuity Plate-to-Column Web Weld: $5/16$ in. (Fillet Welds)

Table 3.2 RBS Connection Key Design Parameters (continued)

(b) Specimen C2: W36×150 Beam Connected to a W14×257 Column

RBS Dimensions: $a = 7$ in., $b = 25$ in., $c = 2.5$ in.
Plastic Section Modulus of RBS Section, $Z_{RBS} = 416.7$ in^3; $\frac{Z_{RBS}}{Z_{beam}} = 0.72$
Probable maximum moment, $M_{pr} = 2196.3$ kip-ft
Shear force at the center of the RBS, $V_{RBS} = 173.1$ kips
Probable maximum moment at the face of the column, $M_f = 2477$ kip-ft
Plastic moment of the beam based on the expected yield stress, $M_{pe} = 2662.9$ kip-ft
$\phi_d M_{pe} = 2662.9 \geq M_f = 2477$ kip-ft (OK)
Strong-Column/Weak-Beam Ratio: $\frac{\sum M_{pc}^*}{\sum M_{pb}^*} = 1.56 \geq 1.0$ (OK)
Panel Zone Demand-Capacity Ratio (DCR) = $\frac{688.2}{723.8} = 0.95 \leq 1.0$ (OK)
No Doubler Plates Required
Continuity Plate Flange Weld Forces (Normal, Shear, and Resultant): $P_{cp} = 157$ kips, $V_{cp} = 62.8$ kips, $R_{cp} = \sqrt{P_{cp}^2 + V_{cp}^2} = 169.1$ kips
Continuity Plate Web Weld Force (Shear): $\sum P_{cp} = 157$ kips
Continuity plate thickness: t_{cp}= 5/8 in.
Continuity Plate-to-Column Flange Weld: $1/2$ in. (Fillet Welds)
Continuity Plate-to-Column Web Weld: $9/16$ in. (Fillet Welds)

Table 3.3 Comparison of Continuity Plate and Weld Design

	Specimen C1		Specimen C2	
	Proposed Procedure	AISC 341	Proposed Procedure	AISC 341
Required Continuity Plate Forces (kips)	$P_{cp} = 157.6$ $V_{cp} = 26.7$	N.A.	$P_{cp} = 157.0$ $V_{cp} = 62.8$	N.A.
Continuity Plate Thickness	3/4 in.	$1/2$ in. ($= t_{bf}/2$)	$5/8$ in.	$1/2$ in. ($= t_{bf}/2$)
Continuity Plate-to-Column Flange Weld	Fillet Weld ($9/16$ in.)	CJP Weld	Fillet Weld ($1/2$ in.)	CJP Weld
Continuity Plate-to-Column Web Weld	Fillet Weld ($5/16$ in.)	Fillet Weld ($3/16$ in.)	Fillet Weld ($9/16$ in.)	Fillet Weld ($3/8$ in.)

Table 3.4 Strength Check of Continuity Plates

Specimen No.	Equation (2.31)			
	Moment Component, $\left(\frac{P_{cp}e}{Z_{xn}F_{ycp}}\right)$	Normal Force Component, $\left(\frac{P_{cp}}{F_{ycp}A_n}\right)^2$	Shear Force Component, $\left(\frac{V_{cp}}{\frac{F_{ycp}}{\sqrt{3}}A_n}\right)^4$	Σ
C1	0.14	0.78	0.01	0.93
C2	0.36	0.80	0.15	1.31

Table 3.5 Base Metal Mechanical Properties

Spec. No.	Component	Steel Type/ Heat No.	Yield Stress (ksi)[a]	Tensile Strength (ksi)	Elong. (%)[b]
C1	Beam Flange (W30×116)	A992 443484	56.9 (56.5)[b]	75.6 (72.0)[b]	34.5 (28.0)[b]
	Beam Web (W30×116)		58.5	73.2	39.5
	Column Flange (W24×176)	A992 442208	57.2 (57.5)[b]	70.6 (72.5)[b]	39.1 (27.0)[b]
	Column Web (W24×176)		58.5	72.2	37.3
	Continuity Plate (3/4 in.)	A572 Gr. 50 SB15106	68.1 (58.0)[b]	85.6 (81.0)[b]	36.9 (25.0)[b]
C2	Beam Flange (W36×150)	A992 60114091/04	53.5 (57.0)[b]	74.9 (75.1)[b]	38.3 (26.4)[b]
	Beam Web (W36×150)		57.9	74.7	38.1
	Column Flange (W14×257)	A992 317275	52.3 (57.0)[b]	74.3 (75.0)[b]	37.7 (26.0)[b]
	Column Web (W14×257)		54.8	74.8	38.6
	Continuity Plate (5/8 in.)	A572 Gr. 50 813K75180	54.1 (57.6)[b]	79.8 (82.6)[b]	35.1 (22.5)[b]

[a] Yield strength determined by the 0.2% strain offset method.
[b] Values in parentheses from Certified Mill Test Reports, others from testing at UCSD.

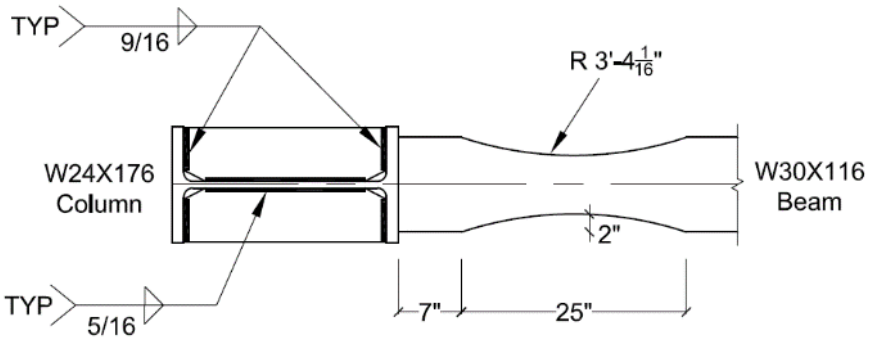

(a) Plan View

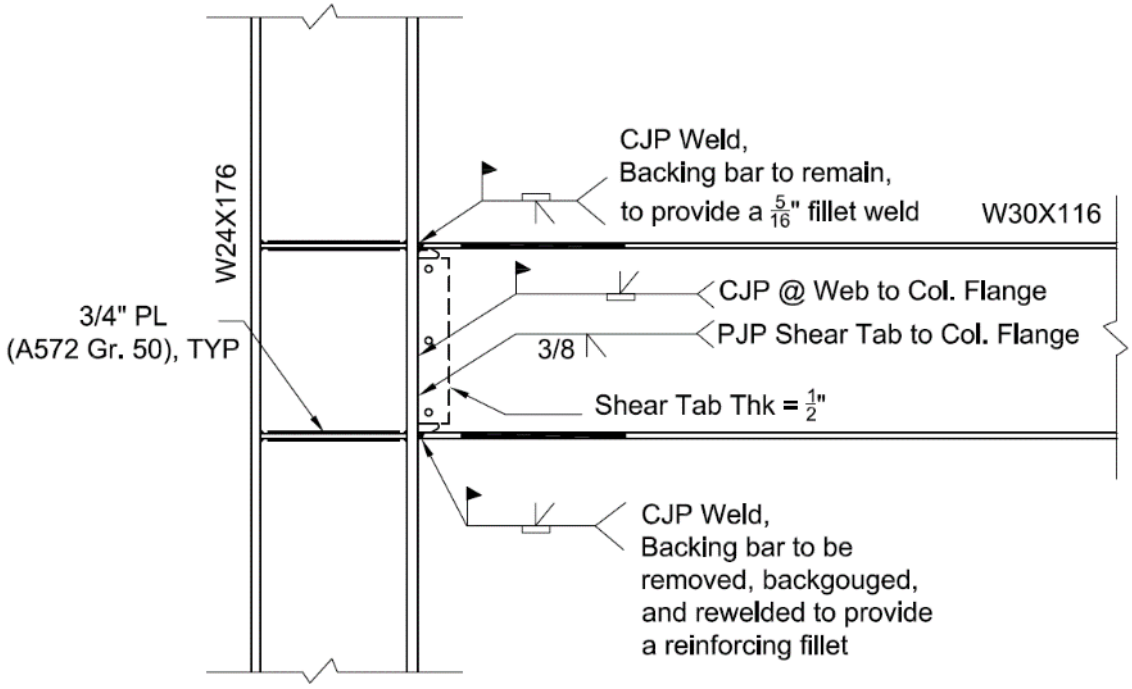

(b) Elevation View

Figure 3.1 Specimen C1 Connection Detail

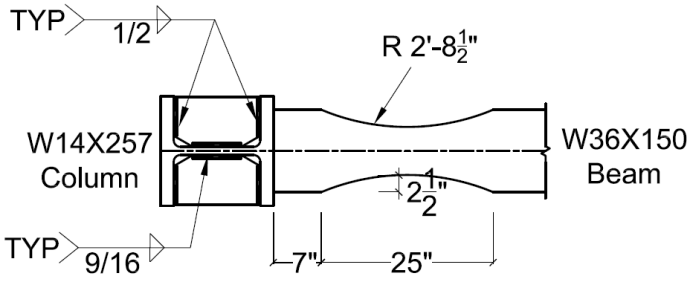

(a) Plan View

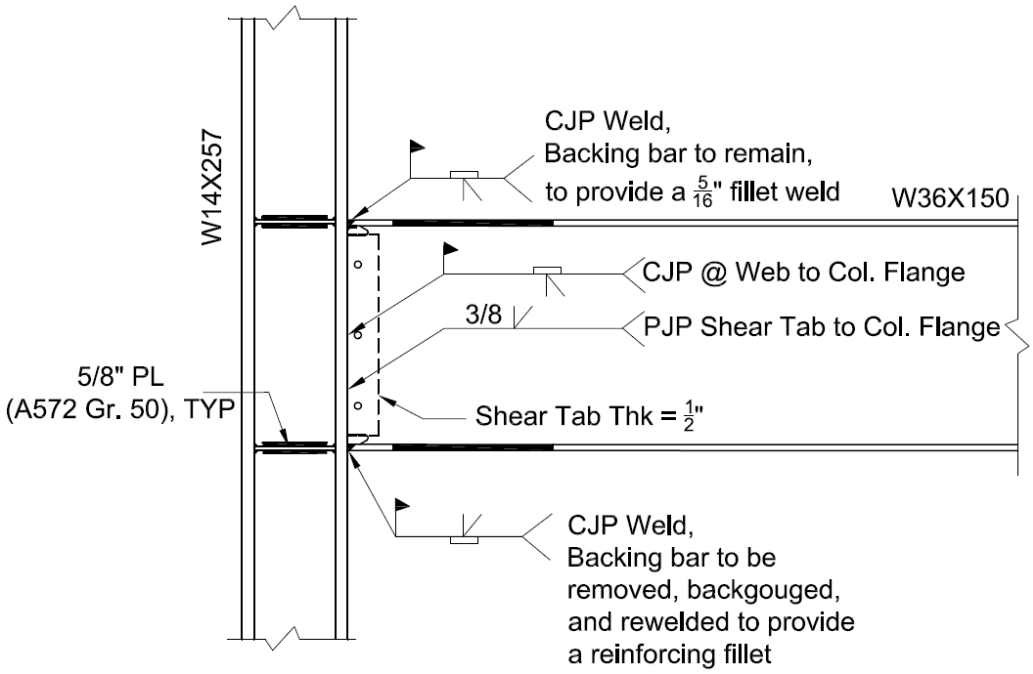

(b) Elevation View

Figure 3.2 Specimen C2 Connection Detail

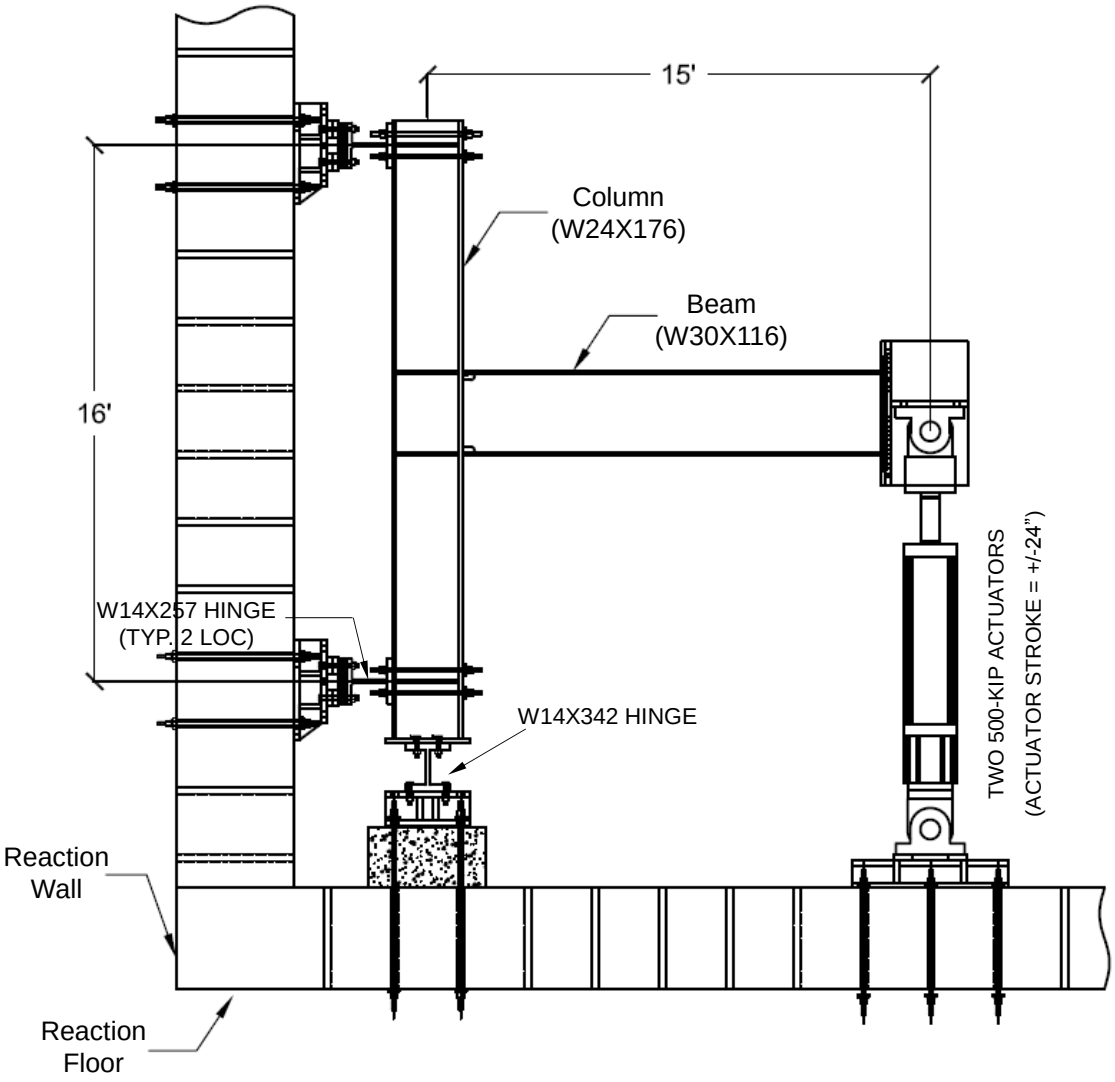

Note: Lateral bracing system not shown

(a) Specimen C1

Figure 3.3 Test Setup

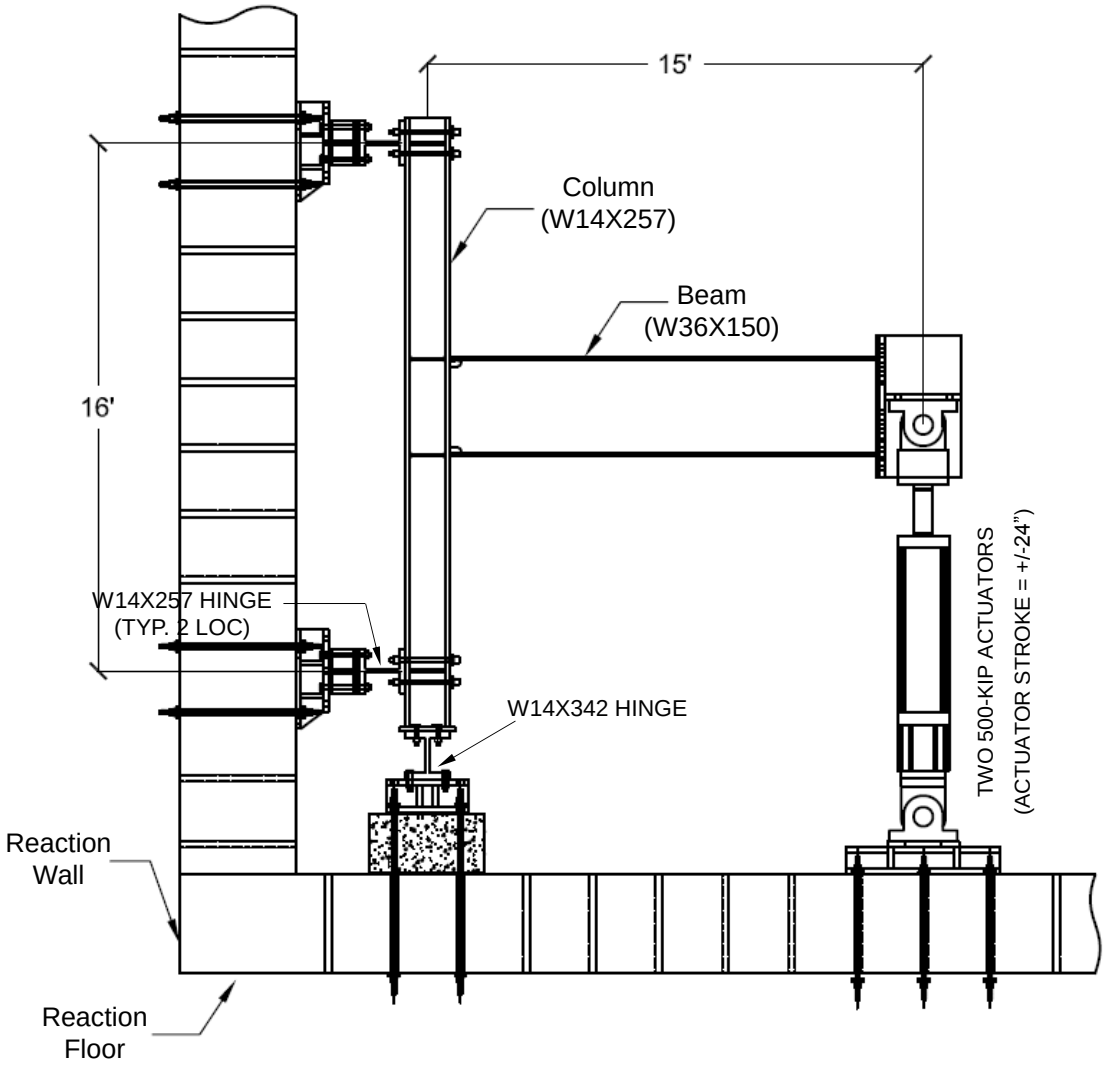

Note: Lateral bracing system not shown

(b) Specimen C2

Figure 3.3 Test Setup (continued)

(a) Top End

(b) Bottom End

Figure 3.4 Hinge Supports

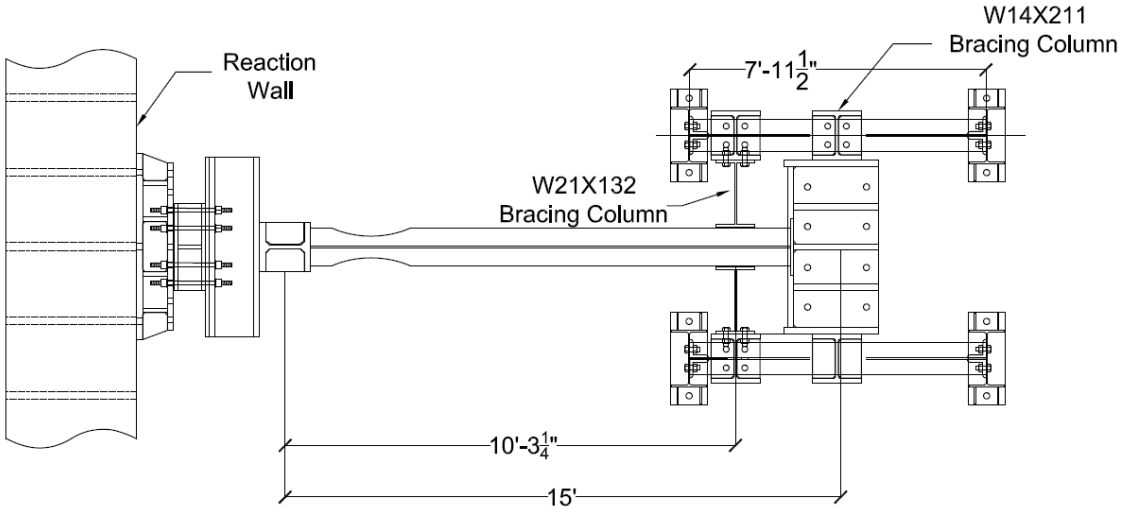

(a) Plan View

(b) View from West

(c) View from South-East

Figure 3.5 Beam Lateral Bracing System

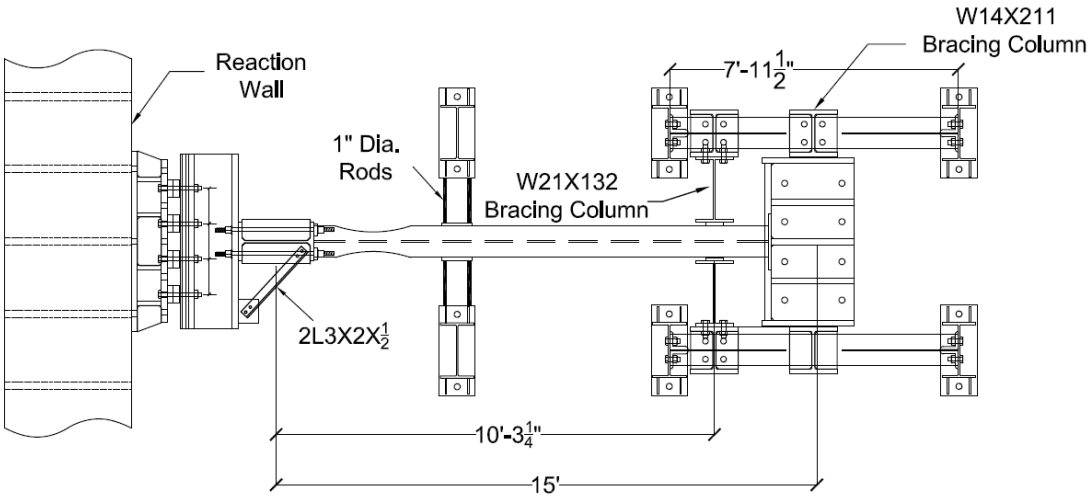

(a) Plan View

(b) View from East

(c) View from West

(d) Column Top Bracing

Figure 3.6 RBS and Column Top Bracings (Specimen C1 with a Deep Column)

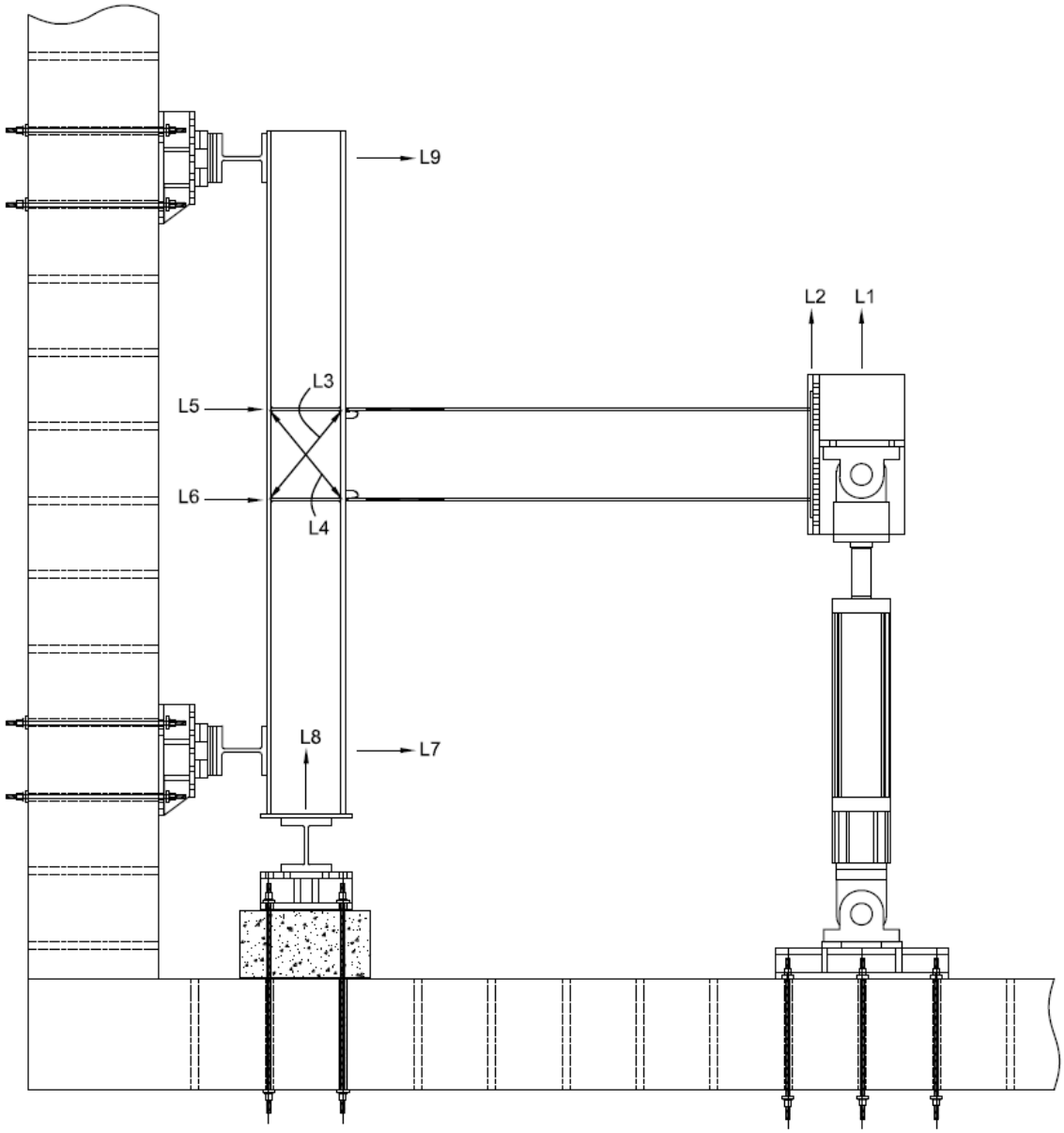

Figure 3.7 Location of Displacement Transducers

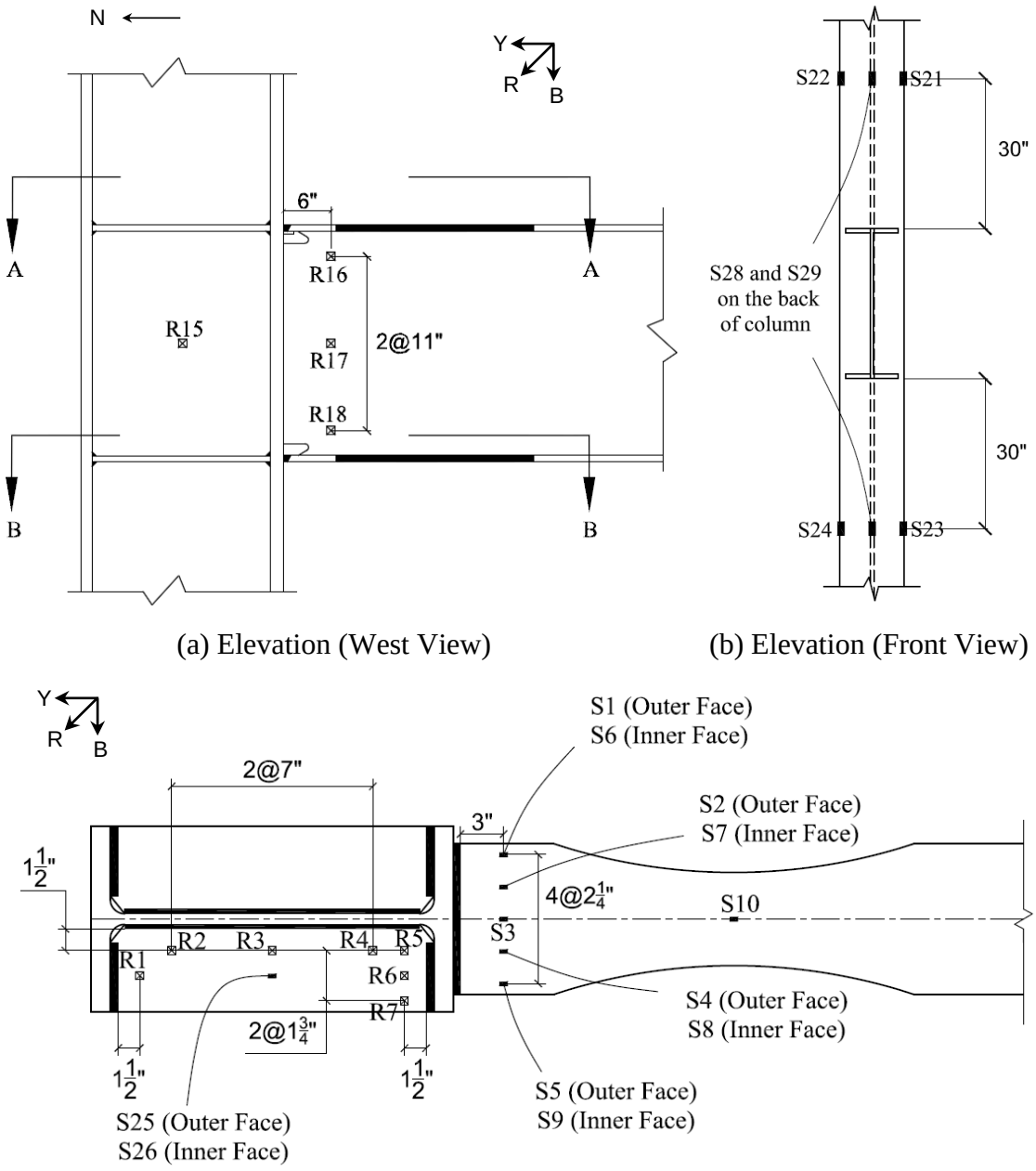

(a) Elevation (West View)

(b) Elevation (Front View)

(c) View A-A

Figure 3.8 Specimen C1 Strain Gage and Rosette Locations

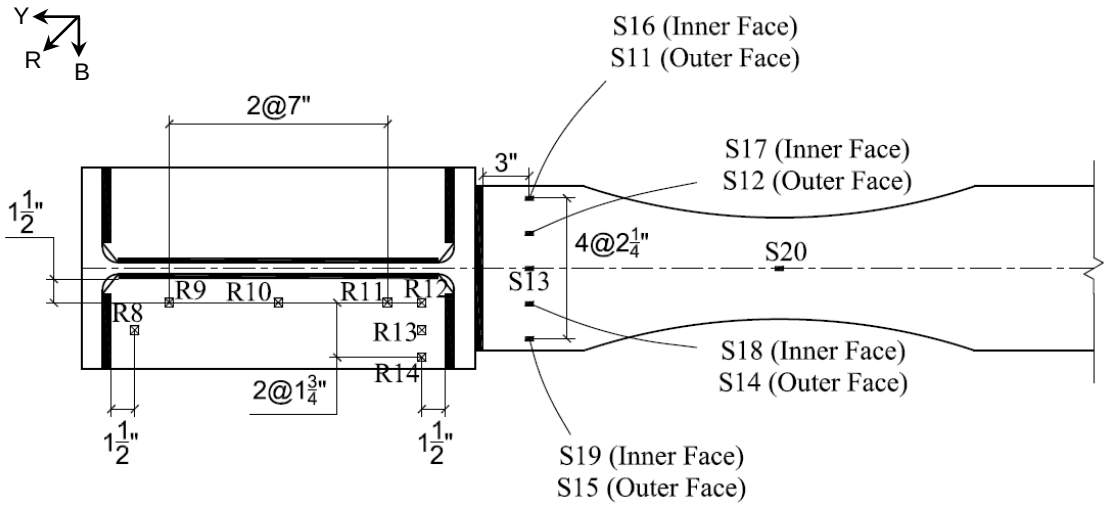

(c) View B-B

Figure 3.8 Specimen C1 Strain Gage and Rosette Locations (continued)

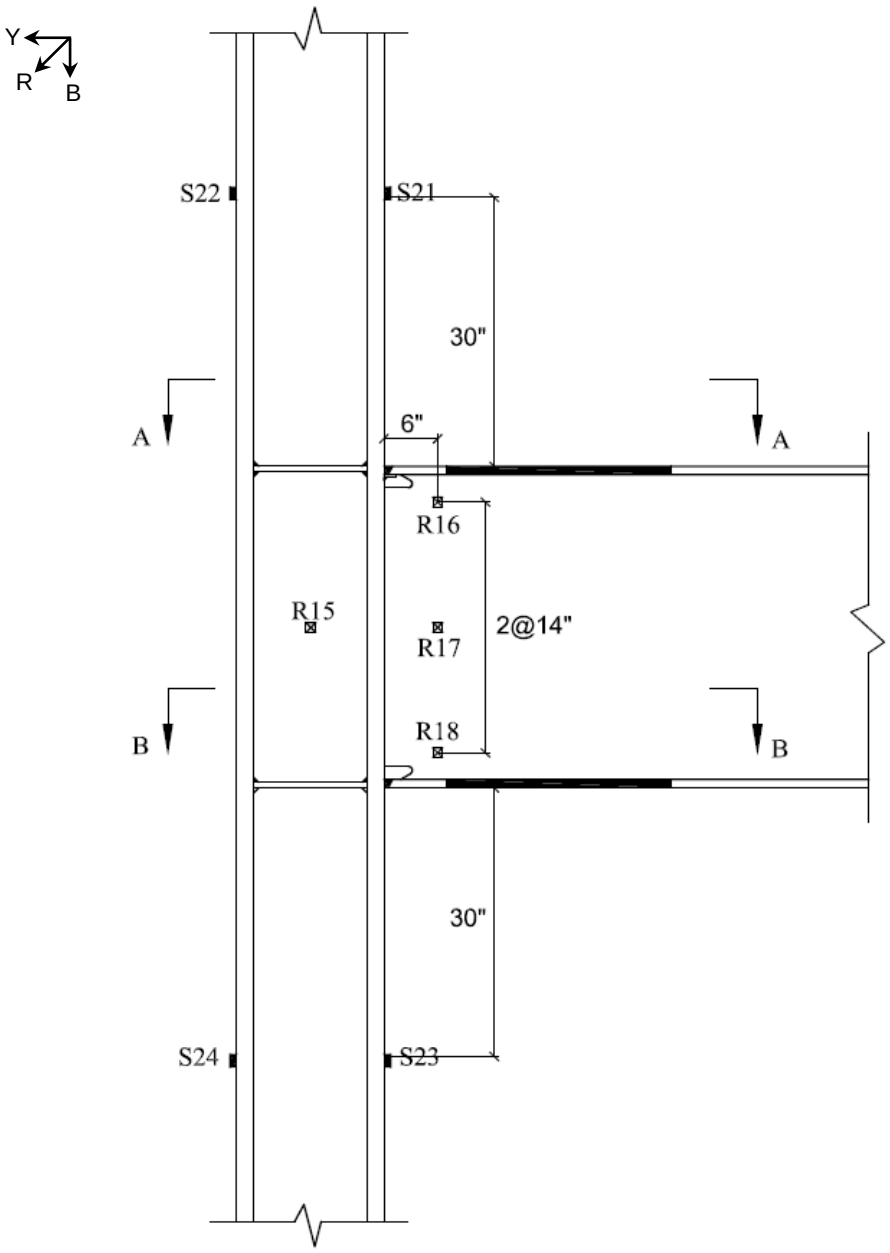

(a) Elevation (West View)

Figure 3.9 Specimen C2 Strain Gage and Rosette Locations

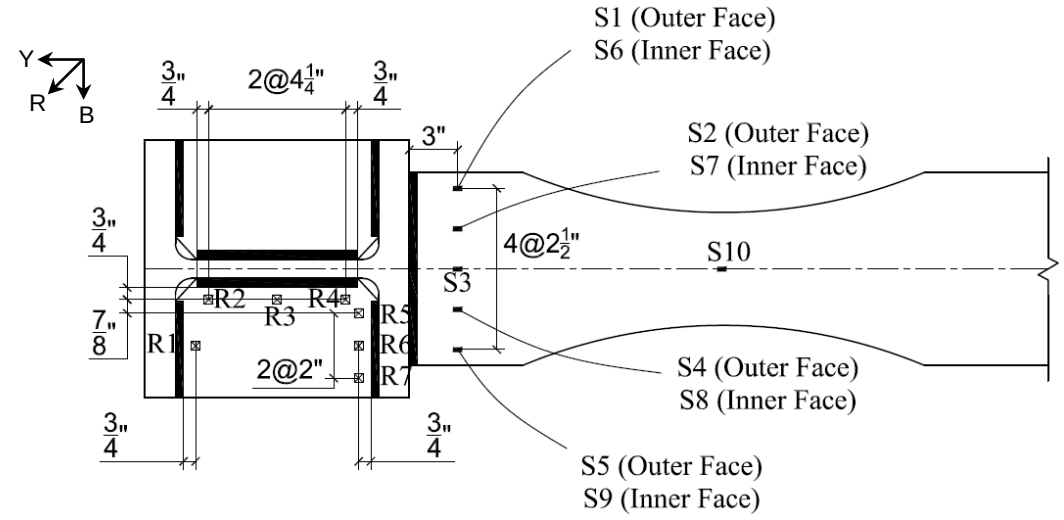

(b) View A-A

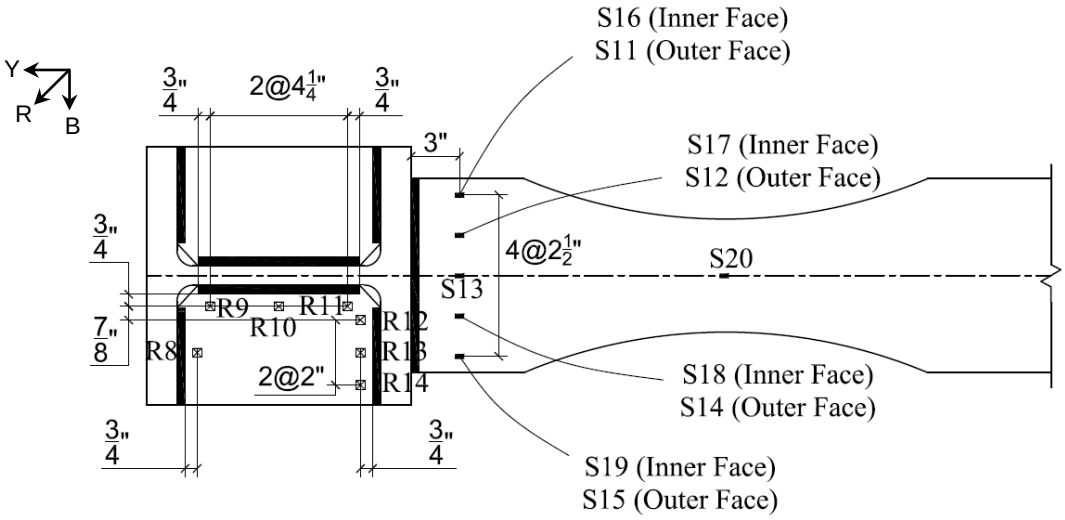

(c) View B-B

Figure 3.9 Specimen C2 Strain Gage and Rosette Locations (continued)

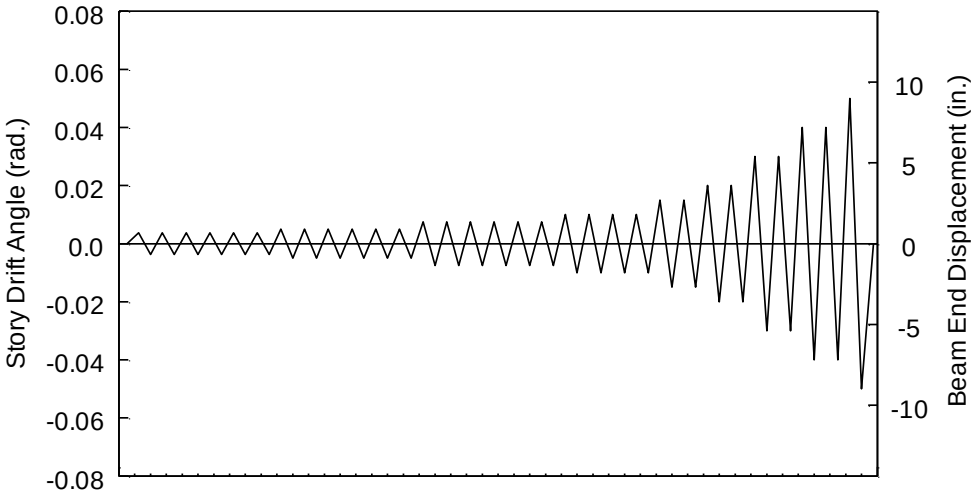

(a) Specimen C1

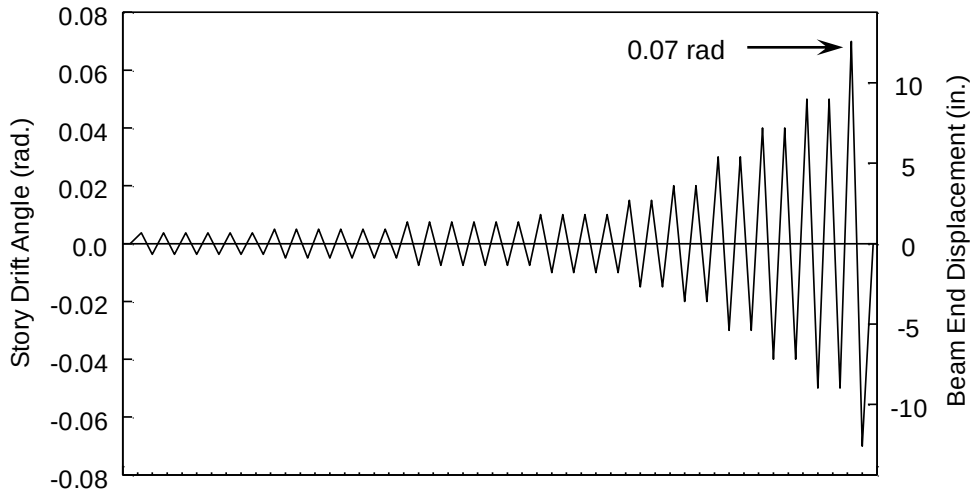

(b) Specimen C2

Figure 3.10 Loading Protocol

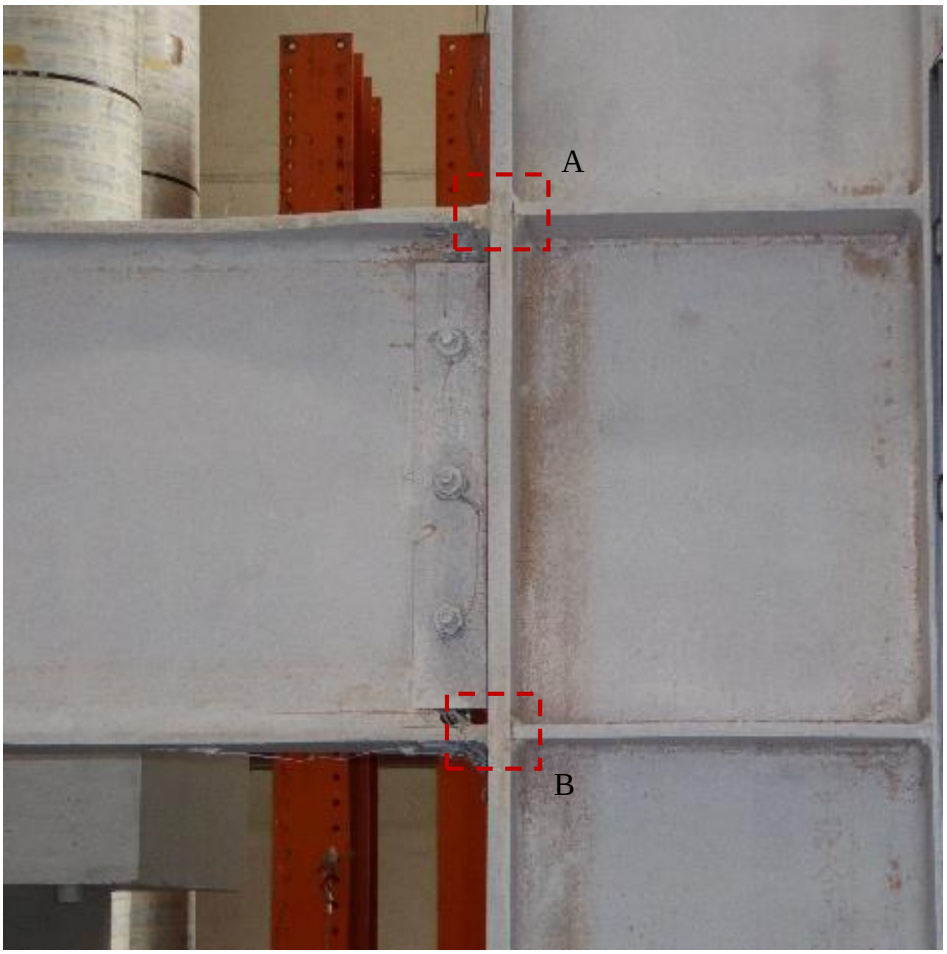

(a) Global View from East

(b) Detail A

(c) Detail B

Figure 3.11 Specimen C1 Connection Prior to Testing

(a) Global View from East

(b) Yielding in Beam Top and Bottom Flanges

Figure 3.12 Specimen C1 at End of -0.01 rad Drift Cycles

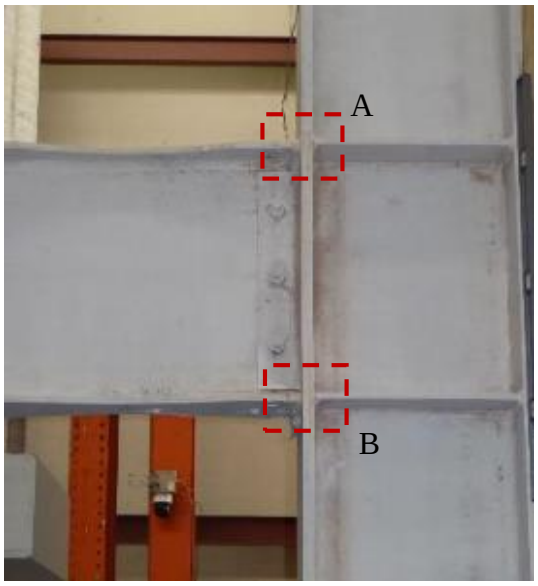

(a) Global View from East

(b) Minor Panel Zone Yielding

(c) Spread of Yielding to Beam Web

(d) Detail A

(e) Detail B

Figure 3.13 Specimen C1 at -0.015 rad Drift (2nd Cycle)

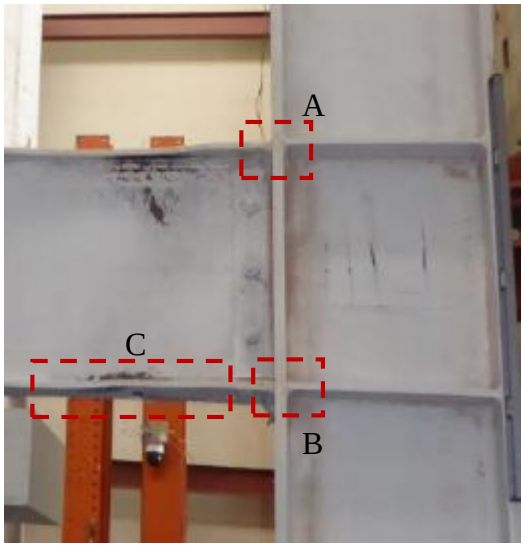

(a) Global View from East

(b) Detail A

(c) Detail B

(d) Detail C (Beam Flange Local Buckling)

(e) Beam Lateral-Torsional Buckling

Figure 3.14 Specimen C1 at -0.03 rad Drift (2nd Cycle)

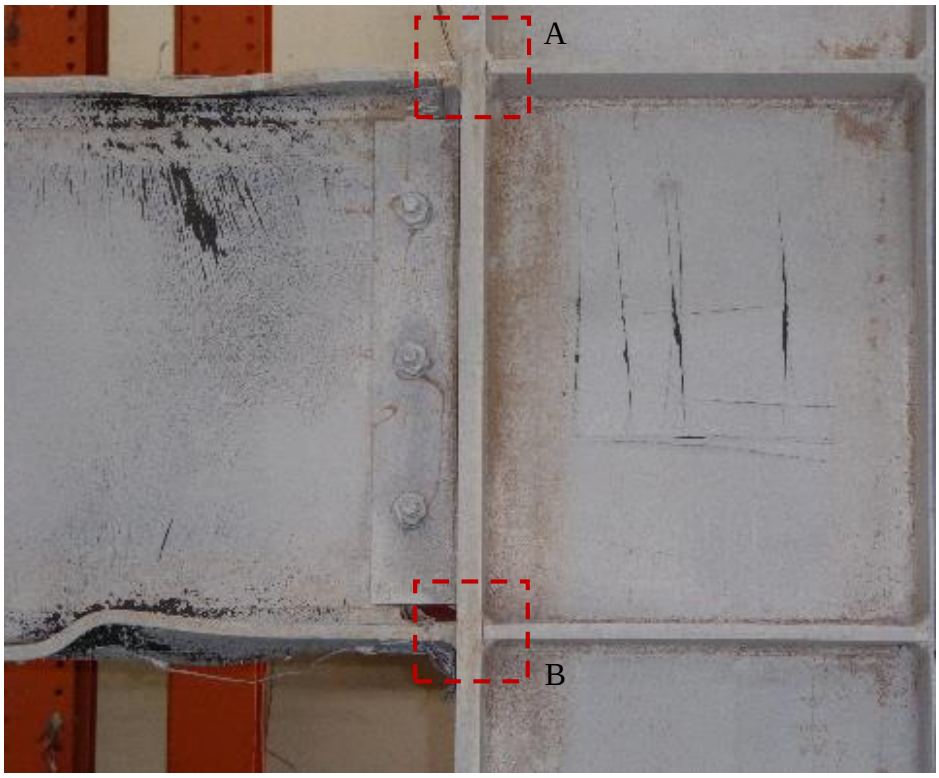

(a) Global View from East

(b) Detail A

(c) Detail B

Figure 3.15 Specimen C1 at -0.04 rad Drift (2nd Cycle)

(a) at +0.05 rad Drift

(b) View from East (at -0.05 rad Drift)

(c) View from West (at -0.05 rad Drift)

Figure 3.16 Specimen C1 at 0.05 rad Drift (1st Cycle)

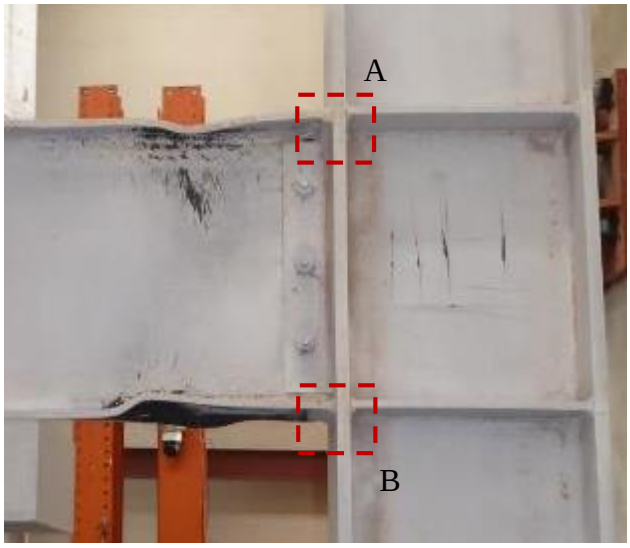

(a) Global View from East

(b) Detail A, View from East

(c) Detail A, view from Bottom

(d) Detail B, View from East

(e) Detail B, View from Bottom

Figure 3.17 Specimen C1 at Test Completion

(a) -0.03 rad Drift (2nd Cycle)

(b) -0.04 rad Drift (2nd Cycle)

(c) -0.05 rad Drift (1st Cycle)

Figure 3.18 Specimen C1 Beam Lateral-Torsional Buckling

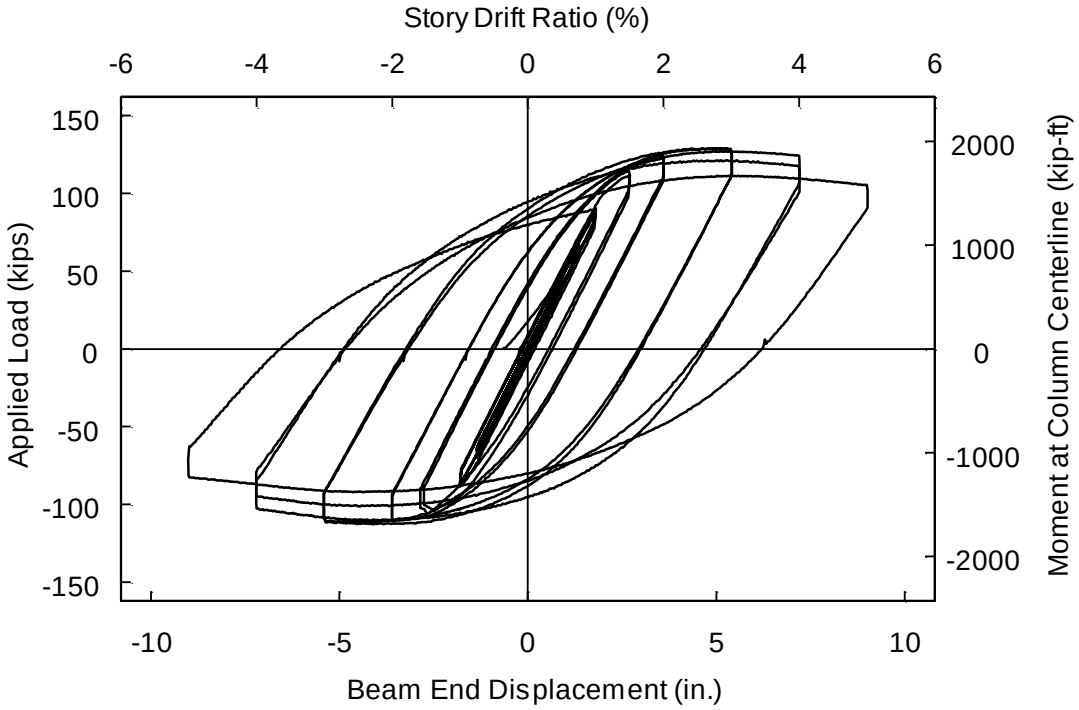

Figure 3.19 Specimen C1 Load versus Beam Tip Displacement Relationship

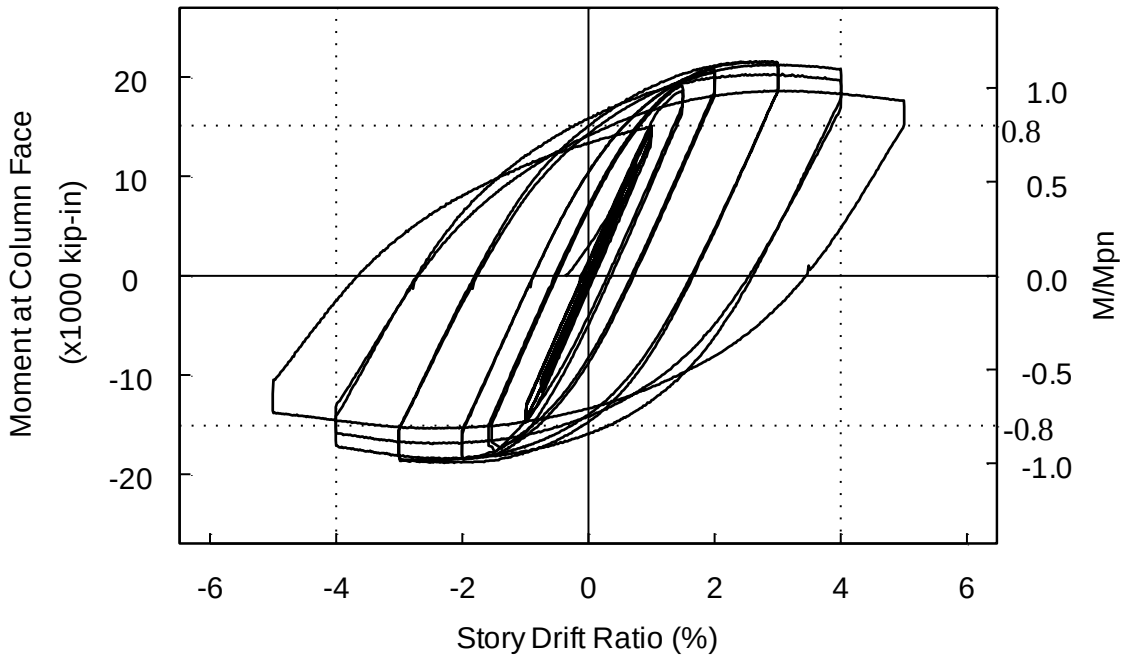

Figure 3.20 Specimen C1 Moment versus Story Drift Angle Relationship

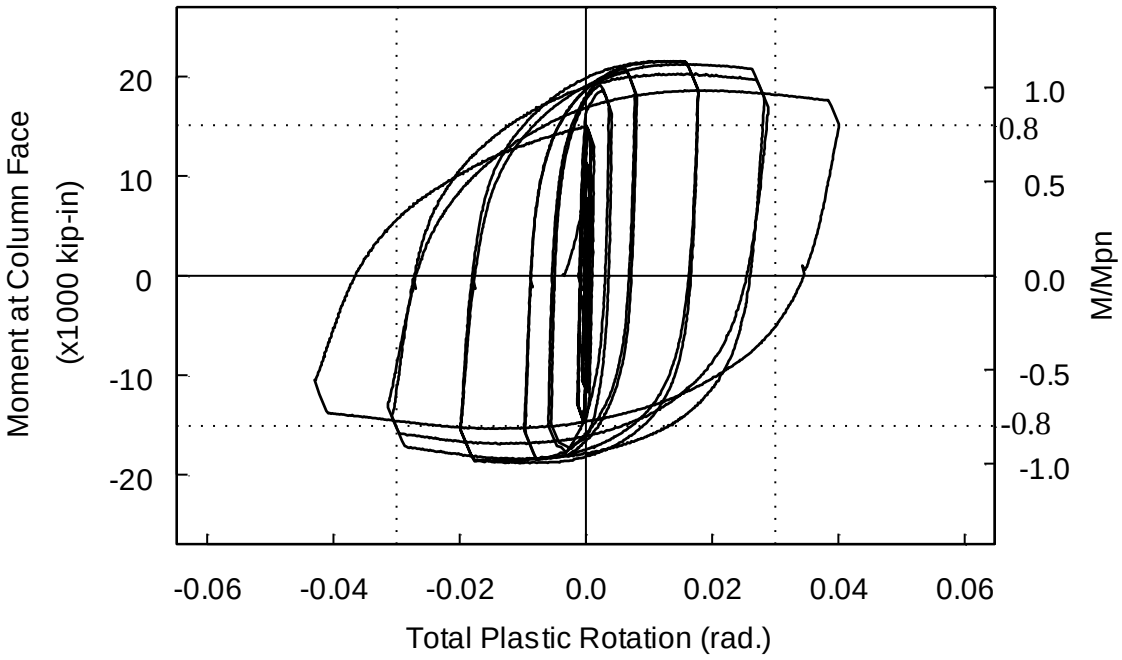

Figure 3.21 Specimen C1 Moment versus Total Plastic Rotation Relationship

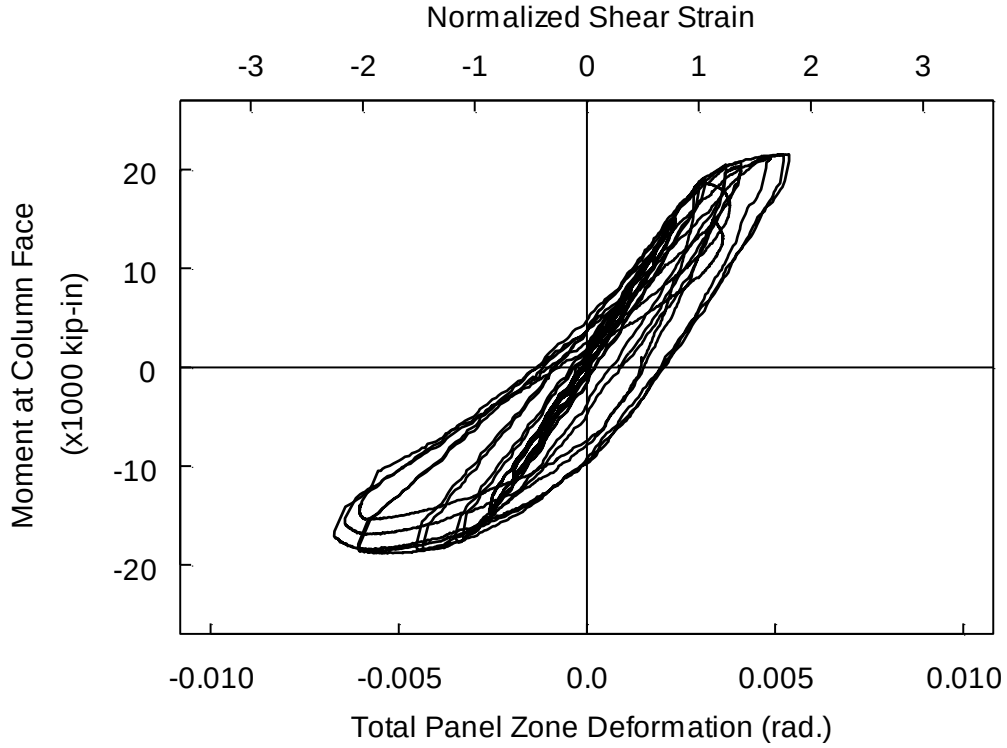

Figure 3.22 Specimen C1 Moment versus Total Panel Zone Shear Deformation Relationship

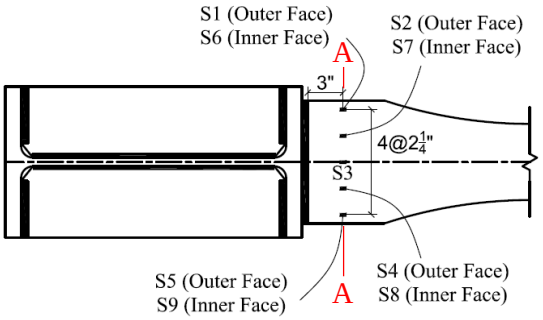

Beam Top Flange

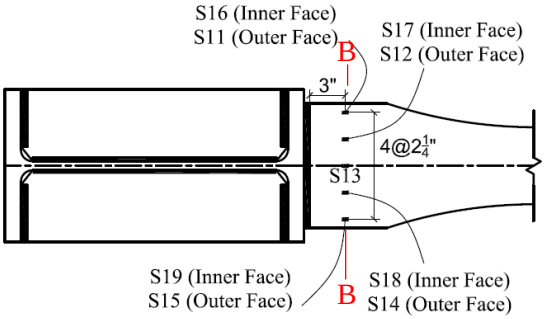

Beam Bottom Flange

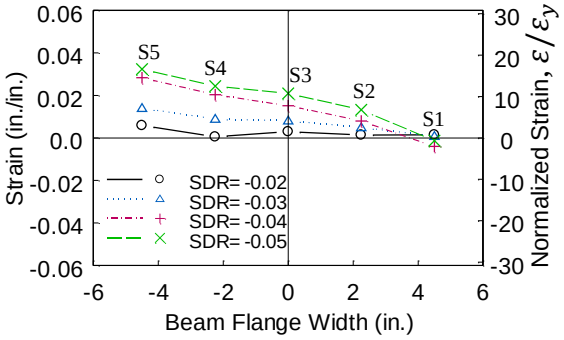

(a) at Section A-A, Outer Face

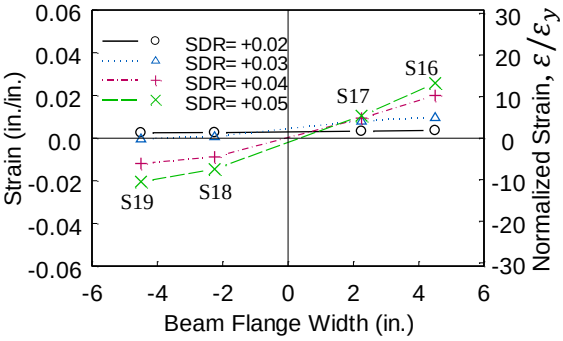

(c) at Section B-B, Inner Face

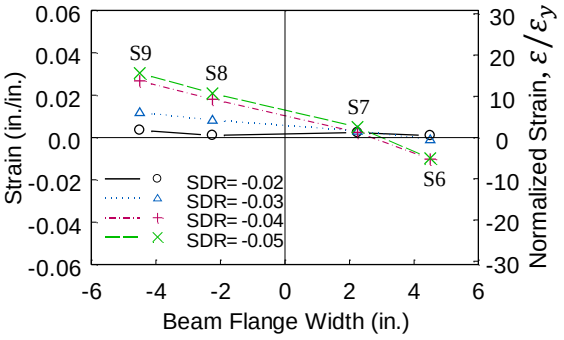

(b) at Section A-A, Inner Face

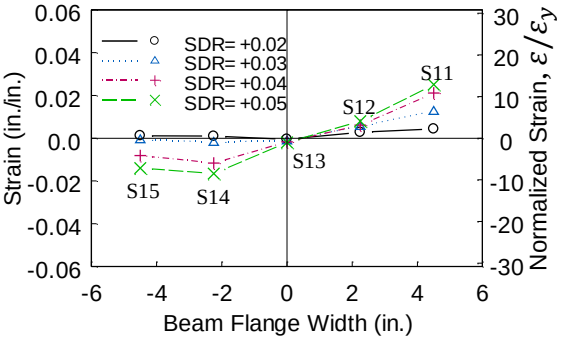

(d) at Section B-B, Outer Face

Figure 3.23 Specimen C1 Beam Flange Flexural Strain Profiles

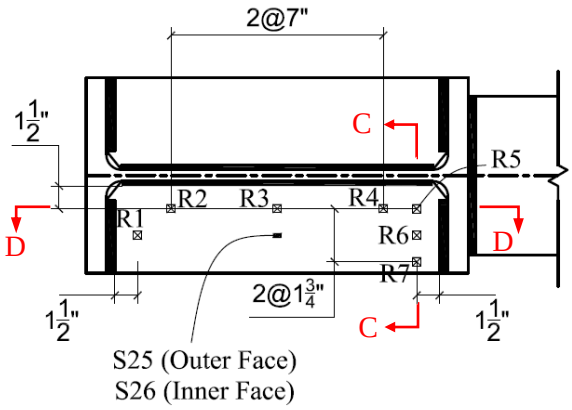

Top Continuity Plate

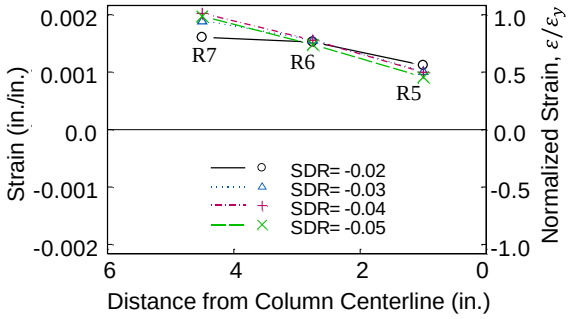

(a) Strain Normal to Flange Weld at Section C-C

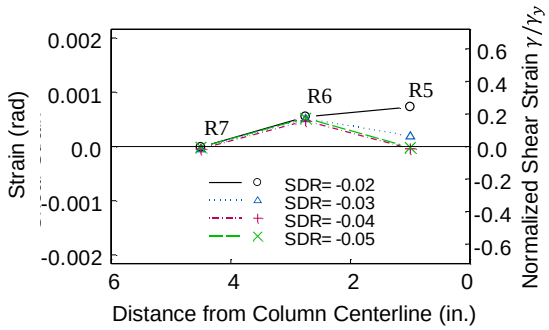

(b) Shear Strain at Section C-C

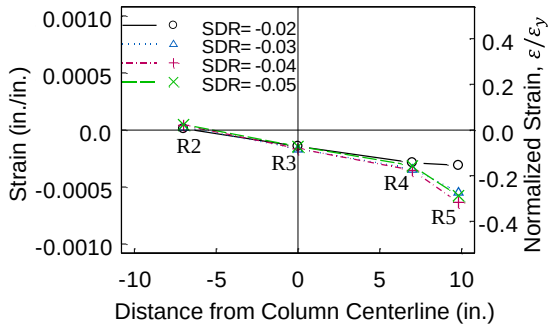

(c) Strain Normal to Web Weld at Section D-D

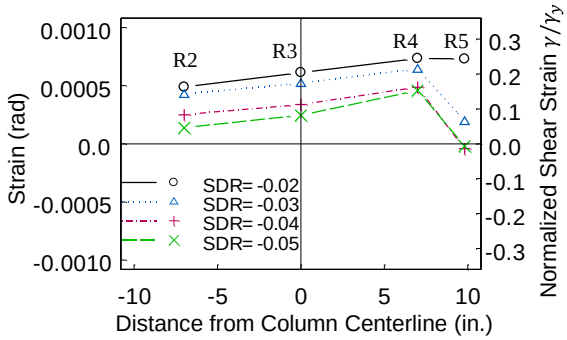

(d) Shear Strain at Section D-D

Figure 3.24 Specimen C1 Top Continuity Plate Strain Profiles

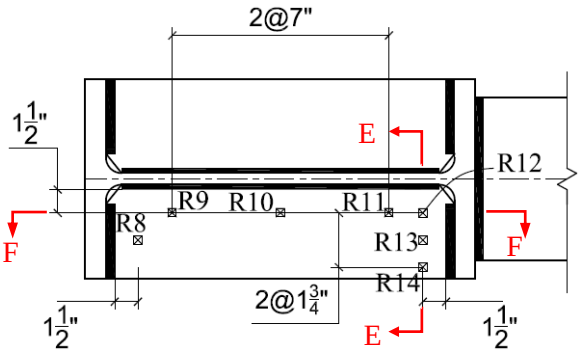

Bottom Continuity Plate

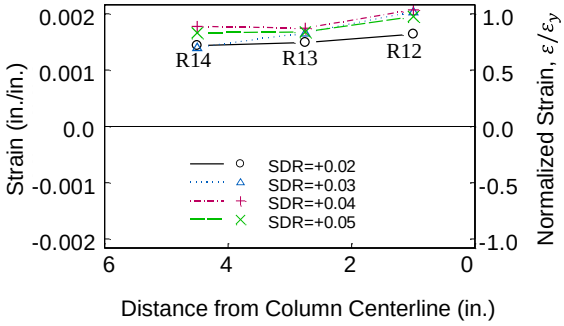

(a) Strain Normal to Flange Weld at Section E-E

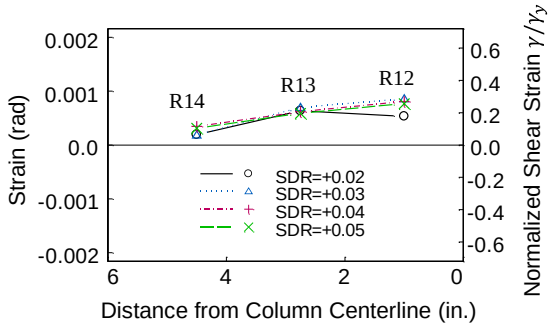

(b) Shear Strain at Section E-E

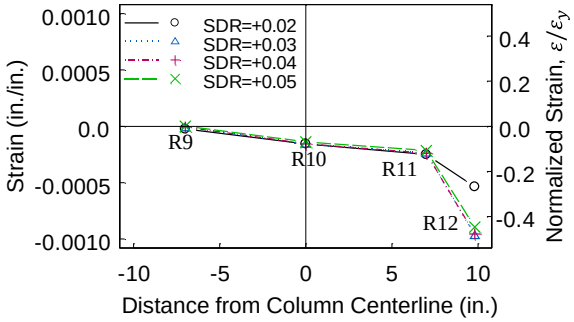

(c) Strain Normal to Web Weld at Section F-F

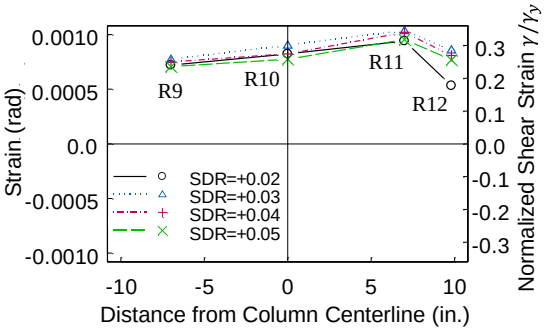

(d) Shear Strain at Section F-F

Figure 3.25 Specimen C1 Bottom Continuity Plate Strain Profiles

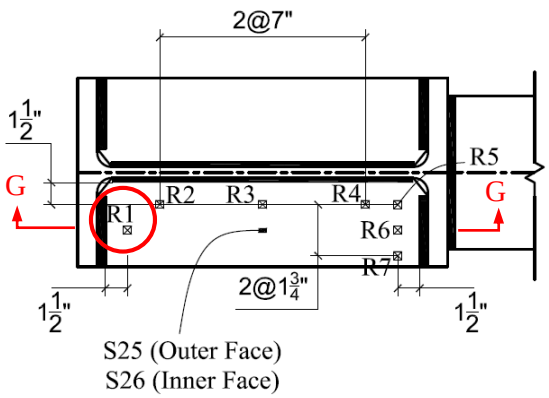

Top Continuity Plate

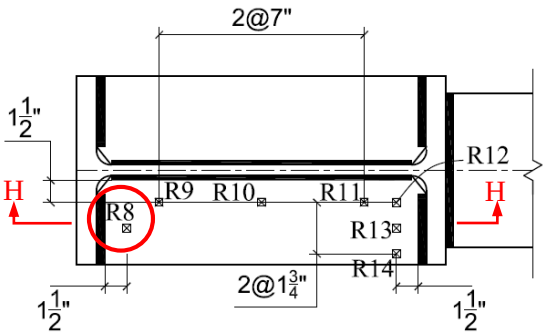

Bottom Continuity Plate

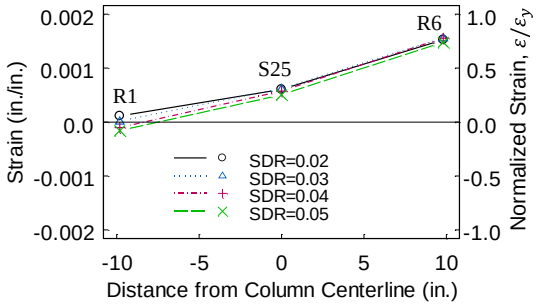

(a) Normal Strain at Section G-G

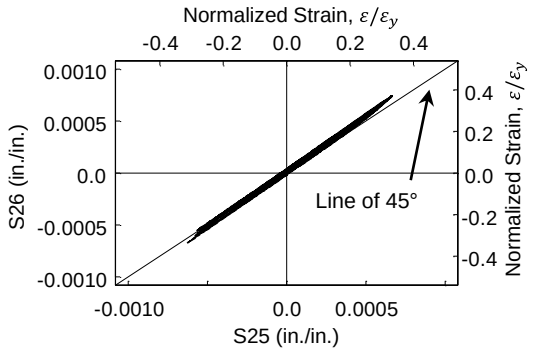

(b) Plot of S25 vs S26

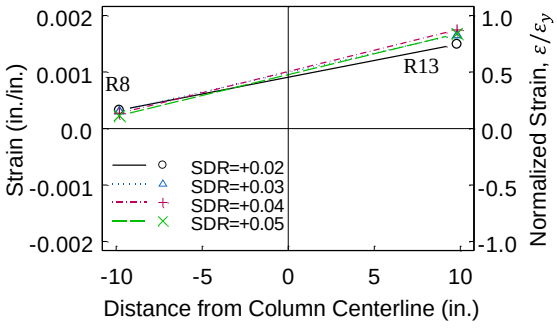

(c) Normal Strain at Section H-H

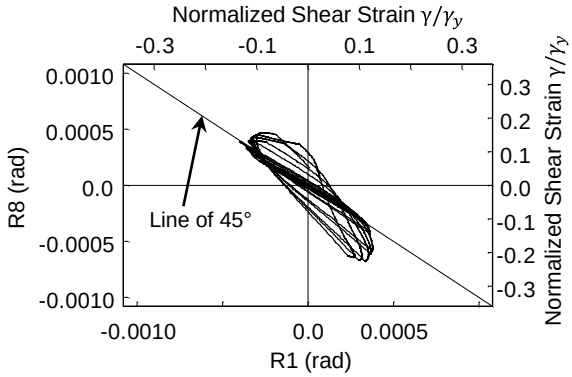

(d) Shear Strain Plot of R8 vs R1

Figure 3.26 Specimen C1 Top and Bottom Continuity Plates Strain Profiles

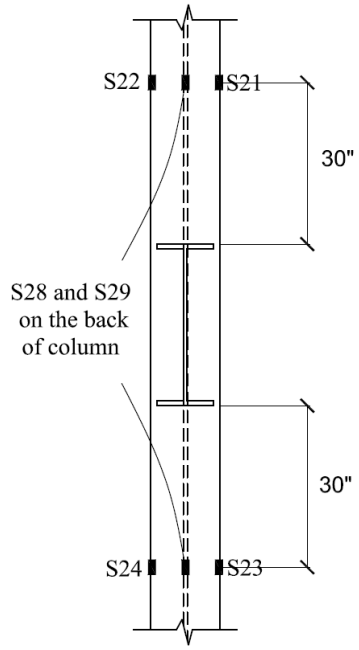

(a) Location of Strain Gages on the South Face of the Column

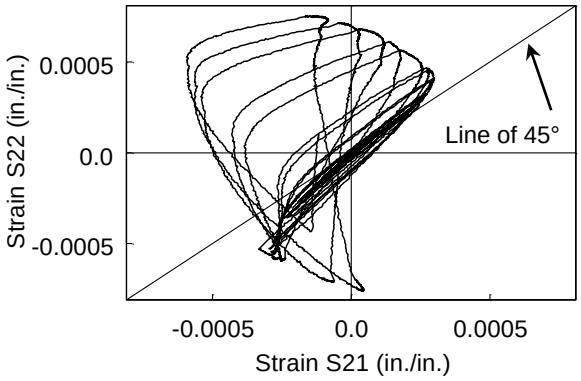

(b) Plot of S21 vs S21

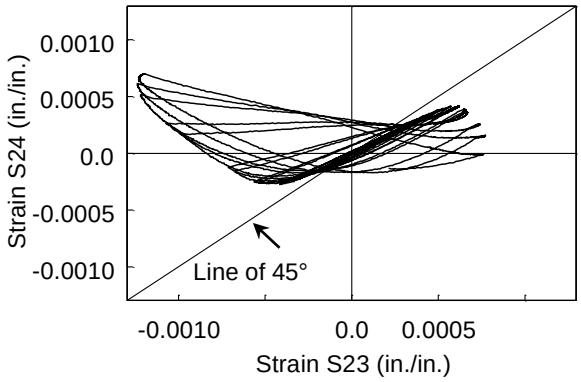

(c) Plot of S23 vs S24

Figure 3.27 Specimen C1: Effect of Column Twisting on Column Flexural Strains

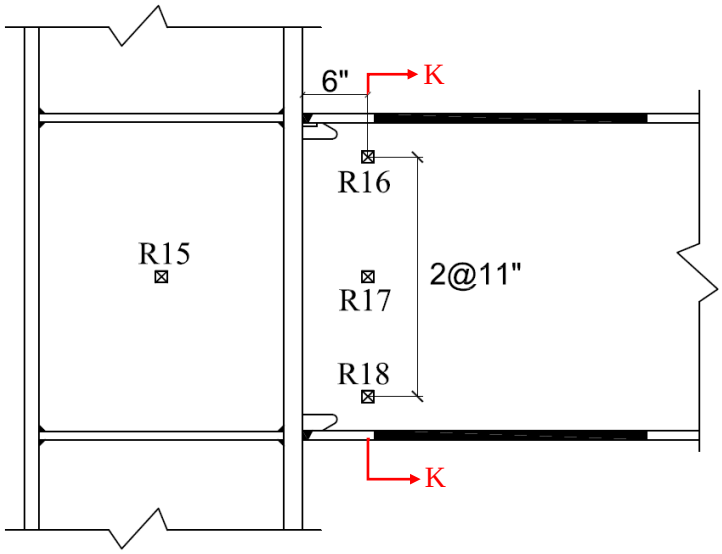

(a) Section K-K

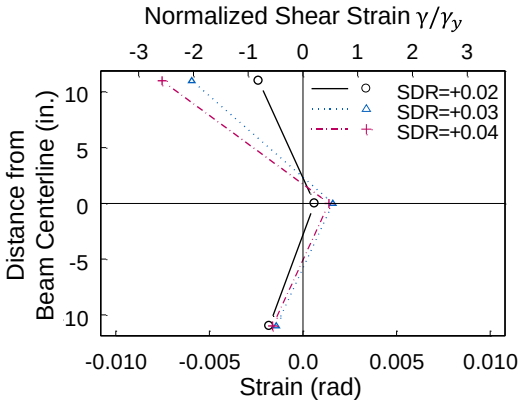

(b) Positive Excursions

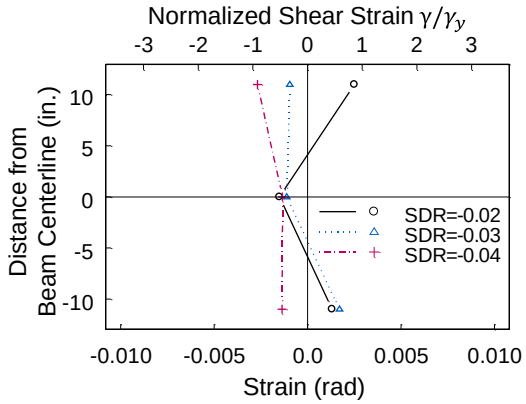

(c) Negative Excursions

Figure 3.28 Specimen C1 Beam Web Shear Strain Profiles

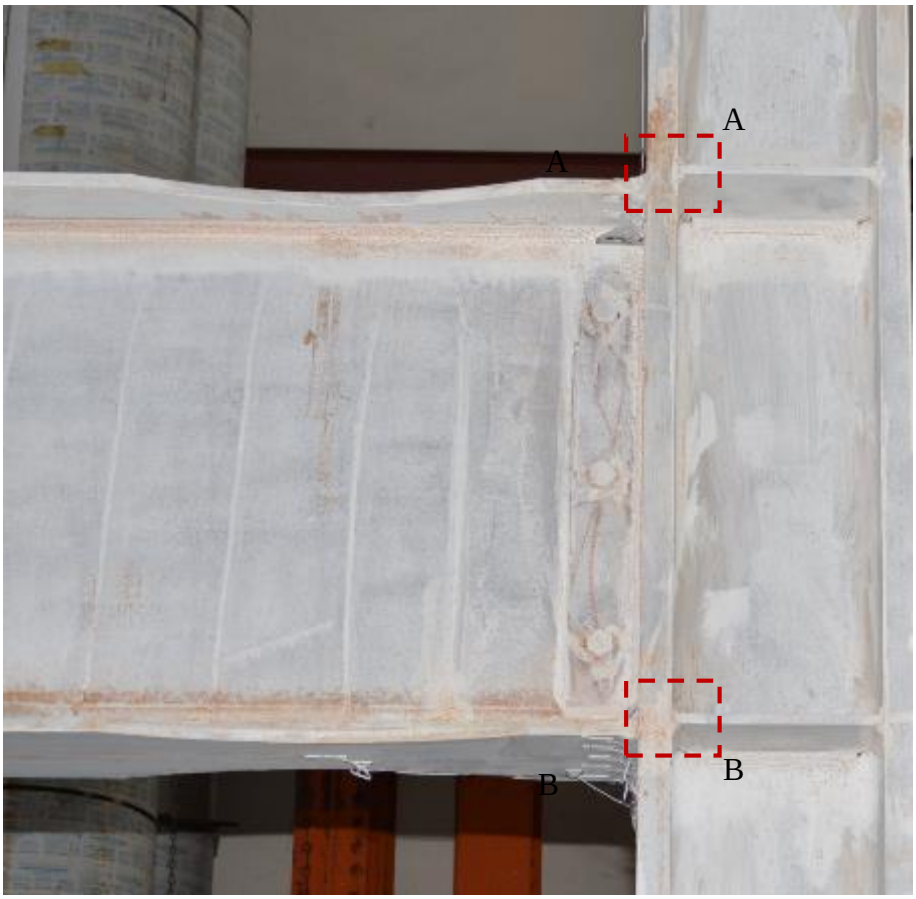

(a) Global View from East

(b) Detail A

(c) Detail B

Figure 3.29 Specimen C2 Connection Region Prior to Testing

Figure 3.30 Specimen C2 Panel Zone Minor Yielding at Completion of 0.0075 rad Drift Cycles

Figure 3.31 Specimen C2 Beam Flange Yielding at Completion of 0.01 rad Drift Cycles

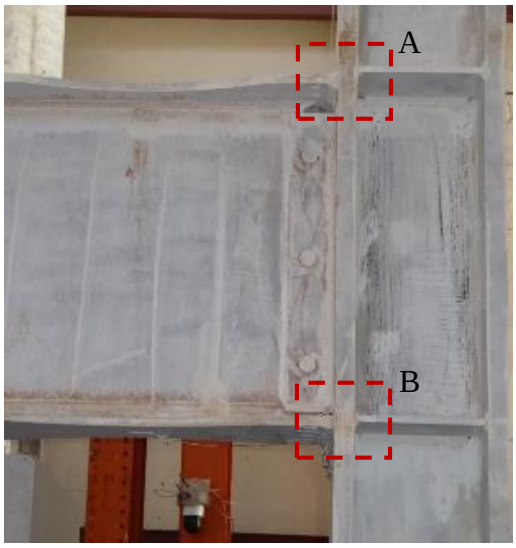

(a) Global View from East

(b) Detail A

(c) Detail B

Figure 3.32 Specimen C2 Connection at -0.015 rad Drift (2nd Cycle)

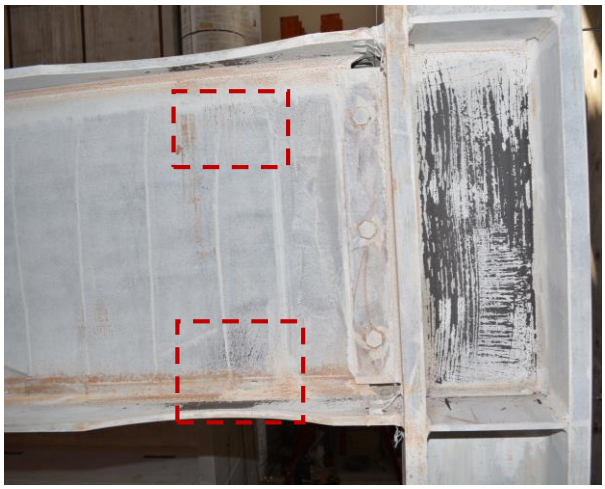

(a) Spread of Yielding to Beam Web

(b) Column Flange Yielding Due to Column Kinking (Back Side)

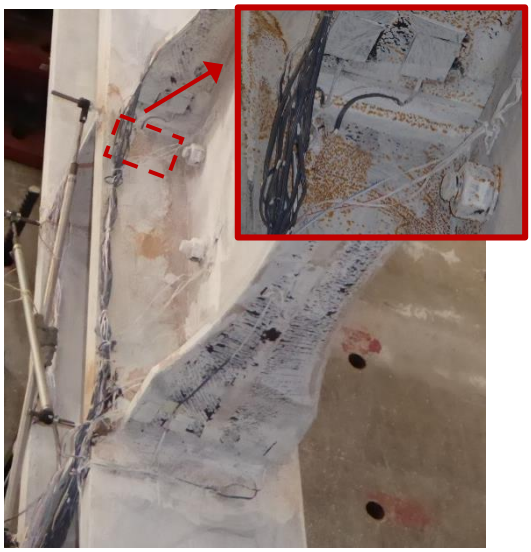

(c) Column Flange Yielding Due to Column Kinking (Front Side)

Figure 3.33 Specimen C2 Connection at -0.03 rad Drift (2nd Cycle)

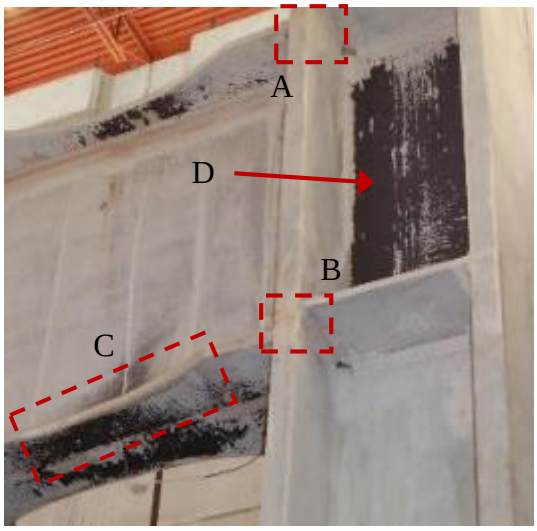

(a) Global View from East

(b) Global View from West

(c) Detail A

(d) Detail B

(e) Detail C, Minor Flange and Web Local Buckling

(f) Detail D, Significant Panel Zone Yielding and Column Kinking

Figure 3.34 Specimen C2 Connection at -0.04 rad Drift (2nd Cycle)

(a) View from East

(b) View from West

Figure 3.35 Specimen C2 at -0.05 rad Drift (2nd Cycle)

(a) Global View from East

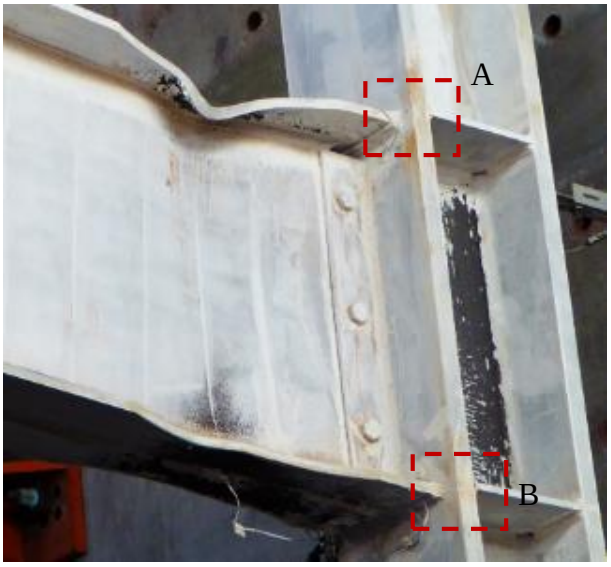

(b) Global View from South East

(c) Detail A

(d) Detail B

Figure 3.36 Specimen C2 at +0.07 rad Drift (1st Cycle)

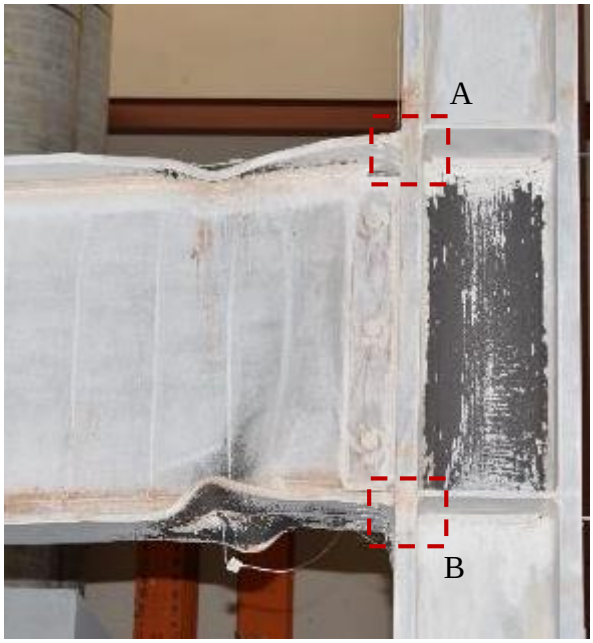

(a) Global View from East

(b) Detail A, View from East

(c) Detail A, view from Bottom

(d) Detail B, View from East

(e) Detail B, View from Bottom

Figure 3.37 Specimen C2 Connection at -0.07 rad Drift (1st Cycle)

(a) -0.05 rad Drift (2nd Cycle)

(b) -0.07 rad Drift (1st Cycle)

Figure 3.38 Specimen C2 Beam Lateral-Torsional Buckling

(a) View from East

(b) View from West

(c) Close-up View

Figure 3.39 Specimen C2 Complete fracture of Beam Bottom Flange at Test Completion

(a) Yielding in Bottom Continuity Plate

(b) Column Flange Yielding Due to Column Kinking (Back Side)

(c) Column Flange Yielding Due to Column Kinking (Front Side)

Figure 3.40 Specimen C2 Continuity Plate and Column Flanges Yielding at Test Completion

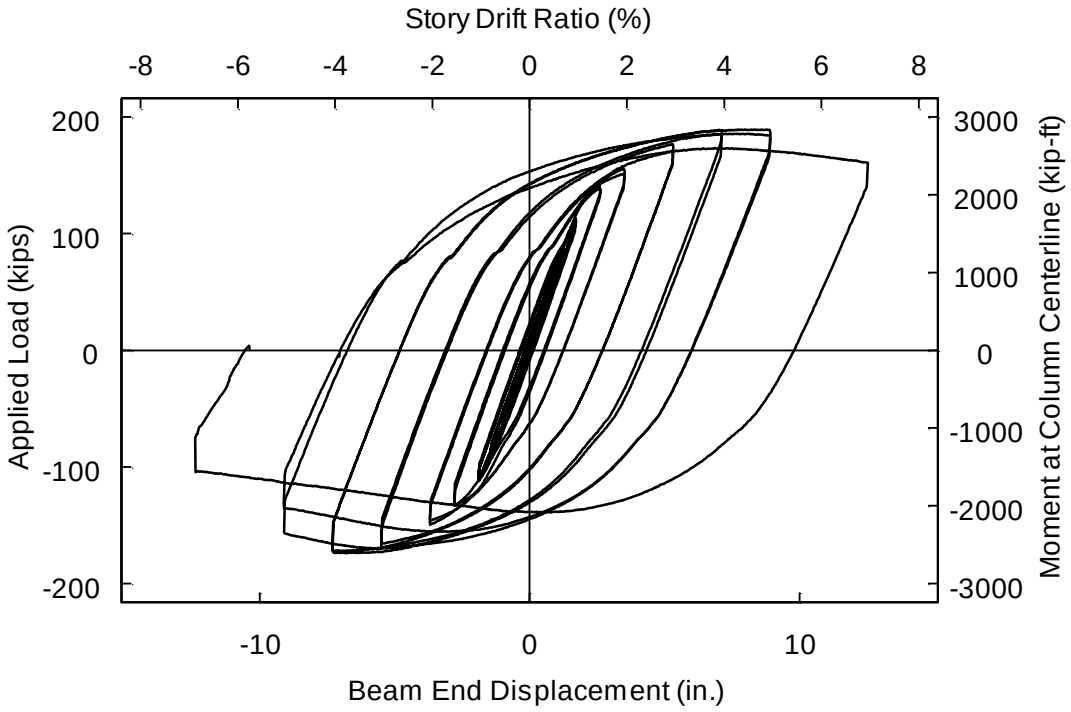

Figure 3.41 Specimen C2 Load versus Beam Tip Displacement Relationship

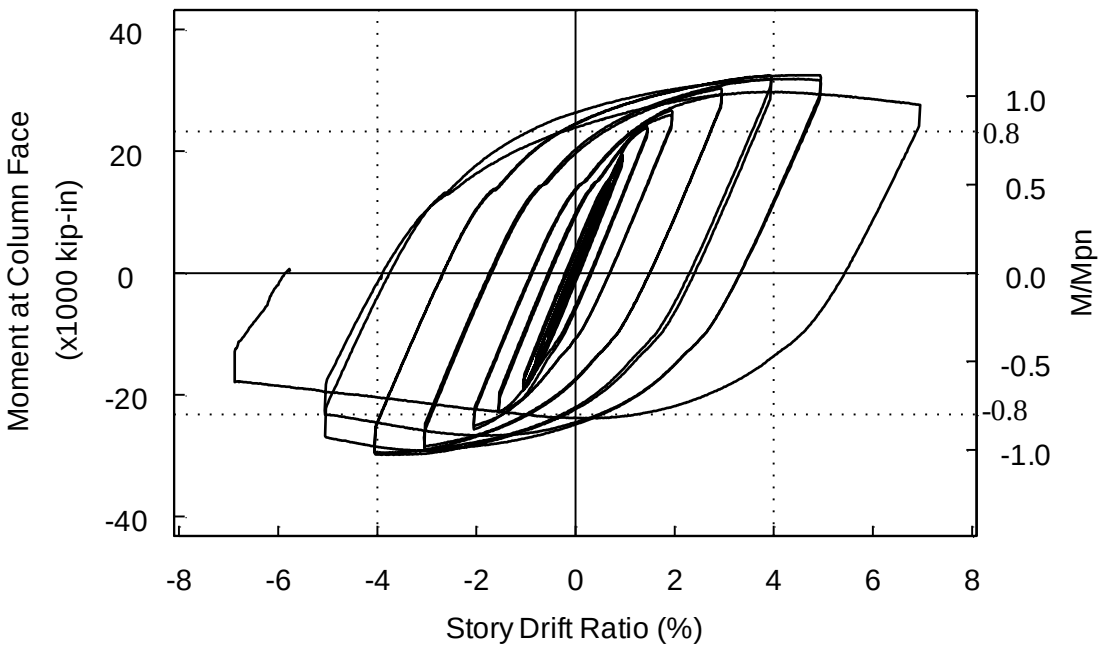

Figure 3.42 Specimen C2 Moment versus Story Drift Angle Relationship

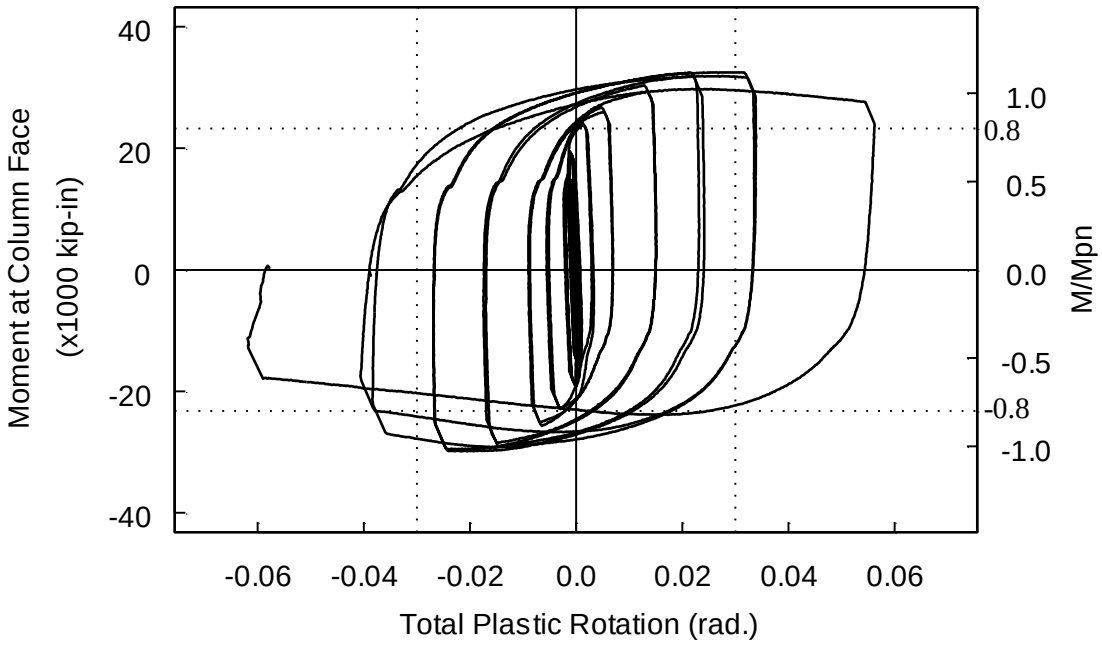

Figure 3.43 Specimen C2 Moment versus Total Plastic Rotation Relationship

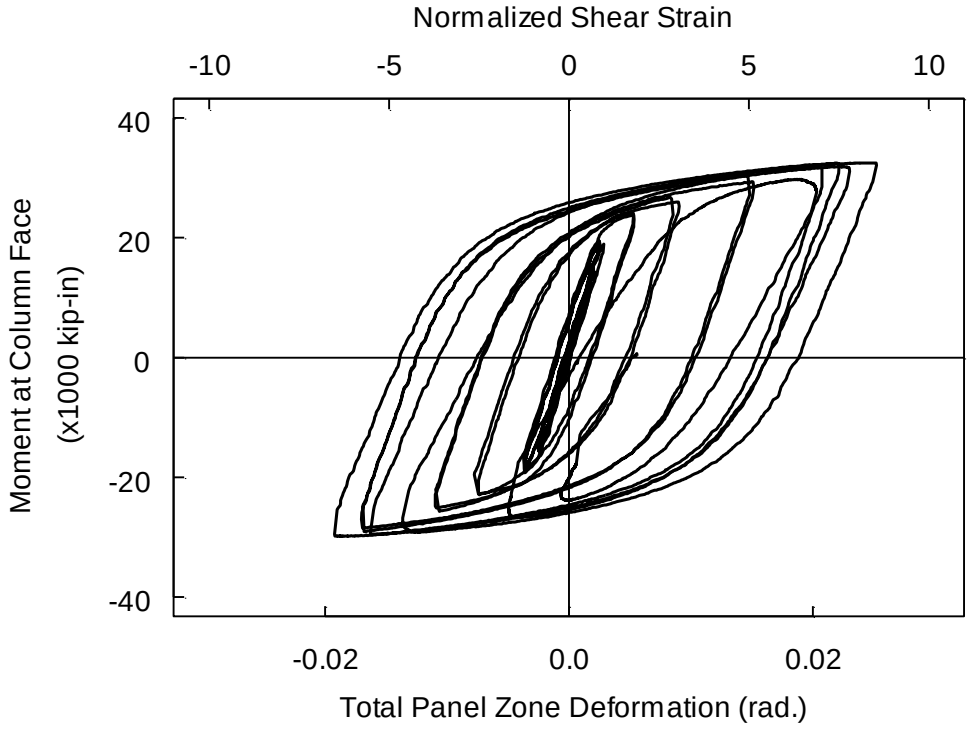

Figure 3.44 Specimen C2 Moment versus Total Panel Zone Shear Deformation Relationship

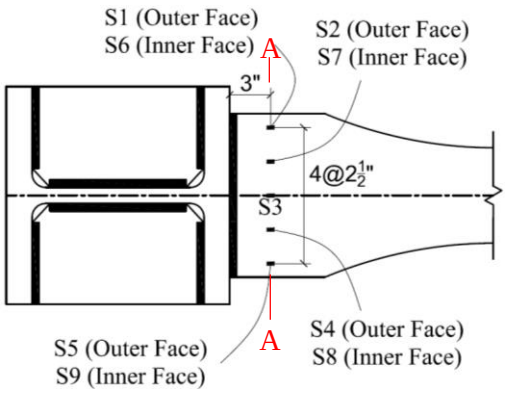

at Beam Top Flange

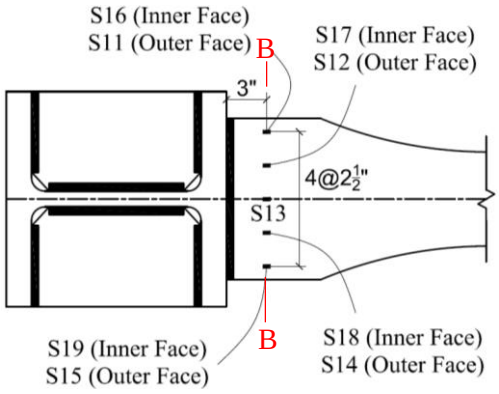

at Beam Bottom Flange

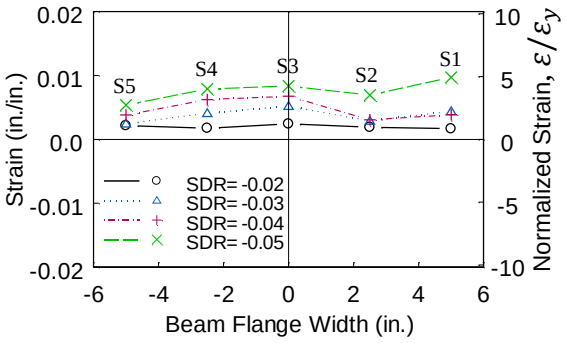

(a) at Section A-A, Outer Face

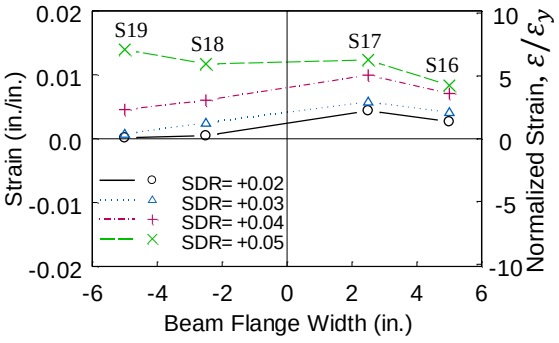

(c) at Section B-B, Inner Face

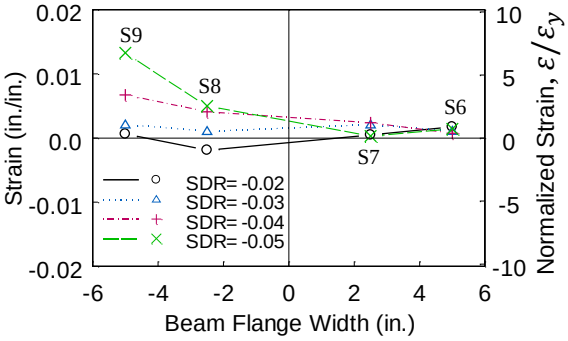

(b) at Section A-A, Inner Face

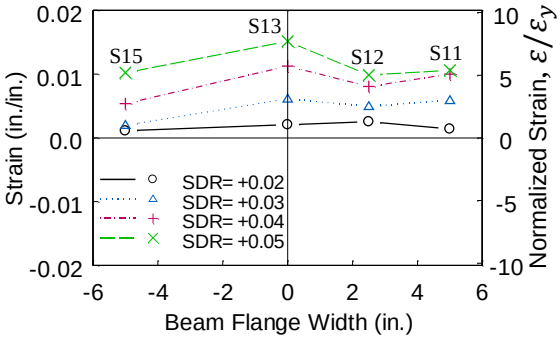

(d) at Section B-B, Outer Face

Figure 3.45 Specimen C2 Beam Flange Flexural Strain Profiles

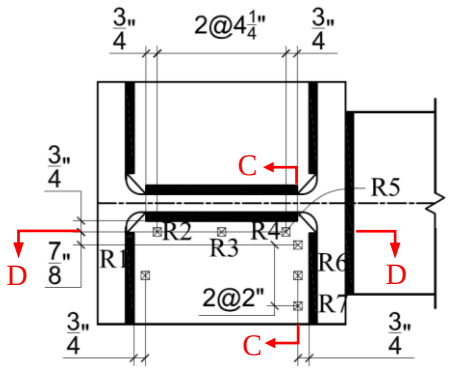

Top Continuity Plate

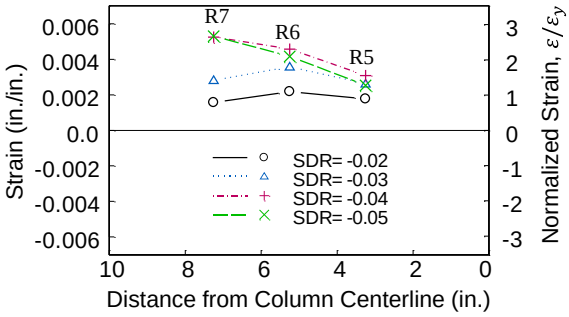

(a) Strain Normal to Flange Weld at Section C-C

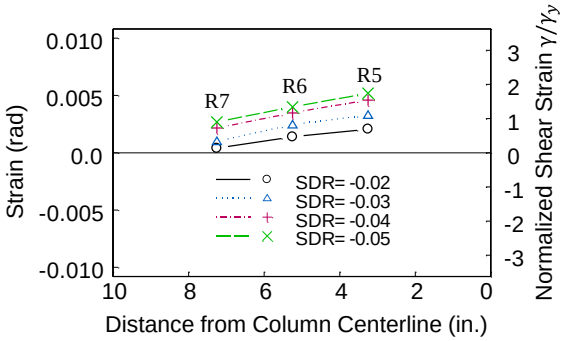

(b) Shear Strain at Section C-C

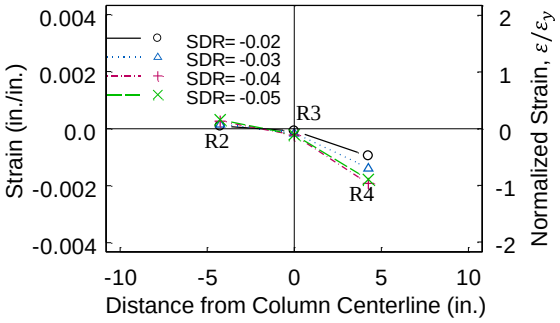

(c) Strain Normal to Web Weld at Section D-D

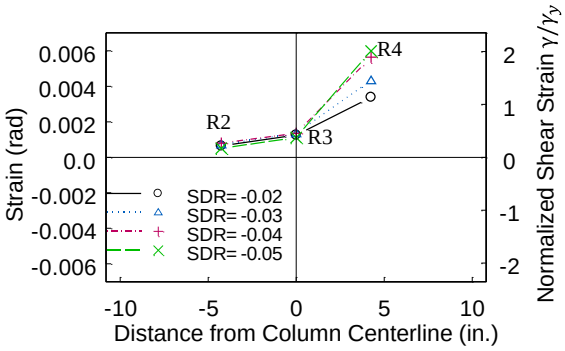

(d) Shear Strain at Section D-D

Figure 3.46 Specimen C2 Top Continuity Plate Strain Profiles

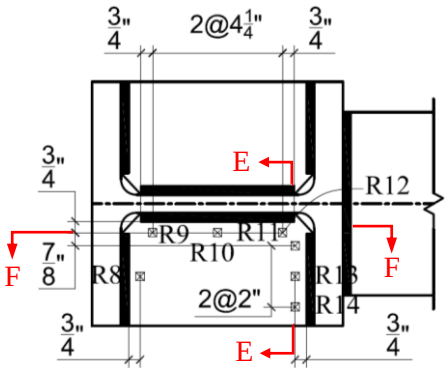

Bottom Continuity Plate

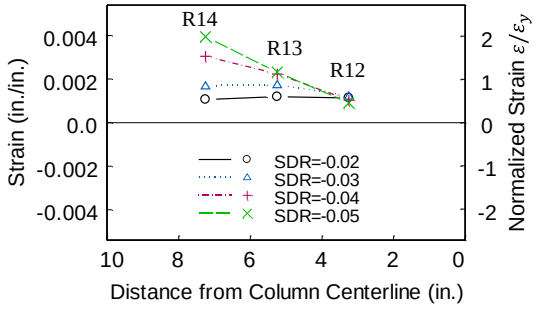

(a) Strain Normal to Flange Weld at Section E-E

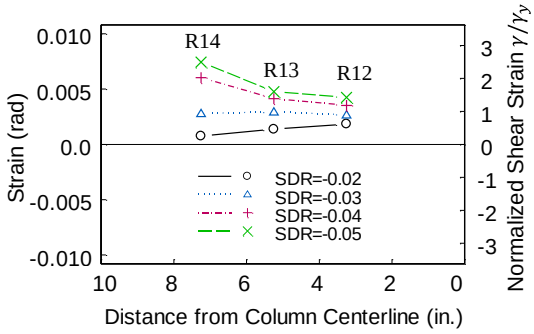

(b) Shear Strain at Section E-E

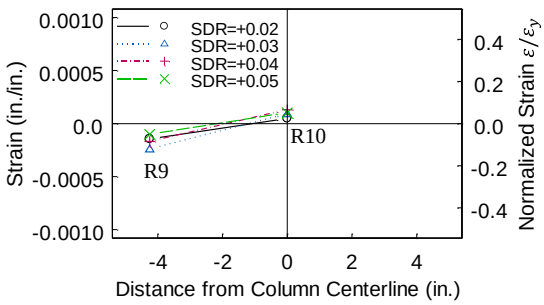

(c) Strain Normal to Web Weld at Section F-F

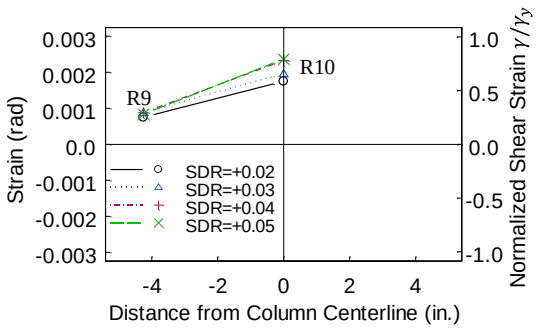

(d) Shear Strain at Section F-F

Figure 3.47 Specimen C2 Bottom Continuity Plate Strain Profiles

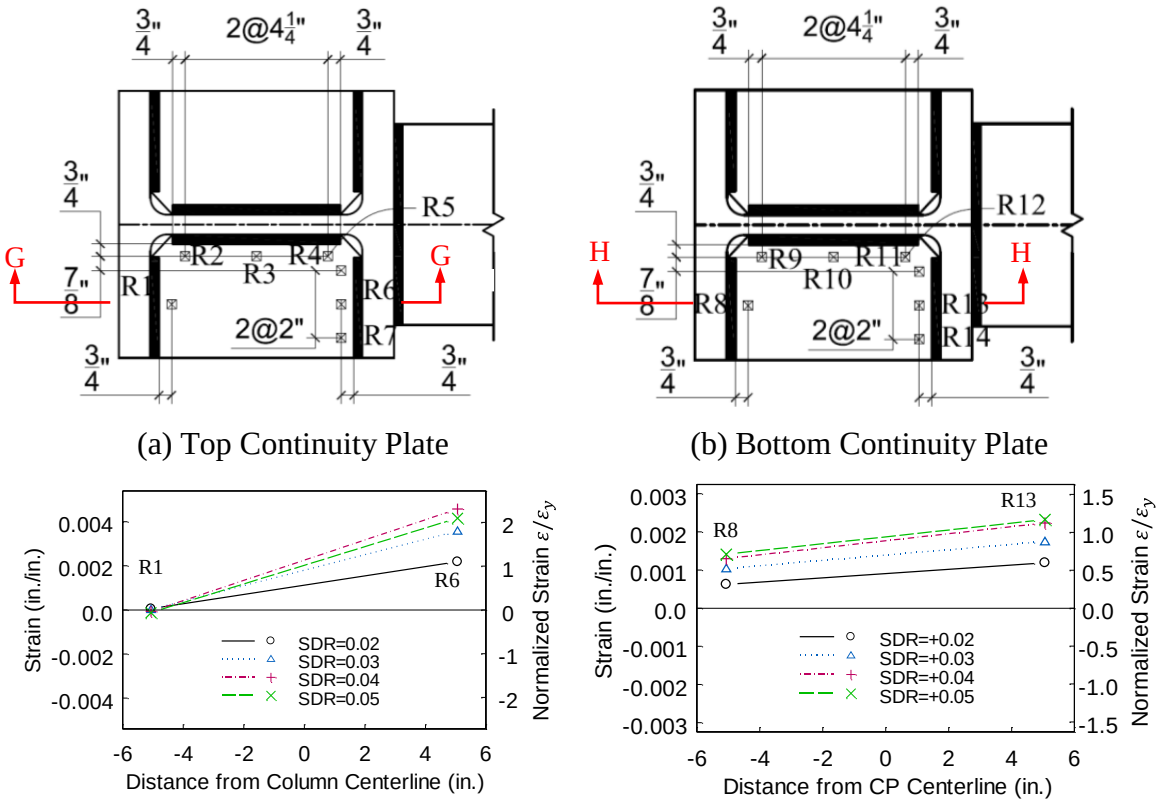

(a) Top Continuity Plate

(b) Bottom Continuity Plate

(c) Normal Strain at Section G-G

(d) Normal Strain at Section H-H

Figure 3.48 Specimen C2 Top and Bottom Continuity Plates Strain Profiles

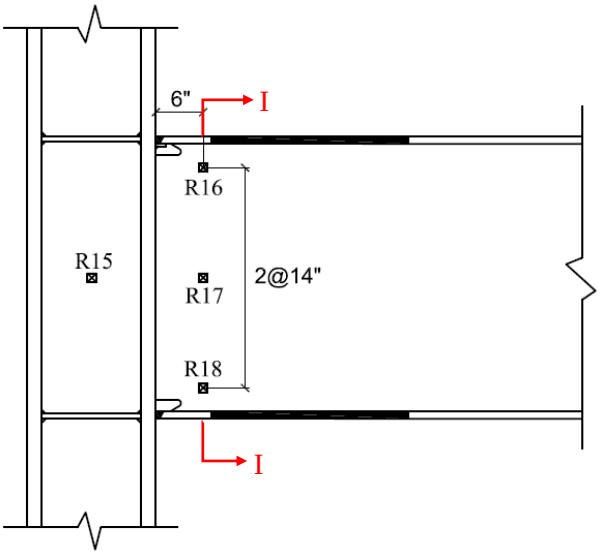

(a) Section I-I

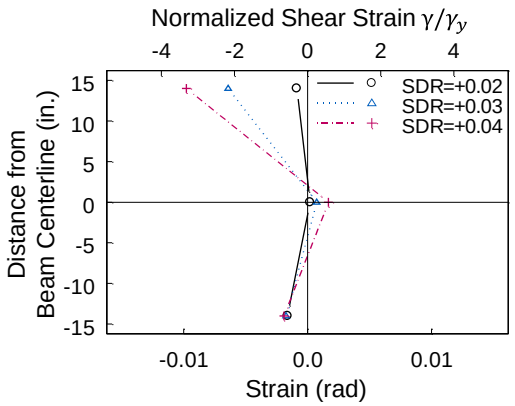

(b) Positive Excursions

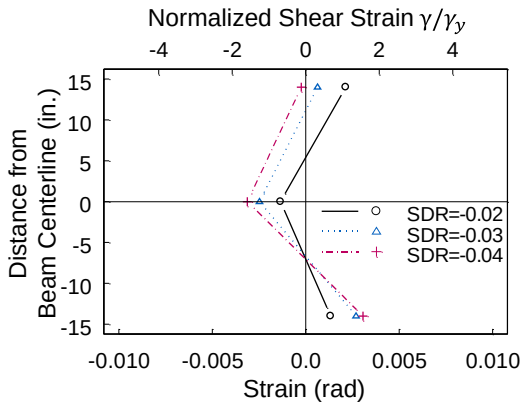

(c) Negative Excursions

Figure 3.49 Specimen C2 Beam Web Shear Strain Profiles

4 ANALYSIS OF CONTINUITY PLATE WELDING TEST RESULTS AND FINITE ELEMENT SIMULATION

4.1 Global Response and Failure Mode Comparison

To experimentally verify a proposed design procedure for the continuity plate weld design, the main variable between the two specimens tested in this research was the column shape; Specimen C1 had a deep (W24) column and Specimen C2 had a shallow (W14) column. Testing showed that fillet welded continuity plates did not experience any damage, and the performances of both RBS connection specimens were no different from those with CJP welds between the continuity plates and the column flanges. Since deep column is prone to twist (Chi and Uang 2002), extra bracings were provided at the top flange near the RBS region and the top end of the column (Figure 3.6); the former was to simulate the bracing effect provided by the concrete slab. Despite this effort, the effect of using a deep column was still significant, as explained below.

The global responses of both specimens are compared in Figure 4.1. Strain gage readings in the column showed that column twisting started at 1.5% drift (Section 3.8.2.2). Therefore, lateral-torsional buckling (LTB) of the beam was more significant [Figure 4.2(a)]. Such coupled column twisting-beam LTB phenomenon caused the strength of the connection to peak at 3% drift and then started to degrade thereafter [Figure 4.1(a)]. Since the simulated top flange bracing was only effective in positive bending, the figure also shows that the strength reached in the negative bending direction was less. For Specimen C2 with a W14 column, column twisting was much less a concern. Therefore, this specimen could reach a higher strength, and strength degradation did not occur until after 4% drift.

The higher strength of C2 also means a higher shear in the panel zone, which together with a slightly higher DCR ratio in designing the panel zone (Table 3.2) explains why C2 experienced more significant panel zone shear yielding than C1 [Figure 4.2(b)].

Figure 4.3 summarizes the percentage contributions from the beam, panel zone, and column to the total beam end displacement of both specimens. As expected, beam contributed the most to the total end displacement. For the reason explained above, panel zone of Specimen C2 contributed more to the total displacement; the percentage contribution reduced after 4% drift because the connection strength degraded thereafter. The panel zone of Specimen C1 could have deformed more, but was limited by the coupled deep column twisting-beam LTB mode.

The amount of energy dissipated by each specimen is presented in Figure 4.4, where the energy has been normalized by the plastic moment, M_p, computed based on the tensile coupon test results. The deep-column specimen dissipated less energy.

4.2 Finite Element Analyses

It is difficult to experimentally construct the freebody diagram of the continuity plate from strain gage measurements. Instead, finite element analysis (FEA) by using the commercial software ABAQUS/CAE (2014) was conducted. Freebody diagrams established from the FEA are then compared with those established from the proposed procedure.

Four node, thick-shell brick elements (Type S4R in ABAQUS) were used to model the specimens. Typical steel properties ($E = 29{,}000$ ksi, $\nu = 0.3$) were used in the model to describe the elastic material characteristics. Also for inelastic behavior, following the work of Chaboche (1986), material parameters that could simulate both the kinematic and

isotropic hardening responses of an A992/A572 steel coupon under cyclic loading were incorporated (Ozkula 2017). Equation solver was chosen to be the Direct Sparse Solver and the Newton's iterative method was used for solving nonlinear equilibrium equations. Figure 4.5 shows the FEA models of both specimens. Figure 4.6 compares the experimental and predicted global response of each specimen; the correlation is satisfactory. A comparison of the deformed shapes is presented in Figure 4.7.

Figure 4.8 and Figure 4.9 shows the continuity plate freebody diagrams for both specimens. For one-sided moment connections, the proposed procedure assumes that the left (i.e., the non-loaded column flange) side has no normal force; the normal force from the beam flange is transferred completely to the column web through the continuity plates. The FEA shows that the non-loaded column flange does resist a portion of the normal force from the beam flange; the percentage is higher for shallow columns than for deep columns. This will reduce the shear forces in both the web weld and flange welds. Therefore, the proposed design procedure is somewhat conservative for continuity plate weld design. The conservatism increases when a shallow column is used.

Parts of chapters 4, have been accepted for publication of the material as it may appear in *Engineering Journal*, 2017, Mashayekh, A., and Uang, C.M. The dissertation author was the primary researcher and author of this material.

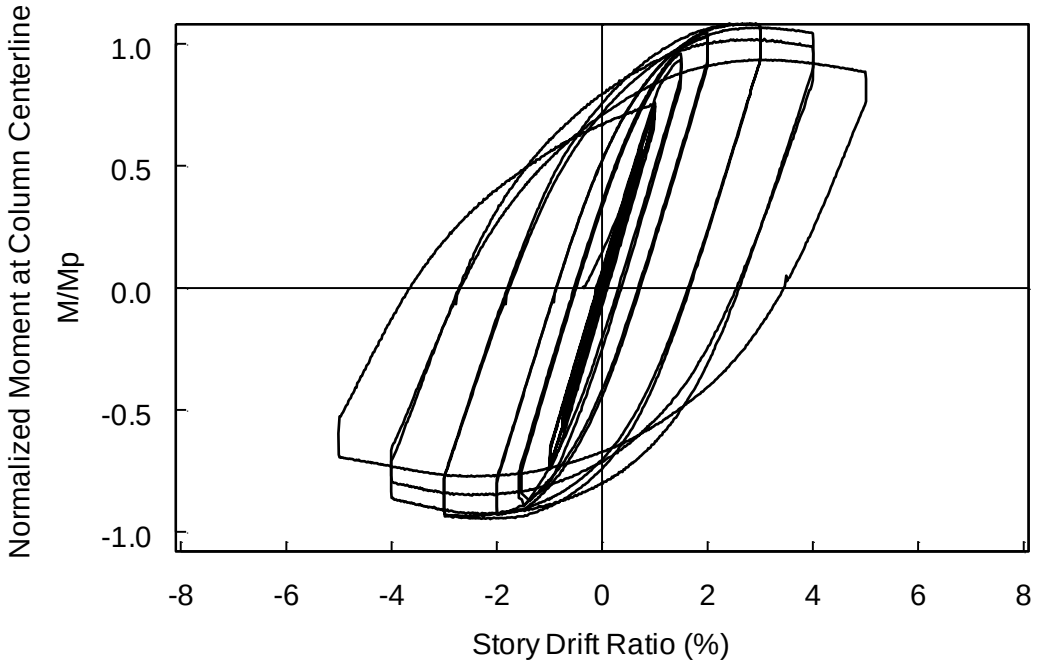

(a) Specimen C1

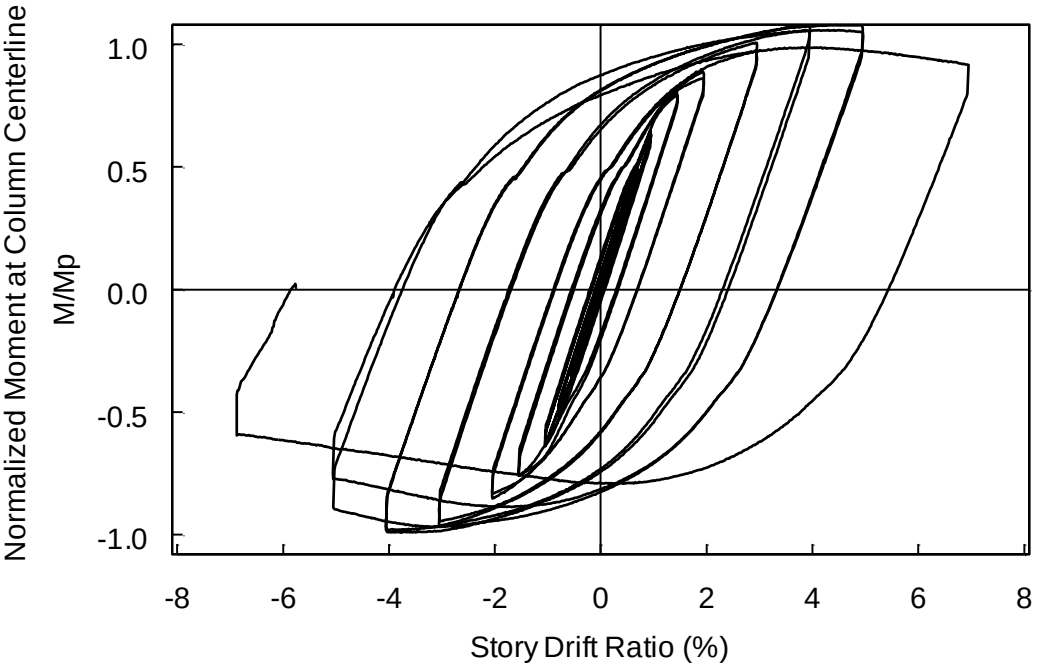

(b) Specimen C2

Figure 4.1 Comparison of Global Responses

(a) Specimen C1

(b) Specimen C2

Figure 4.2 Comparison of Buckling Mode at 4% Drift

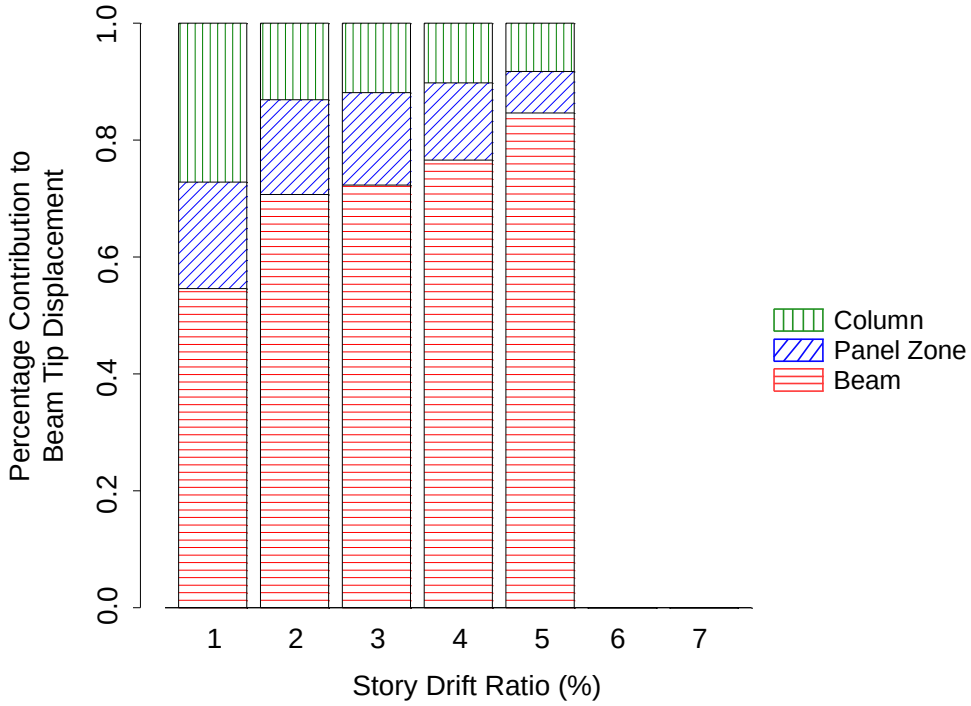

(a) Specimen C1

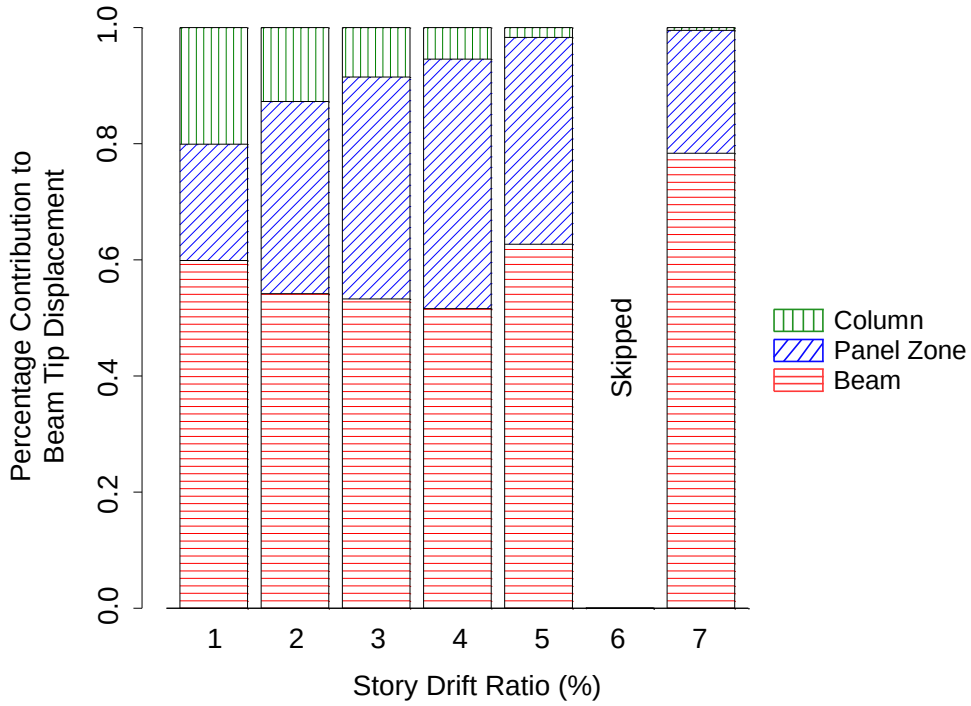

(b) Specimen C2

Figure 4.3 Components of Beam End Displacement

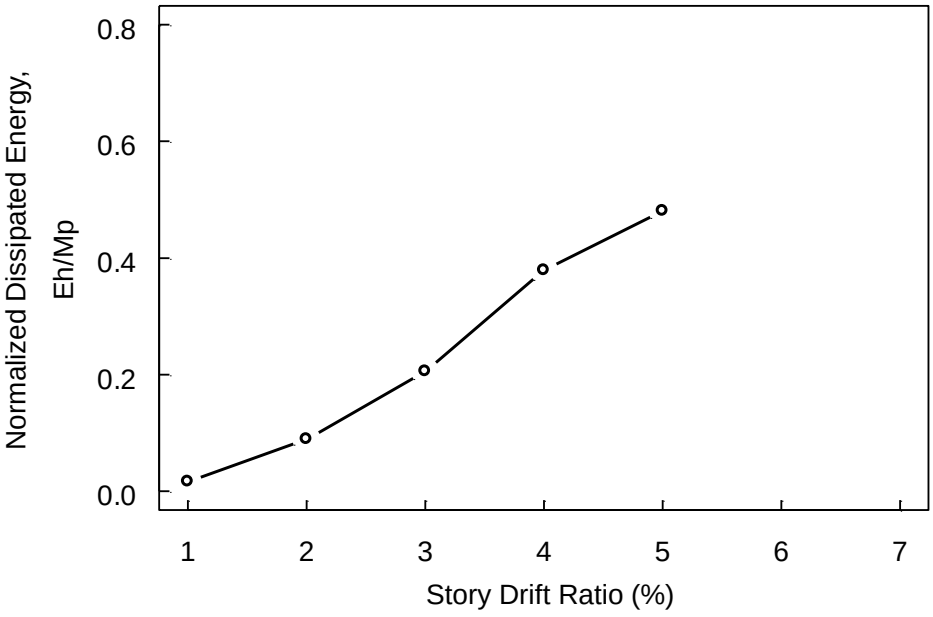

(a) Specimen C1

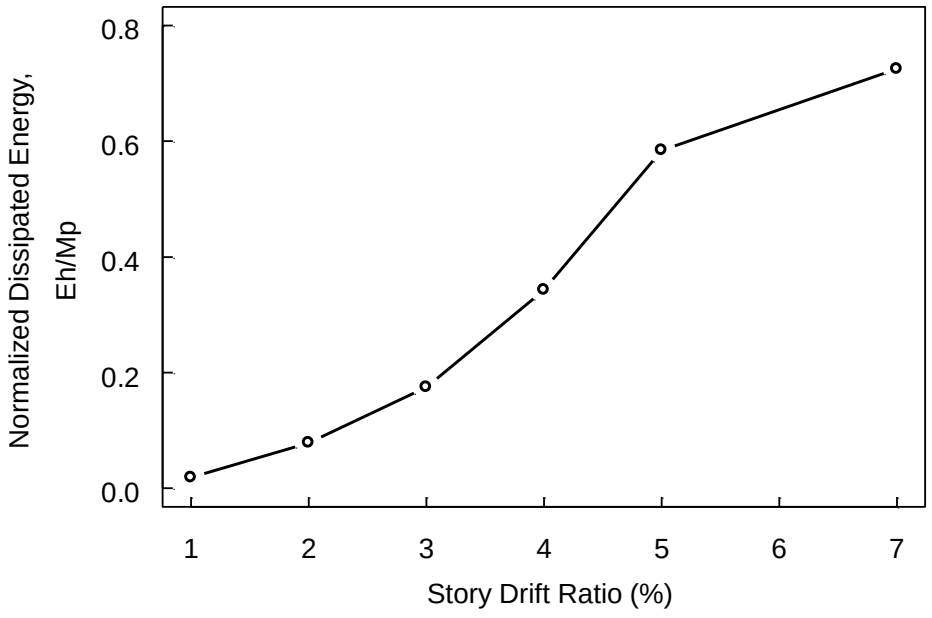

(b) Specimen C2

Figure 4.4 Normalized Dissipated Energy

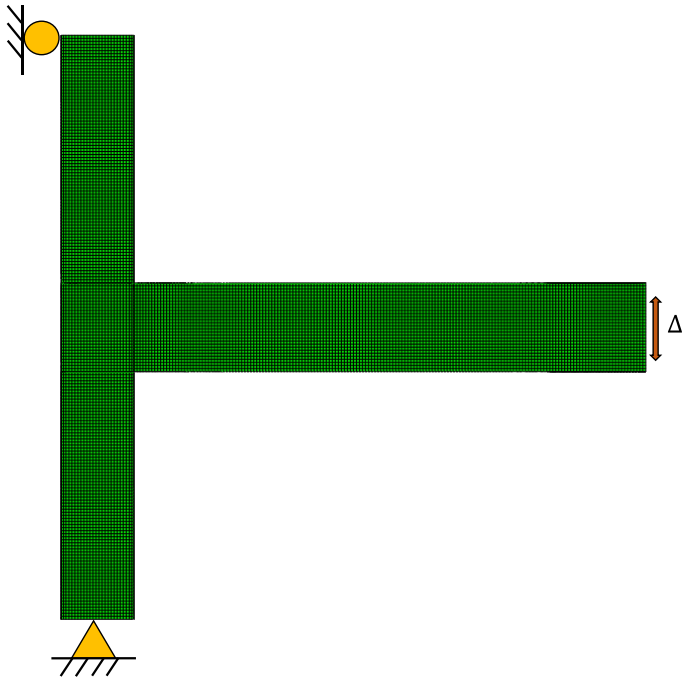

(a) Specimen C1

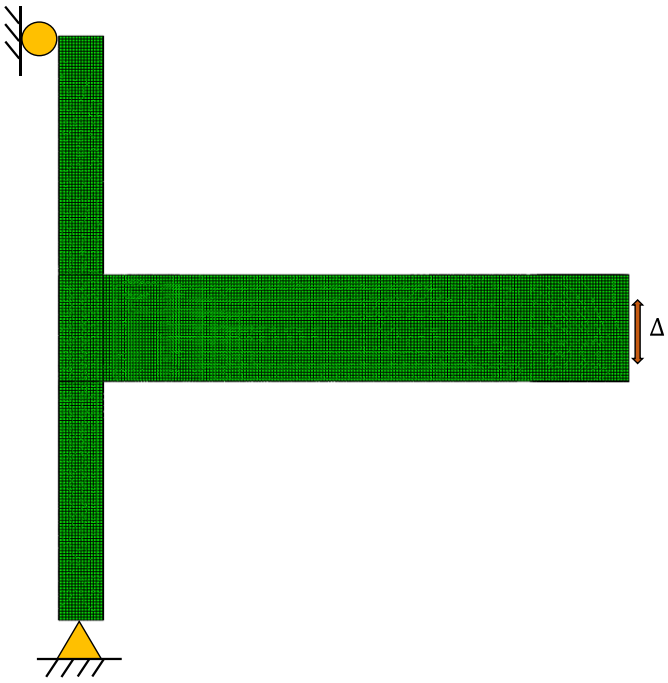

(b) Specimen C2

Figure 4.5 FEM Models

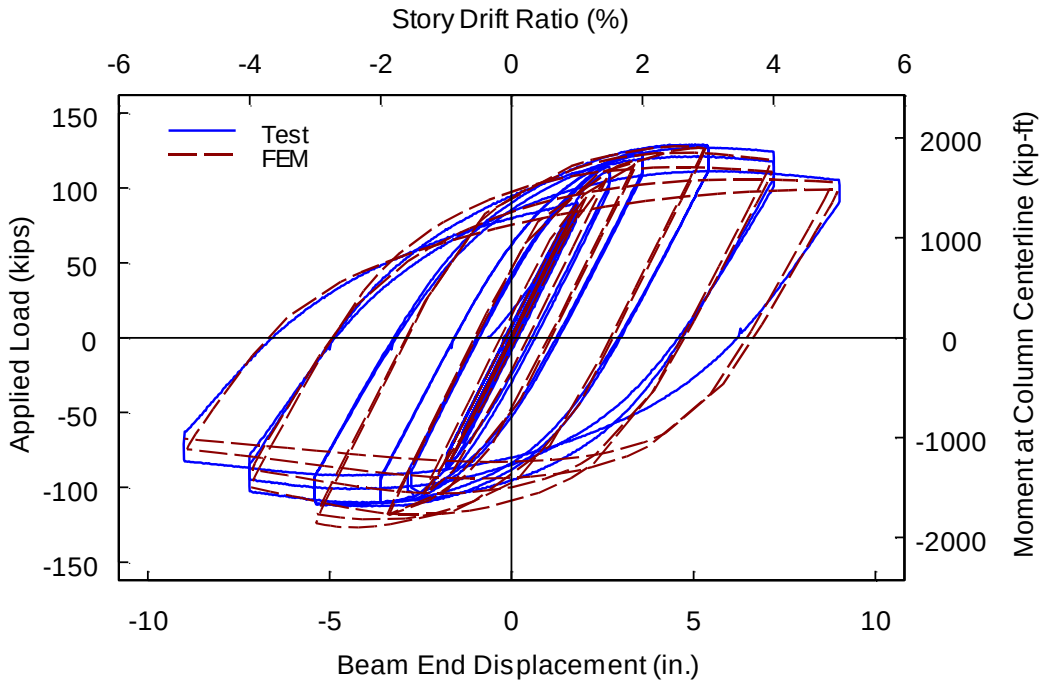

(a) Specimen C1

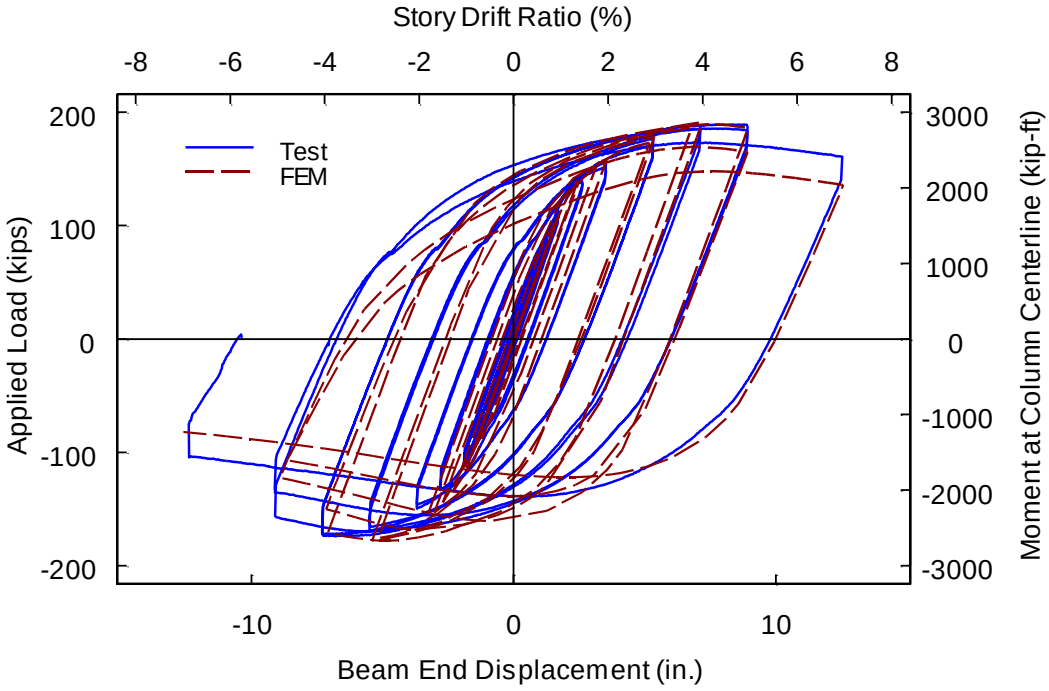

(b) Specimen C2

Figure 4.6 Correlation of Global Responses

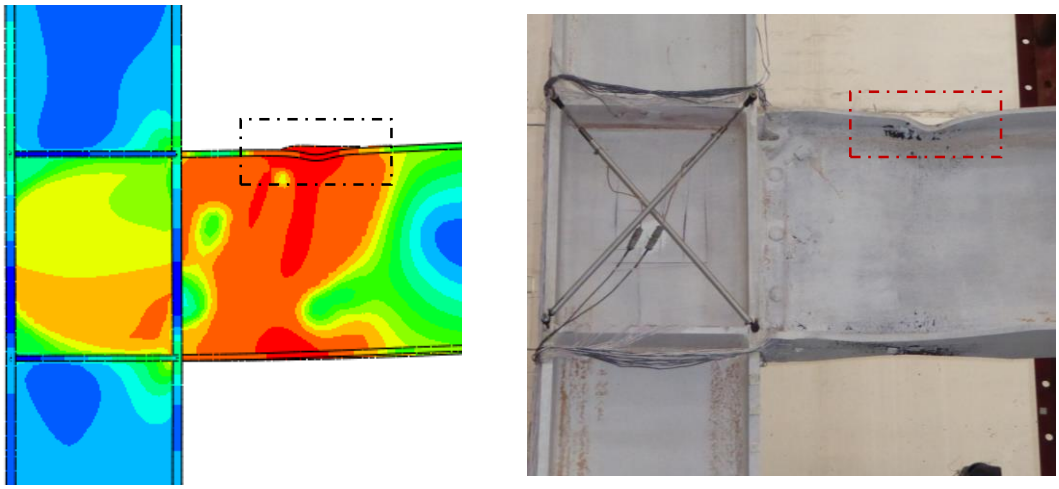

(a) Specimen C1 (at +4% Drift)

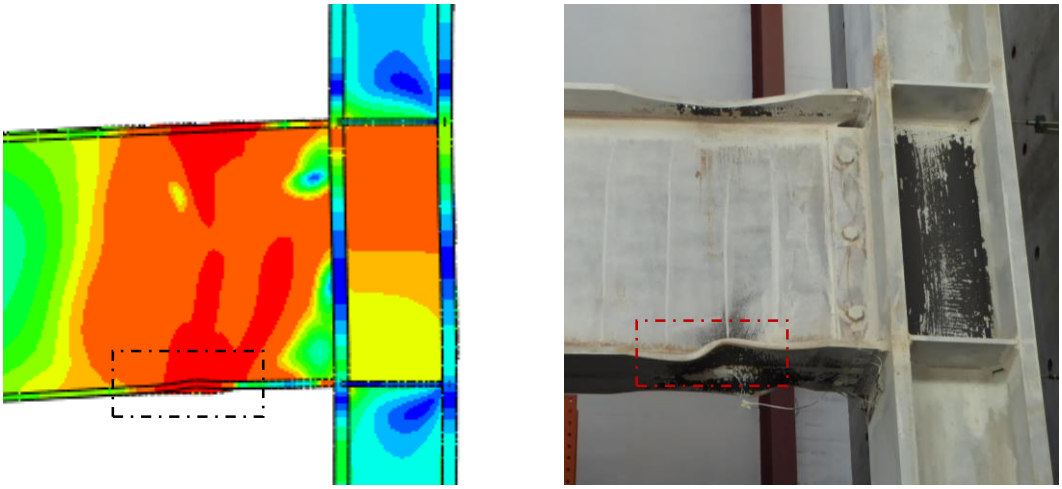

(b) Specimen C2 (at -5% Drift)

Figure 4.7 Correlation of Deformed Configurations

(a) Forces Predicted by Tran et al. (2013)

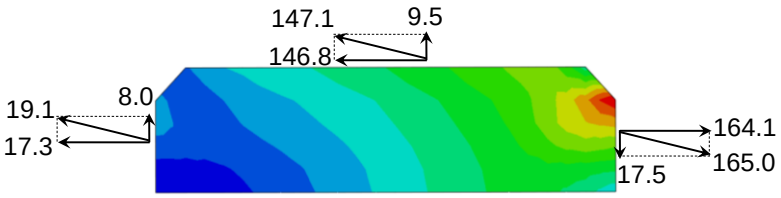

(b) Forces from FEM Analysis

Figure 4.8 Specimen C1 Comparison of Forces Acting on Continuity Plate

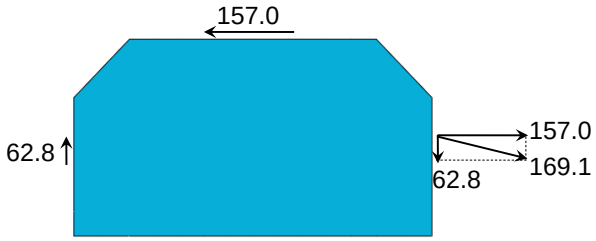

(a) Forces Predicted by Tran et al. (2013)

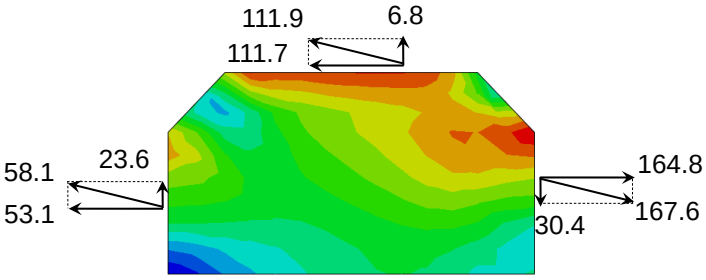

(b) Forces from FEM Analysis

Figure 4.9 Specimen C2 Comparison of Forces Acting on Continuity Plate

5 TEST PROGRAM ON SLOPED MOMENT CONNECTIONS

5.1 General

For a sloped connection, the top and bottom flanges frame into the column with acute and obtuse angles. Refer to Figure 5.1 for the "heel" and "toe" locations in a sloped connection as defined by Kim et al. (2016). For the example shown in Figure 5.1(a), note that the heel is located at the top flange at the left end and at the bottom flange at the right end of the beam. Assuming an orthogonal beam-to-column connection configuration, AISC 358 specifies a stringent welding requirement for steel backing removal, back-gouging, and fillet reinforcing for the bottom flange weld, while a more relaxed requirement is specified for the top flange weld. For the design of Reduced Beam Section (RBS) moment connection, AISC 358 provides guidelines on the selection of the dimensions *a*, *b*, and *c* (Figure 5.2). In a sloped connection, it is not clear how the AISC 358 requirements are applied because the RBS can be oriented to be either parallel to the column centerline or perpendicular to the beam span (Figure 5.3).

Study on the sloping effect was limited. To support the design and performance evaluation of an LAX TBIT Extension Project that used the non-orthogonal steel moment connections, full-scale testing of two large-size Reduced Beam Section (RBS) moment connections specimens with a W36×231 beam and a W36×302 column was conducted (Figure 5.4); the beam framed into the column with a slope from the orthogonal of 28° (Kim et al. 2010). See Figure 5.5 for the connection details. For this particular project, the contractor preferred to weld the beam and column in the horizontal position before the

welded frames were erected into position (Figure 5.6). Note that both beam flanges were beveled from the underside and the beam CJP welding was performed in a vertical position.

Cyclic testing showed that both specimens experienced brittle fracture at the top flange (i.e., heel location in this configuration) soon after the 0.04 rad drift cycle was completed (Figure 5.7 and Figure 5.8). Although the connections successfully passed the acceptance criteria of AISC 341 (AISC 2016a) for use in an SMF, the brittle nature of the failure mode was not characteristic of an orthogonal RBS connection where a ductile response was expected. Finite element simulation (Kim et al. 2016) conducted after the testing showed that the force demand at both flanges of the beam was not equal. The force demand at the heel location was always higher and increased with the angle of inclination. The RBS in tested specimens was oriented like that shown Figure 5.3(a). But finite element simulation suggested that orienting the RBS to be perpendicular to the beam span as shown in Figure 5.3(b) would reduce the demand at the heel location.

To provide additional data for consideration by the AISC Connection Prequalification Review Panel for the development of design requirements for sloped connections, two full-scale moment connections were tested. Although the sloped condition can exist in any prequalified connections in AISC 358, only the RBS connection was evaluated in this study.

5.2 Test Specimens

One orthogonal RBS connection, designated as Specimen C2 with a W36×150 and a W14×257 column of A992 steel, was tested and presented in Chapter 3; see Figure 3.2 for the connection detail. To evaluate the effect of sloped angle, two RBS specimens with the same beam and columns sizes were tested in this research. The beams were framed

into the columns with a 25° angle. The centerline of the RBS section was parallel to the column centerline, while the centerline of the RBS section in Specimen S2 was perpendicular to the beam span. Figure 5.10 and Figure 5.11 show the connection detail of both specimens. For the LAX test specimens, the heel location was located at the top flange level. To confirm that the heel location was more vulnerable to fracture, however, the beams in this research were sloped such that the heel location was located at the bottom flange level.

5.3 Test Setup

The test setup is shown in Figure 5.12. The inflection points were assumed to be at the mid-height of each story. Inflection points were simulated by mounting the column ends to two W14×257 hinge sections on its back side and a W14×342 on its bottom positioned to experience weak-axis bending (see Figure 3.4). A corbel was bolted to the free end of the beam and attached to two 220-kip hydraulic actuators. Lateral restraint was provided on both sides of the specimen at the corbel location (see Figure 5.14).

5.4 Material Properties

ASTM A992 steel was specified for the beams and columns. The continuity plates were fabricated from ASTM A572 Gr. 50 steel. Table 3.5 summarizes the steel mechanical characteristics obtained from tensile coupon tests conducted at UCSD (Appendix A).

5.5 Specimen Construction and Inspection

Beams and the columns were fabricated by a commercial fabricator before they were delivered to UCSD. To simulate the field conditions, the specimens were erected in the upright position and then welding of the beam to the column flange were conducted in the UCSD laboratory.

5.6 Instrumentation

A combination of displacement transducers, strain gage rosettes, and uniaxial strain gages were used to measure the global and local responses. Figure 5.15 shows the location of displacement transducers. Displacement transducer L1 was used to control the stroke of the hydraulic actuators and the beam end displacement. L2 was used to detect any slippage, if occurred, between the corbel and the beam end plate. L3 and L4 were used to measure the panel zone shear deformation. L5 and L6 were used to measure the column deformation. L7, L8, and L9 were used to monitor the displacements at the column end supports, which were anticipated to be negligible. Rosettes and uni-axial strain gages were used to measure the strains in the connection region (see Figure 5.16 to Figure 5.17).

5.7 Data Reduction

The total Inelastic Rotation (θ_p) of the specimen was calculated by dividing the inelastic component of the beam tip displacement (δ_p), measured at the actuator line of action, by the beam span length from the column centerline to the actuator line of action:

$$\theta_p = \frac{\delta_p}{L} = \frac{1}{L}(\delta_{total} - \delta_e) = \frac{1}{L}\left(\delta_{total} - \frac{P}{K}\right) \tag{2.1}$$

where δ_{total} is the total beam tip deflection measured by displacement transducer L1, P is the applied load, and K is the elastic stiffness determined from the initial low-amplitude test results. The panel zone component was determined from displacement transducers L3 and L4. Together with the measurement of transducers L5 and L6, the component of the total beam tip deflection due to column deformation can also be established. For orthogonal connections, the procedure to determine the contributions from beam, column,

and panel zone deformations can be found in Uang and Bondad (1996). For sloped connections, however, the data reduction procedure has been revised (see Appendix C).

5.8 AISC Acceptance Criteria

According to Section E3.6b of AISC 341 (AISC 2016a), beam-to-column connections used in Special Moment Frames shall satisfy the following requirements:

(1) the connection shall accommodate a story drift angle of at least 0.04 rad, and

(2) the measured flexural resistance of the connection, determined at the column face, shall equal at least $0.8M_p$ of the connected beam at a story drift angle of 0.04 rad, where M_p is the nominal plastic moment of the beam.

5.9 Loading Sequence

Testing was conducted in a displacement control mode. The loading sequence used for all specimens was the standard loading sequence specified in Section K2 of AISC 341. This loading sequence specifies a series of load cycles at different Story Drift Angles (hereinafter referred to as "drift"), with the distance from the intersection of column and beam centerlines to the actuator line of action being used in calculating the drift angle (see Figure 5.18). The loading history begins with six cycles each at 0.00375, 0.005, and 0.0075 rad drifts. These are followed by four cycles at 0.01 rad drifts, two cycles at 0.015 rad drifts, two cycles at 0.02, 0.03, 0.04 rad drifts, etc., up to failure. Figure 5.19 shows the loading history.

5.10 Test Results of Specimen S1

5.10.1 Observed Performance

Figure 5.20 shows the connection of the specimen prior to testing. This specimen had an RBS cut parallel to the column centerline. Initial yielding of the beam top flange was observed at the end of 0.0075 rad drift cycles (Figure 5.21). Yielding of the panel zone and the beam bottom flange occurred at 0.01 rad drift (Figure 5.22). Beam yielding extended to the beam web at 0.015 rad drift (Figure 5.23). A small crack at the bottom end of the beam web-to-column flange CJP weld was observed at the end of 0.02 rad drift cycles [Figure 5.24(b)]. Significant panel zone yielding and column flange kinking also caused yielding on both the back and front faces of the column at the beam bottom flange level [Figure 5.24(d) and (e)].

At the end of second cycle at +0.03 rad drift, the fracture at the beam web CJP weld propagated upward into the web (Figure 5.25). In addition, another fracture from the weld access hole occurred, and a minor crack at the beam flange CJP weld was noticeable. These three cracks at the heel location were closed when the direction of loading was reversed (Figure 5.26). Minor local buckling in the beam bottom flange was visible, but no fracture occurred at the toe (i.e., top flange) location.

At the end of first cycle at +0.04 rad drift, fractures in the beam web CJP weld and the beam weld access hole, but not at the beam bottom flange CJP weld, propagate further (Figure 5.27). Beam flange and web local buckling was obvious when the direction of loading was reversed [Figure 5.28(a)], and a minor crack at the beam top flange CJP weld was observed [Figure 5.28(d)]. The fracture from the beam web CJP weld had passed through one bolt hole in the shear tab, and the fracture from the weld access hole had

propagated into the bottom flange and fractured a large portion of the beam flange during the second cycle at +0.04 rad drift (Figure 5.29). As a result, the beam flexural strength at the column face had degraded below 80% of the beam nominal plastic moment. Figure 5.30 depicts the yielding and buckling pattern when the direction of the load was reversed. Figure 5.31 shows lateral-torsional buckling of the beam. Figure 5.32 shows the global view as well as the damage state of the specimen at +0.05 rad drift. The beam bottom flange had ruptured completely and the test was stopped. Significant column flange yielding at the beam bottom flange level due to column flange kinking is shown in Figure 5.33.

5.10.2 Recorded Response

5.10.2.1 Global Response

A plot of the load versus the beam tip displacement is shown in Figure 5.34. The vertical axis on the right shows the moment at the column centerline. The relationship between the moment at the column face and the story drift angle is shown in Figure 5.35. The vertical axis on the right shows the moment at the column face normalized by the nominal plastic moment (M_{pn}) of the beam. Vertical dotted lines indicate 0.04 rad drift as required by AISC 341 for Special Moment Frame. The specimen completed one cycle at a story drift angle of 0.04 rad before the moment at the column face degraded below $0.8M_{pn}$.

Figure 5.36 shows the relationship between the moment at the column face and the total plastic rotation. Figure 5.37 and Figure 5.38 show the response of the panel zone (see Appendix C for derivation detail). The average panel zone deformation in Figure 5.37 was

based on the diagonal displacement transducers. Flaking of the whitewash indicated that shear yielding in the panel zone was not uniform [e.g., see Figure 5.27(a)]. Based on the measured strains of strain rosette R1 (Figure 5.16), the local shear strain at the center of the panel zone was also computed and used for the response plot in Figure 5.38. Figure 5.39 shows that column had yielded. This yielding was caused by the column flange kinking [Figure 5.33(c)], not plastic hinge formation in the column.

5.10.2.2 Local Response

Figure 5.40 shows the flexural strain profile comparison at the extreme fibers of the beam top and bottom flanges at 0.02, 0.03, and 0.04 rad drifts. Strain readings shown for the bottom and top flanges correspond to those produced by the positive and negative drift cycles, respectively. (Readings from strain gages S13 and S14 are not reliable and, therefore, are not shown.) Figure 5.41 also shows the beam flange strain responses. It is obvious that the strains on the bottom flange (heel location) are higher than those on the top flange (toe location). To demonstrate that such strain concentration only occurred near the column face, strain readings at the RBS location are compared in Figure 5.42 (Response up to 3% drift is plotted because measured strains beyond that drift level were affected by beam buckling.) It is clear that while the strain demand of both beam flanges is similar at a location away from the column face, this is not true at a location next to the column face. Figure 5.43 shows that strain demand on the bottom continuity plate (S22) is higher than the one on the top continuity plate (S21). This is in agreement with the higher strain demand observed at the beam bottom flange near the heel location (Figure 5.40).

5.11 Test Results of Specimen S2

5.11.1 Observed Performance

Figure 5.44 shows the connection of the specimen prior to testing. This specimen had an RBS cut perpendicular to the beam span. Initial yielding of the beam top flange was observed at the end of 0.0075 rad drift cycles (Figure 5.45). Yielding of the panel zone and the beam bottom flange was observed at 0.01 rad drift (Figure 5.46). At the end of second excursion to +0.02 rad drift, beam yielding had extended to the beam web and a small crack at the bottom end of the beam web-to-column flange CJP weld was observed [Figure 5.47(b) and (d)]. At the same drift level, significant panel zone yielding and the associated column flange kinking also caused yielding on both the back and front faces of the column at the beam bottom flange level (Figure 5.47).

At the end of second cycle at +0.03 rad drift, the fracture at the beam web CJP weld propagated upward [Figure 5.48(d)]. In addition, two minor cracks at the beam flange CJP weld were noticeable [Figure 5.48(b) and (e)]. There was no indication of damage on the beam top flange at the toe location upon the completion of the 0.03 rad drift cycles (Figure 5.49). A fracture from the weld access hole occurred when the beam was displaced to the first +0.04 rad drift [Figure 5.50(b)]; the fracture had reached the beam flange too [Figure 5.50(c) and (d)]. The beam bottom flange CJP weld crack was only slightly worse than the previous state, however, the fracture from the beam web CJP weld had increased in length [Figure 5.50(b)]. Also, beam flange and web local buckling was obvious (Figure 5.51). At the end of first -0.04 rad drift cycle, a minor crack at the beam top flange CJP weld was observed (Figure 5.52). By this time, the specimen had completed one cycle at 0.04 rad

drift and the flexural strength at the column face had not degraded below 80% of the nominal plastic moment of the beam.

The fracture from the weld access hole propagated to a larger portion of the beam flange width once the specimen was displaced to the second +0.04 rad drift [Figure 5.53(c) and (d)]. Local buckling in the beam top flange occurred [Figure 5.53(a)]. Figure 5.54 shows the connection at the end of second cycle at -0.04 rad drift. There was no new sign of damage at the toe location. Figure 5.55 shows the specimen at the end of first excursion to +0.05 rad drift. At this level of drift the beam bottom flange had completely ruptured [Figure 5.56(c)] and the test was stopped. Figure 5.57(a) and (b) show the lateral-torsional buckling of the beam at the second cycle of +0.03 and +0.04 rad drifts, respectively. Significant column flange yielding at the beam bottom flange level due to column flange kinking is shown in Figure 5.58.

5.11.2 Recorded Response

5.11.2.1 Global Response

A plot of the load versus the beam tip displacement is shown in Figure 5.59. The relationship between the moment at the column face and the story drift angle is shown in Figure 5.60. The vertical axis on the right shows the moment at the column face normalized by the nominal plastic moment (M_{pn}) of the beam. Vertical dotted lines indicate 0.04 rad drift as required by AISC 341 for Special Moment Frame. The specimen completed two cycles at a story drift angle of 0.04 rad before the moment at the column face degraded below $0.8M_{pn}$.

Figure 5.61 shows the relationship between the moment at the column face and the total plastic rotation. Figure 5.62 and Figure 5.63 show the response of the panel zone. The average panel zone deformation in Figure 5.62 was based on the diagonal displacement transducers. Based on the measured strains of strain rosette R1 (Figure 5.17), the local shear strain at the center of the panel zone was also computed and used for the response plot in Figure 5.63. Figure 5.64 shows that column had yielded; the yielding was mainly caused by column flange kinking to accommodate panel zone shear yielding, not due to flexural yielding of the column.

5.11.2.2 Local Response

Figure 5.65 shows the beam flange strain responses. Similar to Specimen S1, the strains on the beam bottom flange (heel location) are much higher than those on the top flange (toe location). Figure 5.66 shows a comparison of strain readings at the RBS location, which, together with the results from Specimen S1 (Figure 5.42), confirms that strain concentration due to the sloping effect occurred at the location near column face only. Figure 5.67 shows that the strain demand on the bottom continuity plate (S22) is higher than that on the top continuity plate (S21), which is in agreement with the higher demand observed at the beam bottom flange near the heel location.

5.12 Comparison of Cyclic Responses

5.12.1 General

The performance of Specimens S1 and S2 together with an orthogonal connection Specimen C2 is compared in this section. These three specimens have the same beam and column sizes, thus facilitating a direct comparison.

5.12.2 Global Response

Figure 5.68 shows the global response comparison of Specimen C2 with Specimens S1 and S2, respectively. It is obvious that the orthogonal connection provided a much more ductile response in comparison to the corresponding sloped connections. Also, Specimens S1 and S2 showed more significant strength degradation compared to Specimen C2. None of the sloped connections survived a complete cycle of 0.05 rad drift before the moment at the column face degraded below $0.8M_{pn}$, while Specimen C2 could sustain two cycles at 0.05 rad drift.

Figure 5.69 shows the global response comparison of Specimens S1 and S2. Specimen S2, which followed the RBS configuration recommended by Kim et al. (2016), performed slightly better than Specimen S1. It sustained two cycles at 0.04 rad drift before the moment at the column face degraded below $0.8M_{pn}$ whereas Specimen S1 underwent only one cycle at 0.04 rad drift. Also, the post-buckling response of Specimen S2 showed more ductile response compared to Specimen S1 since the strength degradation rate was slower. It was expected from the finite element study by Kim et al. that Specimen S2 would have performed much better. But the testing did not show such a significant improvement, mainly because the fractures at the beam web CJP weld and weld access hole dominated the failure mode.

The sloping effect can be further demonstrated by comparing the amount of energy dissipated by each specimen in Figure 5.70, where the energy, E_h, has been normalized by the plastic moment, M_p, of the beam. Although the dissipation of energy is very similar

for all specimens up to the 0.04 rad drift, the total energy dissipated by the orthogonal specimen was doubled as compared to those of the sloped connections.

5.12.3 Local Response

Figure 5.71 and Figure 5.72 show the flexural strain response comparison of Specimens C2 and S1 at the beam bottom flange level (heel location for Specimen S1); these gages were placed at a distance 3 in. away from the column face. The detrimental effect of the sloped connection near the column face is obvious.

5.12.4 Failure Mode

Specimen C2 experienced the typical RBS connection failure mode, i.e., yielding and buckling in the RBS region, and no fracture developed. But two undesirable brittle failure modes developed in the sloped specimens: fracture of the beam web CJP weld and fracture from the weld access hole which then propagated into the beam flange. Both failure modes occurred consistently at the heel location of the sloped connections (Figure 5.73). Significant shear yielding occurred in all three specimens, but this yielding is not expected to affect the failure modes mentioned above.

The fracture mode observed in this test program is also compared to that from Kim et al. (2016) as follows. Two RBS specimens tested by Kim et al. had a sloped angle of 28°, and the heel location corresponded to the top flange of the beams. The heel location for this research project was purposely positioned at the bottom flange level. Both test programs show that fracture always occurred at the heel location. The specimens tested by Kim et al. experienced partial fracture of the CJP weld between the beam web and column, followed by a sudden and brittle fracture of the beam flange CJP weld at the heel location.

For this research, the same fracture of the beam web CJP weld also started first and then propagated into the beam web. Sudden fracture of the beam flange CJP weld did not occur. Instead, a fracture starting from the highest stress concentration point along the curved profile of the weld access hole then developed and propagated rapidly into the beam flange to fracture the entire width of the flange. Despite some minor differences between the fracture mode observed in both test programs, what is common is the undesirable fracture mode in the weld region at the heel location.

Table 5.1 Base Metal Mechanical Properties

Specimen No.	Component	Steel Grade/ Heat No.	Yield Stress (ksi)[a]	Tensile Strength (ksi)	Elong. (%)[b]
S1, S2	Beam Flange (W36×150)	A992 60114091/04	54.4 (57.0)[b]	76.2 (75.1)[b]	40.7 (26.4)[b]
	Beam Web (W36×150)		60.1	79.3	37.7
	Column Flange (W14×257)	A992 315895	55.2 (56.0)[b]	77.7 (75.5)[b]	38.2 (27.0)[b]
	Column Web (W14×257)		54.9	76.6	37.0
	Continuity Plate (1 in.)	A572 Gr. 50 E4E286	57.0 (57.0)[b]	81.3 (78.0)[b]	39.7 (24.0)[b]

[a] Yield strength determined by the 0.2% strain offset method
[b] Values in parentheses from Certified Mill Test Reports, others from testing at UCSD

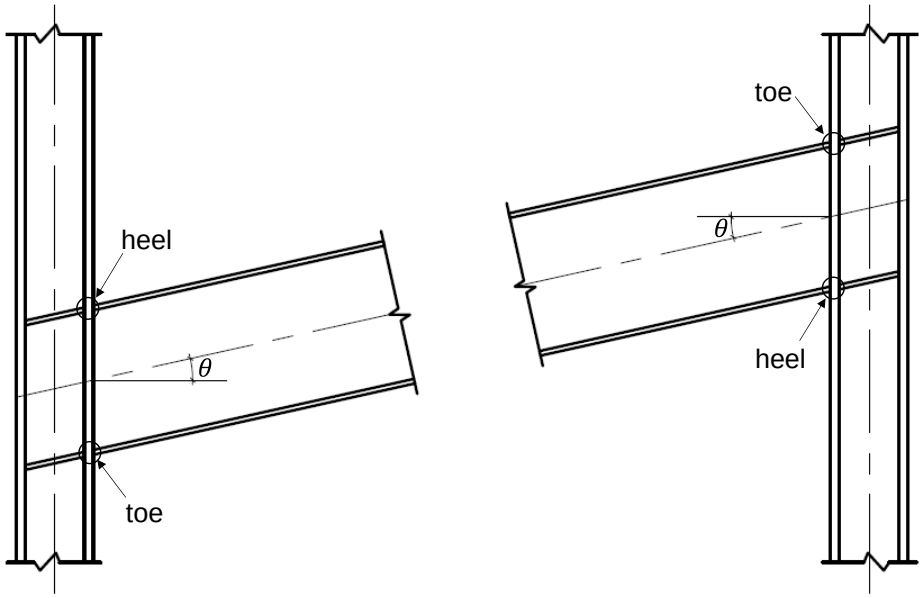

(a) Beam Slopes Upward

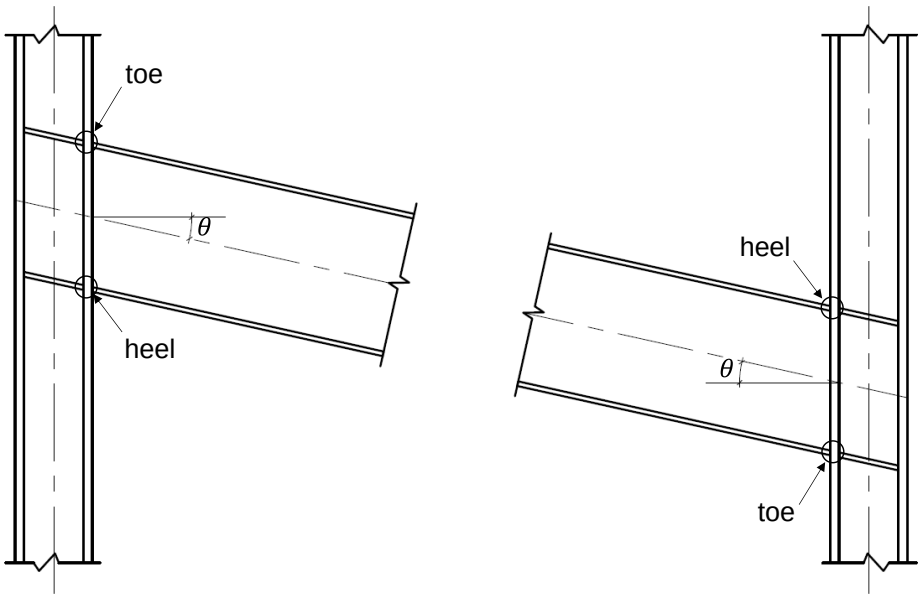

(b) Beam Slopes Downward

Figure 5.1 Definition of Heel and Toe Locations in Sloped Connections

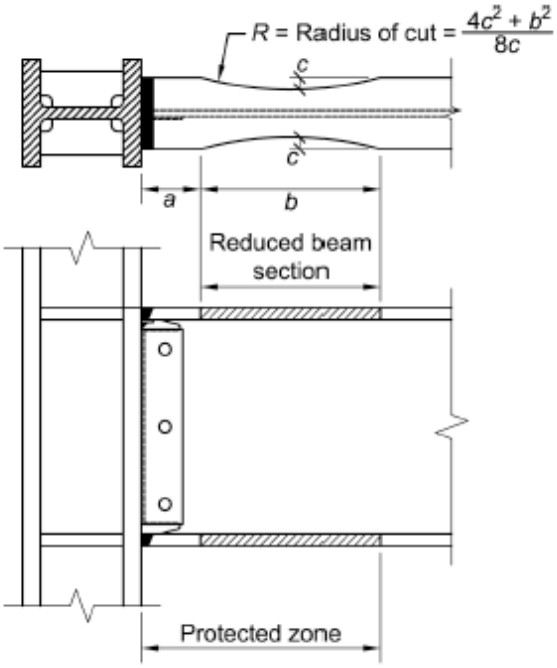

Figure 5.2 RBS Connection (AISC 2010b)

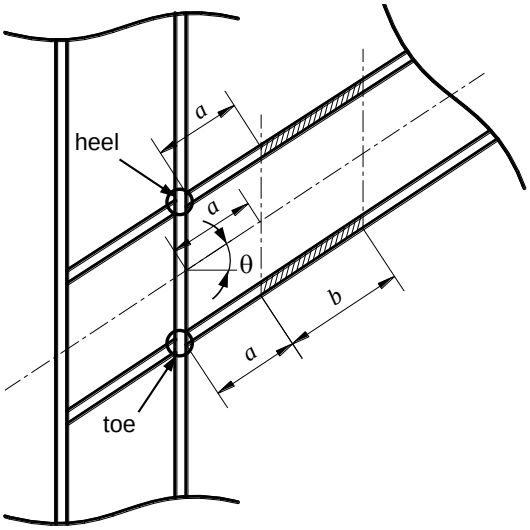

(a) Configuration 1: RBS Parallel to Column Centerline

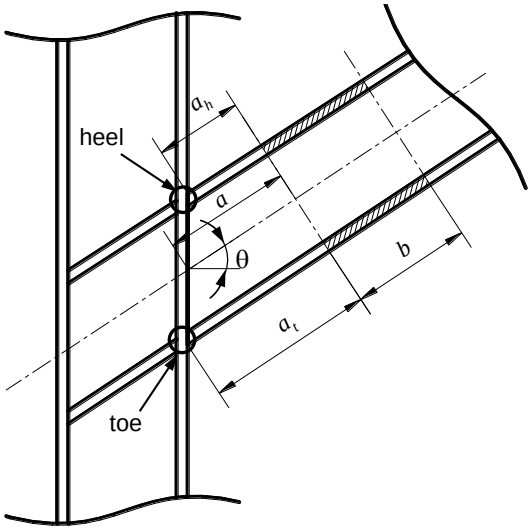

(b) Configuration 2: RBS Perpendicular to Beam Span

Figure 5.3 RBS Configuration in a Sloped Connection (Kim et al. 2016)

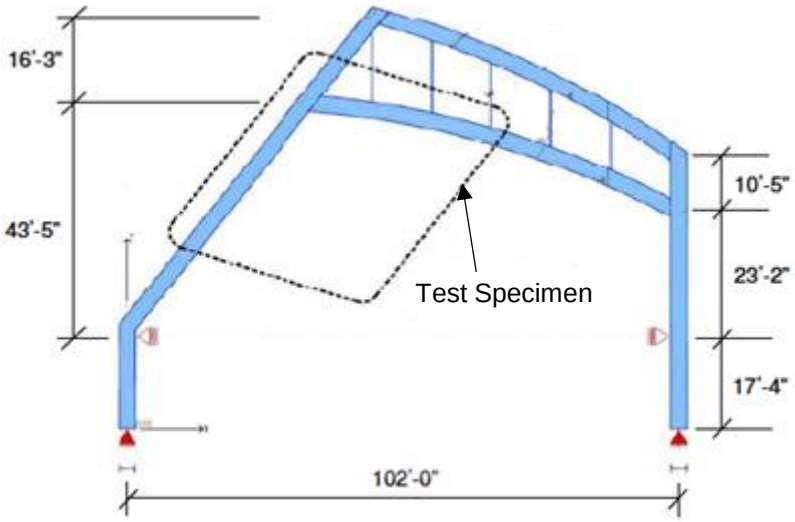

(a) Portion of Frame Simulated in Testing

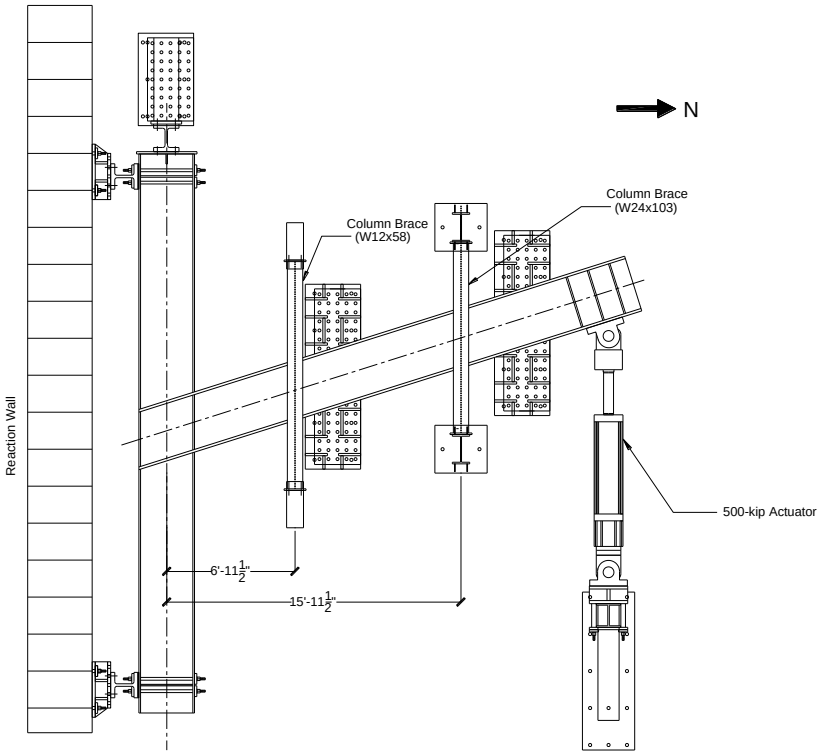

(b) Test Setup

Figure 5.4 LAX Test Setup (Kim et. al. 2010)

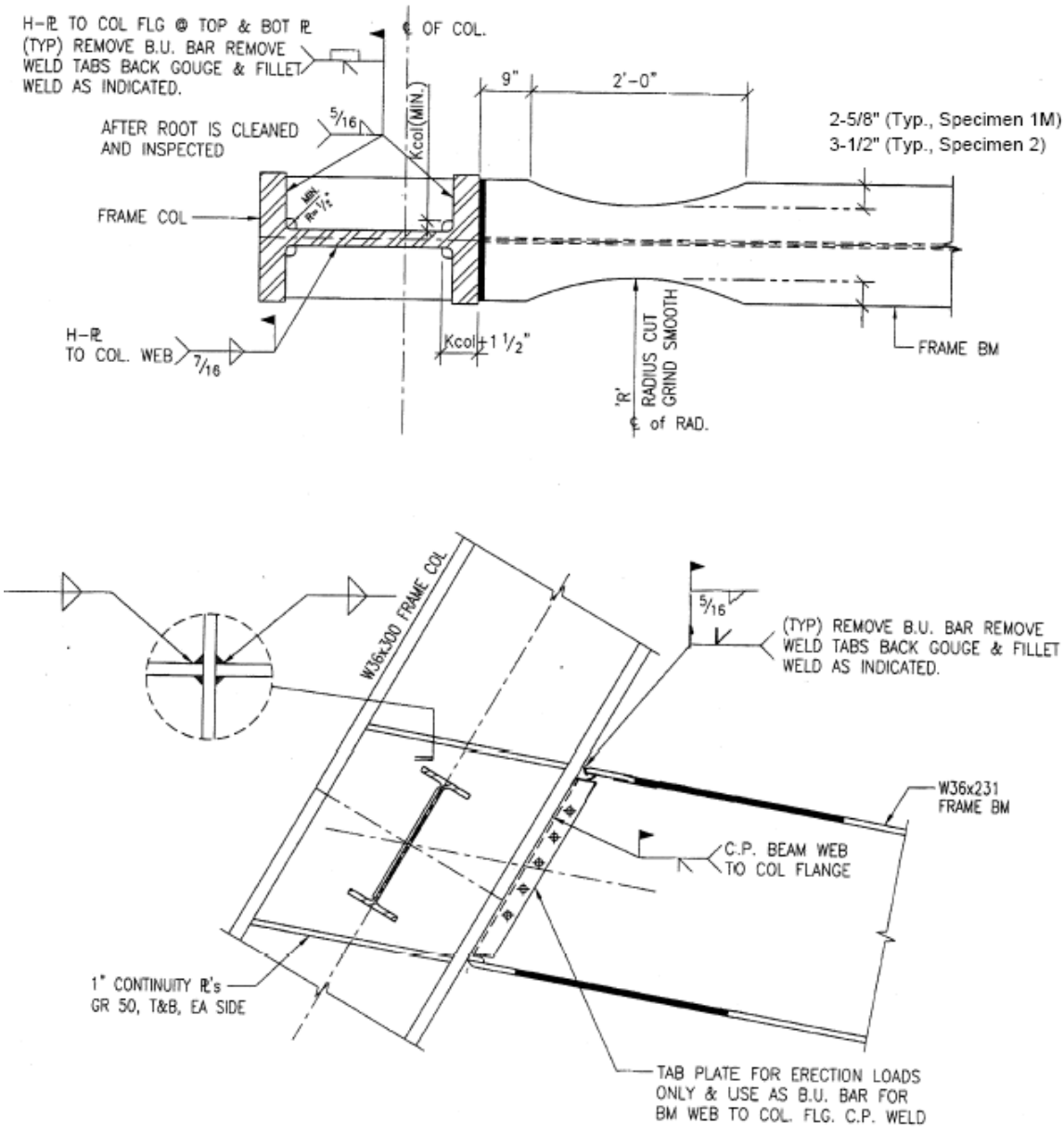

Figure 5.5 Detail of LAX Connection Specimens (Kim et. al. 2010)

Figure 5.6 Erection of SMF with Sloped Connections

(courtesy of T. Kuznik, The Herrick Corporation)

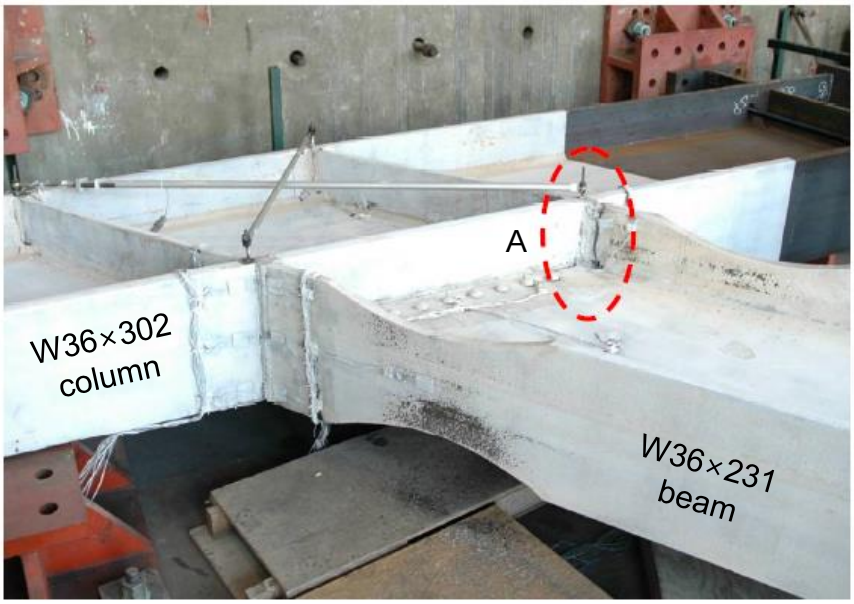

(a) Global View

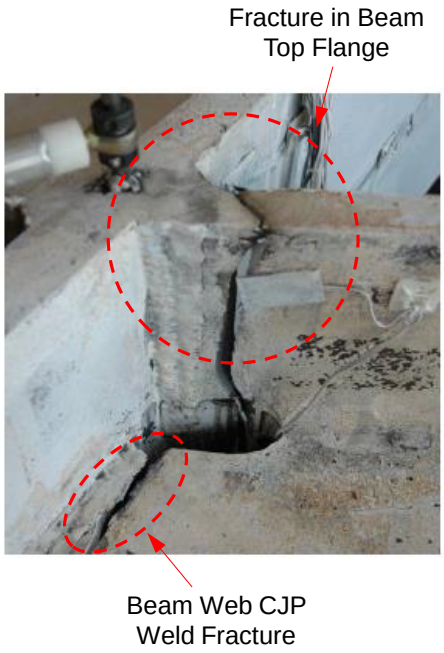

(b) Close-up View of The Fracture

Figure 5.7 Fracture at Heel Location on Specimen 1M (Kim et. al. 2010)

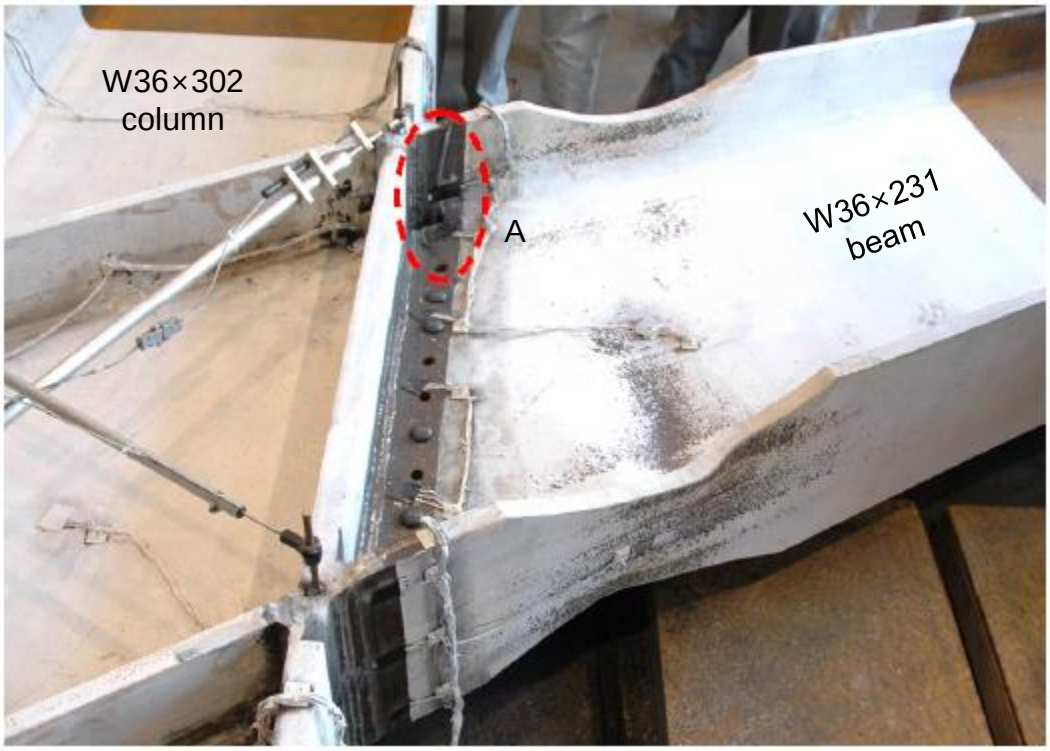

(a) Global View

(b) Close-up View of The Fracture

Figure 5.8 Fracture at Heel Location on Specimen 2 (Kim et. al. 2010)

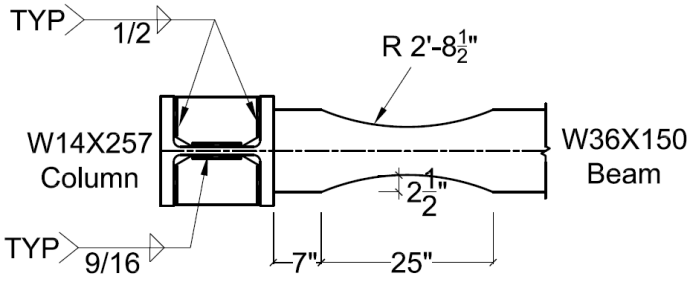

(a) Plan View

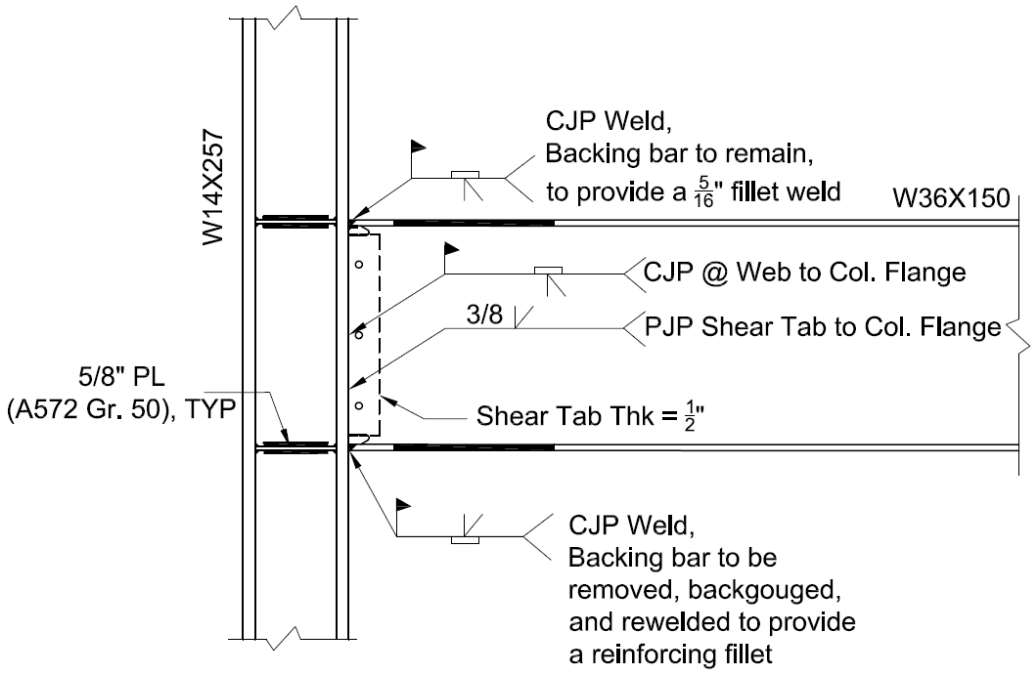

(b) Elevation View

Figure 5.9 Specimen C2 Connection Detail Project

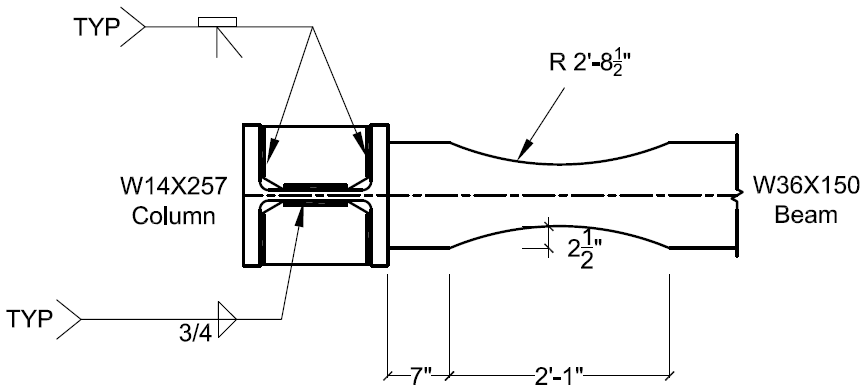

(a) Plan View

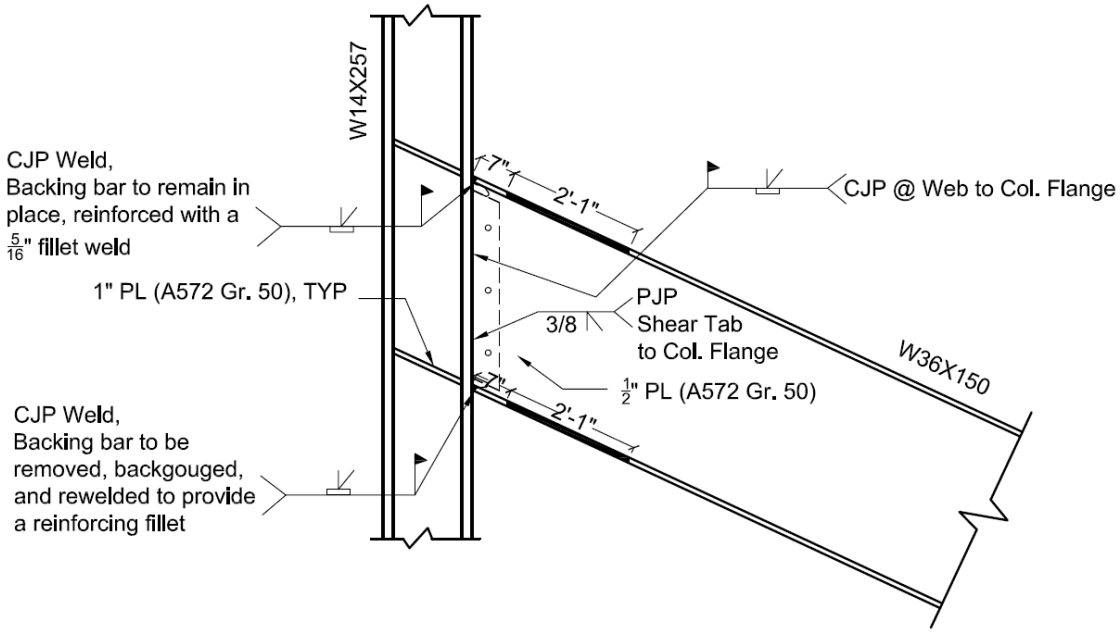

(b) Elevation View

Figure 5.10 Connection Detail for Specimen S1

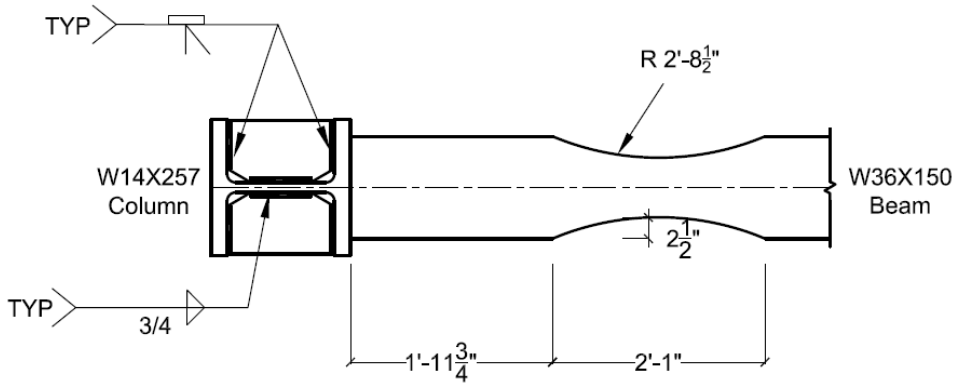

(a) Plan View Beam Top Flange

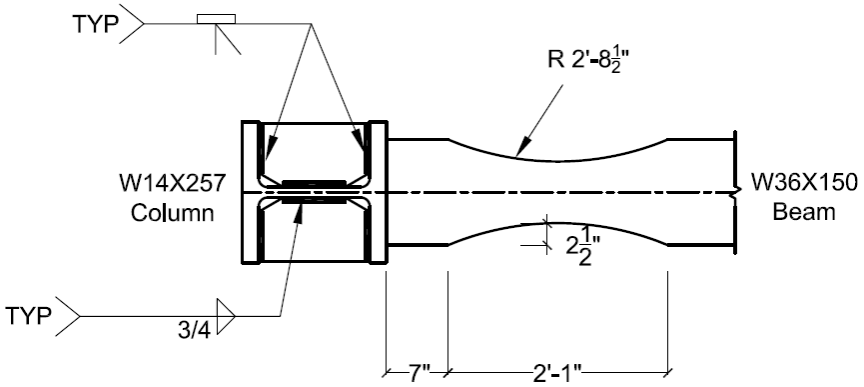

(b) Plan View Beam Bottom Flange

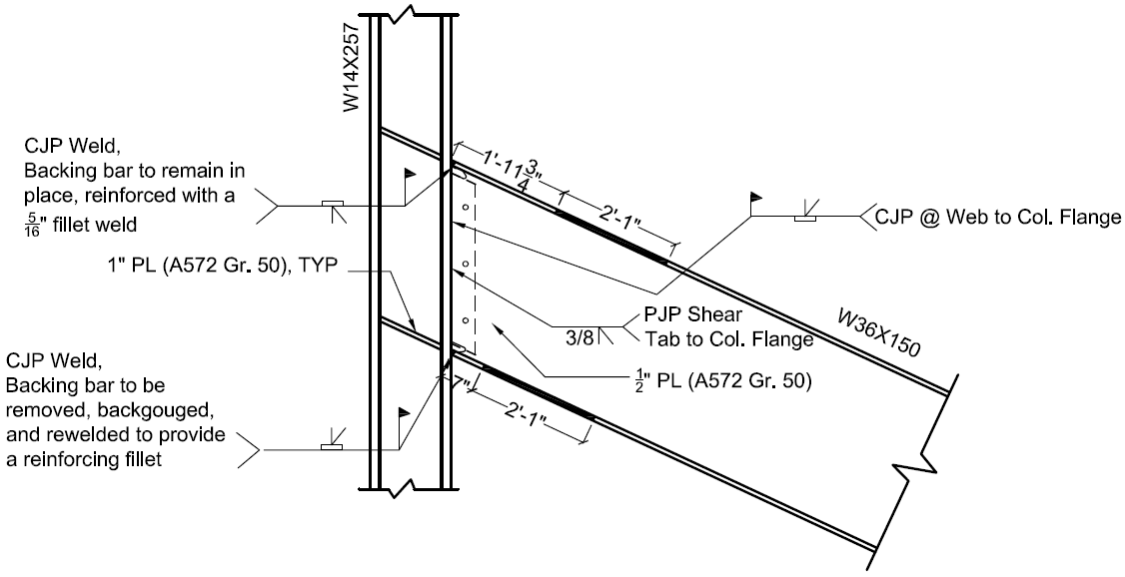

(c) Elevation View

Figure 5.11 Connection Detail for Specimen S2

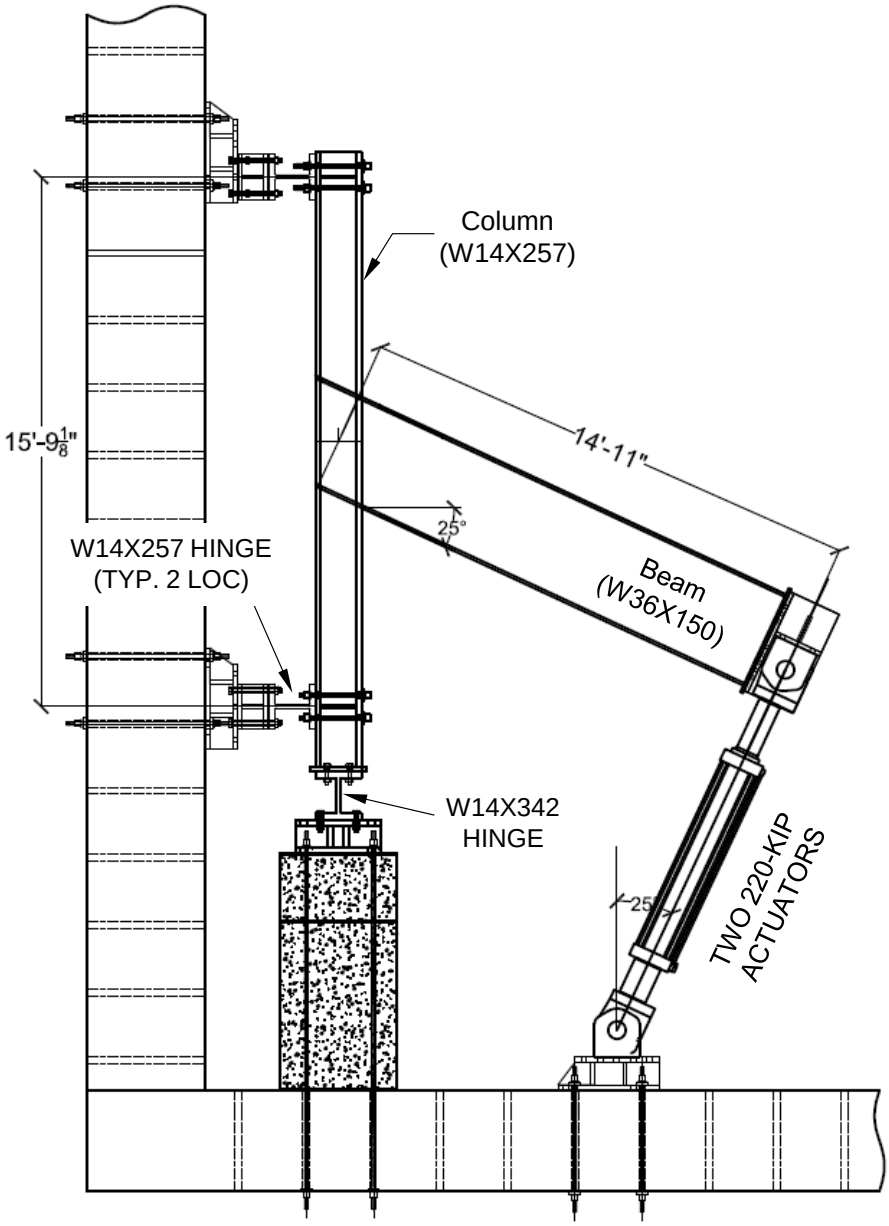

Note: Lateral bracing system not shown

Figure 5.12 Overall Test Setup

(a) Top End

(b) Bottom End

Figure 5.13 Simulated Hinge Support at Column Top and Bottom

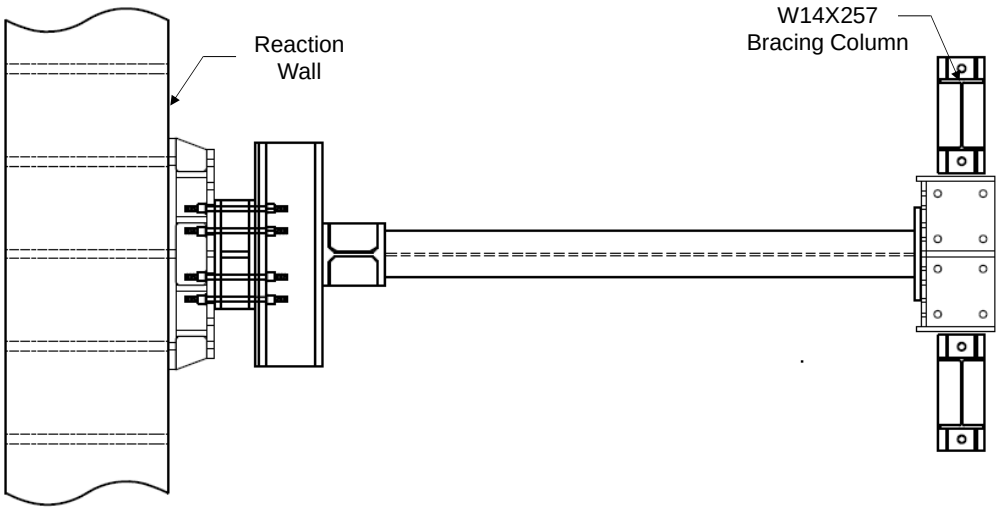

(a) Plan View

(b) View from South

(c) View from West

Figure 5.14 Beam Lateral Bracing System

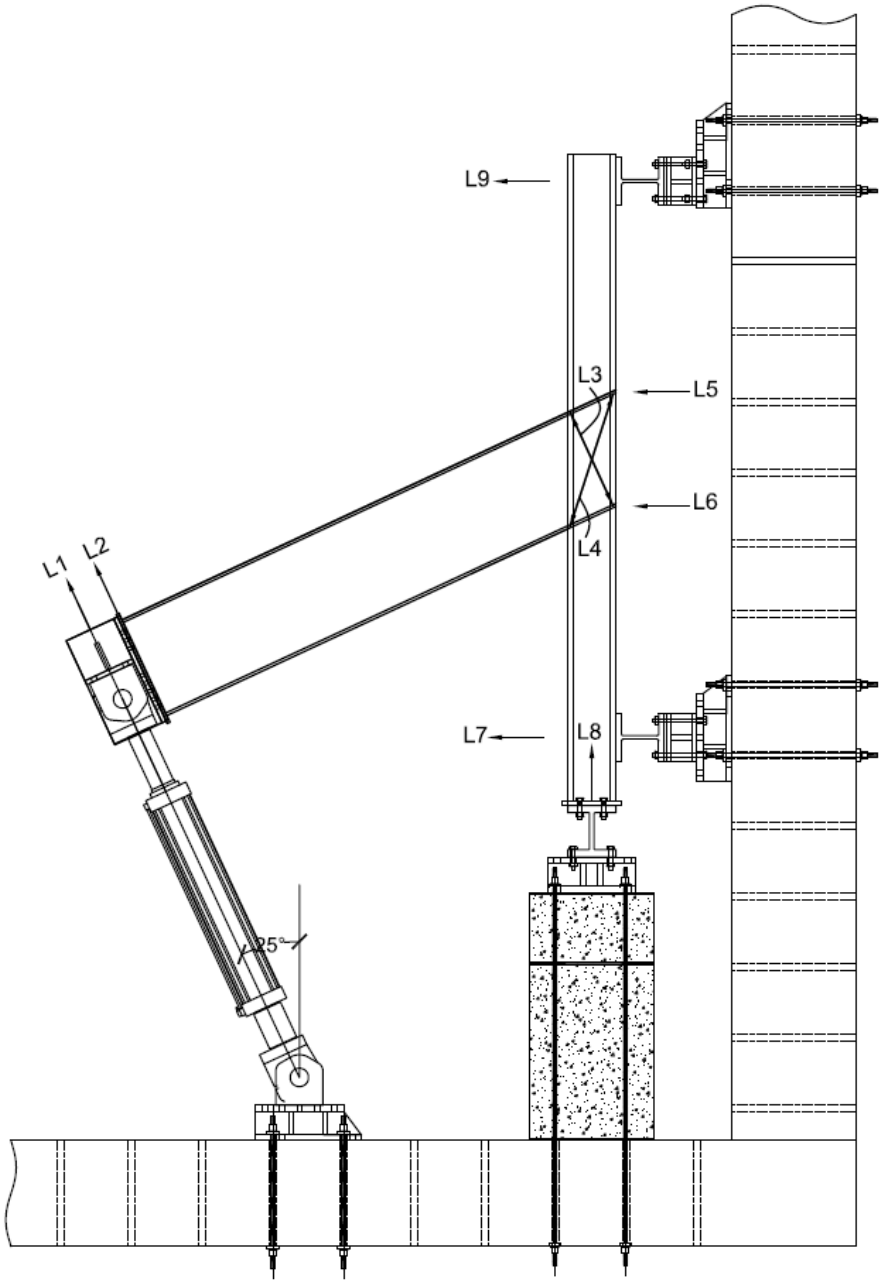

Figure 5.15 Displacement Transducers Location

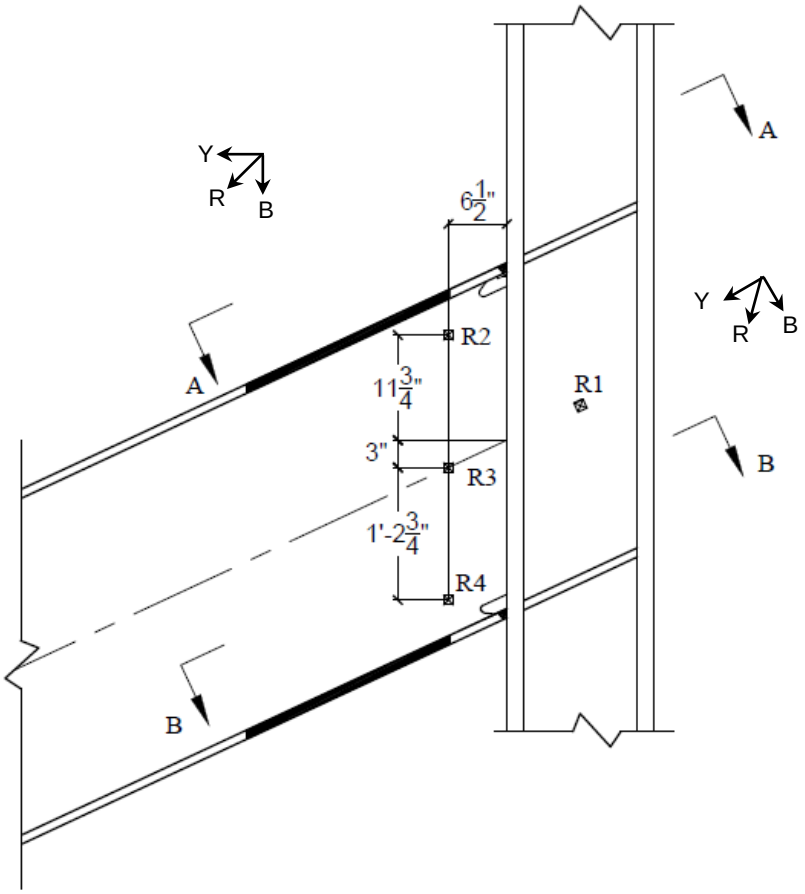

(a) Elevation (East View)

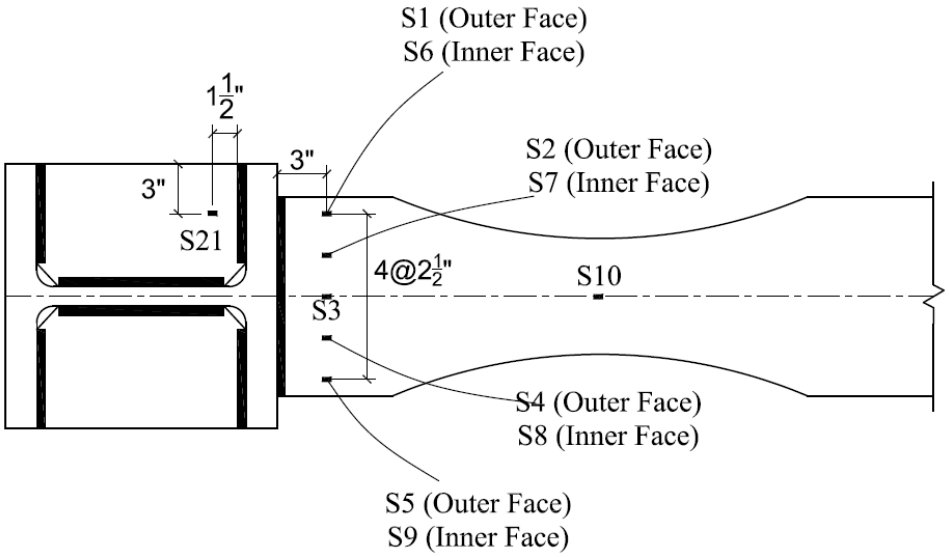

(b) Section A-A

Figure 5.16 Strain Gage and Rosette Location for Specimen S1

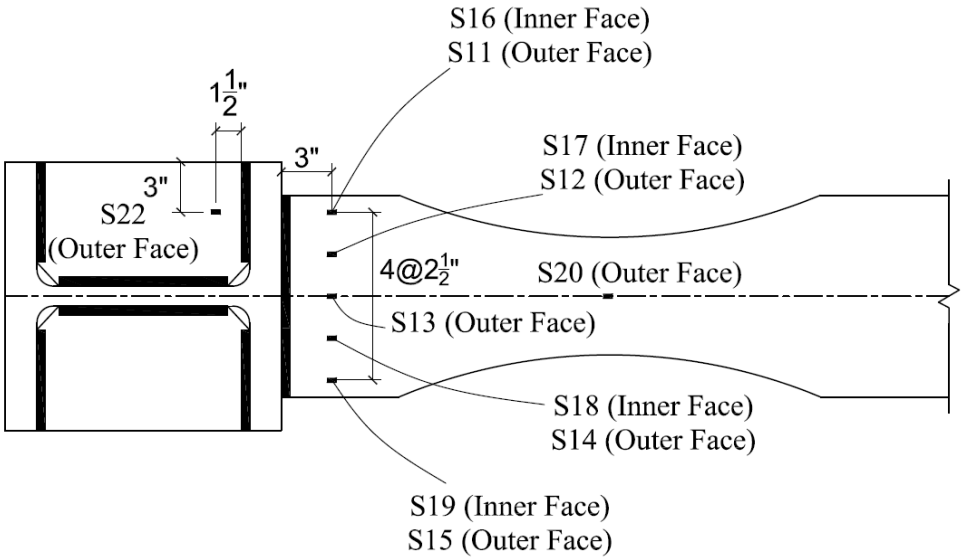

(c) Section B-B

Figure 5.16 Strain Gage and Rosette Location for Specimen S1 (continued)

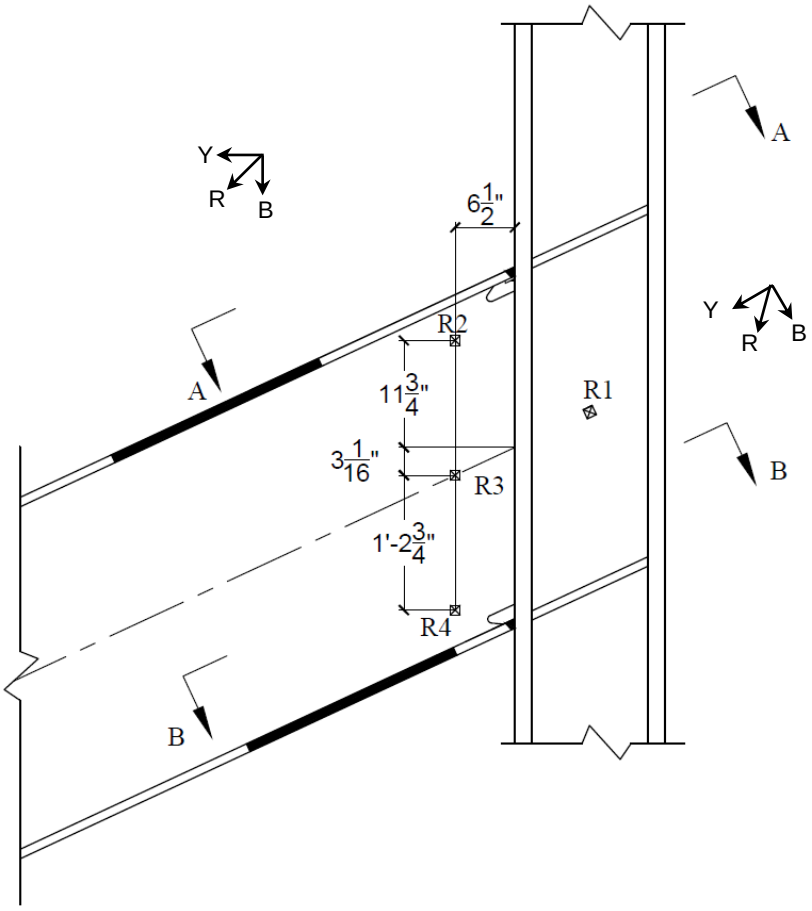

(a) Elevation (East View)

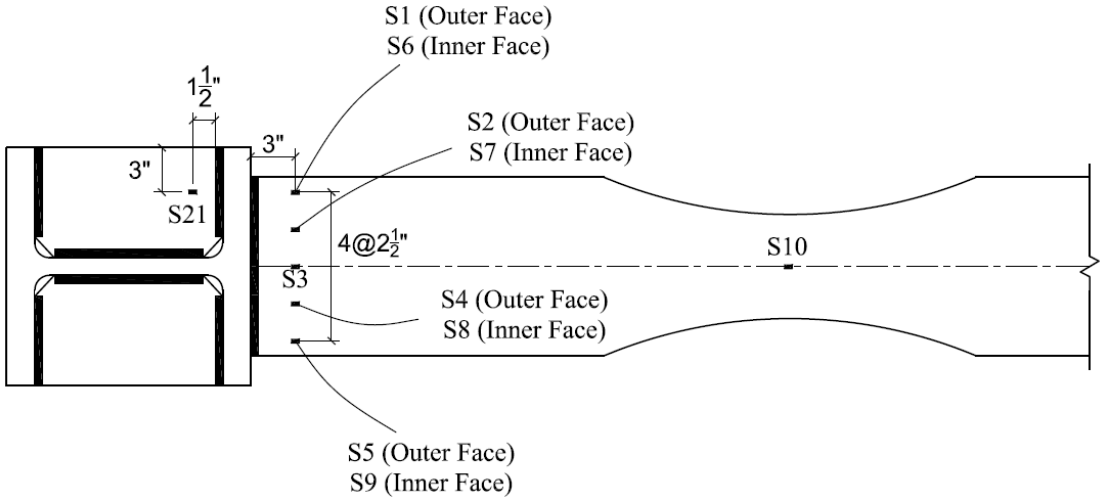

(b) Section A-A

Figure 5.17 Strain Gage and Rosette Location for Specimen S2

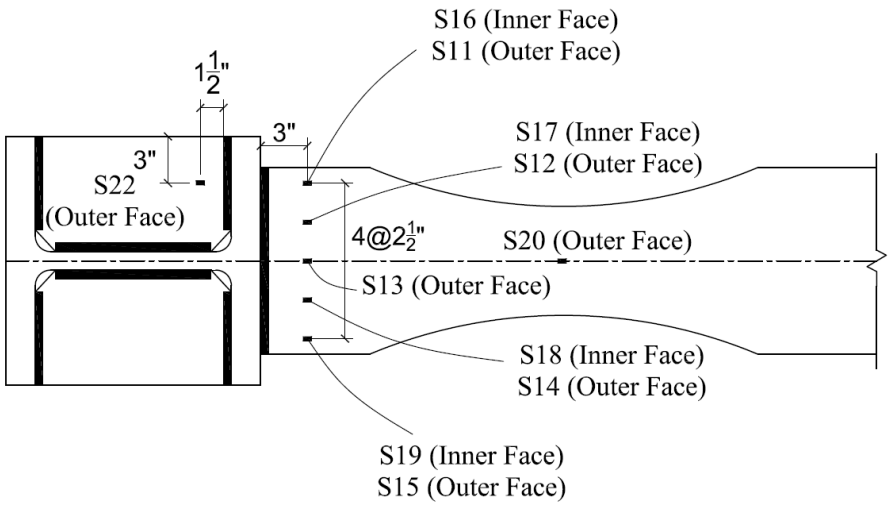

(c) Section B-B

Figure 5.17 Strain Gage and Rosette Location for Specimen S2 (continued)

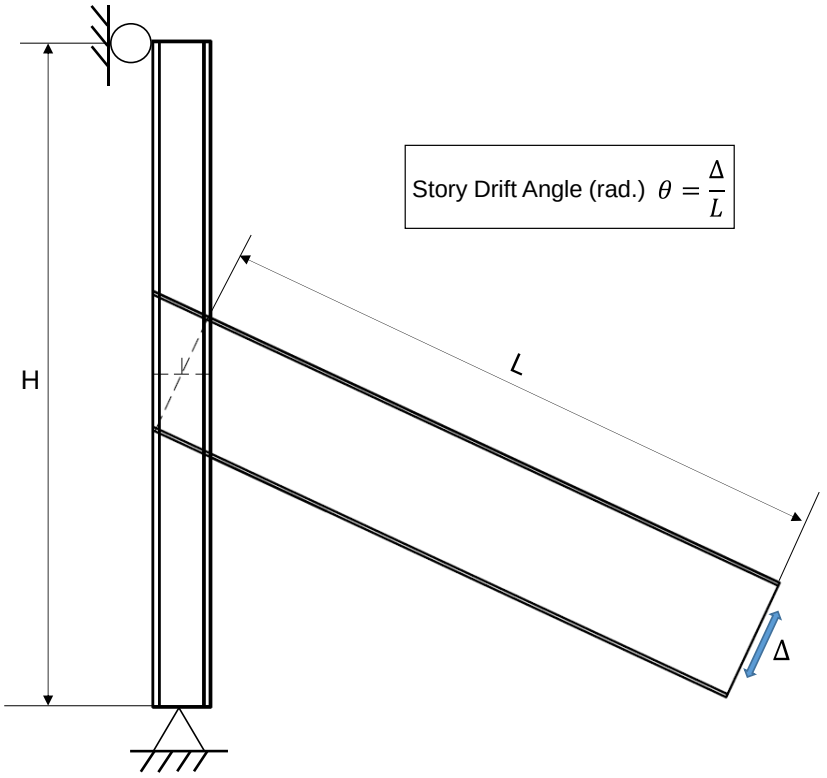

Figure 5.18 Definition of Story Drift Angle for Sloped Connection

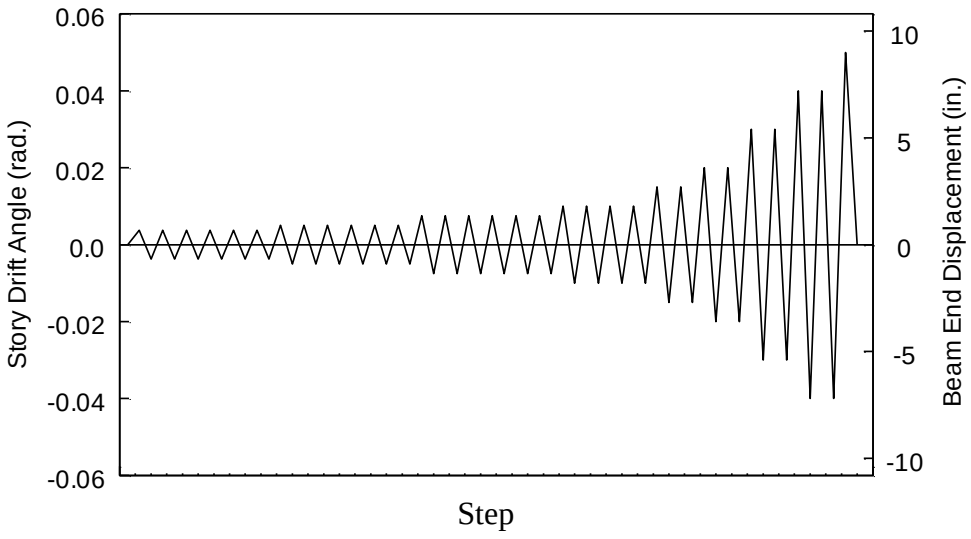

Figure 5.19 Loading Protocol

Figure 5.20 Specimen S1 Connection Prior to Testing

(a) View from South-West

(b) Detail A

Figure 5.21 Specimen S1 Minor Flange Yielding at End of 0.0075 rad Drift

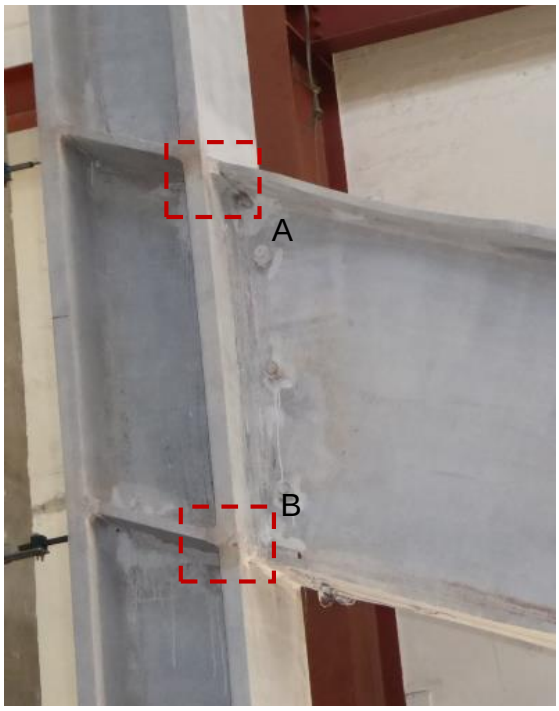

(a) View from West

(b) Panel Zone

(c) Detail A

(d) Detail B

Figure 5.22 Specimen S1 Yielding at +0.01 rad Drift (4th Cycle)

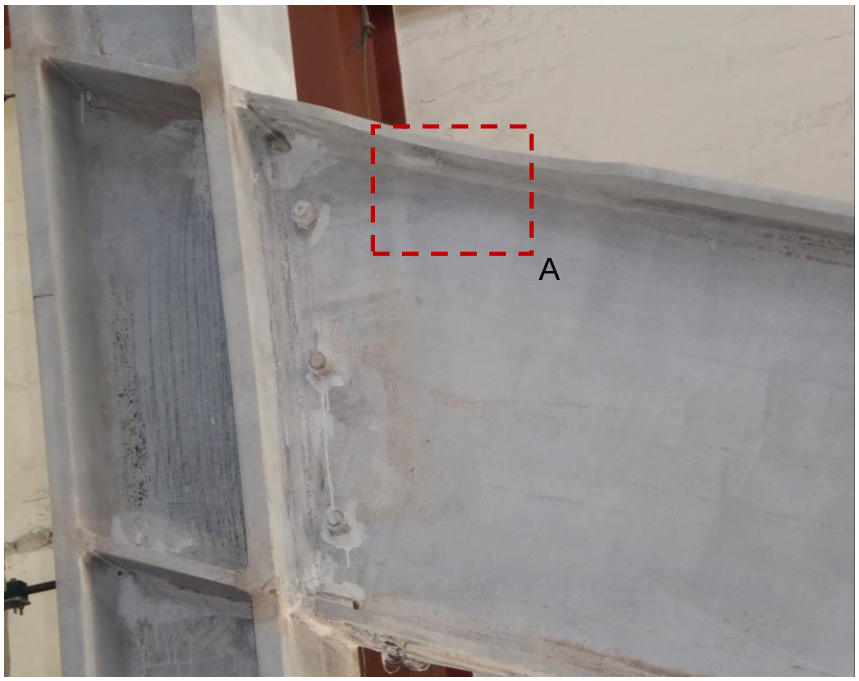

(a) View from West

(b) Detail A, Yielding on Beam Web

Figure 5.23 Specimen S1 Beam Web Yielding at +0.015 rad Drift (2nd Cycle)

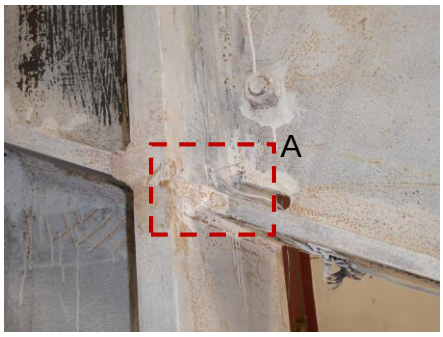

(a) Heel Location

(b) Detail A, Minor Crack at End of Beam Web CJP Weld

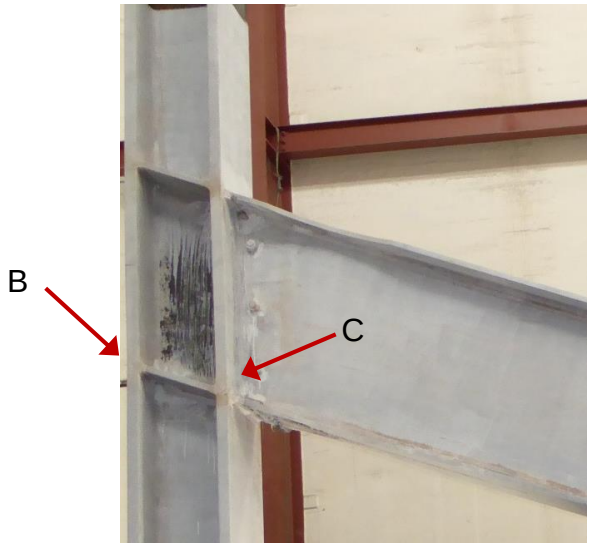

(c) View from West

(d) Detail B, Back Column Flange

(e) Detail C, Front Column Flange

Figure 5.24 Specimen S1 at +0.02 rad Drift (2nd Cycle)

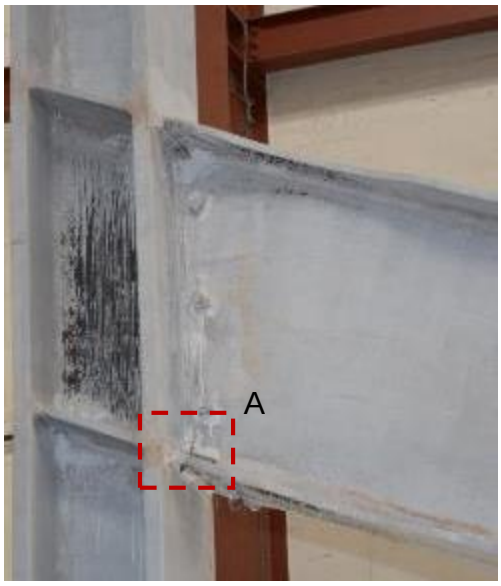

(a) View from West

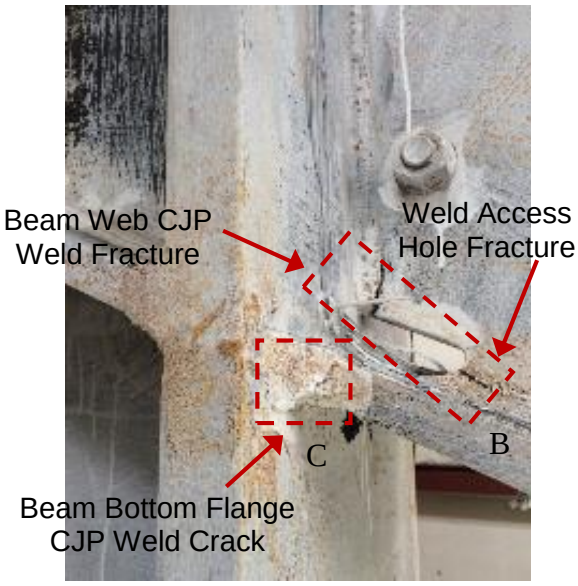

(b) Detail A

(c) Detail B

(d) Detail C

Figure 5.25 Specimen S1 Specimen at +0.03 rad Drift (2nd Cycle)

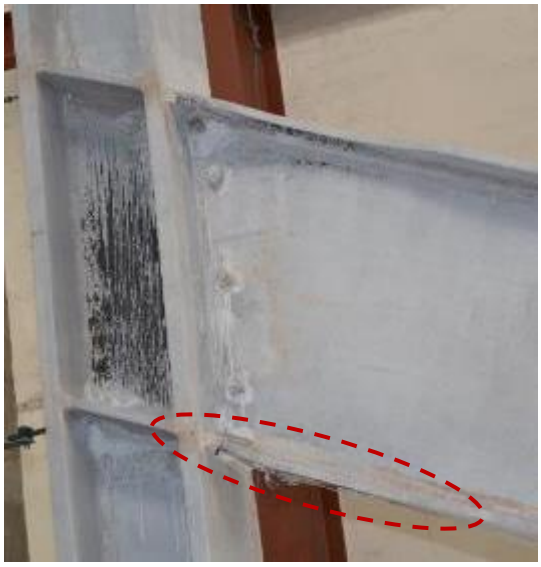

(a) Minor Beam Flange Local Buckling

(b) Closure of Fractures at Beam Bottom Flange Level

(c) Top Flange CJP Weld (No Fracture)

Figure 5.26 Specimen S1 at -0.03 rad Drift (2nd Cycle)

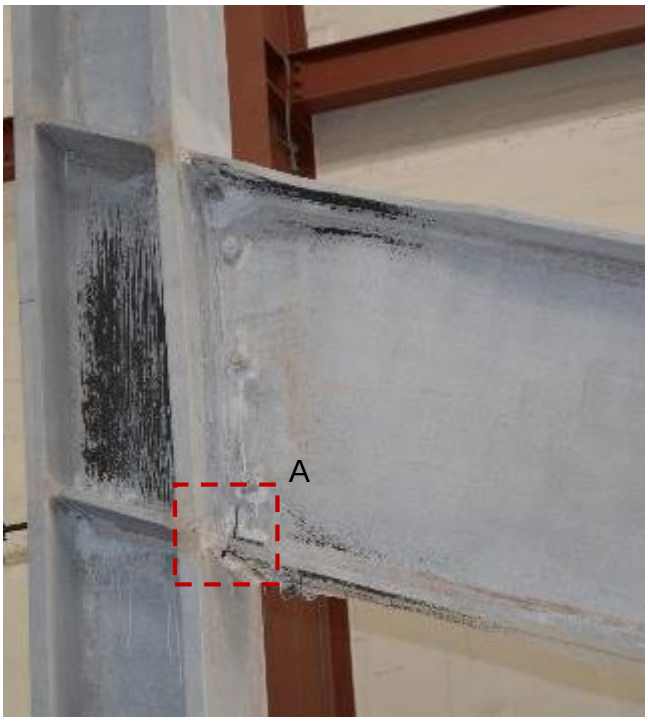

(a) Global View

(b) Detail A (Fractures at Beam Web CJP Weld and Weld Access Hole)

Figure 5.27 Specimen S1 Connection at +0.04 rad Drift (1st Cycle)

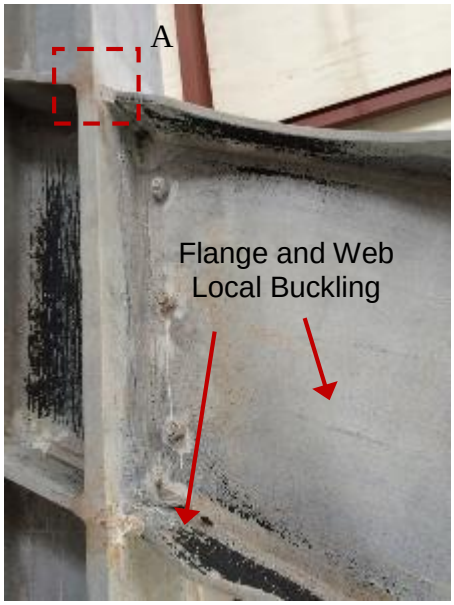

(a) View from West

(b) Detail A (No Fracture)

(c) Beam Top Flange CJP Weld and Weld Access Hole

(d) Beam Top Flange CJP Weld (Minor Crack)

Figure 5.28 Specimen S1 at -0.04 rad Drift (1st Cycle)

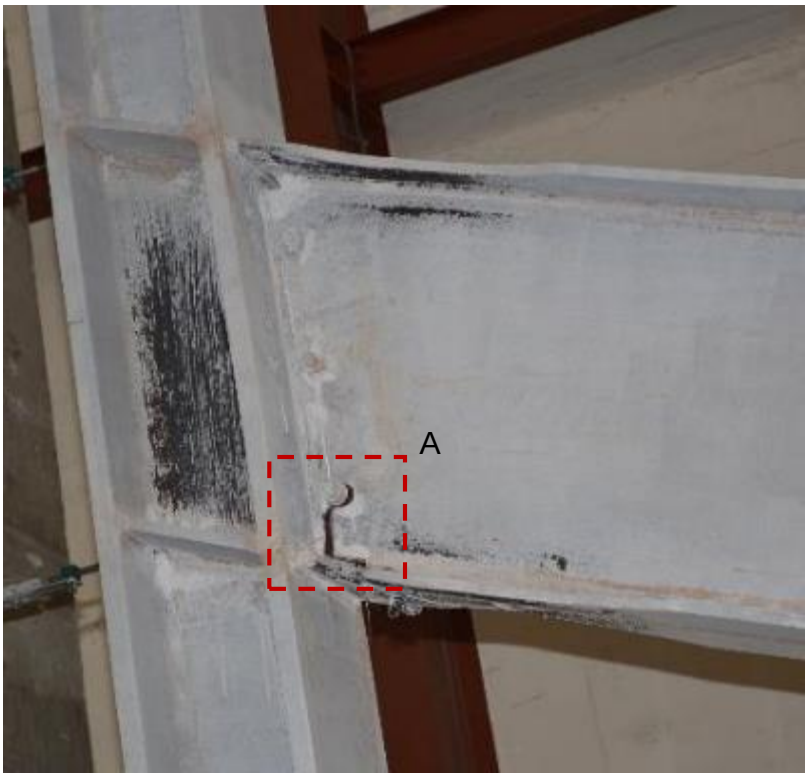

(a) View from West

(b) Detail A

(c) Beam Bottom Flange Fracture

Figure 5.29 Specimen S1 at +0.04 rad Drift (2nd Cycle)

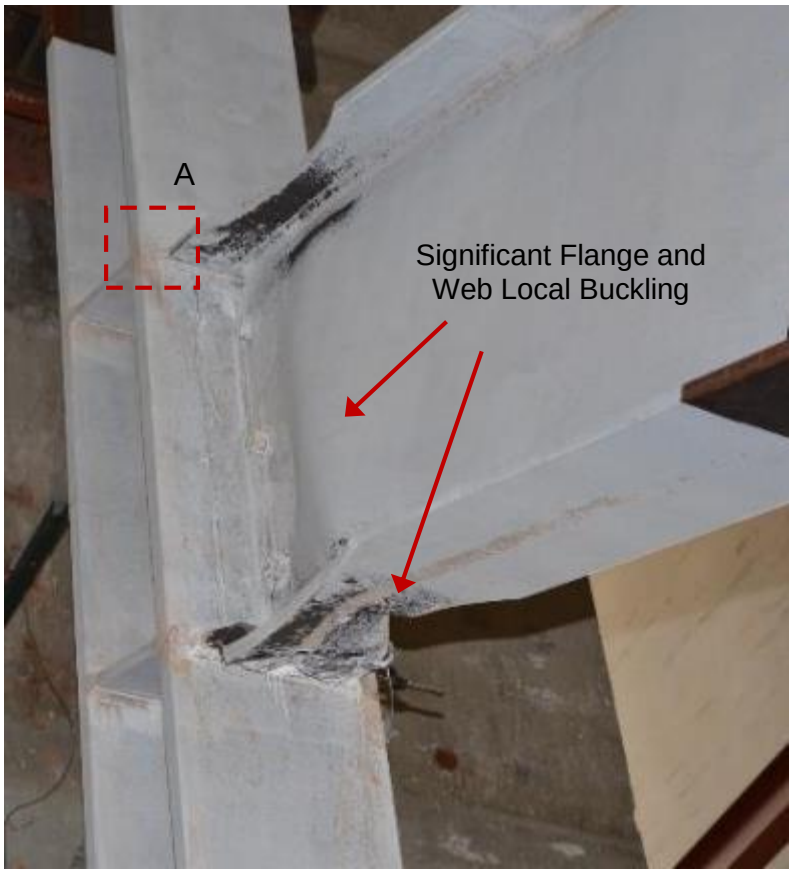

(a) Global View from South-West

(b) Detail A, Top Flange CJP Weld

(c) View of Beam Bottom Flange

Figure 5.30 Specimen S1 at -0.04 rad Drift (2nd Cycle)

(a) -0.04 rad Drift (1st Cycle)

(b) -0.04 rad Drift (2nd Cycle)

Figure 5.31 Specimen S1 Beam Lateral-Torsional Buckling

(a) Global View

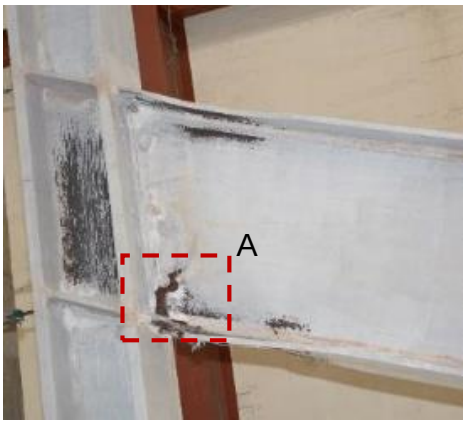

(b) View from West

(c) Detail A

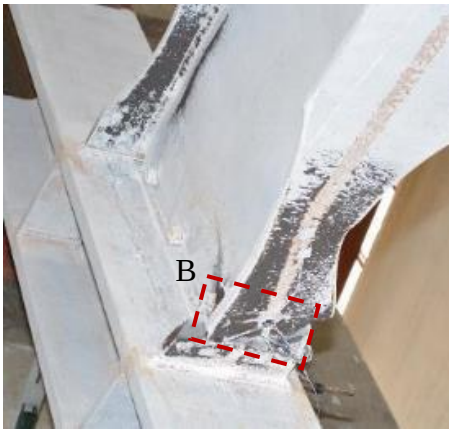

(d) View from Bottom

(e) Detail B

Figure 5.32 Specimen S1 at +0.05 rad Drift (1st Cycle)

(a) View from South West

(b) View from South East

(c) View from Back

Figure 5.33 Specimen S1 Column Flange Yielding at Test Completion

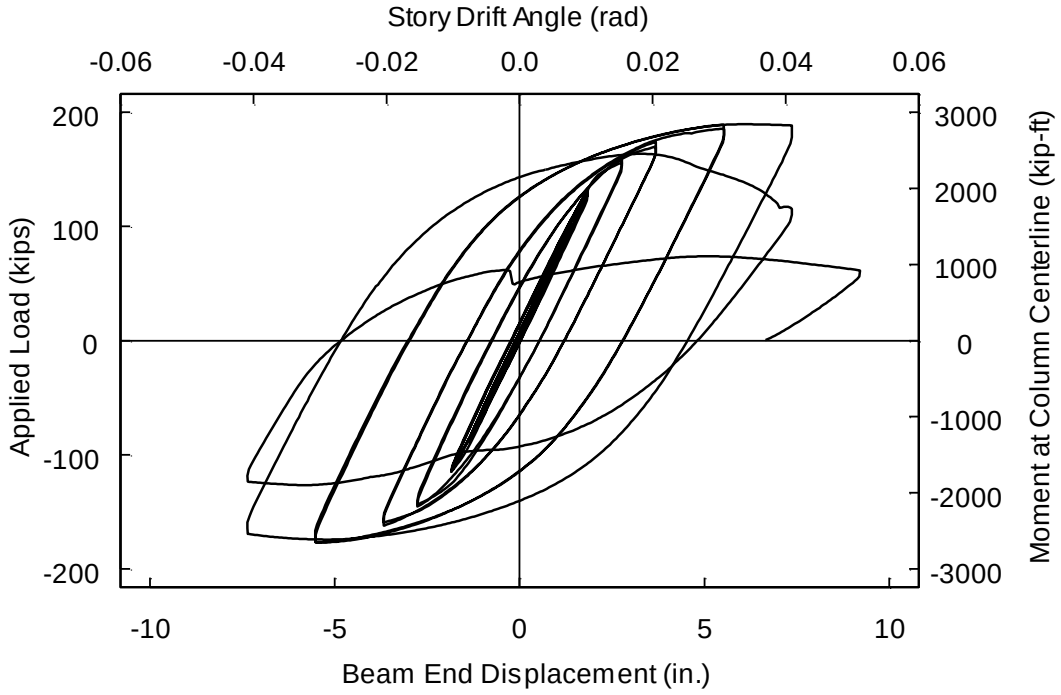

Figure 5.34 Specimen S1 Load versus Beam Tip Displacement Relationship

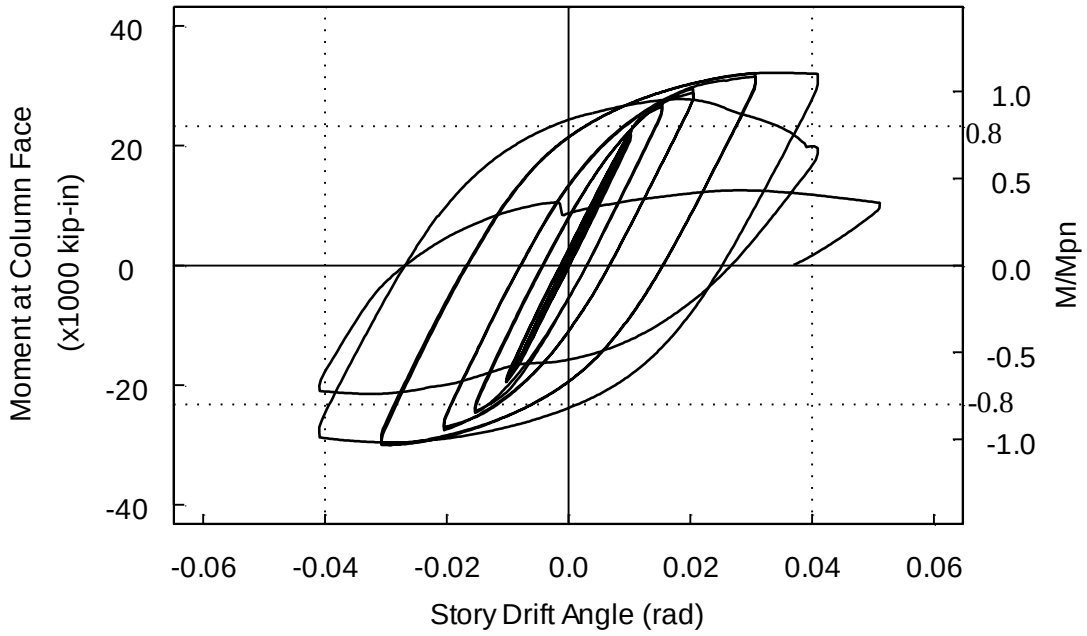

Figure 5.35 Specimen S1 Moment versus Story Drift Angle Relationship

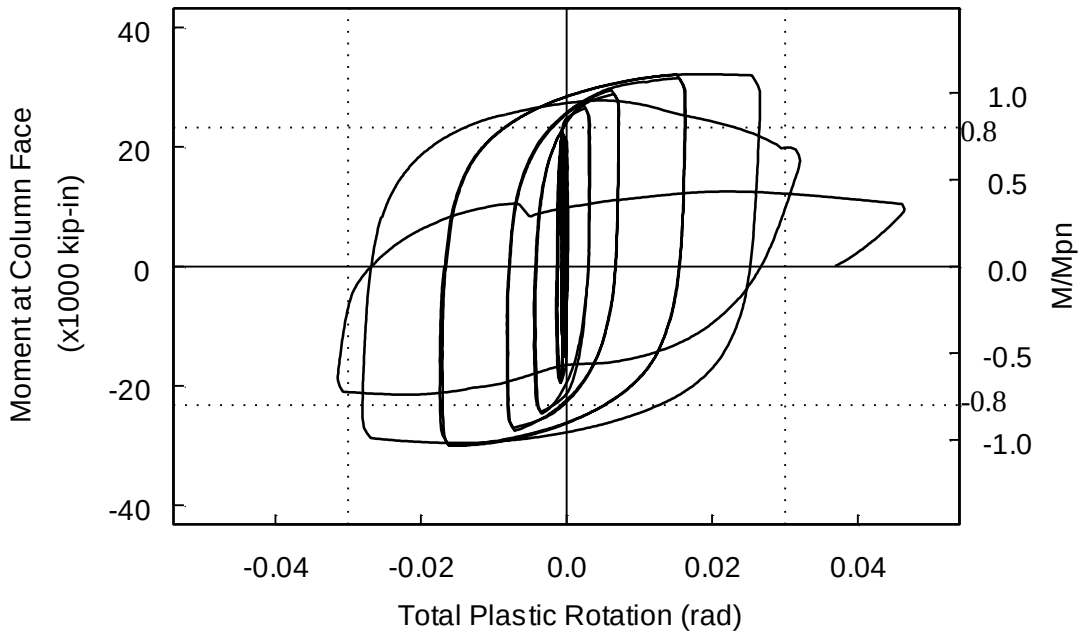

Figure 5.36 Specimen S1 Moment versus Total Inelastic Rotation Relationship

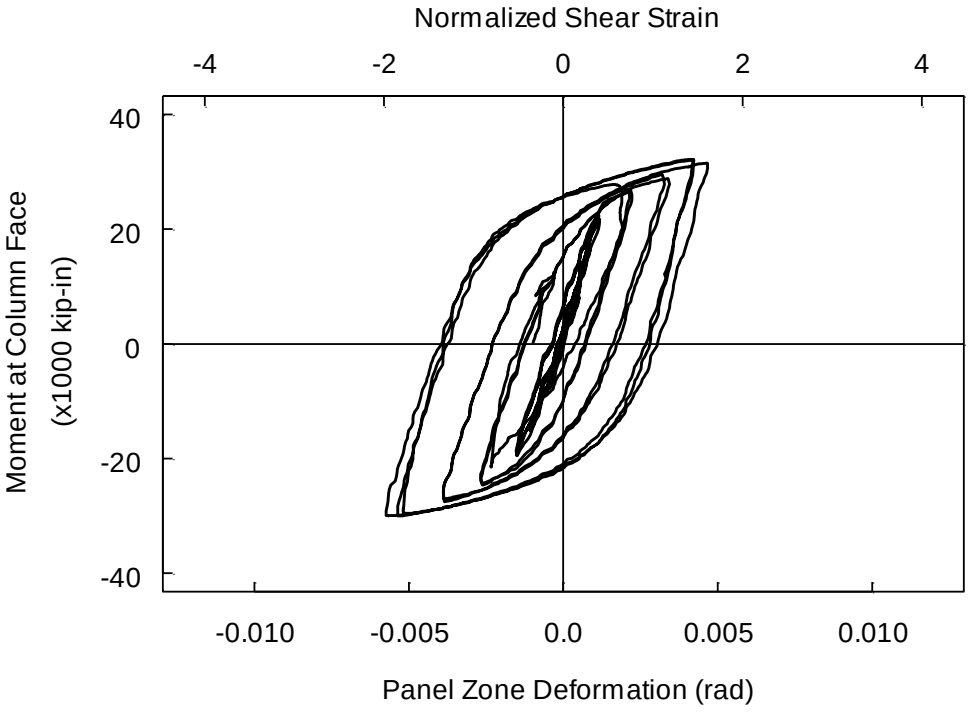

Figure 5.37 Specimen S1 Moment versus Average Panel Zone Shear Strain Relationship

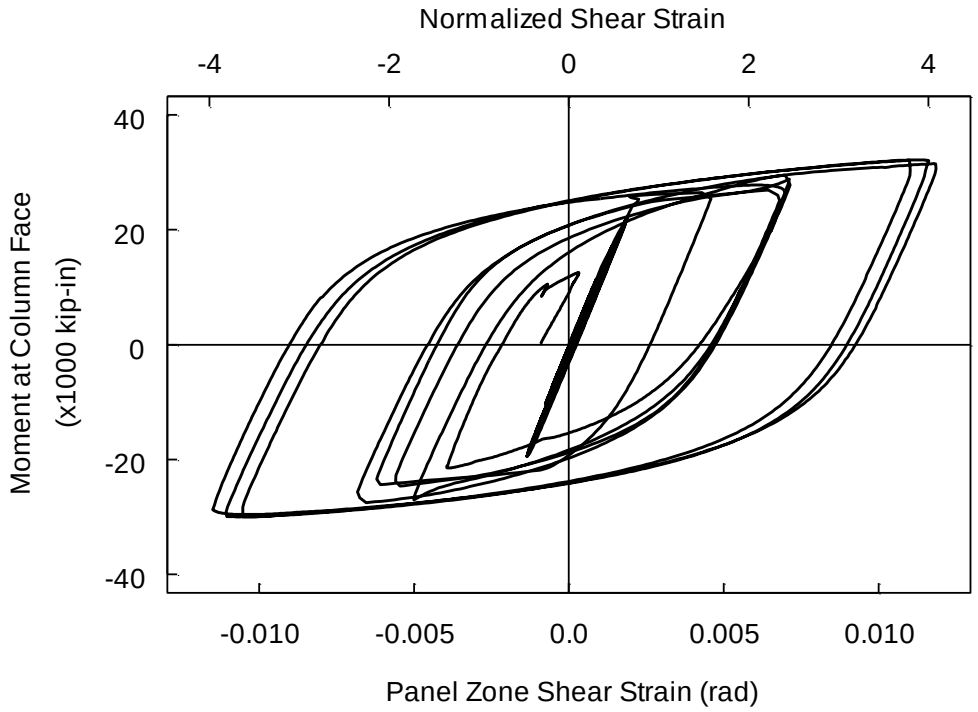

Figure 5.38 Specimen S1 Moment versus Local Shear

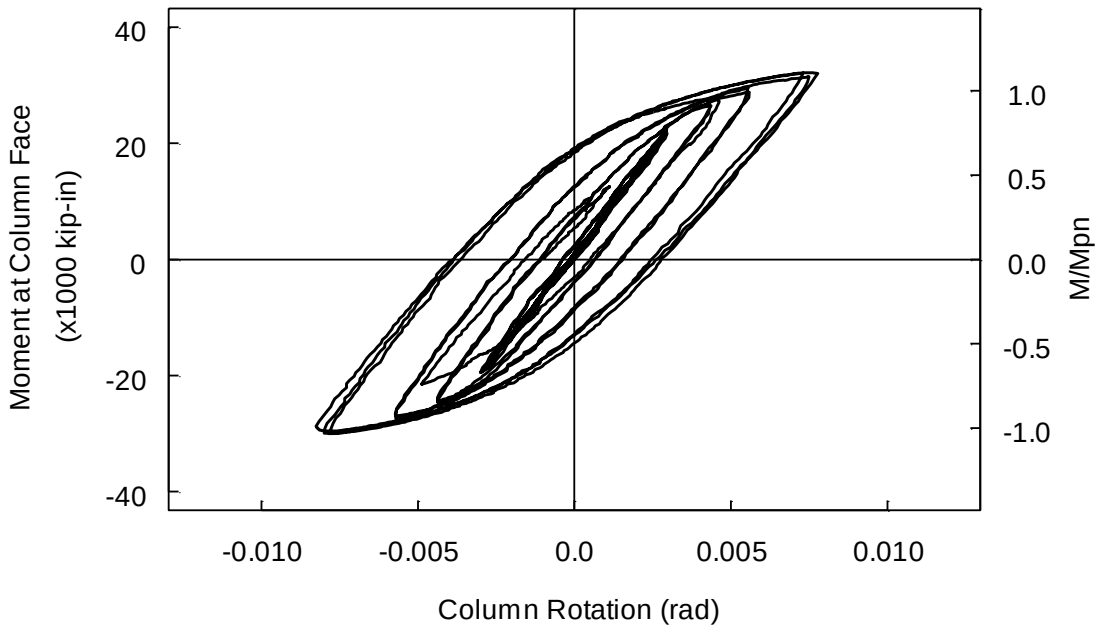

Figure 5.39 Specimen S1 Moment versus Total Column Rotation Relationship

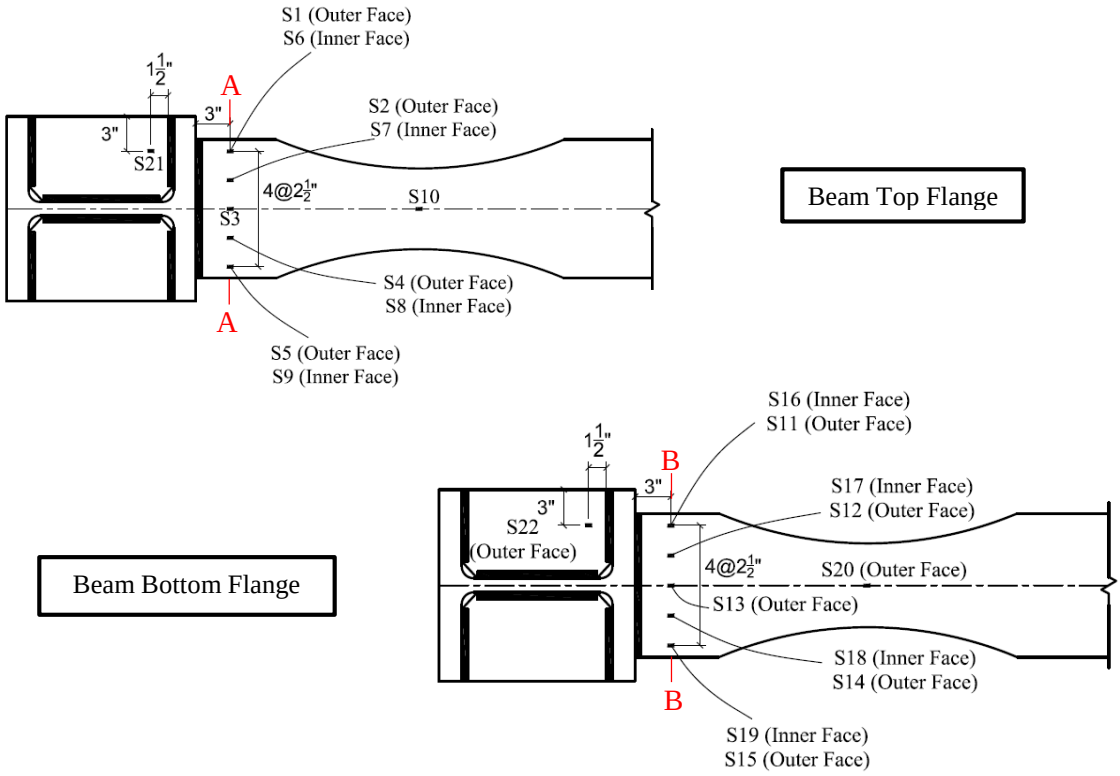

(a) Sections A-A and B-B, on Top and Bottom Flanges

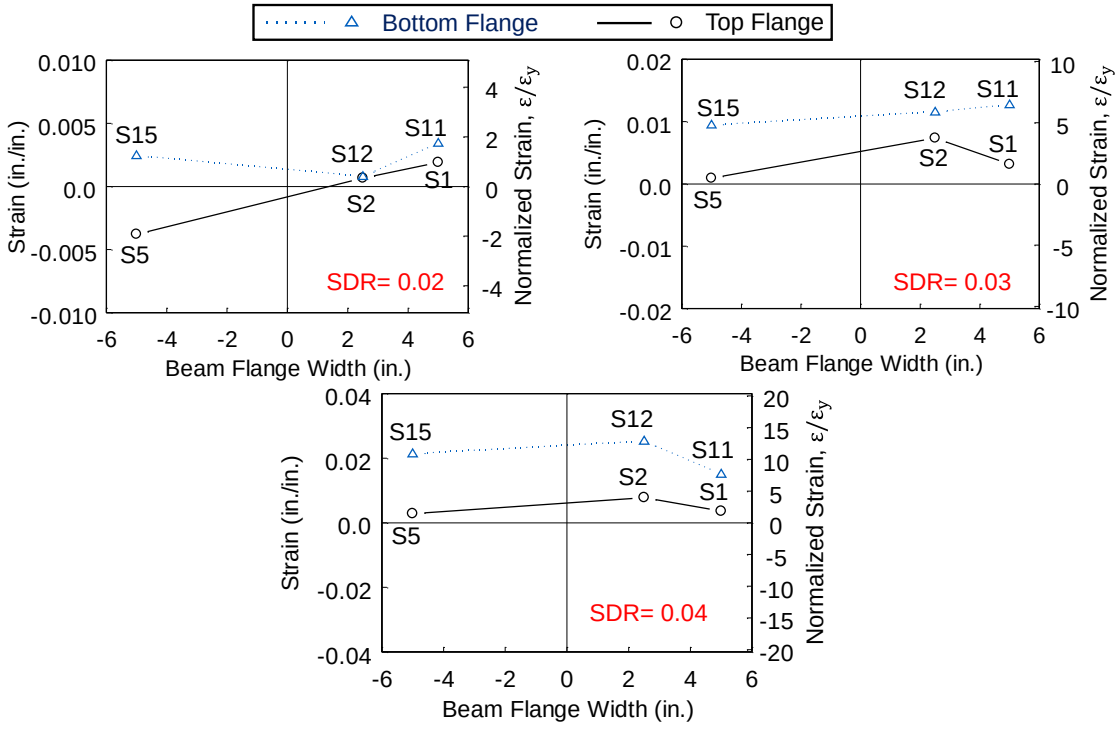

(b) Strain Profiles at 0.02, 0.03 and 0.04 rad Drifts

Figure 5.40 Specimen S1 Beam Flange Flexural Strain Profiles

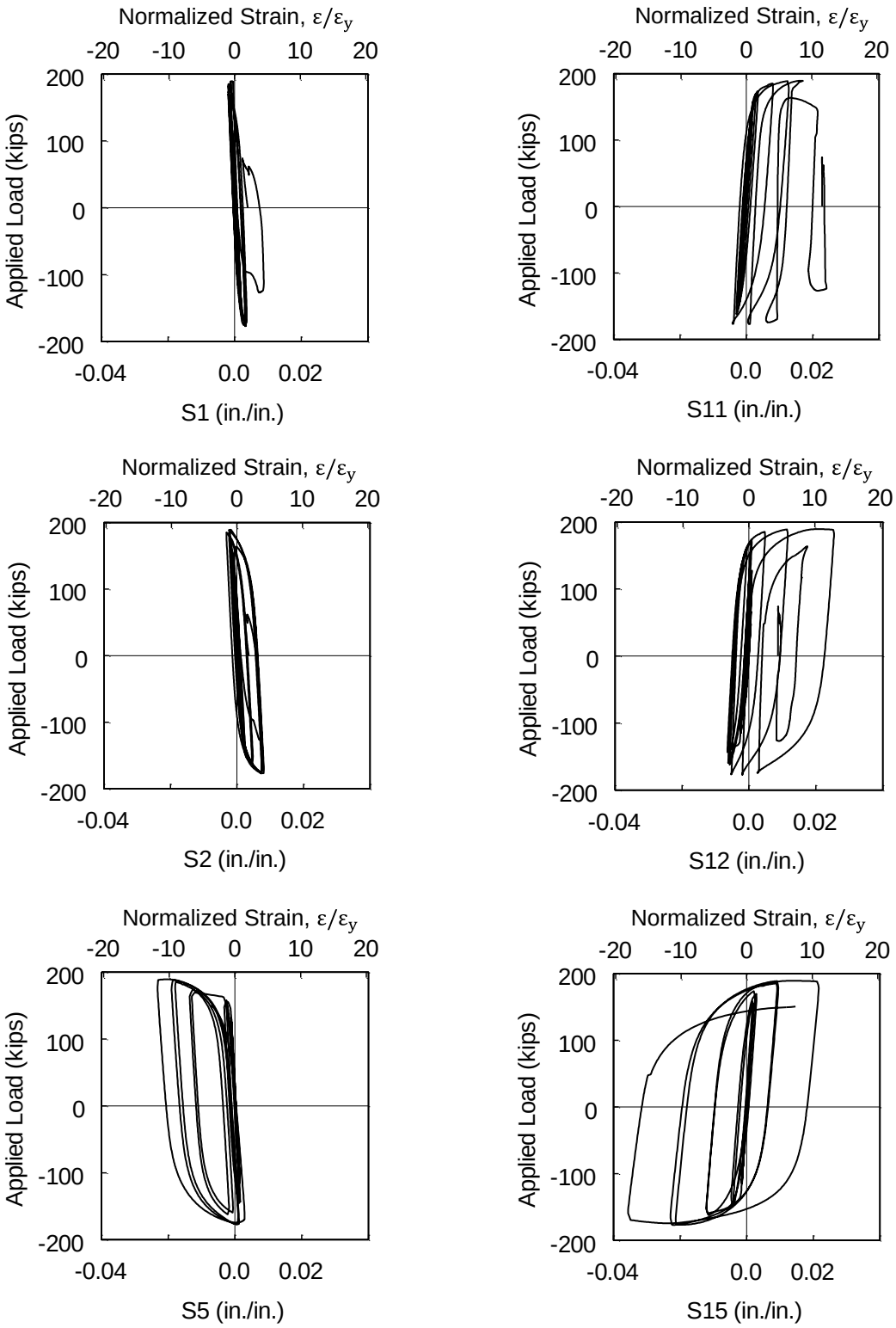

(a) Beam Top Flange Strains (b) Beam Bottom Flange Strains

Figure 5.41 Specimen S1 Applied Load versus Beam Flange Flexural Strains

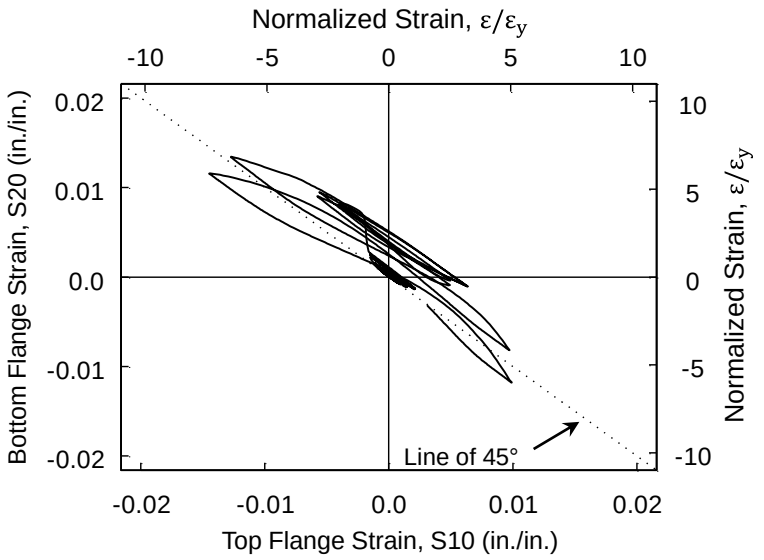

Figure 5.42 Specimen S1 Beam Top versus Bottom Flange Flexural Strains at RBS Location (up to 0.03 rad Drift)

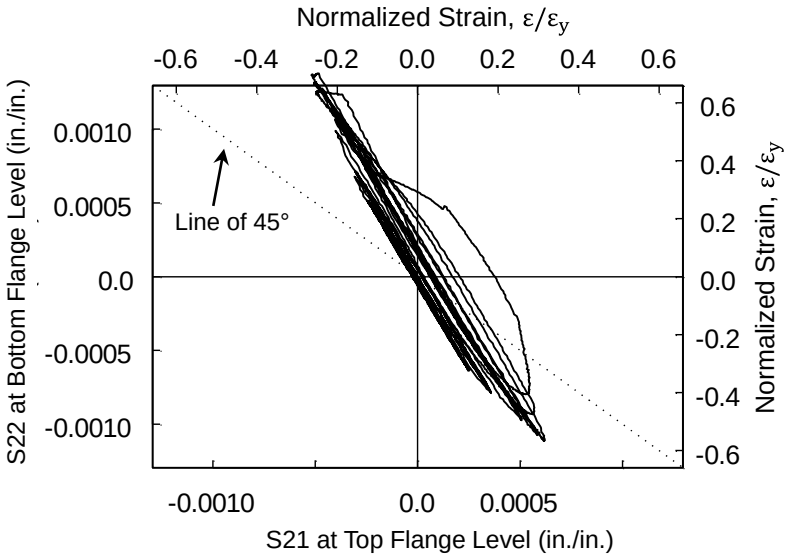

Figure 5.43 Specimen S1 Top versus Bottom Continuity Plate Strains (up to 0.04 rad Drift)

Figure 5.44 Specimen S2 Connection Prior to Testing

(a) View from South-West (b) Detail A

Figure 5.45 Specimen S2 Minor Beam Flange Yielding at End of 0.0075 rad Drift

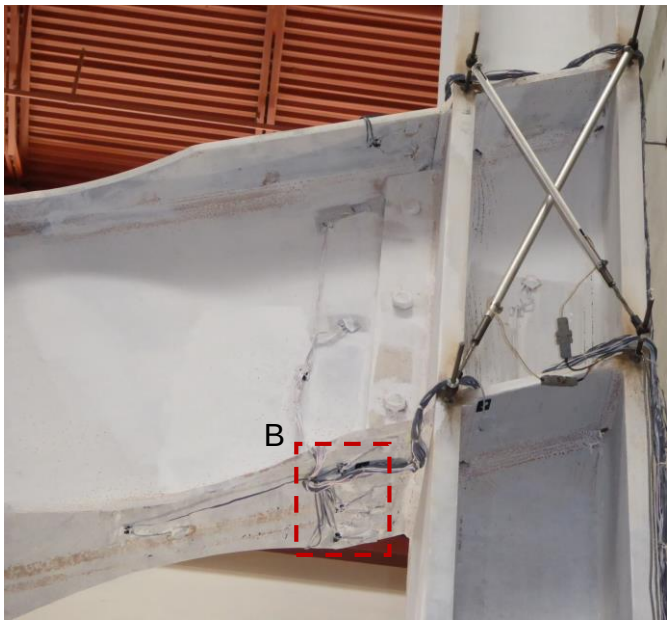

(a) View from East

(b) Panel Zone

(c) Detail A

(d) Detail B

Figure 5.46 Specimen S2 Yielding at +0.01 rad Drift (4th Cycle)

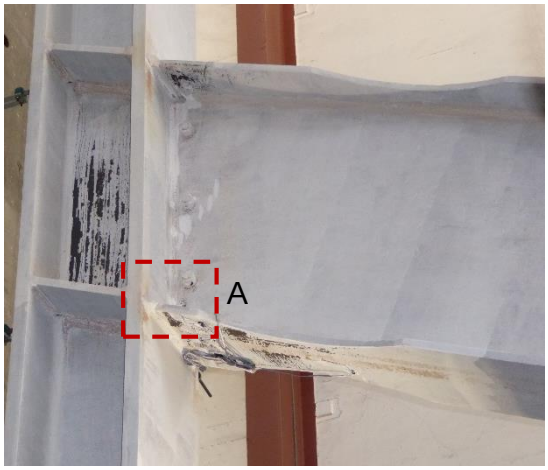

(a) Heel Location

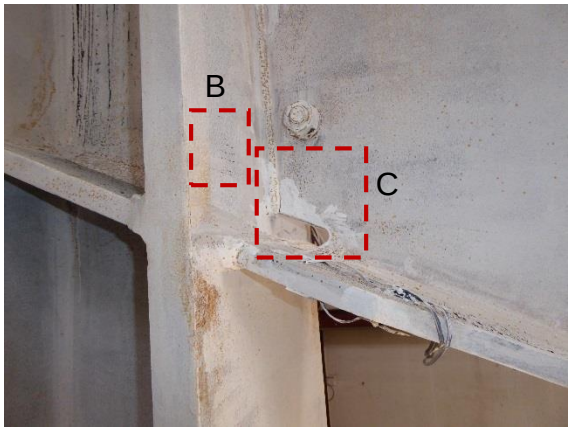

(b) Detail A

(c) Detail B, Back Column Flange

(d) Detail C, Front Column Flange

Figure 5.47 Specimen S2 Connection at +0.02 rad Drift (2nd Cycle)

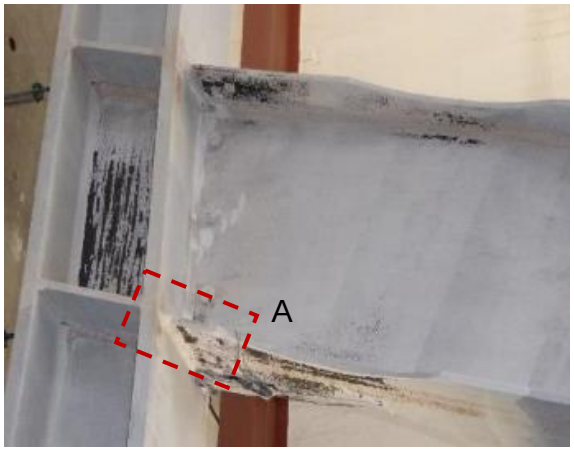

(a) View from West

(b) Detail A

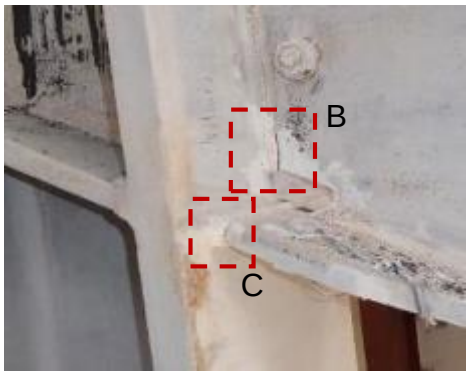

(c) Detail A

(d) Detail B

(e) Detail C

Figure 5.48 Specimen S2 at +0.03 rad Drift (2nd Cycle)

(a) View from West

(b) Detail A, View from West

(c) Detail A, View from Bottom

Figure 5.49 Specimen S2 at -0.03 rad Drift (2nd Cycle)

(a) View from West

(b) Detail A (Fractures at Beam Web CJP Weld, Weld Access Hole and Beam Flange CJP Weld)

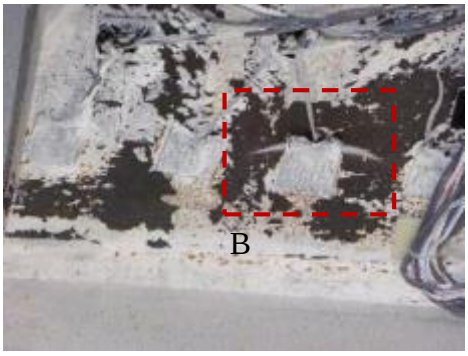

(c) Detail A, View from Bottom

(d) Detail B, Bottom Flange Fracture

Figure 5.50 Specimen S2 Connection at +0.04 rad Drift (1st Cycle)

(a) View from East

(b) View from South-East

Figure 5.51 Specimen S2 Flange and Web Local Buckling at +0.04 rad Drift (1st Cycle)

(a) View from West

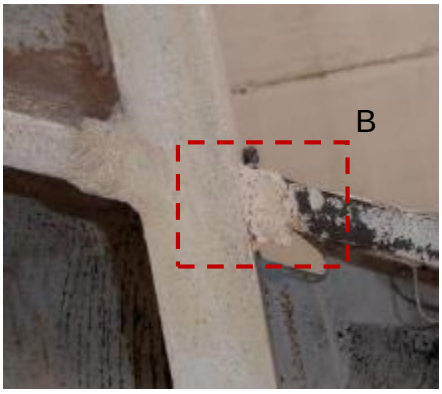

(b) Detail A

(c) Detail B, Minor Beam Top Flange CJP Weld Crack

Figure 5.52 Specimen S2 at -0.04 rad Drift (1st Cycle)

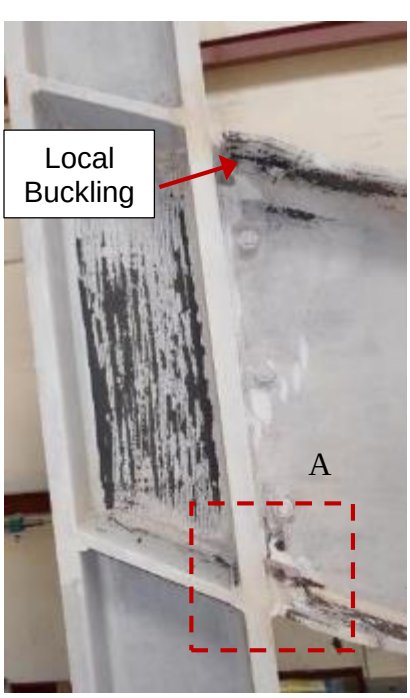

(a) View from West

(b) Detail A (Fractures at Beam Web CJP Weld, Weld Access Hole and Beam Flange CJP Weld)

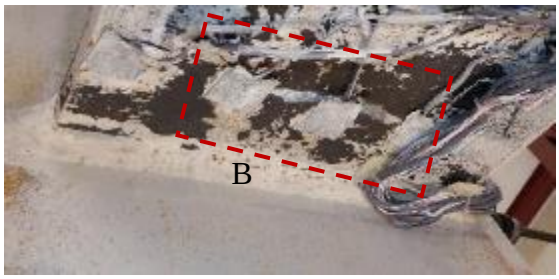

(c) Detail A, View from Bottom

(d) Detail B, Beam Bottom Flange Fracture

Figure 5.53 Specimen S2 at +0.04 rad Drift (2nd Cycle)

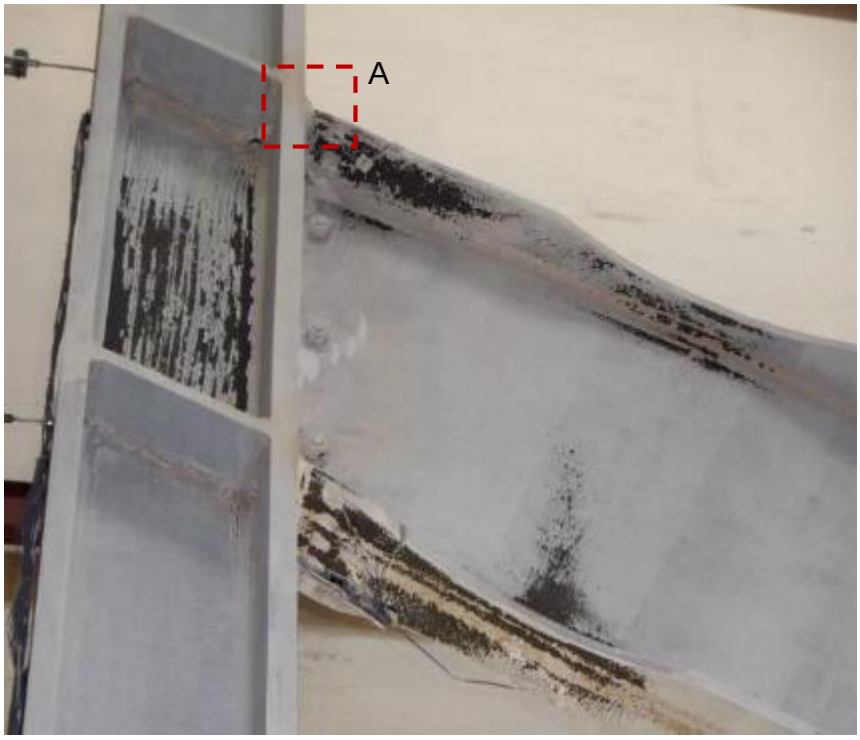

(a) View from South-West

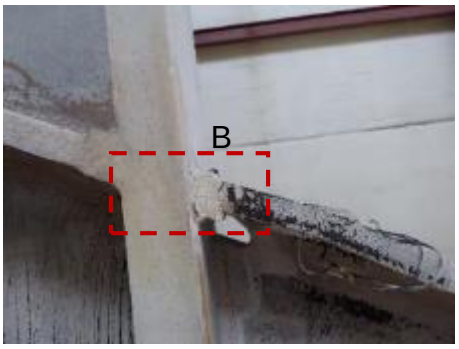

(b) Detail A, Top Flange CJP Weld

(c) Detail B, Minor Beam Top Flange CJP Weld Crack

Figure 5.54 Specimen S2 at -0.04 rad Drift (2nd Cycle)

(a) View from East

(b) View from West

Figure 5.55 Specimen S2 at +0.05 rad Drift (1st Cycle)

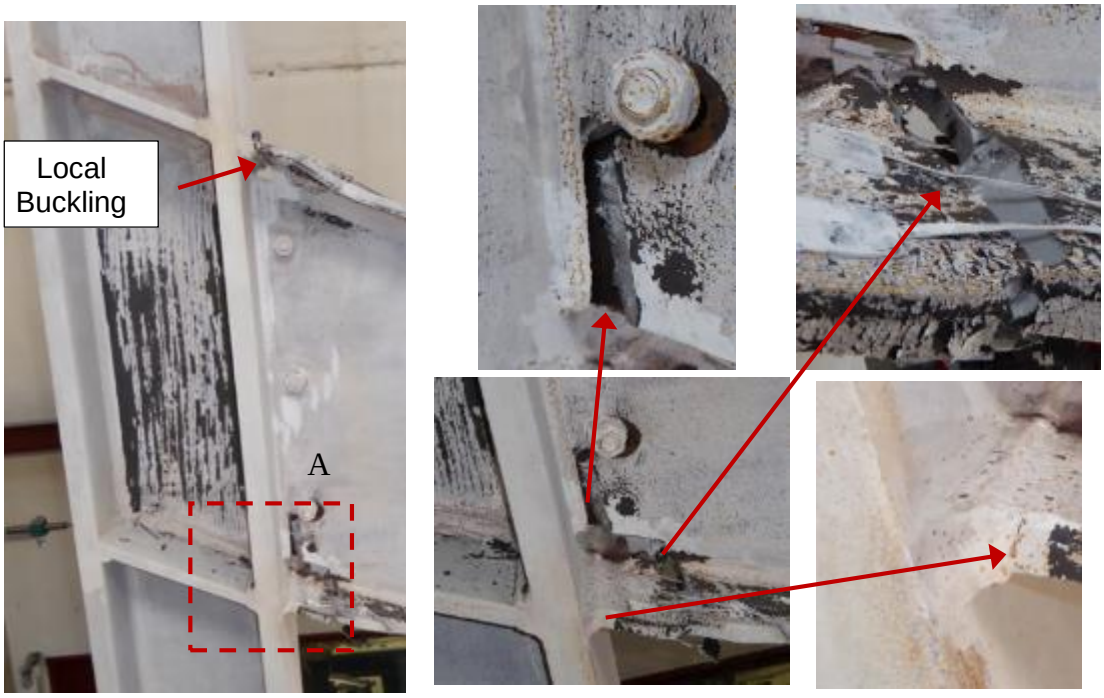

(a) View from West

(b) Detail A (Fractures at Beam Web CJP Weld, Weld Access Hole, and Beam Flange CJP Weld)

(c) Detail A, Complete Fracture of Beam Bottom Flange

Figure 5.56 Specimen S2 Connection at +0.05 rad Drift (1st Cycle)

(a) +0.03 rad Drift (2nd Cycle)

(b) +0.04 rad Drift (2nd Cycle)

Figure 5.57 Specimen S2 Beam Lateral-Torsional Buckling

(a) View from Back (b) View from South West

Figure 5.58 Specimen S2 Column Flange Yielding at Test Completion

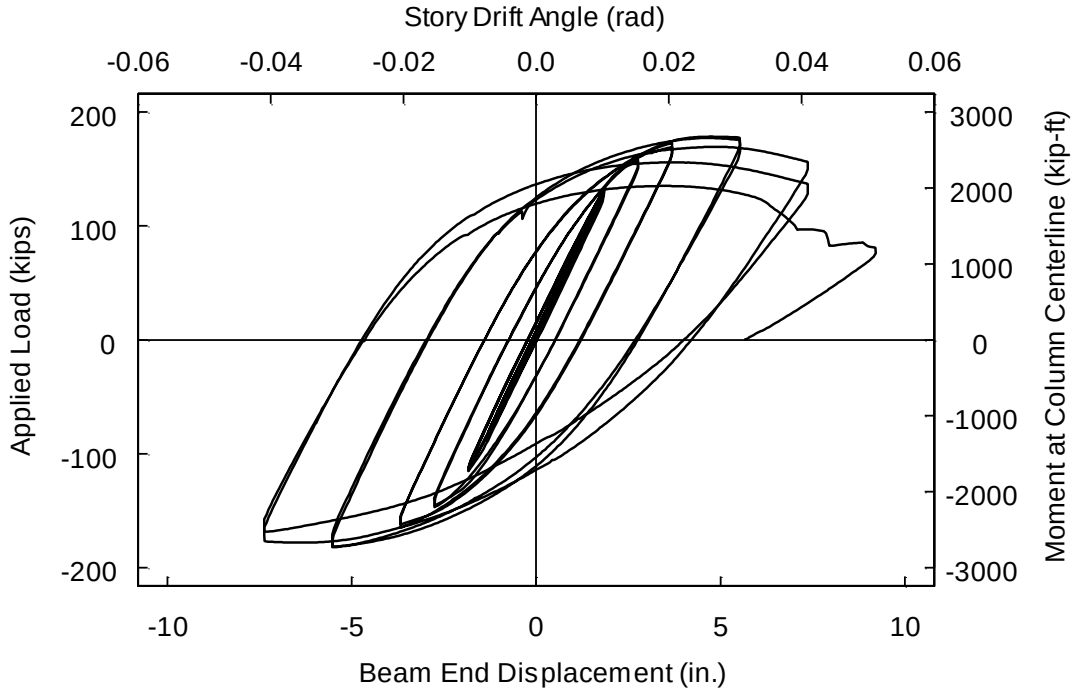

Figure 5.59 Specimen S2 Load versus Beam Tip Displacement Relationship

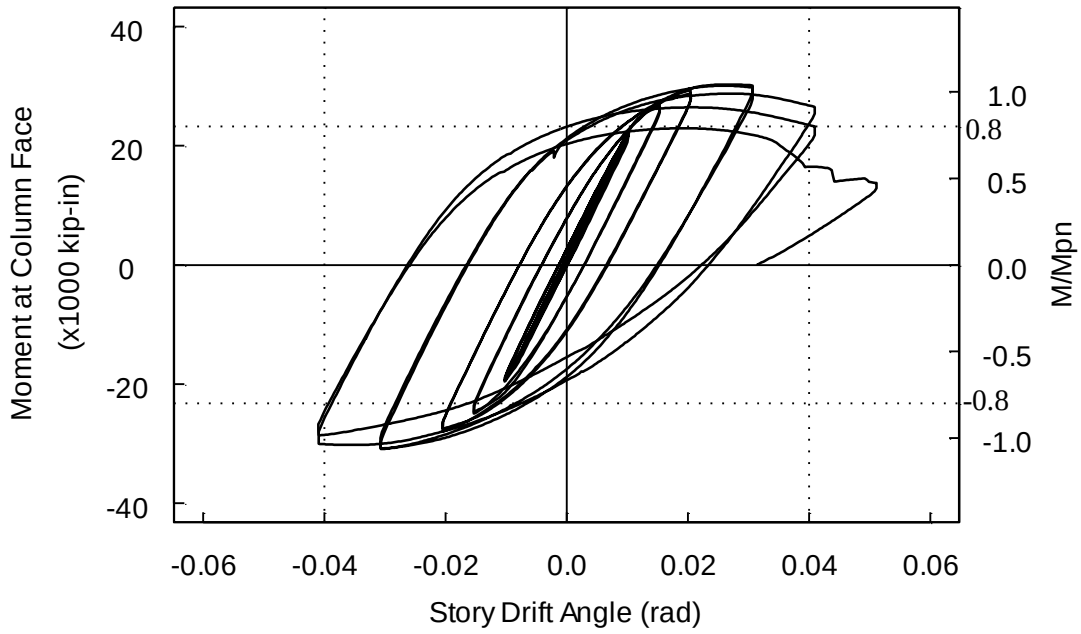

Figure 5.60 Specimen S2 Moment versus Story Drift Angle Relationship

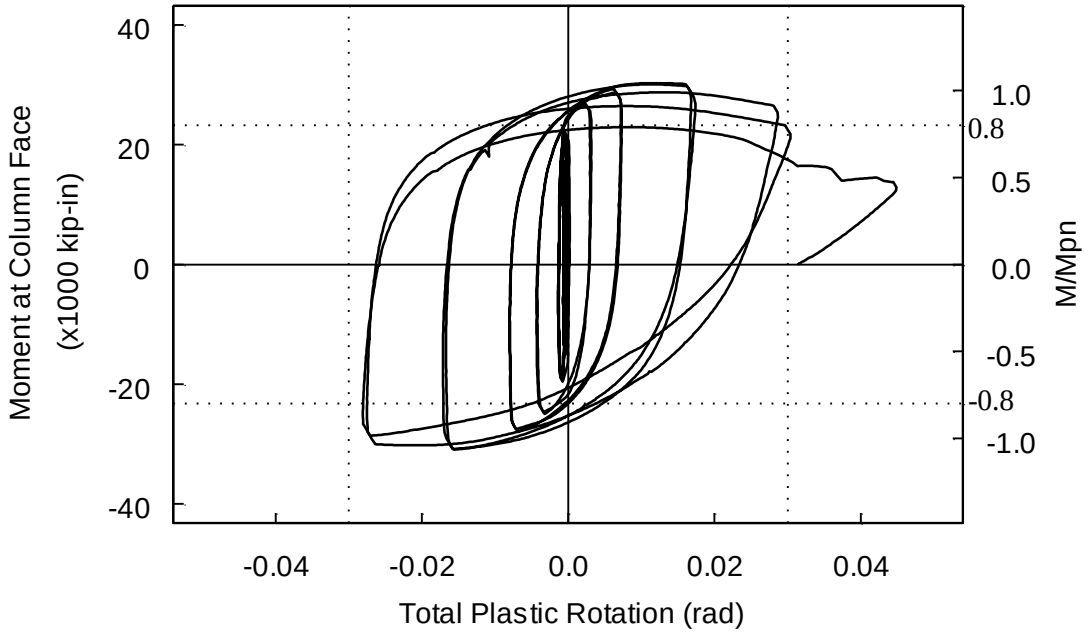

Figure 5.61 Specimen S2 Moment versus Total Inelastic Rotation Relationship

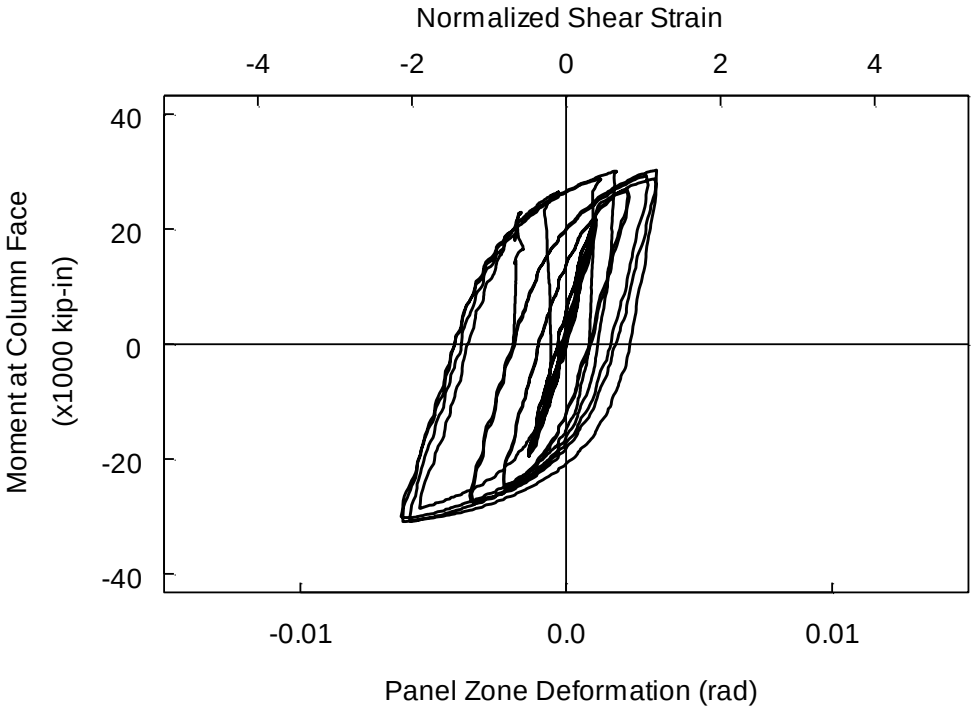

Figure 5.62 Specimen S2 Moment versus Average Panel Zone Shear Strain Relationship

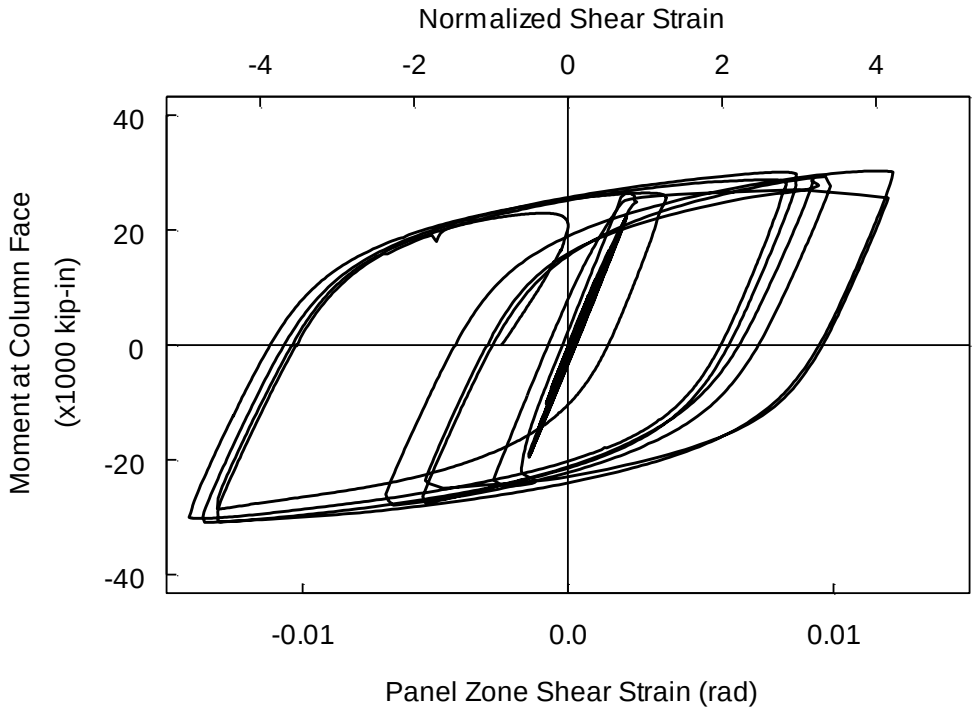

Figure 5.63 Specimen S2 Moment versus Local Shear Strain Relationship

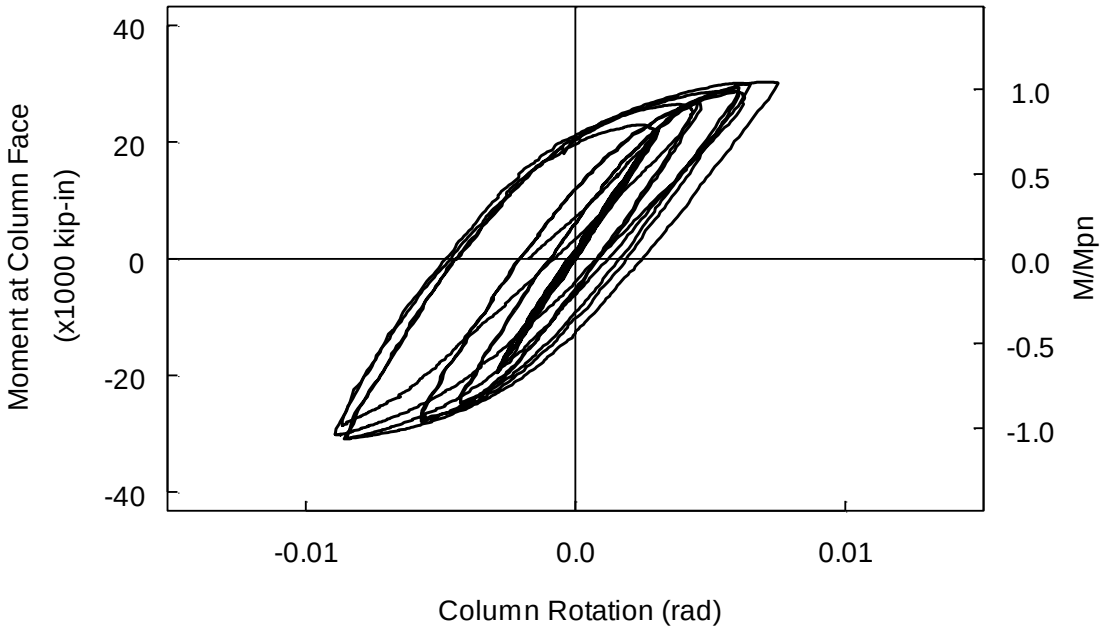

Figure 5.64 Specimen S2 Moment versus Total Column Rotation Relationship

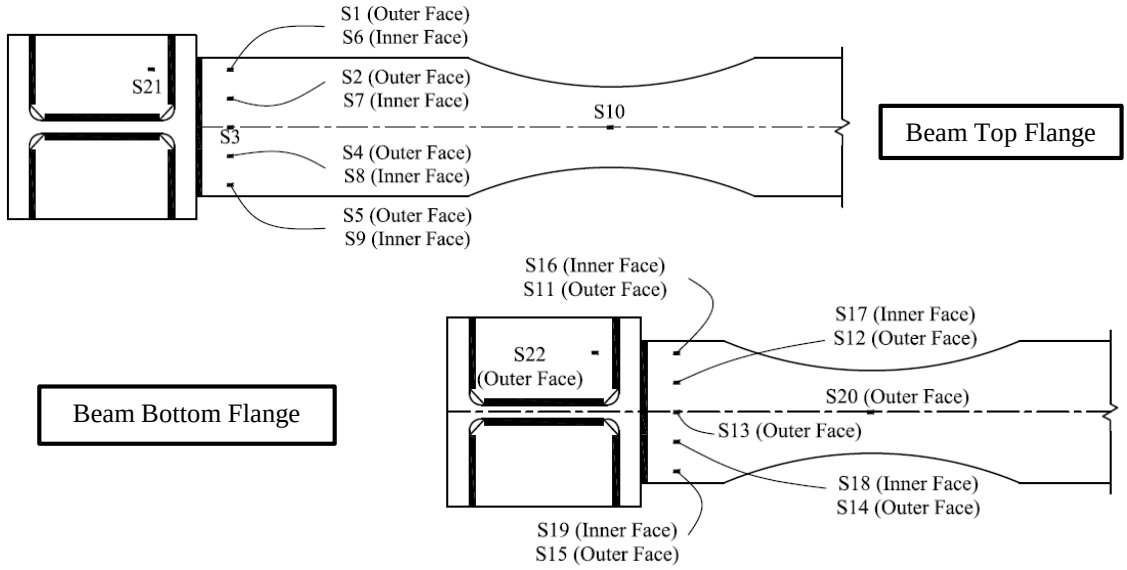

(a) Strain Gage Location

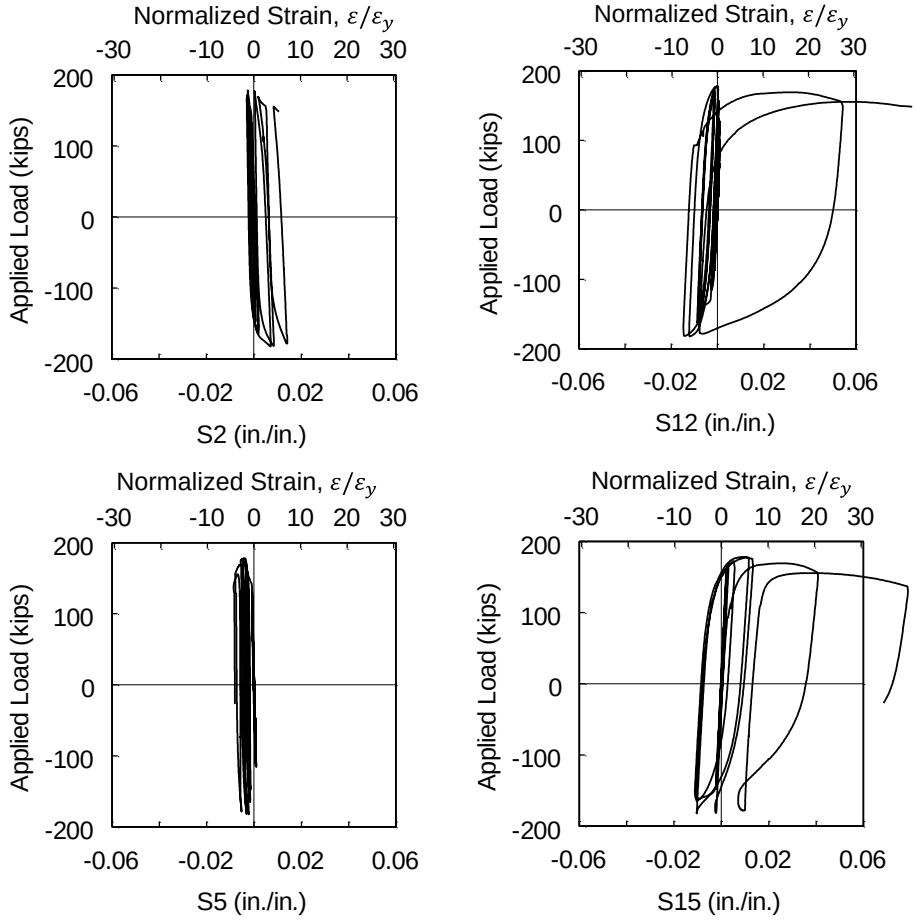

(b) Beam Top Flange Strains (c) Beam Bottom Flange Strains

Figure 5.65 Specimen S2 Applied Load versus Beam Flange Flexural Strains

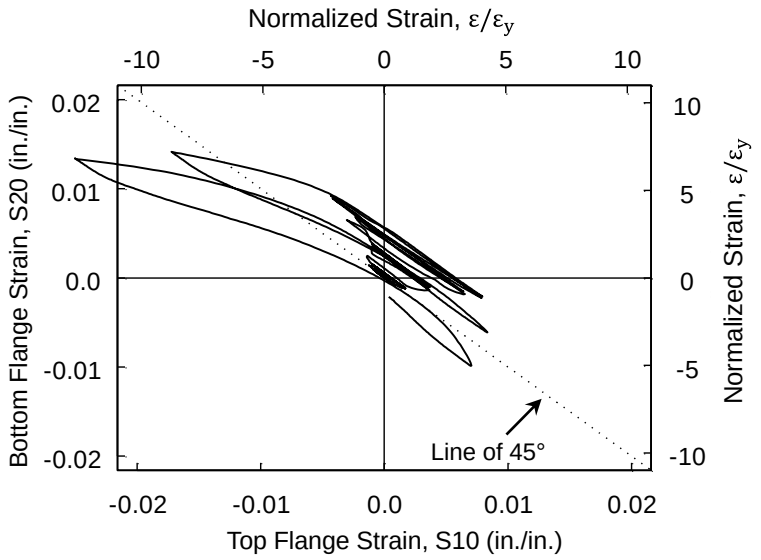

Figure 5.66 Specimen S2 Beam Top versus Bottom Flange Flexural Strains at RBS Location (up to 0.03 rad Drift)

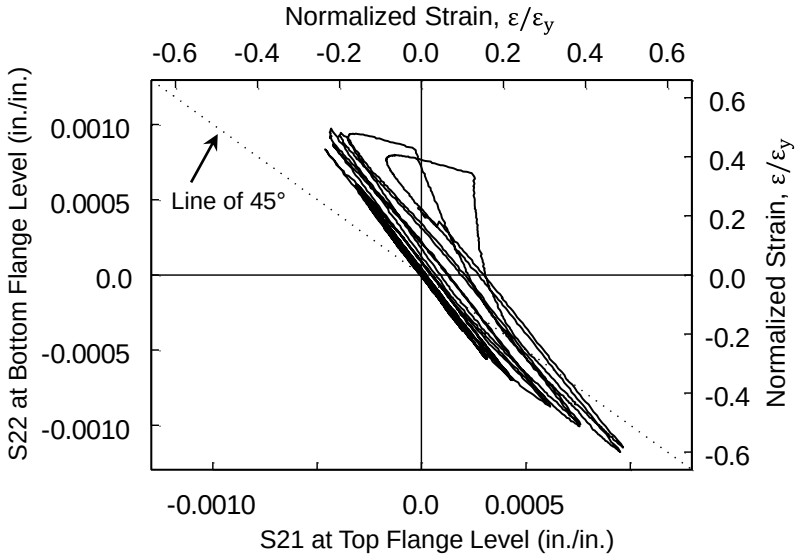

Figure 5.67 Specimen S2 Top versus Bottom Continuity Plate Strains (up to 0.03 rad Drift)

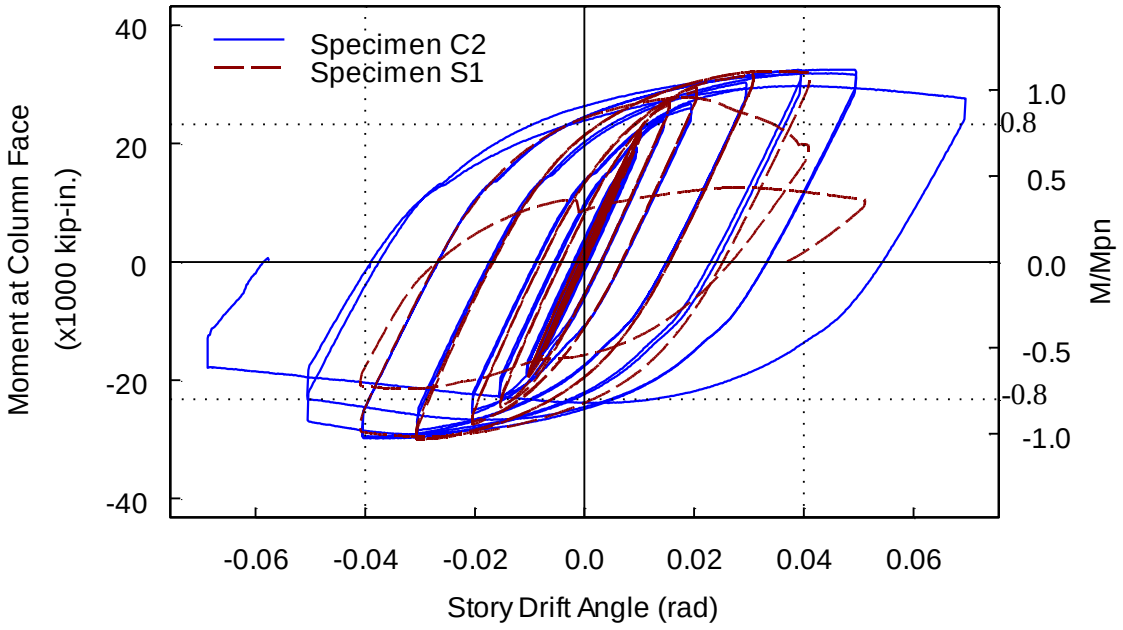

(a) Comparison of Specimen C2 and Specimen S1

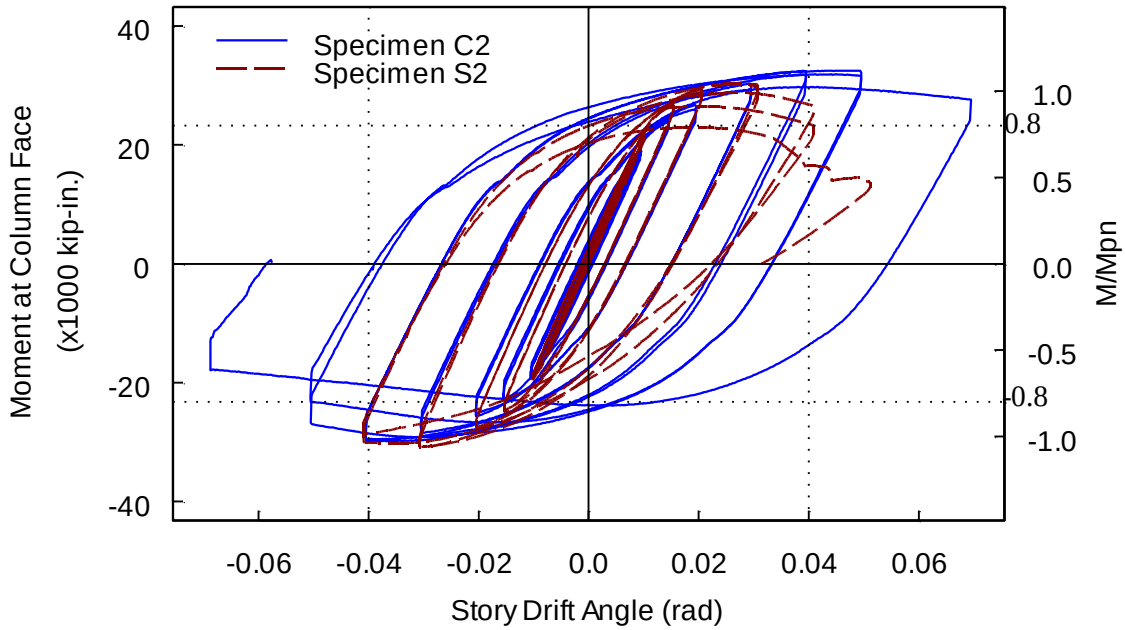

(b) Comparison of Specimen C2 and Specimen S2

Figure 5.68 Global Response Comparison of Specimen C2 with Specimens S1 and S2

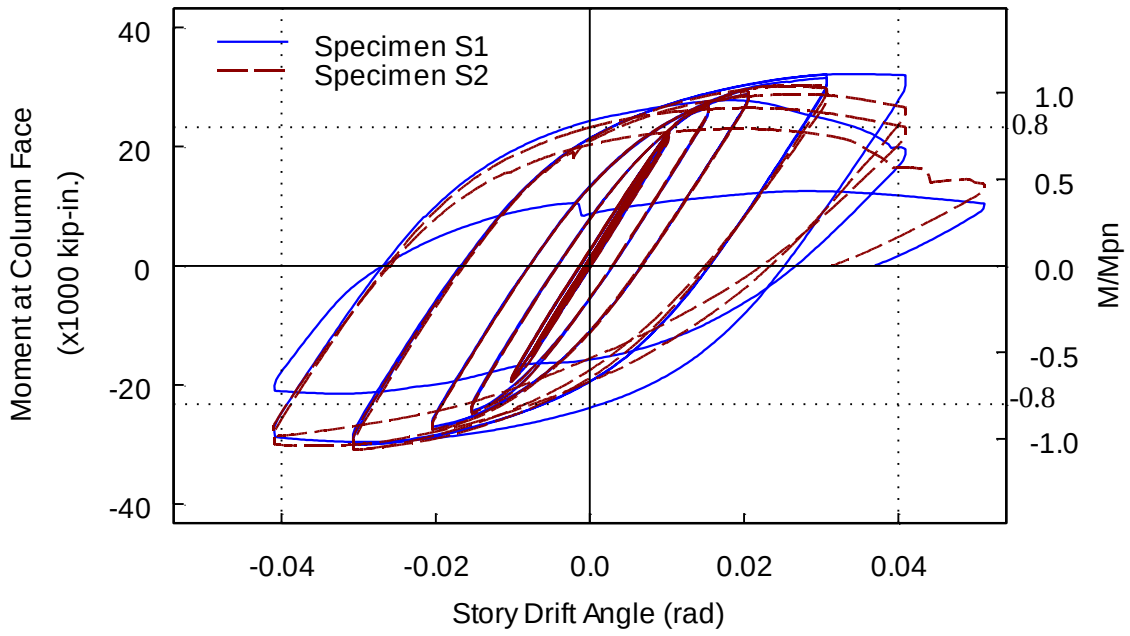

Figure 5.69 Global Response Comparison of Specimen S1 and Specimen S2

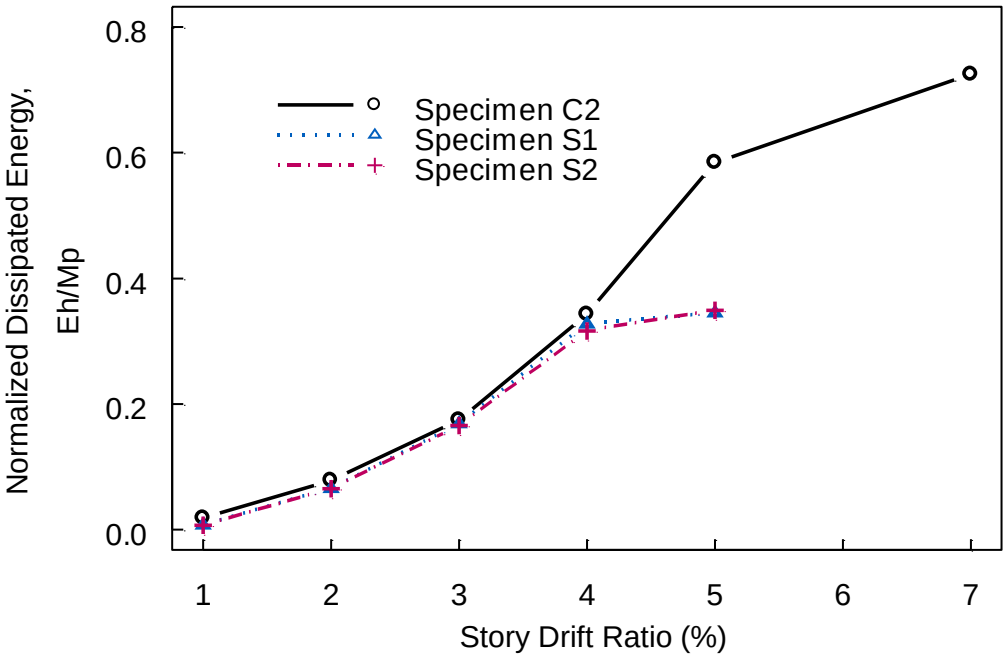

Figure 5.70 Comparison of Normalized Dissipated Energy

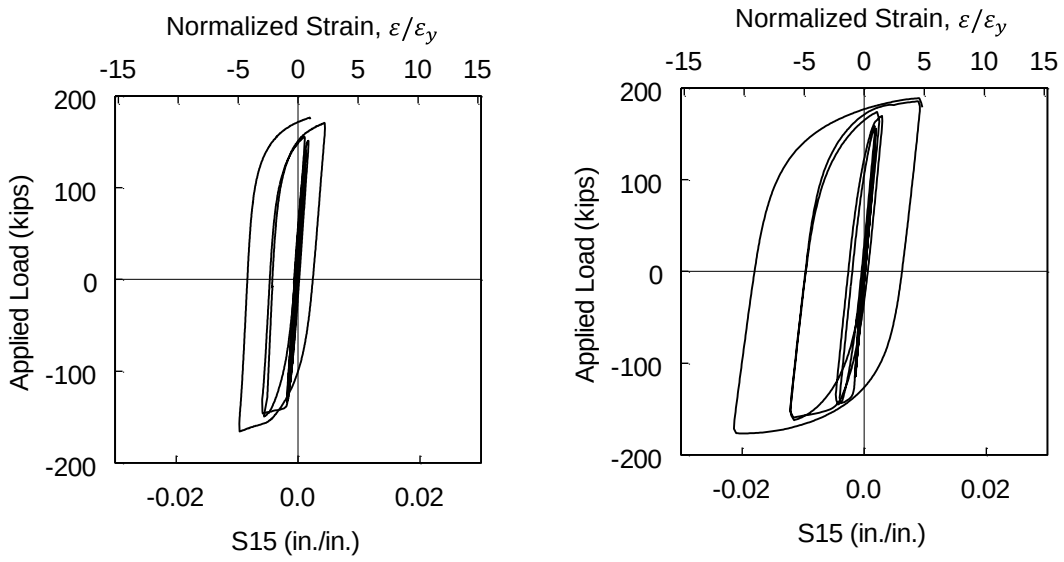

(a) Orthogonal Connection (C2) (b) Sloped Connection (S1)

Figure 5.71 Comparison of Beam Bottom Flange Flexural Strains near Column Face (up to 0.03 rad Drift Cycles)

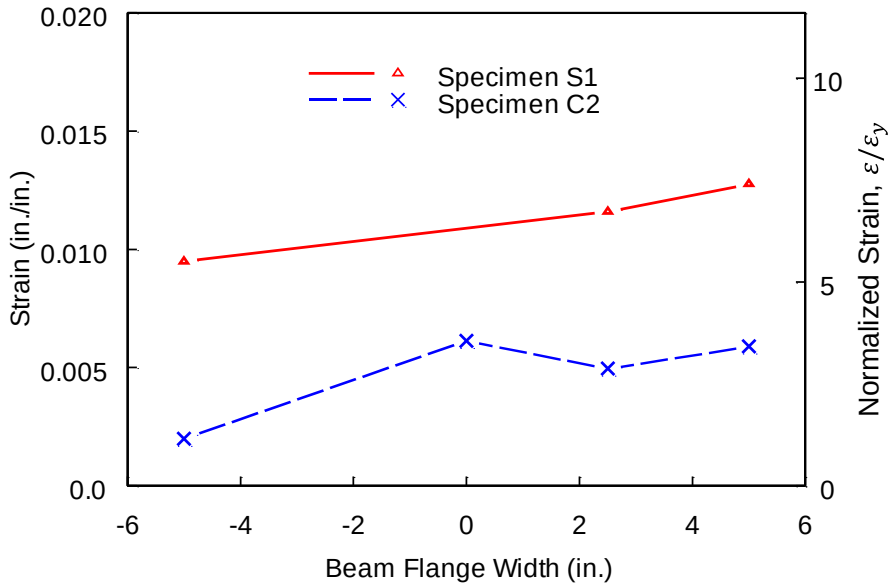

Figure 5.72 Comparison of Beam Bottom Flange Flexural Strain Profiles near Column Face (+0.03 rad Drift)

(a) Specimen C2 (0.05 rad Drift)

(b) Specimen S1 (0.04 rad Drift)

(c) Specimen S2 (0.04 rad Drift)

Figure 5.73 Comparison of Failure Mode

6 ANALYTICAL STUDY OF SLOPED CONNECTIONS

6.1 General

Test results from both this test program and that by Kim et al. (2016) clearly show that the strain demand at the heel location is higher and the welded joint here is vulnerable to brittle fracture in a sloped moment frame connection. Analytical investigations were conducted to evaluate the force demand at the heel location and the threshold beyond which angle measures should be taken to reduce the force demand at the heel location. Based on finite element simulation, a potential solution is also presented in this chapter.

6.2 Finite Element Simulation and Correlation Study

The commercial software ABAQUS/CAE (2014) was used for numerical simulation. Eight-node, linear brick elements (Type C3D8) were selected to model the connection specimens. Typical steel properties ($E = 29000$ ksi, $\nu = 0.3$) were used in the model to describe elastic material characteristics. Following the work of Chaboche (1986), material parameters that can capture both the kinematic and isotropic hardening responses under cyclic loading were incorporated (Ozkula 2017). The same equation solver and solution technique as described in Section 4.2 were chosen. Figure 6.1 shows a representative FEM model for the tested moment frame connection specimen.

To interpret the finite element analysis results, two indices were used to evaluate the strain demand and the vulnerability for brittle fracture:

(1) **PEEQ*:*** It is the equivalent plastic strain normalized by the yield strain (El-Tawil et al. 2000). The PEEQ is defined as:

$$PEEQ = \frac{\sqrt{\frac{2}{3}\varepsilon_{ij}^{p}\varepsilon_{ij}^{p}}}{\varepsilon_y} \tag{6.1}$$

where ε_{ij}^{p} are the plastic strain components in the directions *i* and *j*. This index represents the local plastic strain demand (Chen et al. 2006).

(2) **Rupture Index, *RI:*** This index is defined as follows (El-Tawil et al. 1998):

$$RI = \frac{\varepsilon_p/\varepsilon_y}{\exp\left(-1.5\frac{\sigma_m}{\sigma_{eff}}\right)} \tag{6.2}$$

where ε_p = equivalent plastic strain, σ_m = hydrostatic stress, and σ_{eff} = von-Mises stress. *RI* reflects the potential for ductile fracture.

The indices were monitored at three critical locations at the heel location (Figure 6.3); one at the beam web-to-column flange CJP weld (Location 1), one along the curved profile of the weld access hole (Location 2), and one at the beam flange-to-column flange CJP weld (Location 3).

To validate the accuracy of the finite element modelling technique, a correlation study of two tested specimens (Specimens S1 and S2) was carried out. Figure 6.2 shows a comparison of the experimental and predicted global responses for each test specimen. The correlation is satisfactory up to 0.04 rad drift. Since the finite element simulation could not capture fracture, finite element simulation over-predicted the actual response beyond this drift level. Since the main objective of the analytical study was to predict the maximum force demand at the heel location, which occurred prior to this drift level in the test specimens, finite element simulation still produced meaningful results for predicting the

force demand at the heel location and for developing a potential solution to minimize the sloping effect.

It is difficult to determine experimentally the force distribution at the beam-to-column interface. Therefore, the higher force demand at the heel location is demonstrated from finite element analysis results of Model 2 herein. Figure 6.16 show the contour of absolute maximum principal stress along the beam at 0.01 rad drift. The internal force distribution in the beam flanges and web at the column face is also presented in Figure 6.17; these reaction forces were obtained by integrating the normal and shear stresses in the beam. The higher force demand at the heel location is very obvious. Therefore, the source of fracture at the heel location observed in both Specimens S1 and S2 is very clear.

The computed PEEQ and RI values at three locations for Models S1 and S2 are presented in Figure 6.4; for comparison purposes, each index at each location has been normalized with respect to the value of Model S2. It is observed that there is a slight improvement to use the RBS configuration that is perpendicular to the beam span (Model S2). However, using this configuration alone is still not sufficient because Specimen S2 still experienced fractures. The next section documents an effort to develop a potential scheme that would reduce the force demand at the heel location.

6.3 Truss Analogy for Sloped Connections

6.3.1 Truss Analogy Model

Goel et al. (1997) showed that for an orthogonal steel Special Moment Frame connection, the stress flow close to the column flange, about a distance d_b (beam depth) away from the column face, does not follow the classical Euler-Bernoulli beam theory as the stress flows mainly toward the beam flanges. Consequently, the force demand on the

beam web close to the column flange is less. They introduced a truss analogy model (Figure 6.5) to predict the beam top and bottom flange forces. It was assumed that the beam web at the column face does not participate in resisting any forces coming from the beam toward the column.

The parametric solution to this determinate truss is shown in Figure 6.6, where V is the beam shear; C and T are the compression and tension forces in the beam flanges. Following the same approach, Figure 6.7 shows the same truss model applied to a sloped connection. Several dimensions in the figure follow:

$$p = \frac{d_c}{2\cos(\theta)} \tag{6.3}$$

$$q = \frac{d_b}{2}\tan(\theta) \tag{6.4}$$

$$r = d_b \tag{6.5}$$

$$L_d = L - p - q - r \tag{6.6}$$

Figure 6.8 shows corresponding truss model for the sloped moment frame connection. The member forces and reactions of this truss follows:

$$F_1 = 0.5\zeta V \tag{6.7}$$

$$R_h^A = T + F_1 + 0.5V = T + 0.5(1+\zeta)V \tag{6.8}$$

$$R_h^D = C + F_1 + 0.5V = C + 0.5(1+\zeta)V \tag{6.9}$$

$$R_v^A = R_h^D = \frac{V}{2} \tag{6.10}$$

where F_1 is the horizontal component of member BD force and ζ is defined as follows:

$$\zeta = \frac{d_b\tan(\theta) + d_b}{d_b} = 1 + \tan(\theta)$$

It is clear that the determinate truss model proposed by Goel et al. (1997) will lead to same normal and shear forces at the heel and toe locations (i.e., nodes B and D) if the tension and compression forces (T, C) at nodes B and C are the same. This conclusion is not true in a sloped connection, which is further evidenced by comparing the predicted values with those predicted from finite element analysis in Figure 6.9. An alternate truss analogy model is needed.

6.3.2 Proposed Truss Analogy Model

Since the determine truss model cannot reflect the effect of the angle of inclination, the truss was modified such that node F will move in the direction of the depth this is perpendicular to the beam span (Figure 6.10 and Figure 6.11); the height along the height direction (y in Figure 6.11) is a function of the angle of inclination. In addition, a node G which is located at midway between nodes A and E is added to the model. The following angles and member lengths can be determined from geometry (Figure 6.11):

$$y = d_b\left(0.5 - \frac{\theta}{75}\right) \tag{6.11}$$

$$\alpha = \tan^{-1}\left(\frac{2y}{d_b}\right) \tag{6.12}$$

$$\beta = -\tan^{-1}\frac{\frac{d_b}{2} - y}{\frac{d_b}{2}(1 + \tan(\theta))} \tag{6.13}$$

$$\gamma = -\tan^{-1}\frac{d_b - y}{\frac{d_b}{2}(1 + 2\tan(\theta))} \tag{6.14}$$

$$L_{AF} = \sqrt{\left(\frac{d_b}{2}\right)^2 + y^2} = \text{length of member AF} \tag{6.15a}$$

$$L_{GF} = \sqrt{\left(\frac{d_b}{2}\right)^2 + \mathcal{y}^2} = \text{length of member GF} \tag{9.15b}$$

$$L_{EF} = \sqrt{\left(\frac{d_b}{2}(1 + 2\tan(\theta))\right)^2 + (d_b - \mathcal{y})^2} = \text{length of member EF} \tag{9.15c}$$

This truss is indeterminate to the first degree and, therefore, the matrix stiffness method was used to determine the member forces as follows:

(1) Determine member forces in BF and DF from joint equilibriums at nodes B and D:

$$F_h^{BF} = \frac{V d_b}{4\mathcal{y}} \tag{6.16}$$

$$F_h^{DF} = \frac{V d_b}{4(d_b - \mathcal{y})} \tag{6.17}$$

(2) The matrix stiffness method yields the following:

$$K_{AF} = \frac{1}{L_{AF}}\begin{bmatrix} \cos(\alpha)^2 & \cos(\alpha)\sin(\alpha) \\ \cos(\alpha)\sin(\alpha) & \sin(\alpha)^2 \end{bmatrix} \tag{6.18}$$

$$K_{GF} = \frac{1}{L_{GF}}\begin{bmatrix} \cos(\beta)^2 & \cos(\beta)\sin(\beta) \\ \cos(\beta)\sin(\beta) & \sin(\beta)^2 \end{bmatrix} \tag{6.19}$$

$$K_{EF} = \frac{1}{L_{EF}}\begin{bmatrix} \cos(\gamma)^2 & \cos(\gamma)\sin(\gamma) \\ \cos(\gamma)\sin(\gamma) & \sin(\gamma)^2 \end{bmatrix} \tag{6.20}$$

$$K_{tot} = \sum(K_{AF} + K_{GF} + K_{EF}) \tag{6.21}$$

$$F_F = \begin{bmatrix} -F_h^{BF} + F_h^{DF} \\ V \end{bmatrix} \tag{6.22}$$

$$\Delta_F = K_{tot}^{-1} F_F \tag{6.23}$$

$$F_{AF} = K_{AF}\Delta_F \tag{6.24}$$

$$F_{EF} = K_{EF}\Delta_F \tag{6.25}$$

$$R_h^A = F_{AF}(1,1) + T + F_h^{FB} \tag{6.26}$$

$$R_h^E = -F_{EF}(1,1) + C + F_h^{DF} \quad (6.27)$$

$$R_v^A = F_{AF}(2,1) \quad (6.28)$$

$$R_v^E = F_{EF}(2,1) \quad (6.29)$$

where K_{AF}, K_{GF}, K_{EF} are the member stiffness matrices of members AF, GF, and EF, K_{tot} is the structural stiffness matrix, F_F is the resultant force vector at node F, and Δ_F is the displacement vector of node F.

Note that the proposed truss model converges to that proposed by Goel et al. (1997) when the connection is orthogonal. Also, since the location of node F will be located outside the beam, this truss model is meaningful only up to an angle of inclination equal to about 35°.

To validate this truss model, a comparison of the reactions predicted from both the finite element analysis and the proposed model for Model S2 at 0.01 rad drift is presented in Figure 6.12. As can be seen in the figure, Normal Forces are well predicted and more important is that the significant difference between Normal Forces at the heel and toe locations are well reflected. Shear Forces are not predicted well. Figure 6.13 shows the truss model prediction against the FEM prediction at 0.04 rad drift. (The beam top and bottom flange forces on the right-hand side of the freebody were not equal because beam had experienced buckling at this drift level.) However, it can be seen that the truss model prediction is still reasonable.

The comparison made above was for an angle of inclination fixed at 25°. To further verify the accuracy of the proposed truss model, different angles of inclination (20°, 15°, 10°, 5° and 0°) were also considered. Figure 6.14 shows that the predictions are again reasonable for normal forces.

Finally, two additional beams (W30×116 and W10×49) were analyzed to evaluate the beam depth effect on the accuracy of the proposed truss model (Figure 6.15). Similar to that observed for the W36×150 beam, the prediction from the truss model is still satisfactory.

6.4 A Proposed Scheme for Sloped Connections

It was thought that introducing a discontinuity in the beam web might relax the strain demand at the heel location. Therefore, the idea of creating a slot the beam web was studied. In the following, three different scenarios will be discussed which leads to the proposed slot. While attempting to reduce the force demand at the critical locations, an attention was also paid to the overall flexural strength of the slotted beam.

6.4.1 Scheme 1–Straight Web Slot in an RBS Connection

A straight slot with a round hole at each end in the beam web (Figure 6.18) was first investigated; it is called an SCRBS connection herein. Note that the end of the slot is located at a distance $d_b/6$ away from the *k*-area. Also, dimensions *a* and *b* are the same as those recommended for an RBS connection (AISC 341):

$$0.5b_{bf} \leq a \leq 0.75b_{bf} \tag{6.30}$$

$$0.65d \leq b \leq 0.85d \tag{6.31}$$

where b_{bf} is the beam flange width, and d is the beam depth.

By introducing the slot in Model S2, the effectiveness of Scheme 1 was evaluated by comparing the PEEQ and RI values at three critical locations of Model 2 with and without the slot. Figure 6.19 shows that introducing the straight slot has a significant improvement in reducing these indices. However, the global response comparison in Figure

6.20 shows that introducing the slot would result in a 10% and 5% reductions in the flexural strength in the negative and positive excursions, respectively. It is prudent not to reduce further the flexural strength of an RBS connection.

6.4.2 Scheme 2–Straight Web Slot in a Non-RBS Beam

The second scheme involves the use of the same slot, but the RBS is not used so that the flexural strength is not reduced too much. The connection is called SCFS in this study. Figure 6.21 shows that the global response is not symmetric in the positive and negative excursions, and the flexural strength is no lower than that of Model 2. A comparison of the PEEQ and RI values at three locations in Figure 6.22 also shows the benefit of this scheme. However, these values are higher at a new location, i.e., Location 4 in Figure 6.23. (Note that the PEEQ and RI values at Location 4 are relative to those of Model S2 at Location 2 as they both correspond to base metal, not weld metal.)

6.4.3 Scheme 3–Curved Web Slot in a Non-RBS Beam

To reduce the values of PEEQ and RI at Location 4, a curved one is introduced in this scheme, which is called an SRBWS connection herein. Figure 6.24 shows the geometry of the proposed curved slot. When compared to that of Model 2, the global response comparison in Figure 6.25 shows the scheme does not produce a flexural strength that tis inferior to that of Model S2. As can be seen in Figure 6.26, the relative indices at all four locations are improved. Since this scheme shows promising results, additional parametric study was conducted and the results are presented in the next section.

6.5 Parametric Study of Proposed Beam Web Slot Scheme

6.5.1 Angle of Slope Effect

In order to see whether the proposed beam web slot scheme is effective for different angles of slope, four extra nonlinear finite element analyses were conducted for angles of slope equal to 20, 15, 10, and 5 degrees. For each angle of slope, the same beam and column size as Model S2 (a W36×150 beam to a W14×257 column) were modeled. One model is Model S2-equivalent; the connection is a RBS connection which is oriented perpendicular to the beam span. Figure 6.28 to Figure 6.31 show the relative indices at four locations for each angle of slope between Model 2 versus proposed connections. As can be seen, overall, the performance of proposed connections are better when using the curved beam web slot. It is, however, worth noting that as the angle of slope decreases, the strain demands at locations close to the heel also decreases. This can be seen in Figure 6.32 and Figure 6.33 where the PEEQ and RI values at Locations 1, 2, and 3 for different angle of slopes have been normalized to those of a 25° angle of slope (Model S2).

Figure 6.34 shows the comparison of the global responses for Model S2 and the proposed connections for each angle of slope. Note that the global strength of the proposed connection is higher than that of Model S2. The reason behind this is that the reduction in the beam plastic section modulus is small when a slot in introduced in the web. To demonstrate the validity of this claim, the following calculation performed for a W36×150 beam is presented.

The maximum reduction in the beam plastic section modulus is at the farthest side of the slot, i.e., at the circular ending point of the slot. To simplify the calculations, it can be conservatively assumed that there is another slot symmetrically located on the other side

of the beam neutral axis (Figure 6.35) such that the plastic neutral axis does not shift. Consequently, the lower bound for the plastic section modulus of the proposed connection is equal to:

$$Z_{SRBWS} = Z_x - (4t_w)(t_w)\left[d_b - 2\left(k + \frac{d_b}{6}\right)\right] \tag{6.32}$$

$$= 581 - (2.5)(0.625)\left[35.9 - 2\left(1.875 + \frac{35.9}{6}\right)\right] = 549.5 \text{ in}^3$$

In the equation above, Z_x is the beam plastic section modulus, t_w is the beam web thickness, d_b is the beam depth, and k is distance from the edge of the beam flange to the end of the fillet for hot-rolled section as specified in the AISC Steel Construction Manual.

The calculation above, which is conservative, shows about 6% reduction in the plastic section modulus of the beam (or 6% reduction in the flexural strength of the connection). Therefore, strength of a proposed connection is very similar to a connection which has no slot in the beam web, and the only source that can cause noticeable reduction in the connection strength is if there is instability due to buckling. The instability appears to be less as the angle of slope decreases (Figure 6.34).

6.5.2 Beam Depth Effect

In order to build up more confidence on the performance of the proposed connection, two extra beam sizes with an angle of slope equal to 25° were investigated. Each connection was modeled once with the proposed scheme and once with an RBS (perpendicular to the beam span). One case study was on a W30×116 beam and one on a very shallow beam, W10×49. As can be seen from Figure 6.36 and Figure 6.37, overall,

the indices show improved performance when the connection utilized the proposed beam web slot scheme. Also, the load-displacement response for both cases show that the proposed connection is stronger (Figure 6.38 and Figure 6.39).

6.6 Critical Angle of Slope for a W36×150 Beam

It was shown in the previous section that the proposed slot scheme can reduce the strain demand at locations close to the heel for sloped connections. It was then of interest to see beyond what angle of slop the use of slotted beam web is necessary. Since the final failure of both specimens (S1 and S2) was governed by the fracture at the beam weld access hole ear the heel location, it was decided to define the threshold for the angle of slope to be associated with a case when there is potentially no fracture at the beam weld access hole. Moreover, no-fracture criterion was restricted to be up until end of 0.04 rad drift cycles. PEEQ index was used to judge whether fracture may occur for a specific angle of slope. As mentioned in Chapter 5 that fracture of the beam weld access hole for Specimen S1 occurred at the end of second cycle of +0.03 rad drift, while for Specimen S2 fracture happened at the end of first excursion to +0.04 rad drift. Consequently, PEEQ values for both specimens at the corresponding drift ratios were first computed. PEEQ values were found to be 728 and 717 for Specimens S1 and S2, respectively. In the next step, PEEQ index for specimens with 20, 15, 10, and 5 degrees angle of slope was computed at the end of 0.04 rad drift cycles. The corresponding values for each angle of slope were found to be 778, 817, 581, and 582. Based on the values of PEEQ, it was concluded that sloped connections with an angle of slope beyond 10° will potentially develop fracture at the beam weld access hole by the end of 0.04 rad drift cycles, while those with angles of slope equal to or less than 10° (closer to an orthogonal connection) will likely be safe.

Consequently, an angle of slope equal to 10° can be considered as a threshold for sloped connections with a W36×150 beam, beyond which the proposed beam web slot is required.

6.7 Force Concentration Factor

As mentioned in Section 6.6, for the beam size of W36×150, an angle of slope larger than 10° will potentially lead to a fracture at the beam weld access hole at the heel location and, therefore, use of the proposed connection for angles larger than 10° is required. It was then decided to introduce a design parameter called "Force Concentration Factor", FCF, that can reflect the potential for fracture at the heel location for any sloped connections. The factor is defined as:

$$FCF = \frac{R_h^A}{R_h^A|(\theta = 0°)} \tag{6.33}$$

where R_h^A is the normal force at the heel location in a sloped connection, and $R_h^A|(\theta = 0°)$ is the normal force at the heel location for an orthogonal connection.

In order to find FCF, rather than using the results from FEM analysis, a generalized method was used to first compute the tension and compression forces. In this effort, the tension and compression forces on the right side of the proposed truss are related to the applied shear at the inflection point. This will be presented in the following. Moment (M) at the right side of the truss is equal to:

$$M = VL_d \tag{6.34}$$

where V is the applied shear at the inflection point and L_d is the clear length to the right side of the truss as shown in Figure 6.10. Next is to relate the axial forces (tension and compression forces on the right side of the truss) to this moment via parameter β:

$$P_f = C = T = \beta \frac{M}{d_b} = \beta \frac{VL_d}{d_b} \tag{6.35}$$

As the normal forces in the beam flanges are equal to the normal stress times the area of the beam flange, normal stress needs to be computed too. Assuming the distance between the centroid of the beam flanges is about $0.95d_b$ (d_b = beam depth), then using linear elastic stress analysis:

$$\sigma = \frac{M\left(\frac{0.95d_b}{2}\right)}{I} = \frac{0.95d_b}{2}\left(\frac{M}{I}\right) \tag{6.36}$$

where I is the beam moment of inertia. Therefore, the axial force in the beam flange, P_f, is:

$$P_f = \sigma A_f = \frac{0.95d_b}{2}\left(\frac{Mb_f t_f}{I}\right) = \frac{0.95d_b}{2}\left(\frac{VL_d b_f t_f}{I}\right) \tag{6.37}$$

Equating (6.35) and (6.37), one can solve for β:

$$\beta = 0.95\frac{b_f t_f d_b}{S_x} \tag{6.38}$$

For a W36×150 beam, β equals 0.76. Therefore, the axial forces in the beam flanges will be equal to:

$$C = T = \beta\left(\frac{VL_d}{d_b}\right) \tag{6.39}$$

If the shear force (V) is known, then using Eq. (6.39) all the forces on the right side of the proposed truss model will be determined. Therefore, in order to find FCF, one can assume a value for the shear V and find the corresponding C and T values. Then the truss model for any specific angle of slope can be constructed and be solved using the procedure

described in Section 6.3.2. Also, the truss model needs to be constructed for the orthogonal connectrion and be solved, as well. Then FCF can be found from Eq. (6.33).

6.7.1 Variation of FCF as A Function of Angle of Slope for Model S2

It was of interest to see how the angle of slope will influence the Force Concentration Factor, FCF. To plot Force Concentraion Factor as a function of angle of slope, a shear force, V, of 100 kips was assumed and then the proposed truss model was solved for angles of slope from 0° to 25°. As mentioned in the Section 6.3.2, the truss model is not valid for any angle of slope larger than 35°, therefore a regression analysis was carried out to capture Force Concentration Factor up until angle of 45°. The result of regression analyses gave the following equation:

$$FCF = (4.276 \times 10^{-6})\theta^3 - 1.343 \times 10^{-4}\theta^2 + 6.504 \times 10^{-3}\theta + 1.000 \quad (6.40)$$

In the above equation, θ is the angle of slope, and FCF is the Force Concetraion Factor. Eq. (6.40) was then used to plot FCF versus angle of slope up until an angle of slope equal to 45° (see Figure 6.40). As can be seen the concentration will increase as the angle of slope increases.

6.7.2 Critical Value for FCF

As discussed in Section 6.6, an angle of slope equal to 10° is considered to be a threshold for a W36×150 beam, beyond which the proposed beam web slot is required. Consequently, a critical value for Force Concentration Factor, $FCF_{critical}$, was then associated with a 10° angle of slope which from the figure is equal to 1.06.

6.7.3 Design Implication

As mentioned earlier, the purpose of introducing the Force Concentration Factor is to provide design engineers with a tool to predict potential for fracture at the heel location and then decide whether a SRBWS (or any special treatment) needs to be considered. The design implication can be summarized in the following steps:

(1) Given the beam size, compute $\boldsymbol{\beta}$ based on Eq. (6.38).

(2) With an assumed $\boldsymbol{V}$, find $\boldsymbol{C}$ and $\boldsymbol{T}$ from Eq. (6.35).

(3) Construct the proposed truss model for the sloped connection and load it with the $\boldsymbol{V}$, $\boldsymbol{C}$, and $\boldsymbol{T}$ and solve the truss using the procedure presented in Section 6.3.2.

(4) Construct the proposed truss model for an orthogonal connection using the same beam and load it with the $\boldsymbol{V}$, $\boldsymbol{C}$, and $\boldsymbol{T}$ and solve the truss using the procedure presented in Section 6.3.2.

(5) Compute $\boldsymbol{FCF}$ using Eq. (6.33) and check it against $\boldsymbol{FCF_{critical}} = 1.06$. If $\boldsymbol{FCF} > \boldsymbol{FCF_{critical}}$ then the proposed beam web slot is recommended to use for the sloped connection (the sloped connection is prone to a fracture at the beam weld access hole).

Table 6.1 PEEQ Index Comparison of Models S1 and S2

	Specimen S1	Specimen S2
Location 1	1282	1234
Location 2	1166	1135
Location 3	467	407

Table 6.2 Rupture Index Comparison of Models S1 and S2

	Specimen S1	Specimen S2
Location 1	4978	4909
Location 2	2177	2262
Location 3	1646	1538

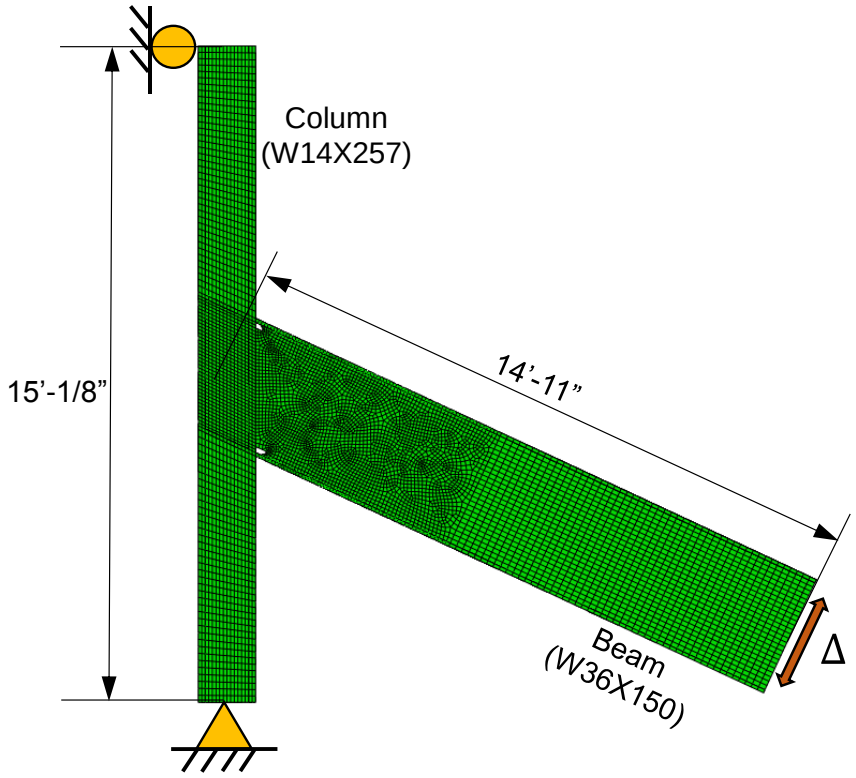

Figure 6.1 FEM Model

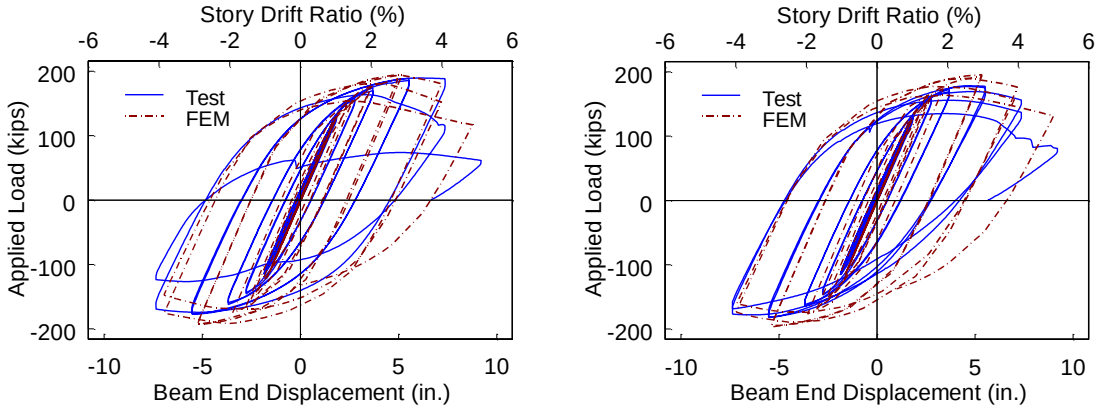

(a) Specimen S1 (b) Specimen S2

Figure 6.2 Correlation of Global Responses

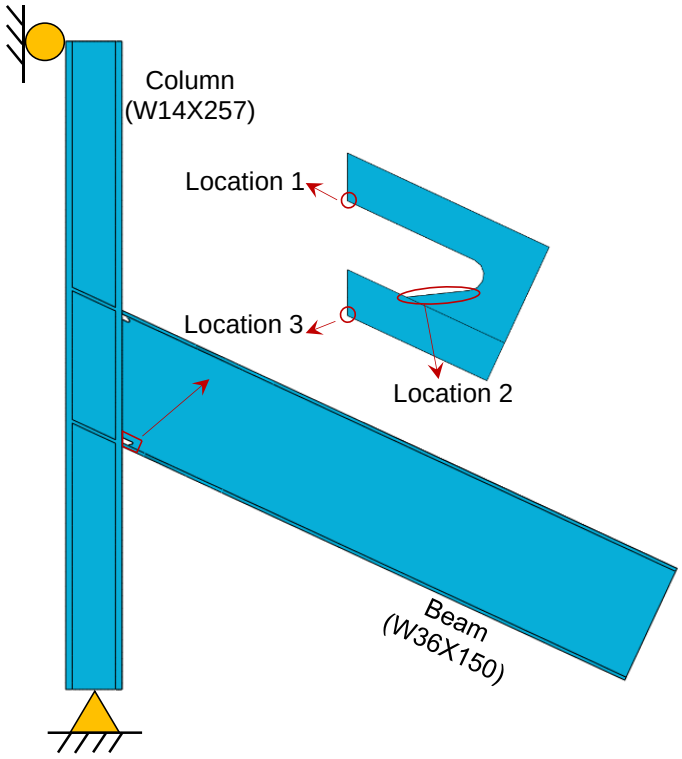

Figure 6.3 Three Locations on the Beam to Monitor PEEQ and Rupture Index

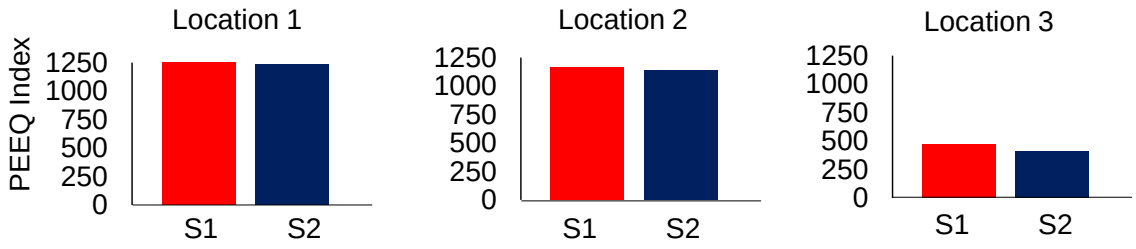

(a) Absolute PEEQ Index

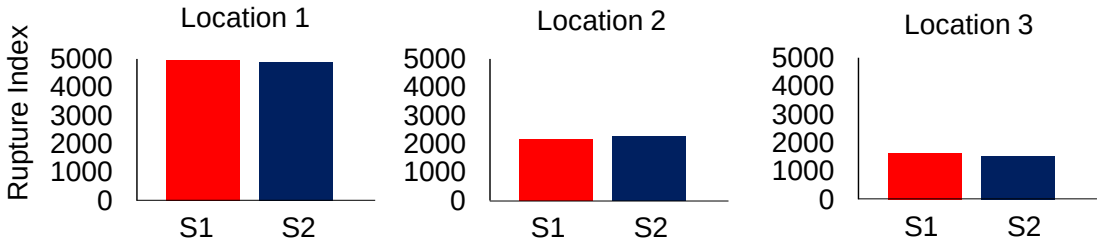

(b) Absolute Rupture Index

Figure 6.4 Specimens S1 and S2 Indices Comparison

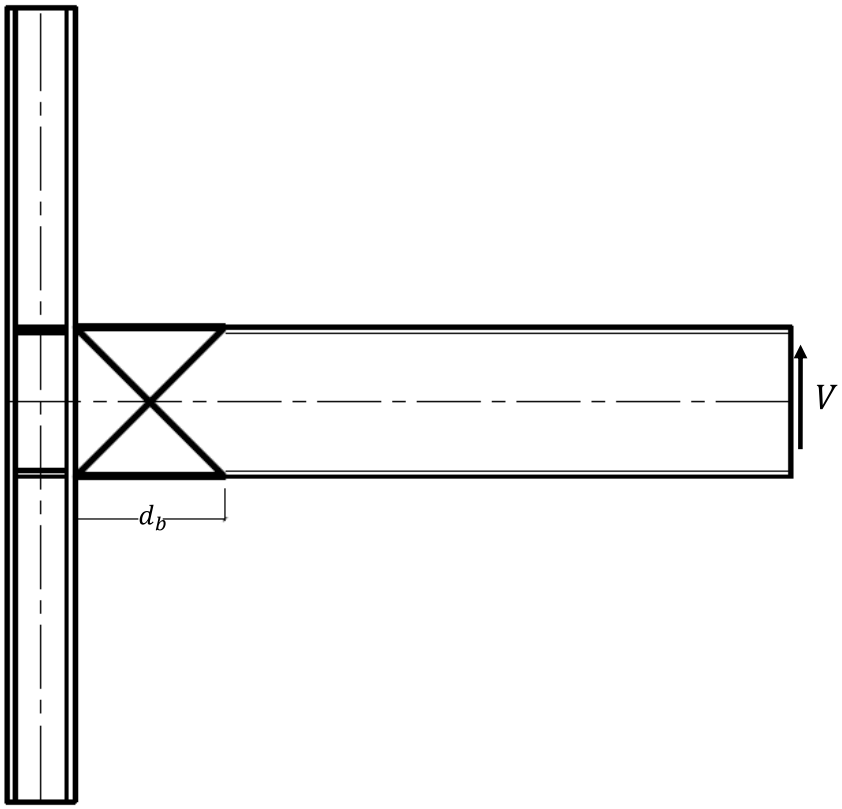

Figure 6.5 Truss Model Proposed (Goel et al. 1997) Overlapped on an Orthogonal Moment Connection

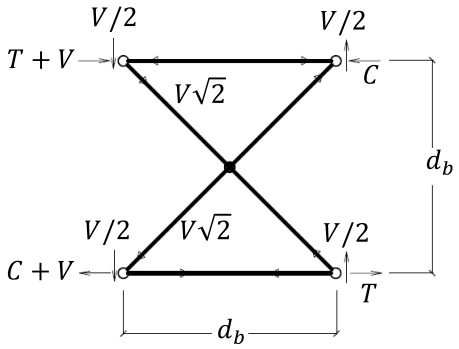

Figure 6.6 Parametric Solution to Truss Model Proposed by Goel et al. (1997) for an Orthogonal Moment Connection

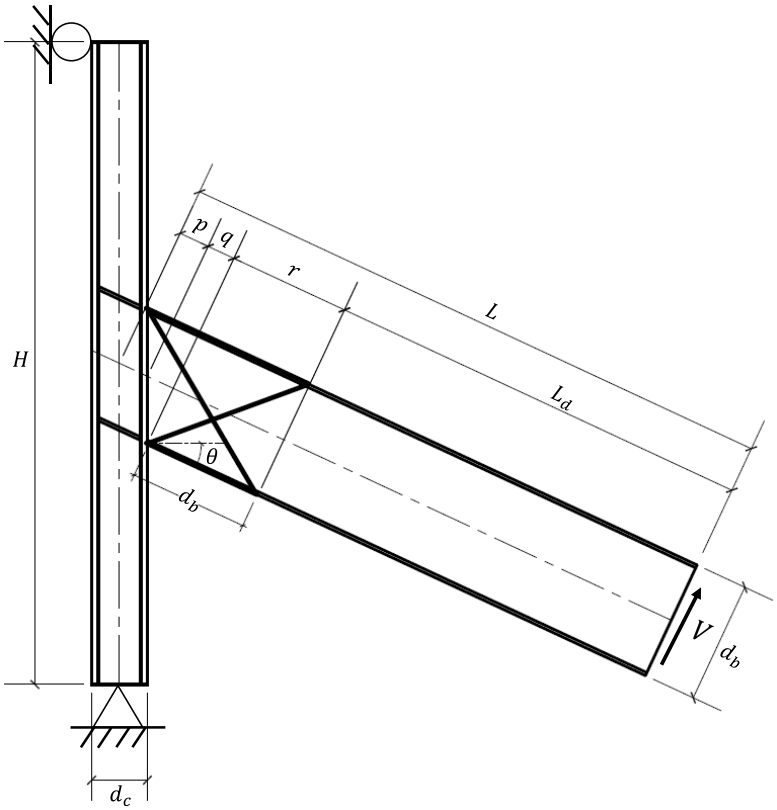

Figure 6.7 Truss Model Proposed by Goel et al. (1997) Overlapped on a Sloped Moment Connection

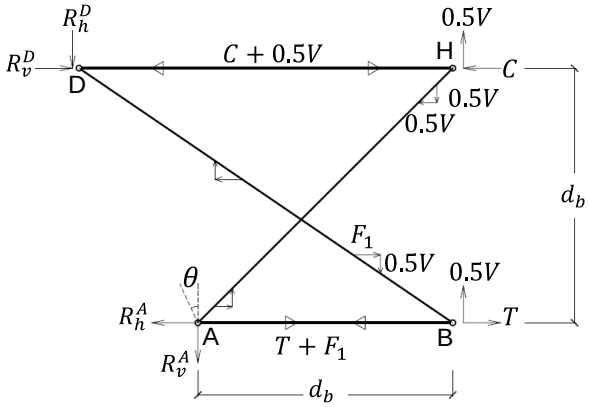

Figure 6.8 Parametric Solution of Goel et al. (1997) Truss Model for a Sloped Moment Connection

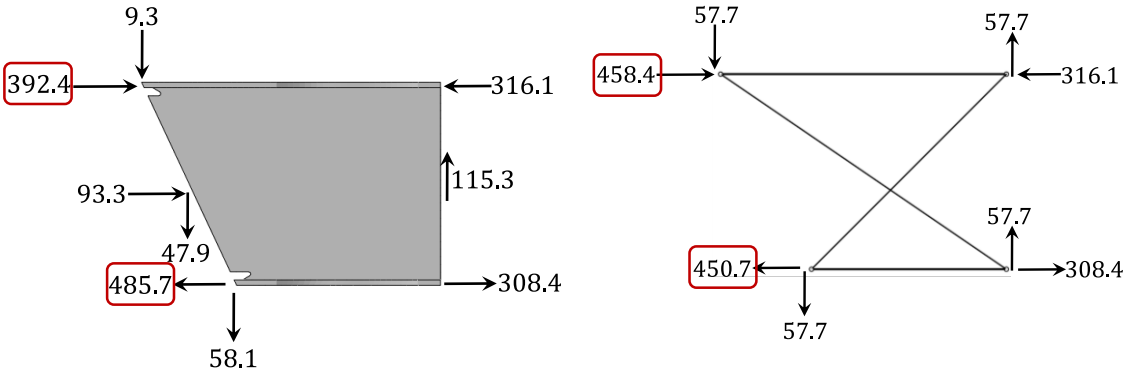

(a) FEM (b) Goel's Model

(units: kips)

Figure 6.9 Comparison of Reaction Forces between Goel et al. Truss Model and FEM at 0.01 rad Drift (Model S2)

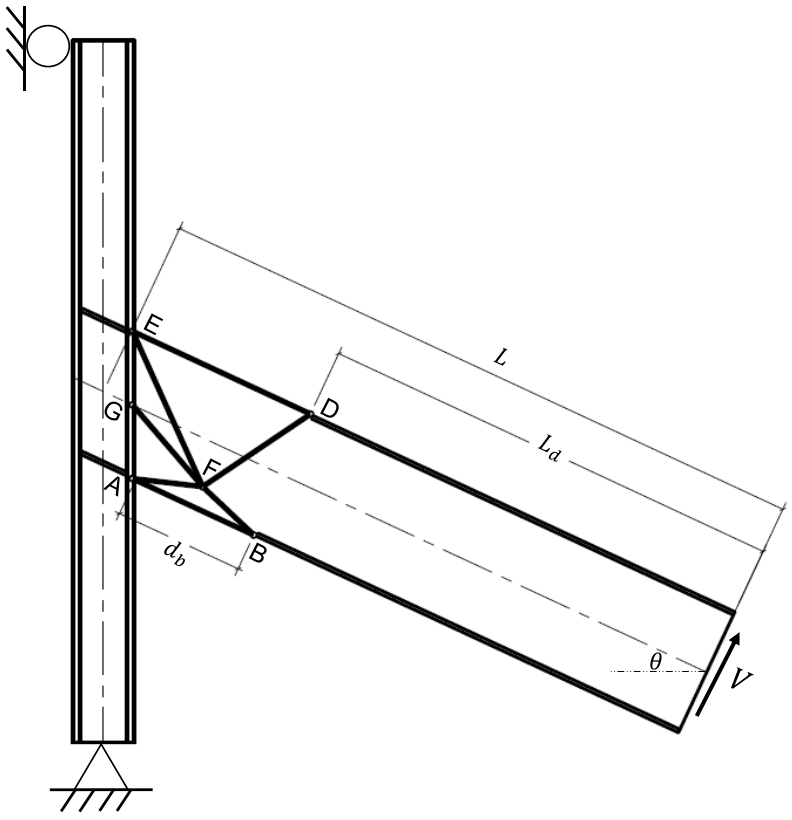

Figure 6.10 Proposed Truss Model Overlapped on a Sloped Connection

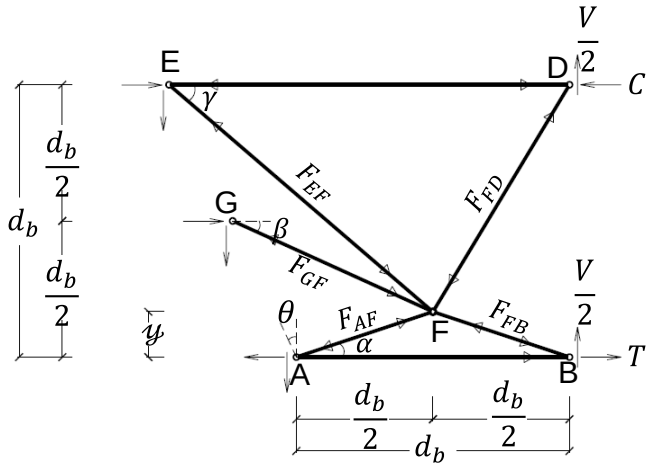

Figure 6.11 Extracted Proposed Truss Model for a Sloped Moment Connection

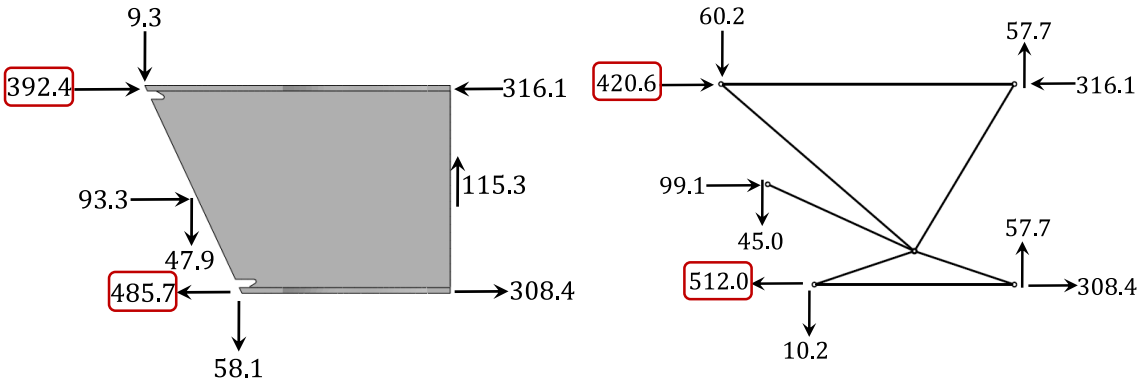

(a) FEM (b) Proposed Truss Model

(units: kips)

Figure 6.12 Comparison of Reaction Forces Based on the Proposed Truss Model and FEM (Model S2 at 0.01 rad Drift)

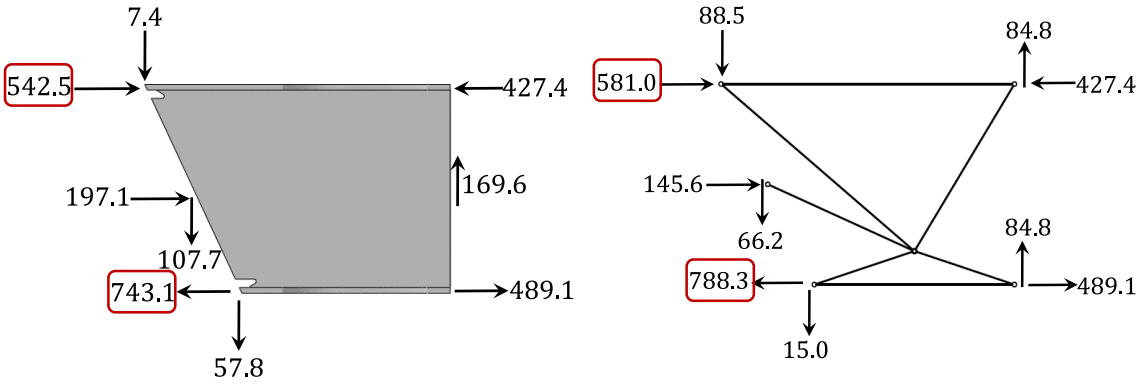

(a) FEM (b) Proposed Truss Model

(units: kips)

Figure 6.13 Comparison of Reaction Forces Based on the Proposed Truss Model and FEM (Model S2 at 0.04 rad Drift)

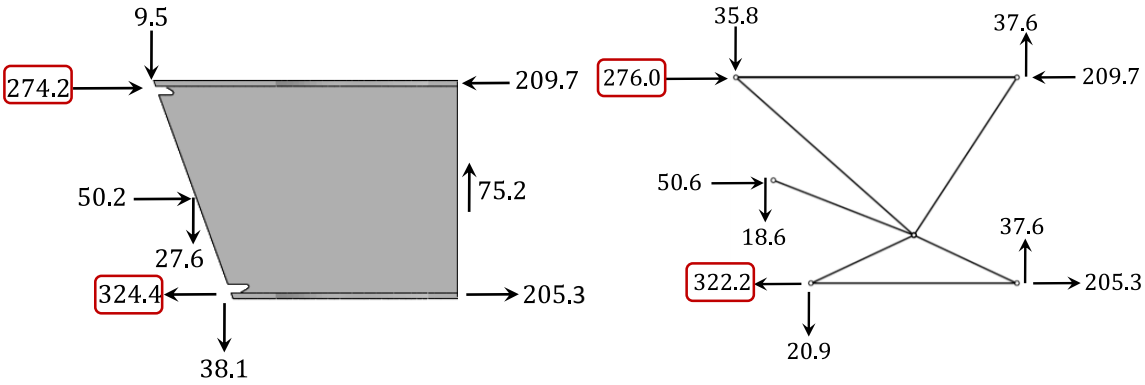

(a) at 0.0075 rad Drift SDR (20° Angle)

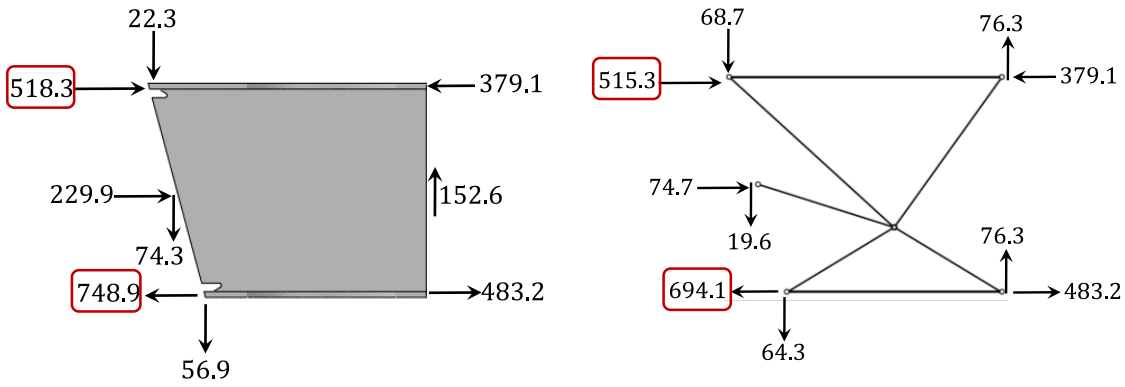

(b) at 0.05 rad Drift (15° Angle)

(units: kips)

Figure 6.14 Comparison of FEM and Proposed Truss Model Predictions: Effect of Angle of Inclination

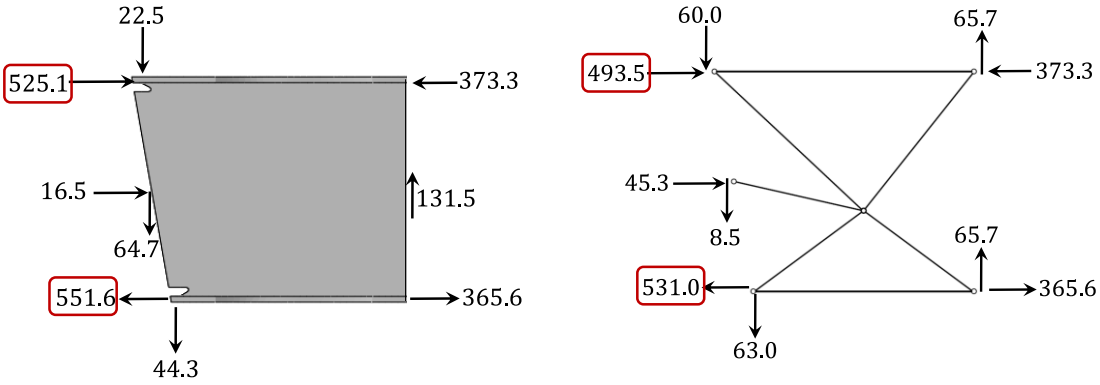

(c) at 0.015 rad Drift (10° Angle)

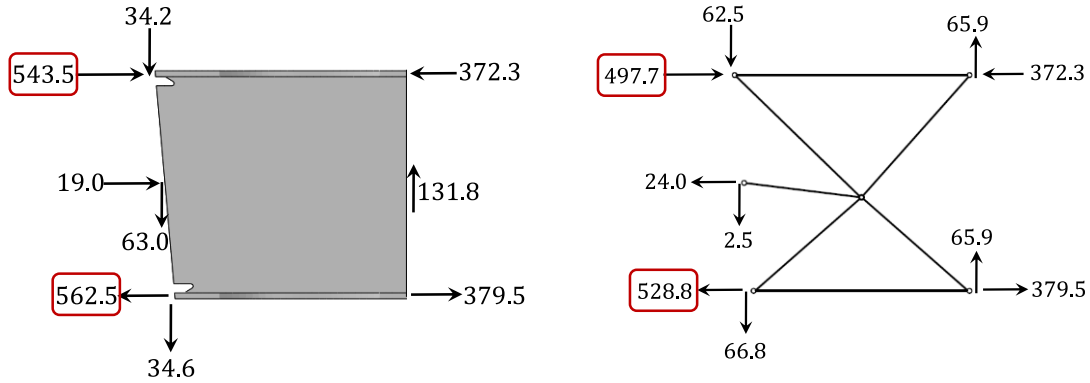

(d) at 0.015 rad Drift (5° Angle)

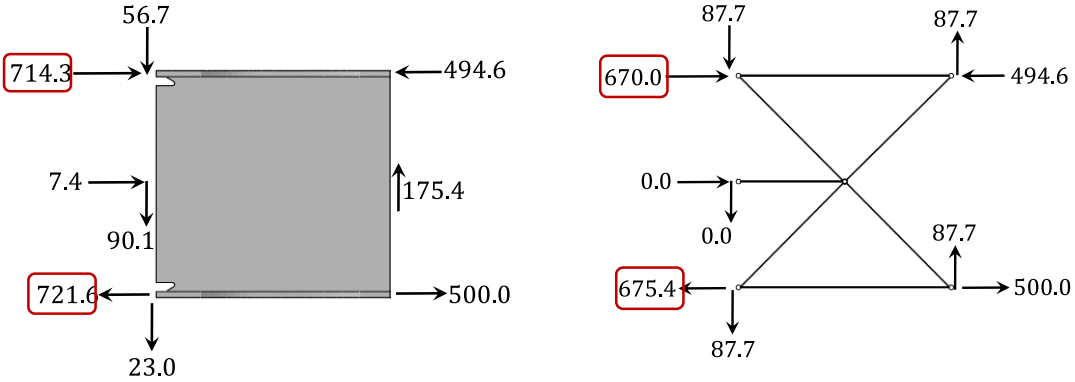

(a) FEM (b) Proposed Truss Model

(e) at 0.03 rad Drift (Orthogonal)

(units: kips)

Figure 6.14 Comparison of FEM and Proposed Truss Model Predictions: Effect of Angle of Inclination (continued)

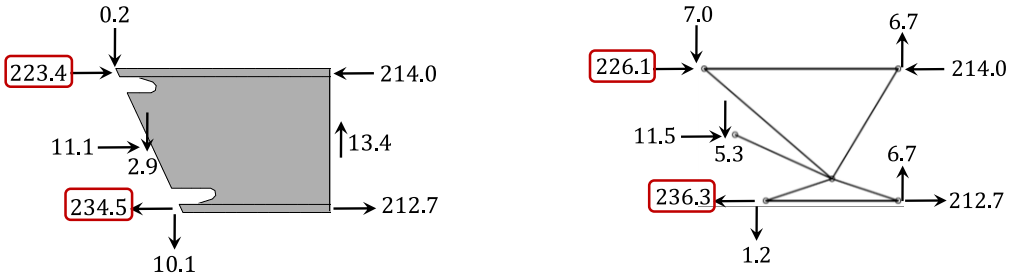

(a) W10×49 Beam (at 0.02 rad Drift)

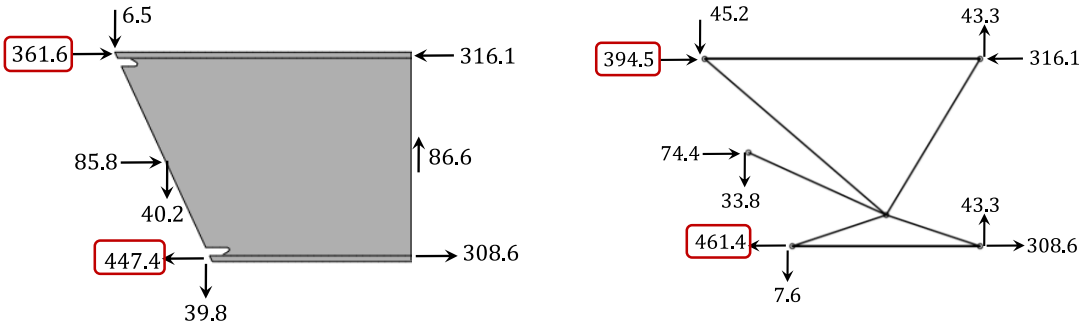

(a) FEM (b) Proposed Truss Model

(b) W30×116 Beam (at 0.01 rad Drift)

(units: kips)

Figure 6.15 Beam Depth Effect on the Proposed Truss Model (Angle of Inclination = 25°)

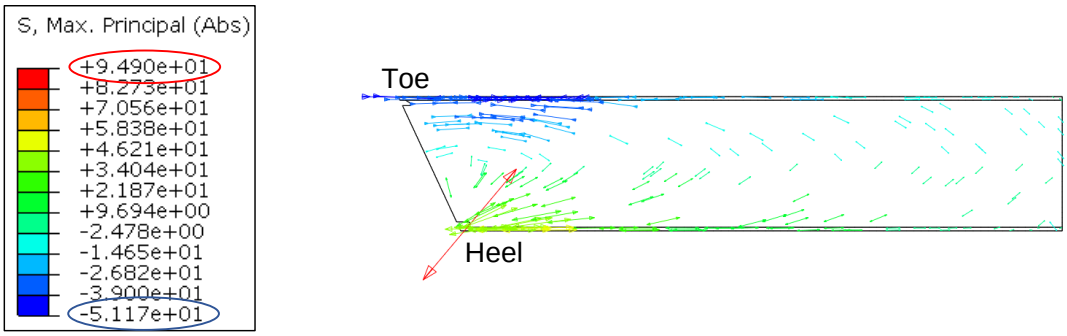

Figure 6.16 Contour of Absolute Maximum Principal Stress at +0.01 rad Drift

(units: kips)

Figure 6.17 Free Body Diagram of Beam for Model S2 (0.01 rad Drift)

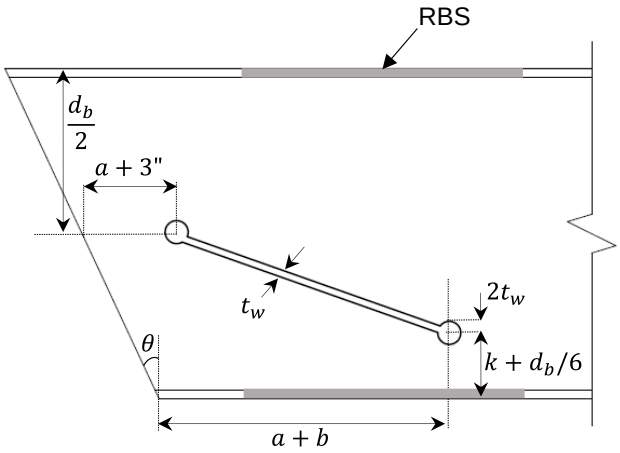

Figure 6.18 Geometry Detail of Straight Cut

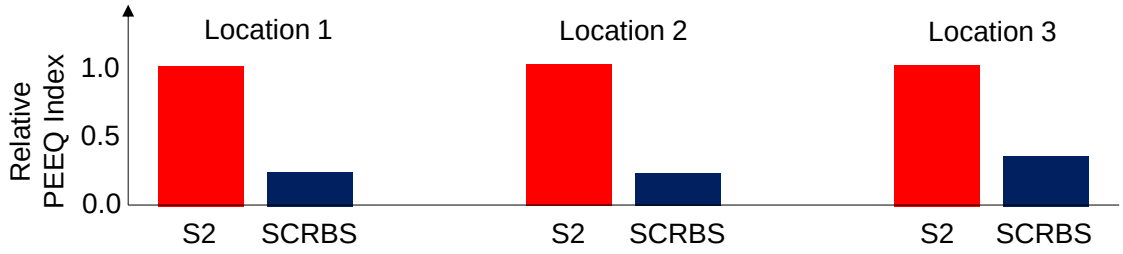

(a) Relative PEEQ Index

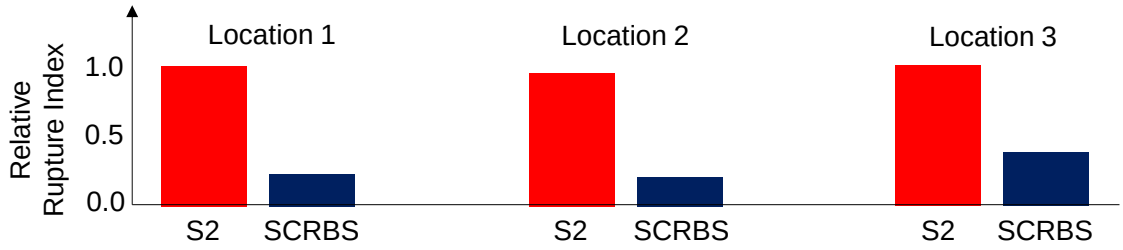

(b) Relative Rupture Index

Figure 6.19 Models S2 and SCRBS Indices Comparison

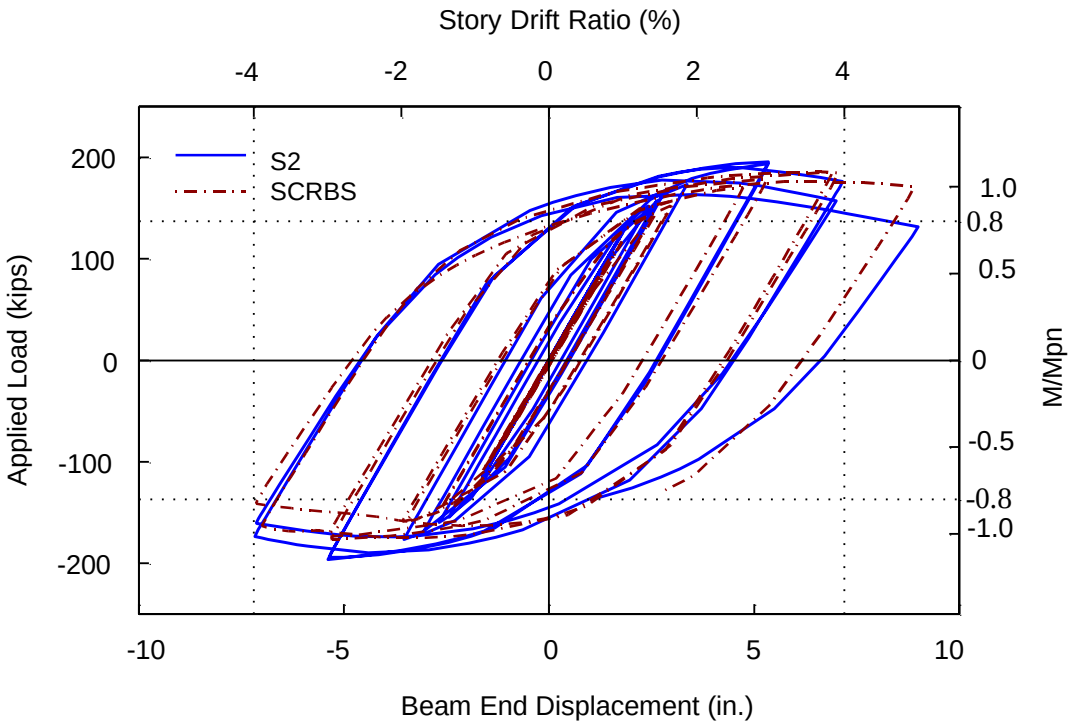

Figure 6.20 Global Response Comparison of Models S2 and SCRBS

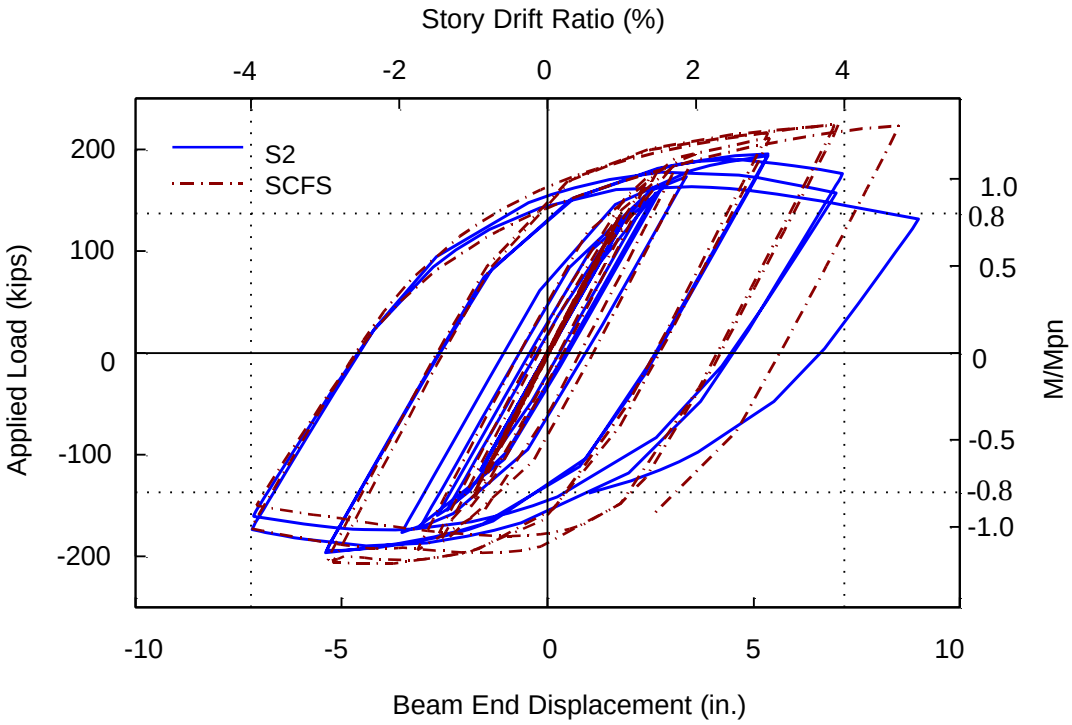

Figure 6.21 Global Response Comparison of Models S2 and SCFS

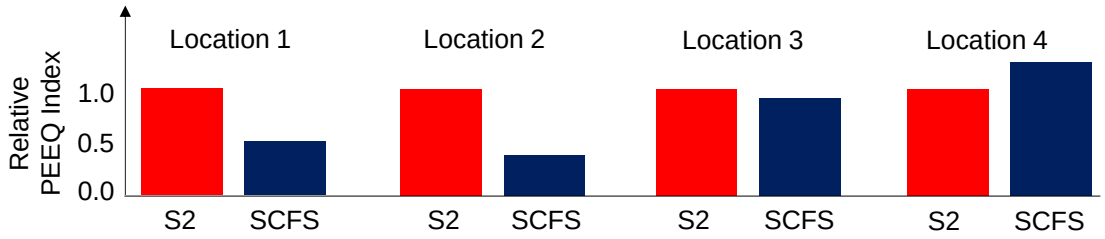

(a) Relative PEEQ Index

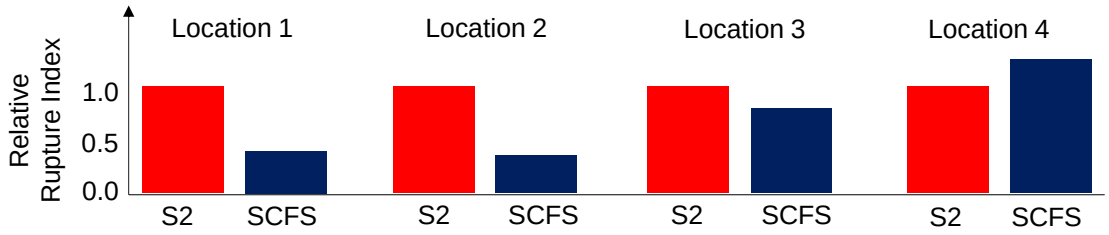

(b) Relative Rupture Index

Figure 6.22 Models S2 and SCFS Indices Comparison

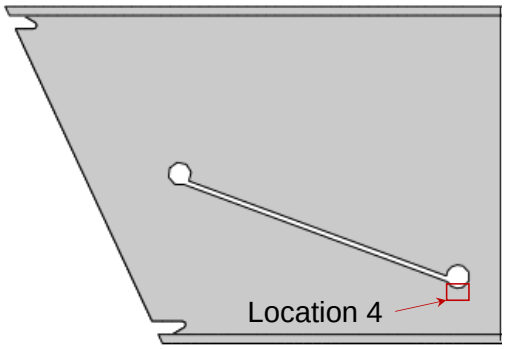

Figure 6.23 Depiction of Location 4 on the Straight Cut

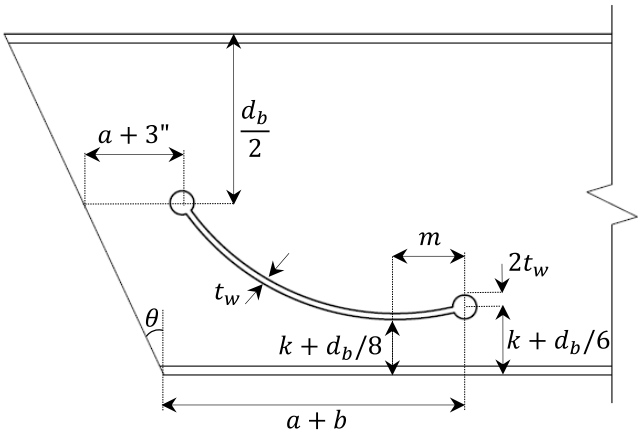

$$m = \frac{1}{5}\left(b - 3" + \frac{d_b}{2}\tan(\theta)\right)$$

Figure 6.24 Detail of Curved Cut (SRBWS)

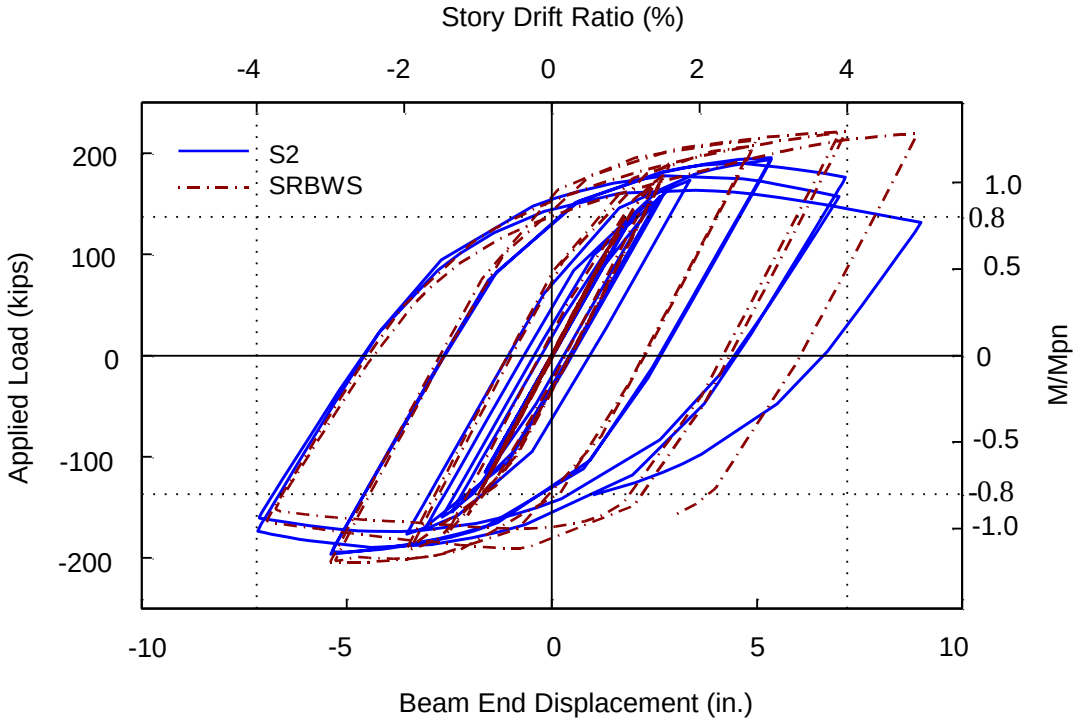

Figure 6.25 Global Response Comparison of Models S2 and SRBWS

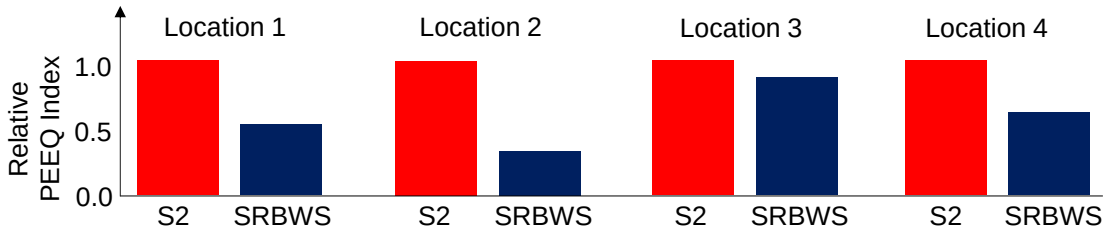

(a) Relative PEEQ Index

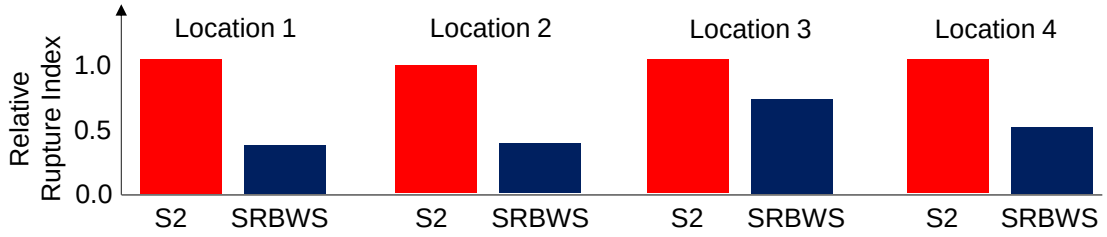

(b) Relative Rupture Index

Figure 6.26 Models S2 and SRBWS Indices Comparison

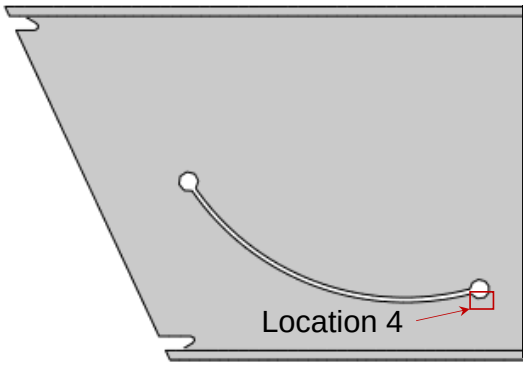

Figure 6.27 Depiction of Location 4 on the Curved Cut

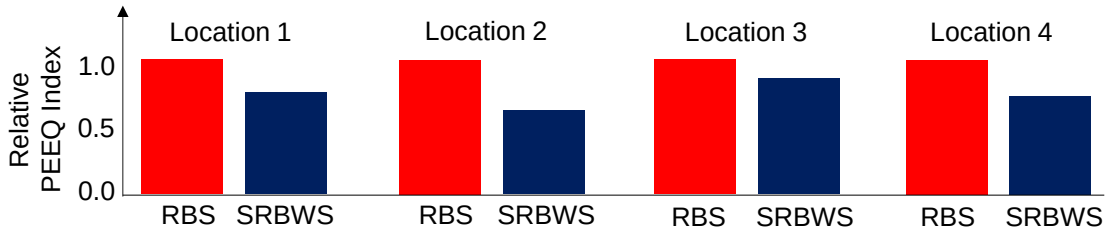

(a) Relative PEEQ Index

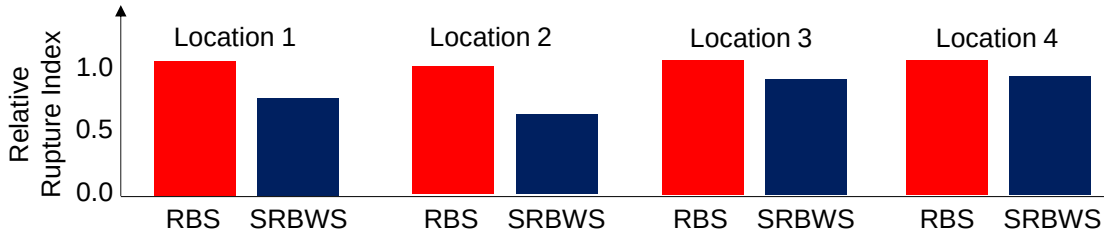

(b) Relative Rupture Index

Figure 6.28 Models RBS and SRBWS Indices Comparison (Angle of Slope = 20°)

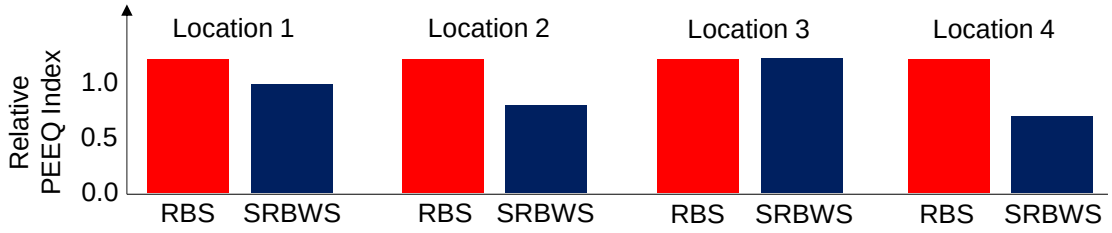

(a) Relative PEEQ Index

(b) Relative Rupture Index

Figure 6.29 Models RBS and SRBWS Indices Comparison (Angle of Slope = 15°)

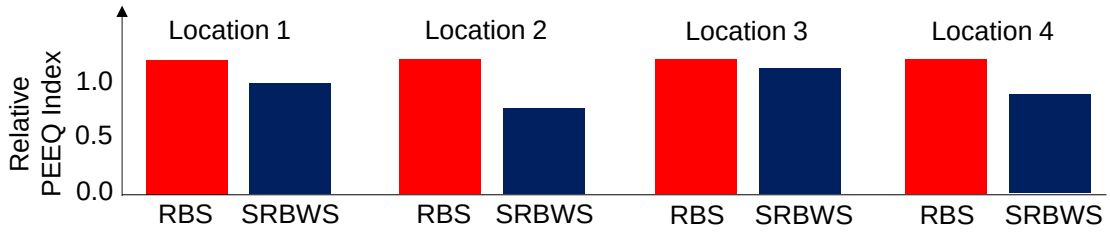

(a) Relative PEEQ Index

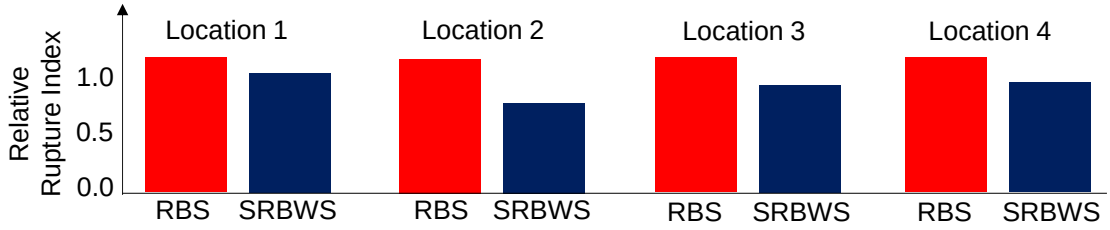

(b) Relative Rupture Index

Figure 6.30 Models RBS and SRBWS Indices Comparison (Angle of Slope = 10°)

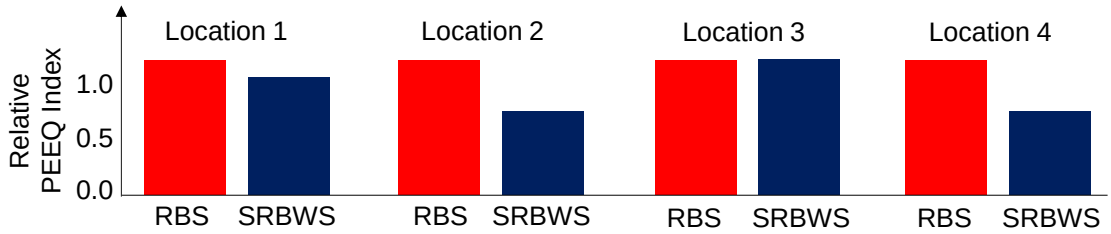

(a) Relative PEEQ

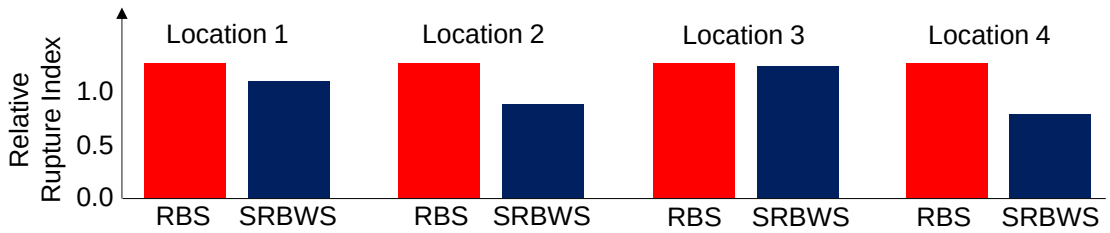

(b) Relative Rupture Index

Figure 6.31 Models RBS and SRBWS Indices Comparison (Angle of Slope = 5°)

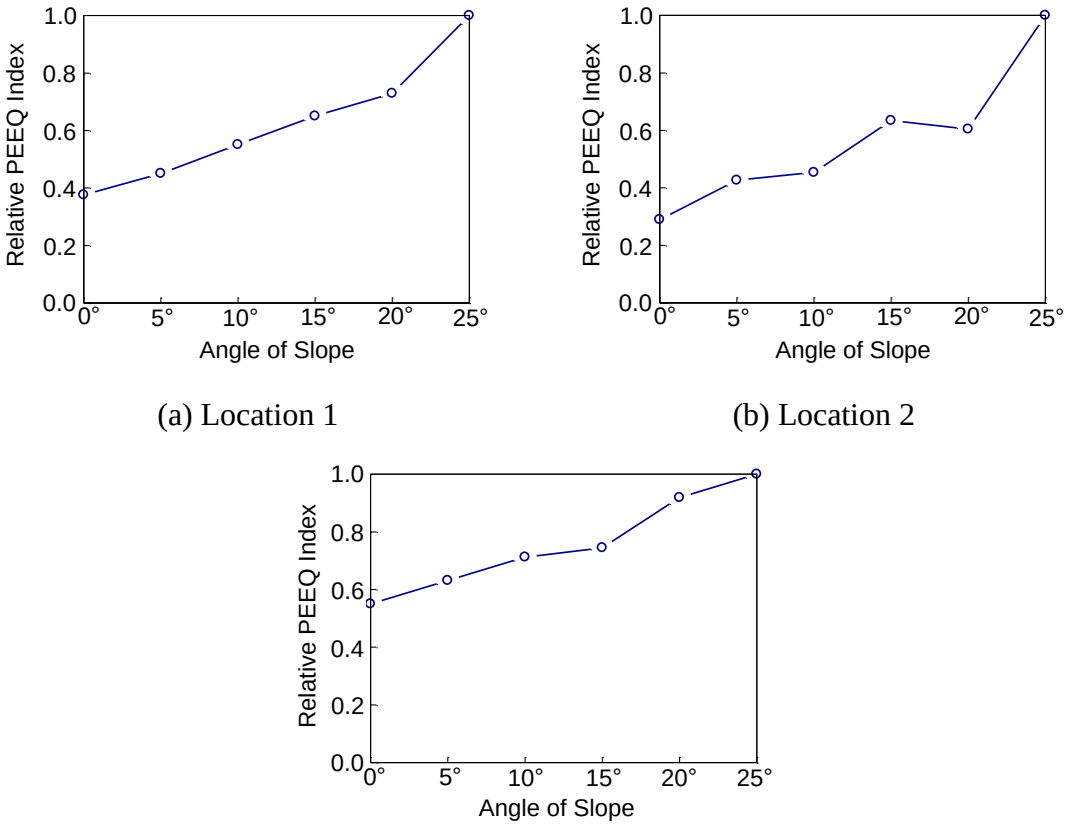

(a) Location 1

(b) Location 2

(c) Location 3

Figure 6.32 PEEQ Index Variation with Angle of Slope

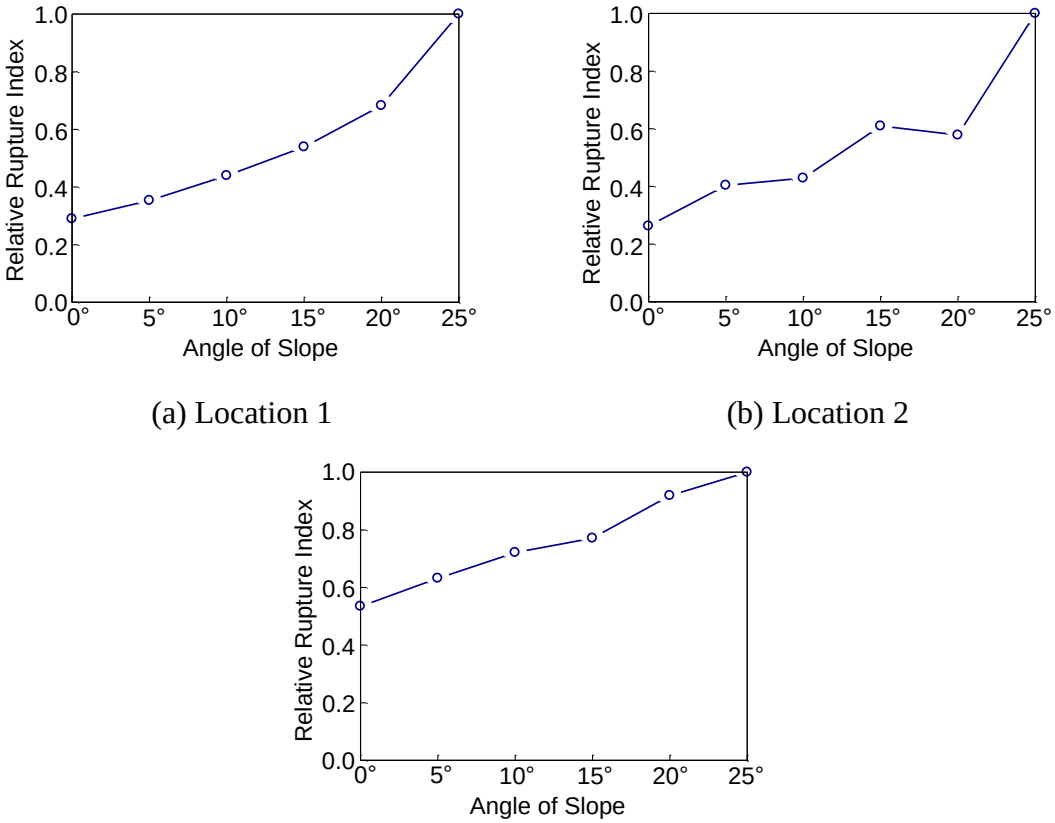

(a) Location 1

(b) Location 2

(c) Location 3

Figure 6.33 Rupture Index Variation with Angle of Slope

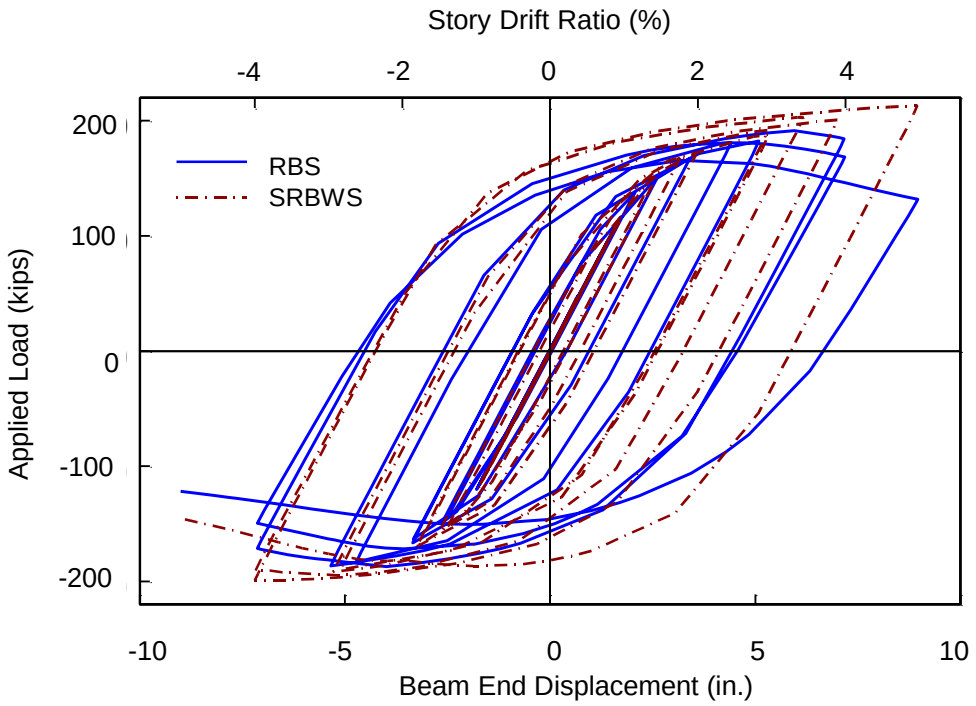

(a) $\theta = 20°$

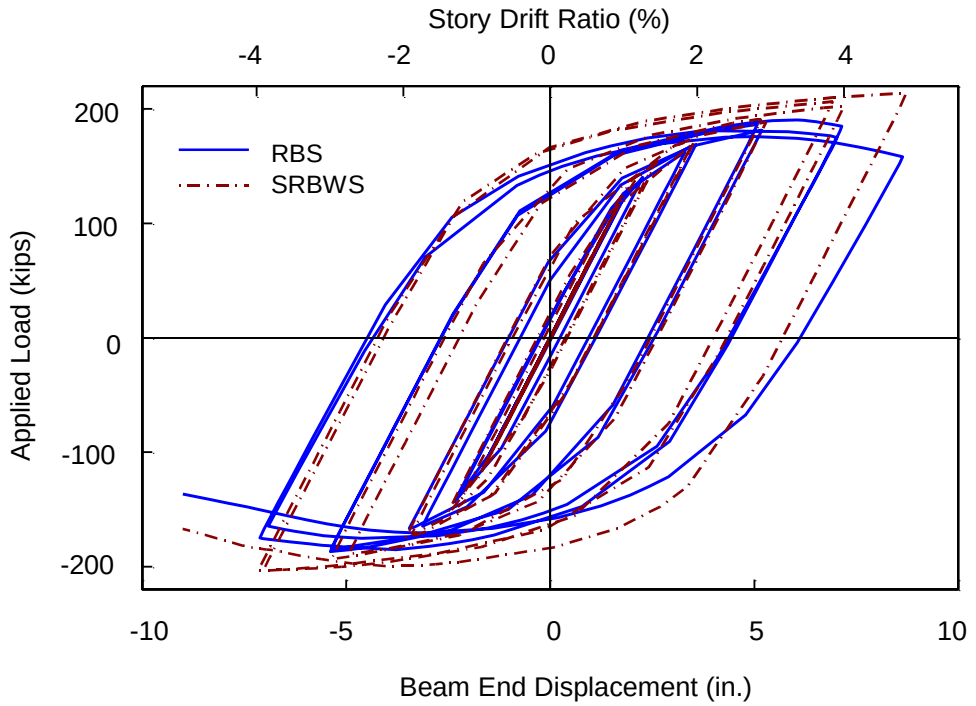

(b) $\theta = 15°$

Figure 6.34 Global Response Comparison between Models RBS and SRBWS

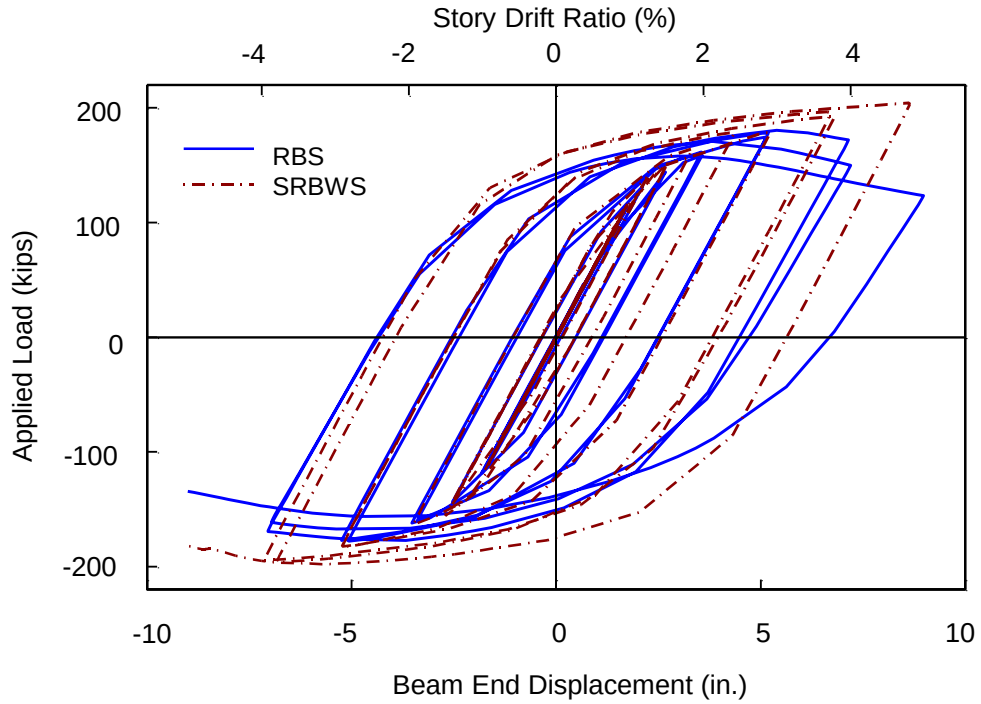

(c) $\theta = 10°$

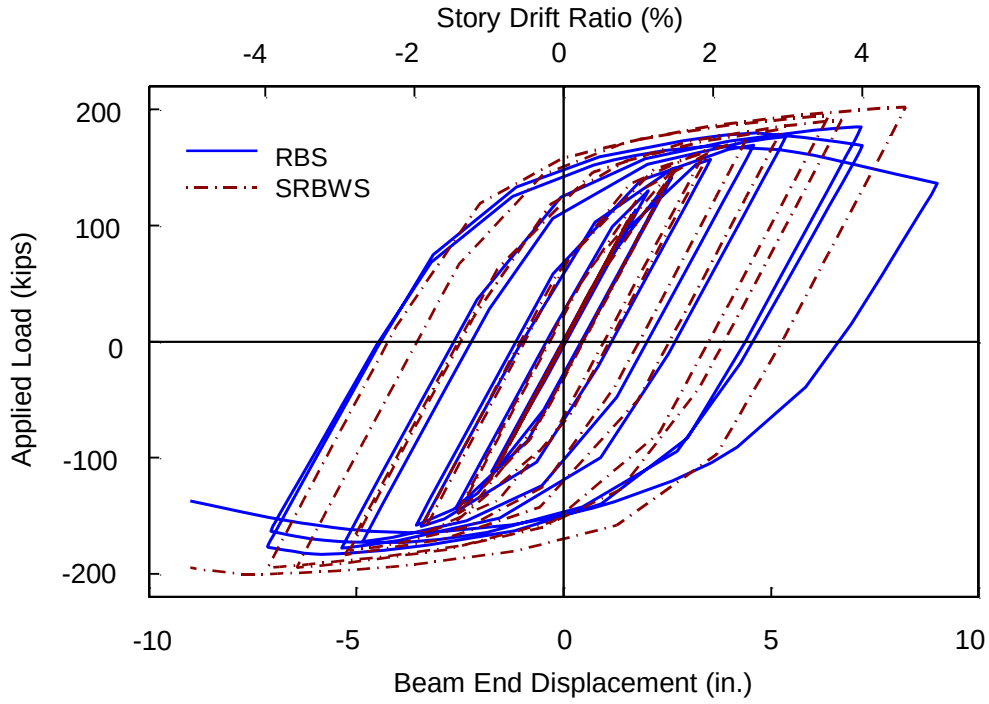

(d) $\theta = 5°$

Figure 6.34 Global Response Comparison between Models RBS and SRBWS (continued)

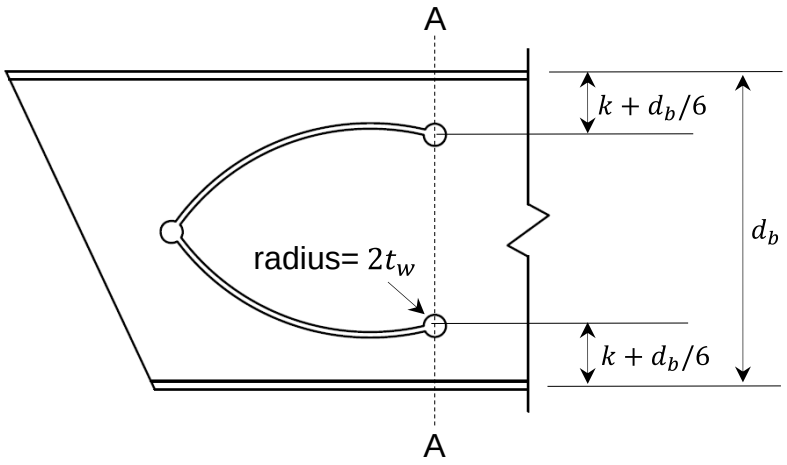

Figure 6.35 Minimum Plastic Section Modulus at Section A-A

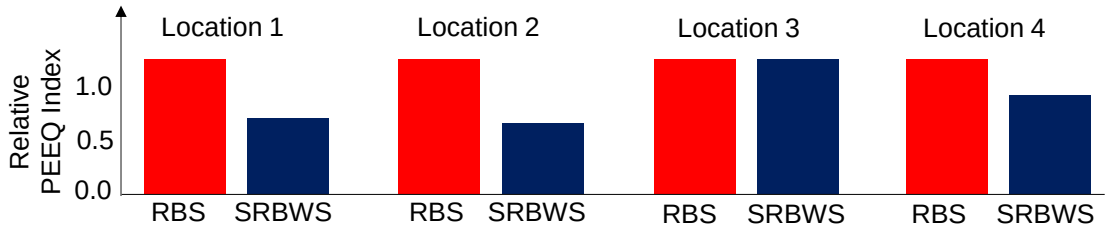

(a) Relative PEEQ Index

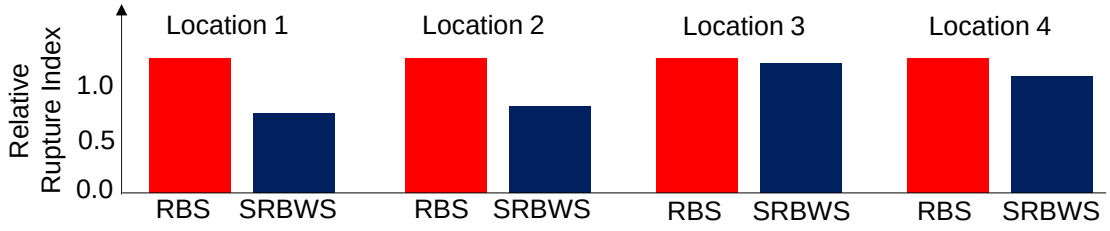

(b) Relative Rupture Index

Figure 6.36 Specimens RBS and SRBWS Indices Comparison (W30×116 Beam with Angle of Slope = 25°)

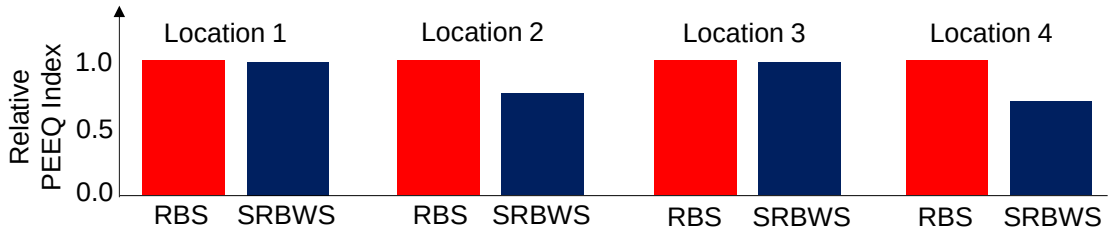

(a) Relative PEEQ Index

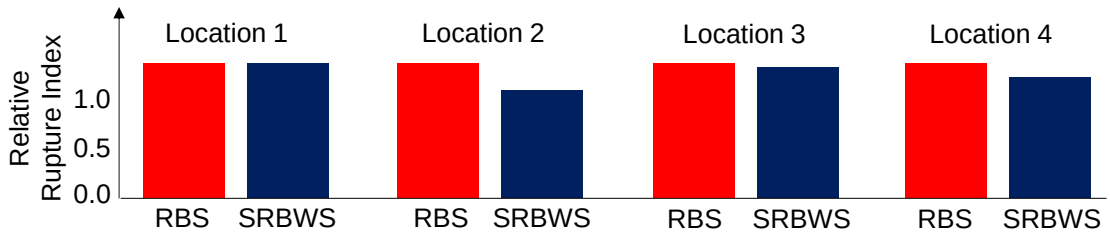

(b) Relative Rupture Index

Figure 6.37 Models RBS and SRBWS Indices Comparison (W10×49 Beam with Angle of Slope = 25°)

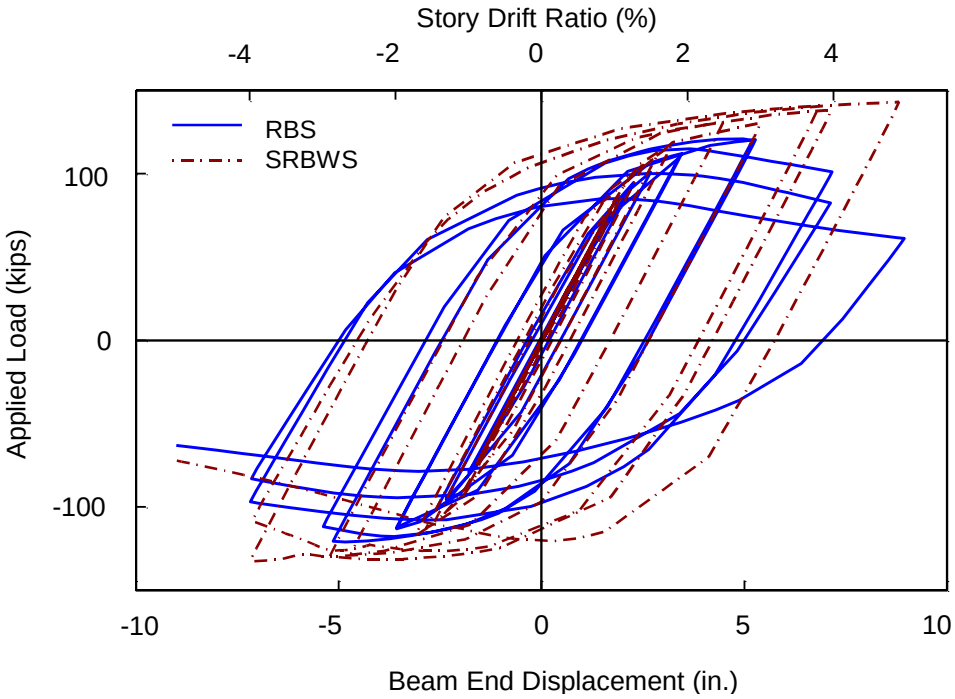

Figure 6.38 Global Response Comparison between Models RBS and SRBWS (W30×116 Beam with $\theta = 25°$)

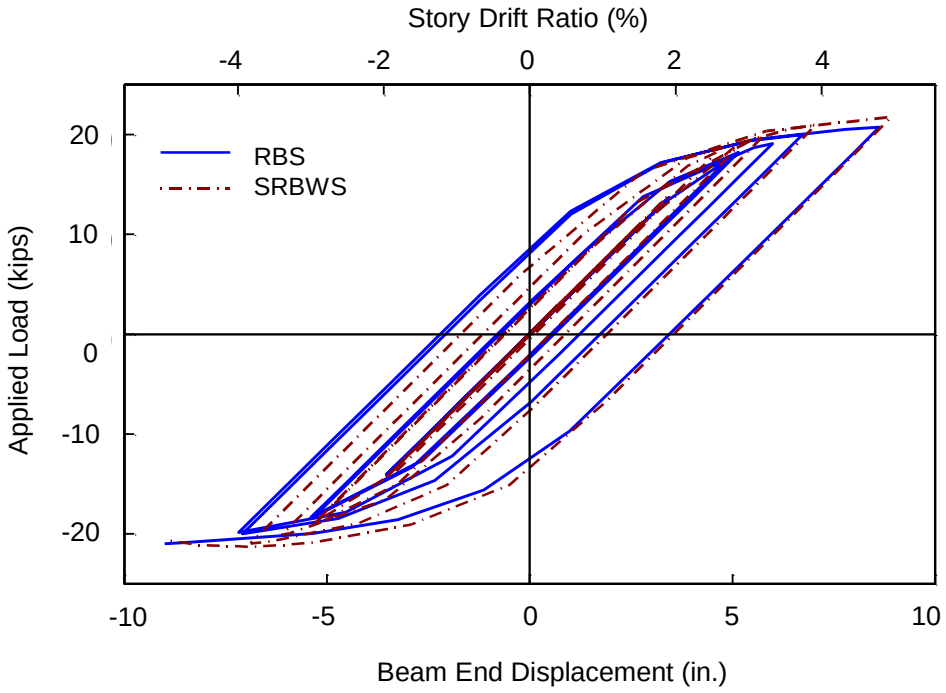

Figure 6.39 Global Response Comparison between Models RBS and SRBWS (W10×49 Beam with $\theta = 25°$)

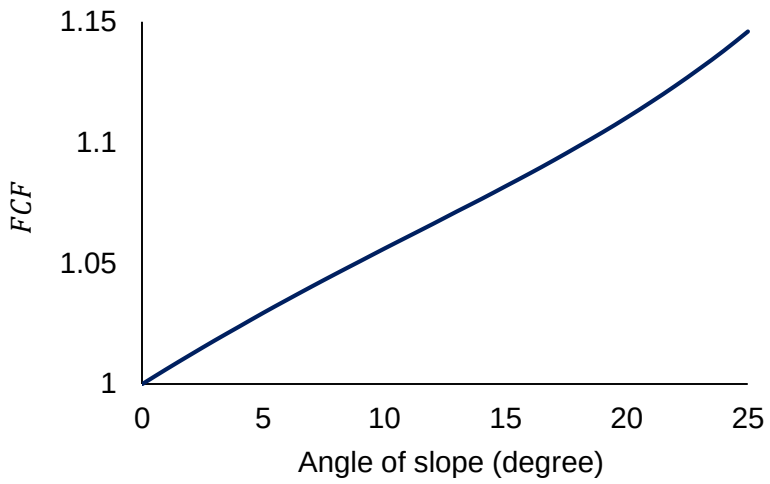

Figure 6.40 Force Concentration Factor Variation with Angle of Slope

7 SUMMARY, CONCLUSIONS, AND FUTURE RESEARCH NEED

7.1 Design of Continuity Plate Welds for Orthogonal Connections

7.1.1 Summary

Based on a weld detail commonly used in steel moment connection tests conducted in the past, AISC 341 requires that continuity plates in a Special Moment Frame (SMF) be connected to the column flanges by complete-joint-penetration (CJP) groove welds. This prescriptive requirement, where the calculation of the required forces in the continuity plates is unnecessary, would increase the fabrication cost. As a first step to allowing for other types of more economical weld joints (e.g., fillet welds or partial-point-penetration groove welds) to be used, it is necessary to have a design procedure to quantify the required forces in the continuity plate. Recently, Tran et al. (2013) proposed a procedure that considers the in-plane flexibility (or stiffness) of the continuity plate relative to the out-of-plane flexibility of the column flange in determining the forces that are transmitted through the continuity plates to the column panel zone.

In the procedure proposed by Tran et al., the edges of the continuity plate next to the column flanges were subjected to both normal and shear forces. This procedure was modified in this research to include the moment component created by the normal force with an eccentricity. As a pilot study to experimentally verify this design procedure, two full-scale, one-sided moment connection specimens with a reduced beam section (RBS) were tested. The specimen design followed AISC 341 and 358, except that the continuity plate thickness and welds were sized based on the modified procedure; the design procedure resulted in fillet welds for the continuity plates. One specimen (C1) used a deep

(W24) column, and the other one (C2) had a shallow (W14) column. The continuity plates of Specimen C2 were also undersized intentionally to evaluate the effect of yielding in the continuity plates on the connection performance. While still satisfying the code requirement, the demand-capacity ratio of the panel zone strength was high (0.90 and 0.95 for C1 and C2, respectively) such that the effect of column flange kinking at the fillet welds locations could be evaluated. A992 steel was specified for the beams and columns, and A572 Gr. 50 steel was used for the continuity plates. Both specimens were tested cyclically by using the AISC loading protocol.

7.1.2 Conclusions

Based on the test results and the associated analytical studies, the following conclusions can be made.

(1) Both specimens performed well and met the 0.04 rad. story drift requirement specified in AISC 341. Using the fillet welds did not affect the performance of the connection; as expected, yielding and buckling in the RBS region as well as shear yielding in the panel zone were observed.

(2) No damage in the fillet welds connecting the continuity plates to the column was observed, indicating that the AISC 341 prescriptive requirement for expensive CJP groove welds can be conservative and may not be always needed.

(3) AISC 341 also specifies a prescriptive requirement for the thickness of the continuity plates: half and full thickness of the beam flange for the exterior and interior moment connections, respectively (the full thickness requirement has been relaxed without any experimental justification to three-quarter the beam flange thickness for the interior connection in the 2016 edition of AISC 341). The proposed design procedure may

result in a continuity plate thickness different from that required by AISC 341. Test results showed that the AISC prescriptive requirement on the thickness of continuity plates may not be needed; the proposed procedure will consider directly the effect of thickness on the required forces in the continuity plates.

(4) The interface between the continuity plate and the column flanges is subjected to not only normal force but also shear force and moment; the moment is produced by the normal force together with an eccentricity (Figure 2.5 and Figure 2.6). The effect of moment and shear can be significant, especially for continuity plates in shallow columns (Table 3.4). The combined effect of normal force, shear force, and moment needs to be considered in checking the strength of continuity plates [Eq. (2.31)].

(5) AISC 341 implicitly assumes that continuity plates shall remain essentially elastic per the capacity design principles. The continuity plate thickness of one specimen (C2) was undersized. Testing showed that the connection performance was not affected although the continuity plates had yielded.

7.1.3 Future Research Need

This pilot test program demonstrated that the prescriptive requirements in AISC 341 that requires a specific continuity plate thickness and expensive CJP groove welds to connect the continuity plates to the column flanges may not always be needed. Only two one-sided moment connections were tested in this research. Before the proposed design procedure can be implemented, additional experimental verification is needed. Further testing should include two-sided moment connections, different connection types, inclusion of doubler plates, use of partial-joint-penetration groove welds, etc.

7.2 Sloped Connections

7.2.1 Summary

AISC 358 provides a number of prequalified connections for seismic applications in Special and Intermediate Steel Moment Frames (SMF and IMF). This design standard implicitly assumes that the beam frames orthogonally into the column in the elevation of the frame and also in plan view. In real-life construction, however, it is not uncommon that this orthogonal condition is violated. Unfortunately, AISC 358cdoes not provide any guideline for sloped connection design.

Two one-sided Reduced Beam Section (RBS) moment connection specimens were tested under cyclic loading to investigate the effect of sloping. Both specimens had a W36×150 beam connected to a W14×257 column with an angle of slope equal to 25°; A992 steel was specified for the beams and columns. The RBS dimensions were identical for both specimens, except that the RBS configuration was oriented parallel to the column centerline and orthogonal to the beam span for Specimens S1 and S2, respectively. In this study, the heel and toe locations at the column face where a beam is framed in are defined as shown in Figure 5.1. The heel location of the two test specimens was at the bottom flange level (Figure 5.10 and Figure 5.11). For comparison purposes, the performance of the orthogonal RBS connection specimen C2 reported in Chapter 3 was also used as a reference to evaluate the sloping effect.

7.2.2 Conclusions

Based on the experimental results, the following conclusions can be made.

(1) Sloping the beam with respect to the column in the vertical plan would produce force concentration at the heel location and the force demand there can be significantly

higher than that at the toe location. The degree of force concentration will increase with the sloping angle with respect to the orthogonal configuration.

(2) Testing from both Kim et al. (2016) and this test program consistently showed the vulnerability for fracture at the heel location. Of the four full-scale specimens tested in both programs, fracture started from the end of the beam web CJP weld that was closest to the heel location. For the specimens tested in this research program, the fracture extended into the beam web. Although the beam flange CJP welds were intact, force concentration also initiated fracture at the weld access hole; the fracture then propagated rapidly into the beam flange and fractured the flange across its entire width. For the specimens tested by Kim et al., the fracture of the beam web CJP weld was followed by a sudden and brittle fracture of the beam flange CJP weld.

(3) Two RBS connection tested by Kim et al. had an RBS configuration parallel to the column centerline [Figure 5.3(a)], the same configuration as that used in Specimen S1. Following the recommendation made by Kim et al., the RBS configuration of Specimen S2 was perpendicular to the beam span, similar to that shown in Figure 5.3(b). Test results from this research program did show that this configuration yielded a better performance than Specimen S1, but the improvement was not that significant as the finite element simulation indicated. This is because the performance of Specimen S2 was overshadowed by the early fractures in the beam web CJP weld and weld access hole at the heel location.

(4) With an orthogonal beam-to-column connection configuration, AISC 358 (AISC 2016b) specifies a stringent welding requirement for steel backing removal, back-gouging, and fillet reinforcing, while a more relaxed requirement is specified for the

top flange weld. For a sloped moment connection, linking this welding requirement to either the top or bottom flange is not appropriate. The more stringent welding requirement should be applied to the heel location. Also, since fracture first started at the end of beam web CJP weld closest to the heel location in the two sloped connection specimens tested in this research project and another two by Kim et al. (2016), using the weld tab for making this weld and then remove it at this critical location per Section 3.4 of AISC 341 is recommended.

Based on the associated analytical study and finite element simulation, the following conclusions can be made.

(5) SRBWS is a potential solution for sloped connections to alleviate the strain demand at the heel location. It also can lead to larger strength of the connection as it has minimal effect on the plastic section modulus of a beam.

(6) A truss analogy model proposed in this work can predict the Normal Forces very well at the heel and toe locations.

(7) A design parameter called Force Concentration Factor, FCF was proposed that can show intensity of the force concentration at the heel location. A critical value for FCF, called FCF_{critical} equal to 1.06 is introduced as an indicator for potential fracture at the heel location.

(8) Using FCF and the proposed truss model, a systematic design approach to predict the potential of fracture for any sloped connections utilizing any beam sizes was introduced.

7.2.3 Future Research Need

This testing program proved that the design codes such as AISC 341 and 358 need an additional chapter dedicated for moment frame connections when the angle between the beam and the column is not 90°. The failure mode observed from the two tests was not what currently researchers expect to see in particular when using RBS connections.

Extensive experimental testing program seems to be required to better understand the performance of sloped connections and introducing a valid design procedure for these connections.

REFERENCES

(1) ABAQUS. (2014). *ABAQUS Standard User's Manual*, Version 6.14, ABAQUS Inc., RI.

(2) AISC. (2010a). "Seismic provisions for structural steel buildings." *AISC 341-10*, Chicago, IL.

(3) AISC. (2010b). "Prequalified connections for special and intermediate steel moment frames for seismic applications." *AISC 358-10*, Chicago, IL.

(4) AISC. (2010c). "Specification for structural steel buildings." *AISC 360-10*, Chicago, IL.

(5) AISC. (2011). "Steel construction manual." *American Institute of Steel Construction*, Chicago, IL.

(6) Astaneh-Asl, A. (1998). "Seismic behavior and design of gusset plates." *Steel Tips*, Structural Steel Educational Council, Moraga, CA.

(7) Bannantine, J., Comer, J., and Handrock, J. (1990). *Fundamentals of metal fatigue analysis*, Prentice-Hall, Englewood Cliffs, NJ.

(8) Barsom, J.M., and Rolfe, S.T. (1987). *Fracture and fatigue control in structures*, Prentice-Hall¸ Englewood Cliffs, NJ.

(9) Bridgman, P.W. (1952). *Studies in large plastic flow and fracture*, McGraw-Hill, New York, NY.

(10) Bruneau, M., Uang, C.M., and Sabelli, R. (2011). *Ductile design of steel structures*, McGraw-Hill, New York, NY.

(11) Chaboche, J.L. (1986). "Time-independent constitutive theories for cyclic plasticity." *Int. J. of Plasticity*, 2(2), 149-188.

(12) Chen, C.C., Lin, C.C., and Lin, C.H. (2006). "Ductile moment connections used in steel column-tree moment-resisting frames." *J. Constr. Steel Res.*, 62(2006), 793-801.

(13) Chi, B., and Uang, C.M. (2002). "Cyclic response and design recommendations of reduced beam section moment connections with deep columns." *J. Struct. Eng.*, 128(4), 464-473.

(14) Coffin, L.F. (1954). "A study of the effects of cyclic thermal stresses on a ductile metal." *Trans. ASME,* 76, 931-950.

(15) Dowswell, B. (2015). "Plastic strength of connection elements." *Eng. J.*, 52, 47-66.

(16) El-Tawil, S., Mikesell, T.D., Vidarsson, E., and Kunnath, S.K. (1998). "Strength and ductility of FR welded-bolted connections." *Rep. No. FEMA/SAC/BD-98/01*, Applied Technology Council, Redwood City, CA.

(17) El-Tawil, S., Mikesell, T., and Kunnath, S.K. (2000). "Effect of local details and yield ratio on behavior of FR steel connections." *J. of Struct. Eng.*, 126(1), 79-87.

(18) FEMA (2000a). "Recommended seismic design criteria for new steel moment-frame buildings." *Rep. No. FEMA-350*, Federal Emergency Management Agency, Washington, DC.

(19) Goel, S.C., Stojadinovic, B., and Lee, K.H. (1997). "Truss analogy for steel moment connections." *Eng. J.*, 34(2), 43-53.

(20) Graham, J.D., Sherbourne, A.N., Khabbaz, R.N., and Jensen, C.D. (1960). "Welded Interior Beam-to-Column Connections." *WRC Bulletin No. 63*, Welding Research Council, New York, NY.

(21) Hajjar, J.F., Dexter, R.J., Ojard, S.D., Ye, Y., and Cotton, S.C. (2003). "Continuity plate detailing for steel moment-resisting connections." *Eng. J.*, 40(4), 189-211.

(22) Kaufmann, E.J., Metrovich, B., and Pense, A.W. (2001). "Characterization of cyclic inelastic strain behavior on properties of A572 Gr. 50 and A913 Gr. 50 rolled sections." *Rep. No. 01-13*, National Center for Engineering Research on Advanced Technology for Large Structural Systems, Lehigh University, Bethlehem, PA.

(23) Kim, D.W., Sim, H.B., and Uang, C.M. (2010). "Cyclic testing of non-orthogonal steel moment connections for LAX TBIT modification." *Rep. No. TR-09/04*, Dept. of Structural Engineering, University of California, San Diego, La Jolla, CA.

(24) Kim, D.W., Ball, S.C., Sim, H.B., and Uang, C.M. (2016). "Evaluation of sloped RBS moment connections." *J. Struc. Eng.*, 142(6), 1-10.

(25) Krawinkler, H. and Zohrei, M. (1983). "Cumulative damage in steel structures subjected to earthquake ground motions." *Computer & Structure*, 16(1-4), 531-541.

(26) Leet, K.M., Uang, C.M., and Gilbert, A.M. (2005). *Fundamentals of structural analysis*, McGraw-Hill, New York, NY.

(27) Lemaitre, J. (1996). *A Course on damage mechanics*, Springer, Berlin.

(28) Mashayekh, A., and Uang, C.M. (2017). "Experimental verification of a procedure for SMF continuity plate weld design." *Eng. J.*, AISC. (accepted)

(29) Mashayekh, A., and Uang, C.M. (2017). "Cyclic response of sloped steel moment connections." *Rep.* No. *SSRP 16-11*, Dept. of Structural Engineering, University of California, San Diego, La Jolla, CA.

(30) Mashayekh, A., and Uang, C.M. (2017). "Experimental verification of a procedure for SMF continuity plate weld design." *Rep. No. SSRP 16-10*, Dept. of Structural Engineering, University of California, San Diego, La Jolla, CA.

(31) McGuire, W., Gallagher, R.H., and Ziemian, R.D. (2000). *Matrix structural analysis*, John Wiley and Sons, New York, NY.

(32) Neal, B.G. (1961). "The effect of shear and normal forces on the fully plastic moment of a beam of rectangular cross section." *J. of Appl. Mech.*, 28(2), 269–274.

(33) Ozkula, G. (2017). "Seismic behavior, modeling, and design of deep wide-flange steel columns for special moment frames." Ph.D. dissertation, Dept. of Structural Engineering, Univ. of California, San Diego, CA.

(34) Parkes, E.W. (1952). "The stress distribution near a loading point in a uniform flanged beam." *Philosophical Transactions of the Royal Society*, 244A, 417-467.

(35) Wood, R.H. (1955). "Yield line theory." *Research Paper No. 22*, Building Research Station.

(36) Prochnow, S.D., Dexter, R.J., Hajjar, J.F., Ye, Y., and Cotton, S.C. (2000). "Local flange bending and local web yielding limit states in steel moment-resisting connections." *Rep. No. ST-00-4*, Dept. of Civil Engineering, University of Minnesota, Minneapolis, MN.

(37) Ricles, J.M., Mao, C., Lu, L.W., and Fisher, J.W. (2000). "Development and evaluation of improved details for ductile welded unreinforced flange connections." *Rep. No. SAC/BD-00/24*, Sacramento, CA.

(38) Ricles, J.M., Mao, C., Lu, L.W., and Fisher, J.W. (2003). "Ductile details for welded unreinforced moment connections subject to inelastic cyclic loading." *Eng. Struct.*, 25(5), 667-680.

(39) Salmon, C.G., Johnson, J.E., and Malhas, F.A. (2009). *Steel structures design and behavior, emphasizing load and resistance factor design*, Pearson Prentice Hall, Upper Saddle River, NJ.

(40) Signes, E.G., Baker, R.G., Harrison, J.D., and Burdekin, F.M. (1967). "Factors affecting the fatigue strength of welded high strength steels." *British Weld. J.*, 14(3), 108-116.

(41) Tran, A.T., Hassett, P.M., and Uang, C.M. (2013). "A flexibility-based formulation for the design of continuity plates in steel special moment frames." *Eng. J.*, 50, 181-200.

(42) Uang, C.M., Tran, A.T., and Hassett, P.M. (2011). "The design of continuity plate welds in special moment frames." *Steel TIPS*, Structural Steel Education Council, Moraga, CA.

(43) Uang, C.M., and Bondad, D. (1996). "Static cyclic testing of pre-northridge and haunch repaired steel moment connection." *Rep. No. SSRP-96-02*, Dept. of Structural Engineering, University of California, San Diego, La Jolla, CA.

(44) Ye, Y., Hajjar, J.F., Dexter, R.D., Prochnow, S.C., and Cotton, S.C. (2000). "Nonlinear analysis of continuity plate and doubler plate details in steel moment frame connections." *Rep. No. ST-00-3*, Dept. of Civil Engineering, University of Minnesota, Minneapolis, MN.

(45) Yu, Q.S., Gilton, C., and Uang, C.M. (2000). "Cyclic response of RBS moment connections: loading sequence and lateral bracing effects." *Rep. No. SSRP-99/13*, Dept. of Structural Engineering, University of California, San Diego, La Jolla, CA.

APPENDIX A. TENSILE COUPON TEST RESULTS

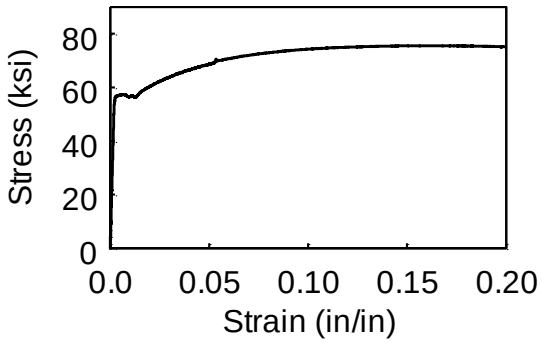

(a) Specimen C1, Beam Flange

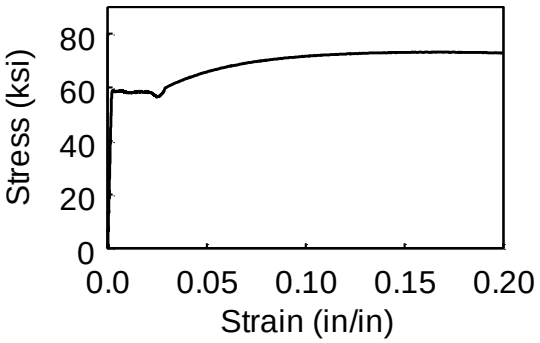

(b) Specimen C1, Beam Web

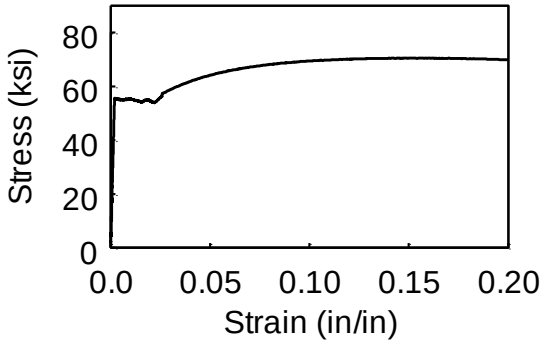

(c) Specimen C1, Column Flange

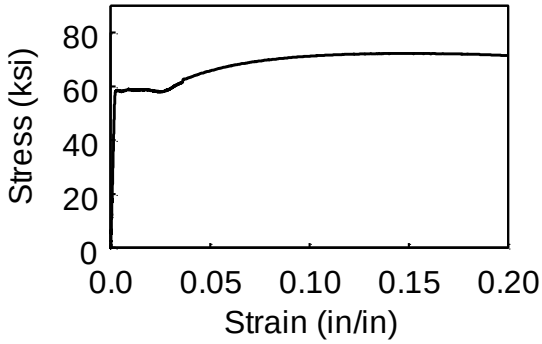

(d) Specimen C1, Column Web

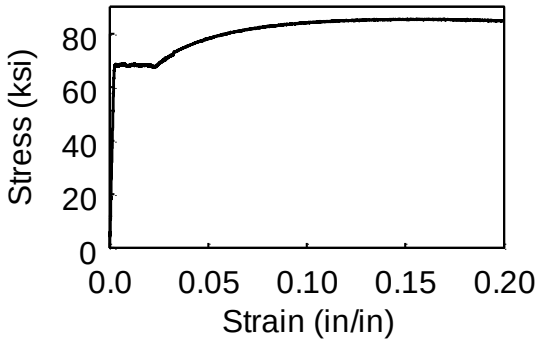

(e) Specimen C1, Continuity Plate

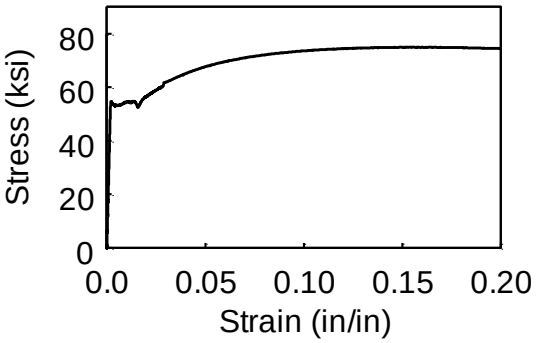

(f) Specimen C2, Beam Flange

Figure A.1 Tensile Coupon Stress-Strain Relationships

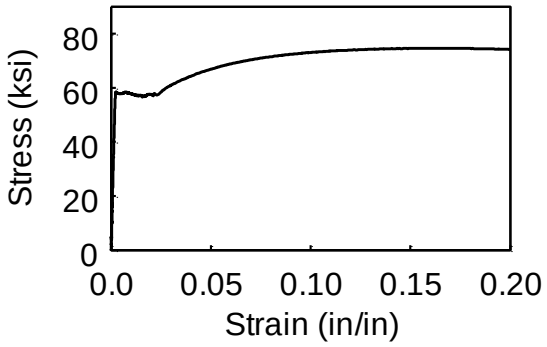

(g) Specimen C2, Beam Web

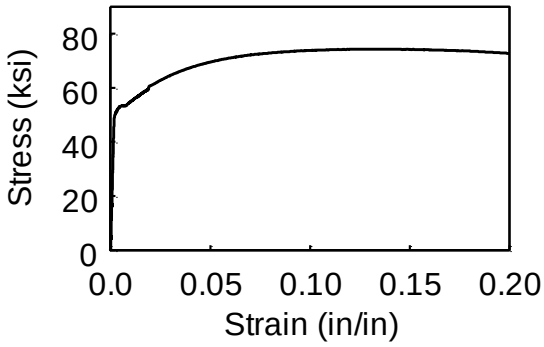

(h) Specimen C2, Column Flange

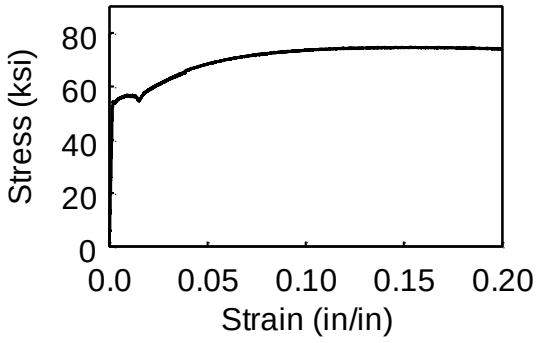

(i) Specimen C2, Column Web

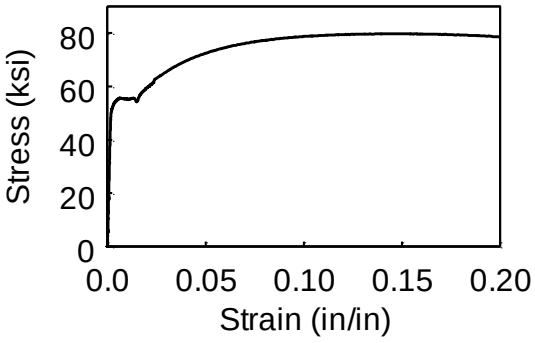

(j) Specimen C2, Continuity Plate

Figure A.1 Tensile Coupon Stress-Strain Relationships (continued)

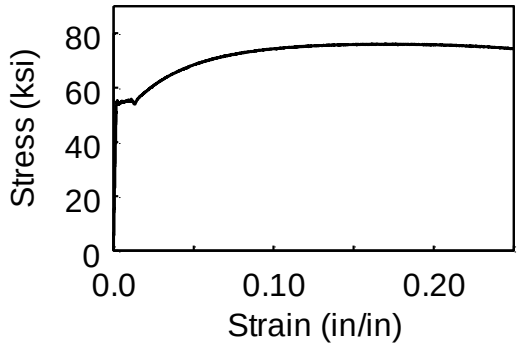

(a) Specimens S1 and S2, Beam Flanges

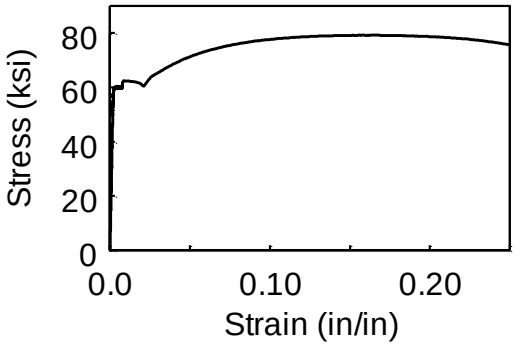

(b) Specimens S1 and S2, Beam Webs

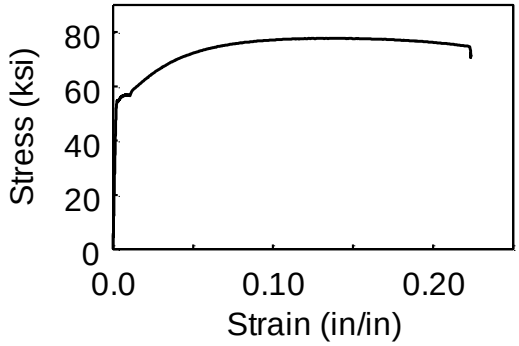

(c) Specimens S1 and S2, Column Flanges

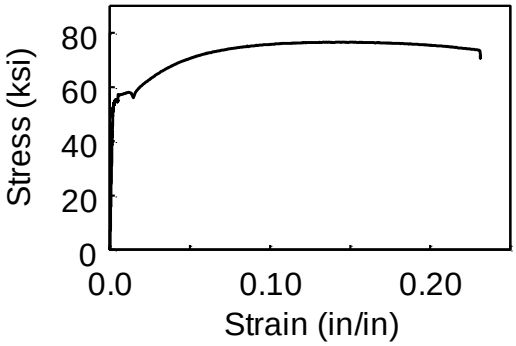

(d) Specimens S1 and S2, Column Webs

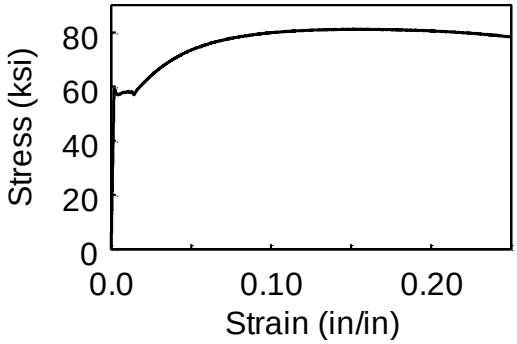

(e) Specimens S1 and S2, Continuity Plates

Figure A.1 Tensile Coupon Stress-Strain Relationships (continued)

APPENDIX B. DATA REDUCTION PROCEDURE FOR SLOPED MOMENT CONNECTIONS

B.1 Problem Statement

Consider the beam-column subassemblage with a sloped moment connection shown in Figure B.1. When a load is applied at the end of the beam, the beam tip deflection, Δ_{total} , and the four displacement measurements $\Delta_1, \Delta_2, \Delta_3$, and Δ_4 can be used to compute the componenets of Δ_{total} contributed by the deformations of the beam, column, and panel zone, respectively. Once each component is separated from the measurements, the plastic rotations of the beam, column, and panel zone then can be computed.

B.2 Separation of Deformations

B.2.1 Panel Zone Deformation

Figure B.2 shows the sloped panel zone deformed in pure shear. From the geometry of the un-deformed configuration in Figure B.2(a), the length d_1, d_2, and angles α, β are

$$d_1 = \sqrt{h^2 + b^2 - 2bh\sin(\theta)} \tag{B.1a}$$

$$d_2 = \sqrt{h^2 + b^2 + 2bh\sin(\theta)} \tag{B.1b}$$

$$\alpha = \sin^{-1}\left(\frac{b\cos(\theta)}{d_1}\right) \tag{B.2a}$$

$$\beta = \sin^{-1}\left(\frac{b\cos(\theta)}{d_2}\right) \tag{B.2b}$$

The shear deformation can be computed from the measurement Δ_3 as follows. Referring to Figure B.2(b), the distance p_1 can be derived from the geometry of triangle $E_2E'_2E_6$ together with Δ_3:

$$\frac{p_1}{\sin(90°)} = \frac{\Delta_3}{\sin(\alpha - \theta)} \tag{B.3}$$

$$p_1 = \frac{\Delta_3}{\sin(\alpha - \theta)} \tag{B.4}$$

Next consider the geometry of triangle $E_2E'_2E_5$ to compute $q_1$and r_1:

$$\frac{p_1}{\sin(90°)} = \frac{q_1}{\sin(\theta)} = \frac{r_1}{\sin(90° - \theta)} \tag{B.5}$$

$$q_1 = p_1 \sin(\theta) \tag{B.6}$$

$$r_1 = p_1 \cos(\theta) \tag{B.7}$$

Therefore, the shear deformation based on measurement Δ_3 is

$$\gamma_1 = \frac{r_1}{h + q_1} \approx \frac{r_1}{h} = \left(\frac{\cos(\theta)}{h \sin(\alpha - \theta)}\right) \Delta_3 \tag{B.8}$$

Similarly, the shear deformation can also be computed from measurement Δ_4 as follows. Use the geometry of triangle $E_3E'_3E_8$ to compute p_2:

$$\frac{p_2}{\sin(90°)} = \frac{\Delta_4}{\sin(\beta + \theta)} \tag{B.9}$$

$$p_2 = \frac{\Delta_4}{\sin(\beta + \theta)} \tag{B.10}$$

Then use triangle $E_3E'_3E_7$ to compute q_2 and r_2:

$$\frac{p_2}{\sin(90°)} = \frac{q_2}{\sin(\theta)} = \frac{r_2}{\sin(90° - \theta)} \tag{B.11}$$

$$q_2 = p_2 \sin(\theta) \tag{B.12}$$

$$r_2 = p_2 \cos(\theta) \tag{B.13}$$

Therefore, the shear deformation based on measurement Δ_4 is

$$\gamma_2 = \frac{r_2}{h + q_2} \approx \frac{r_2}{h} = \left(\frac{\cos(\theta)}{h \sin(\beta + \theta)}\right) \Delta_4 \tag{B.14}$$

When both Δ_3 and Δ_4 measurements are available, the average shear deformation is

$$\bar{\gamma} = \frac{1}{2}(\gamma_1 + \gamma_2) = \frac{1}{2h}\left[\frac{\Delta_3 \cos(\theta)}{\sin(\alpha - \theta)} + \frac{\Delta_4 \cos(\theta)}{\sin(\beta + \theta)}\right] \tag{B.15}$$

The deformed configuration of the beam-column subassemblage due to the panel zone shear deformation is shown in Figure B.3(a). Note that the boundary condition requires that the top end of the column (point A) be lined up vertically with the bottom end of the column (point B). However, due to the panel zone shear deformation, the two points are offset by a horizontal distance $\bar{\gamma}h$. Therefore, the configuration in Figure B.3(a) needs to be rotated counterclockwise by a rigid-body motion of $\bar{\gamma}h/H$ [see Figure B.3(b)]. The panel zone contributions to the beam tip deflection and the relative displacement, $\Delta_1 - \Delta_2$, can be then computed as follows:

$$(\Delta_{total})_{pz} = \bar{\gamma}L_b - \frac{\bar{\gamma}h}{H}(L_d) \tag{B.16}$$

$$(\Delta_1 - \Delta_2)_{pz} = \bar{\gamma}h - \frac{\bar{\gamma}h}{H}h = \bar{\gamma}h\left(1 - \frac{h}{H}\right) \tag{B.17}$$

In the above two equations, L_d is the perpendicular distance between nodes B and C while as L_b is the clear span of the beam.

B.2.2 Column Deformation

Figure B.4 shows the effects of the column rotation to the beam-column subassemblage. As can be seen, the rotation of the column will lead to a rigid body rotation of the beam and the panel zone by an amount θ_c. The contribution to the beam tip deflection and the panel zone deformation follows:

$$(\Delta_{total})_{col} = \theta_c\left(L_b + \frac{b}{2}\right) \tag{B.18}$$

$$(\Delta_1 - \Delta_2)_{col} = \theta_c(h) \tag{B.19}$$

The procedure to compute θ_c is described in Section B.3.

B.2.3 Beam Deformation

The beam deformation contributes only to the beam tip deflection (see Figure B.5):

$$(\Delta_{total})_b = \Delta_b \tag{B.20}$$

B.2.4 Total Deformations

By summing up each individual deformation component (beam, column and panel zone), the total beam tip displacement, Δ_{total}, and the total relative displacement $(\Delta_1 - \Delta_2)_{total}$, can be computed as follows:

$$\begin{aligned}\Delta_{total} &= (\Delta_{total})_{pz} + (\Delta_{total})_{col} + (\Delta_{total})_b \\ &= \bar{\gamma} L_b - \frac{\bar{\gamma} h}{H}(L_d) + \theta_c \left(L_b + \frac{b}{2}\right) + \Delta_b \end{aligned} \tag{B.21}$$

$$\begin{aligned}(\Delta_1 - \Delta_2)_{total} &= (\Delta_1 - \Delta_2)_{pz} + (\Delta_1 - \Delta_2)_{col} \\ &= \bar{\gamma} h \left(1 - \frac{h}{H}\right) + \theta_c (h) \end{aligned} \tag{B.22}$$

B.3 Summary of Data Reduction Procedure

Step 1: Panel Zone Component:

Use Eq. B.15 to compute $\bar{\gamma}$:

$$\bar{\gamma} = \frac{1}{2}(\gamma_1 + \gamma_2) = \frac{1}{2}\left[\frac{\Delta_3 \cos(\theta)}{h \sin(\alpha - \theta)} + \frac{\Delta_4 \cos(\theta)}{h \sin(\beta + \theta)}\right] \tag{B.15}$$

Step 2: Column Component:

The column rotation, θ_c, can be computed from Eq. (B.22) as follows:

$$\theta_c = \frac{(\Delta_1 - \Delta_2)_{total}}{h} - \bar{\gamma}\left(1 - \frac{h}{H}\right) \tag{B.23}$$

Step 3: Beam Component:

The beam component of Δ_{total} can be computed from Eq. (B.21) as follows:

$$\Delta_b = \Delta_{total} - \bar{\gamma} L_b + \frac{\bar{\gamma} h}{H}(L_d) - \theta_c \left(L_b + \frac{b}{2}\right) \tag{B.24}$$

The beam rotation, θ_b, is defined as

$$\theta_b = \frac{\Delta_b}{L_b} \tag{B.25}$$

If desired, L_b can be taken as the distance from the end of the beam to the location of the "plastic hinge" for the purpose of computing the actual plastic rotation capacity.

Step 4: Plastic Rotations

For each deformation component determined in Steps 1 to 3, the plastic rotation is computed by subtracting its elastic portion from the component. For example, the beam plastic rotation, θ_{bp}, is computed as follows:

$$\theta_{bp} = \theta_b - \theta_e$$
$$= \theta_b - \frac{P}{K} \quad \text{(B.26)}$$

Where P is the load effect (e.g., applied actuator force or moment at the face of column), and K is the elastic stiffness determined from the initial (elastic) portion of the P versus θ_b curve.

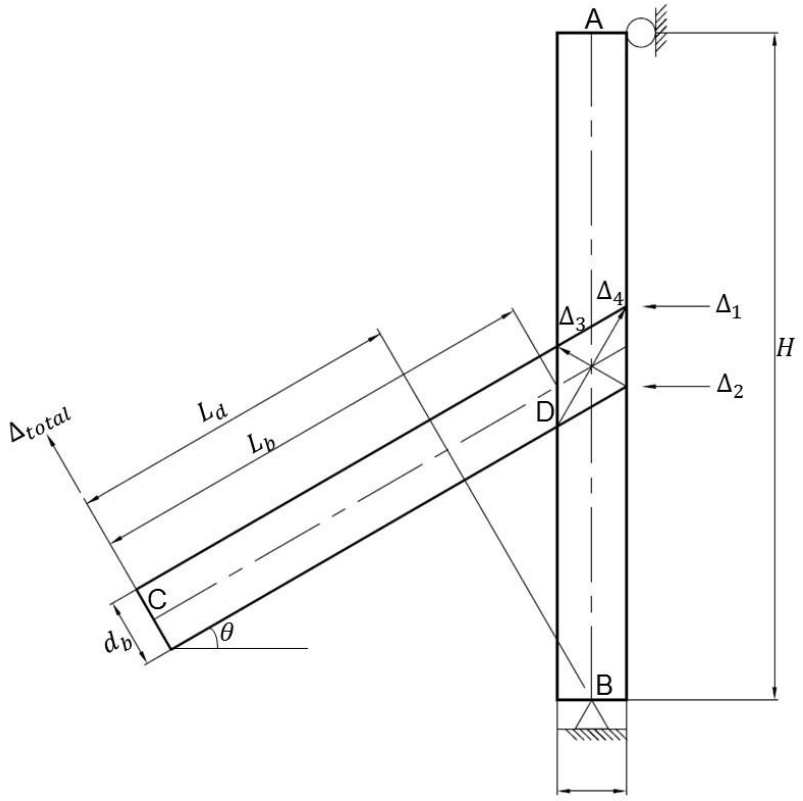

Figure B.1 Sloped Moment Connection Test Specimen

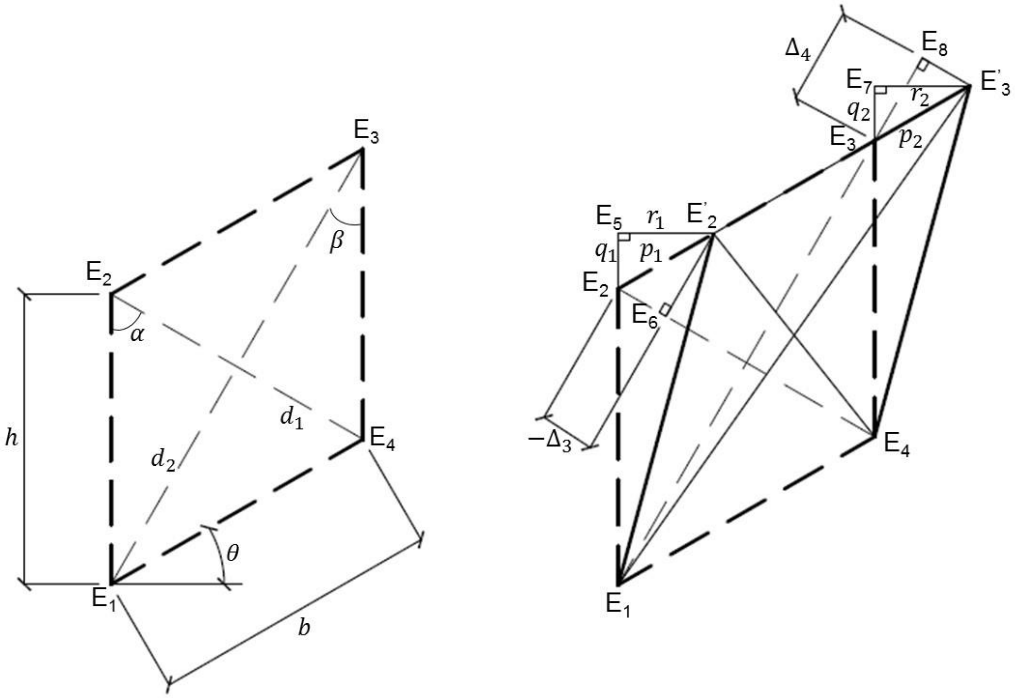

(a) Undeformed Panel Zone (b) Deformed Panel Zone

Figure B.2 Panel Zone Deformation

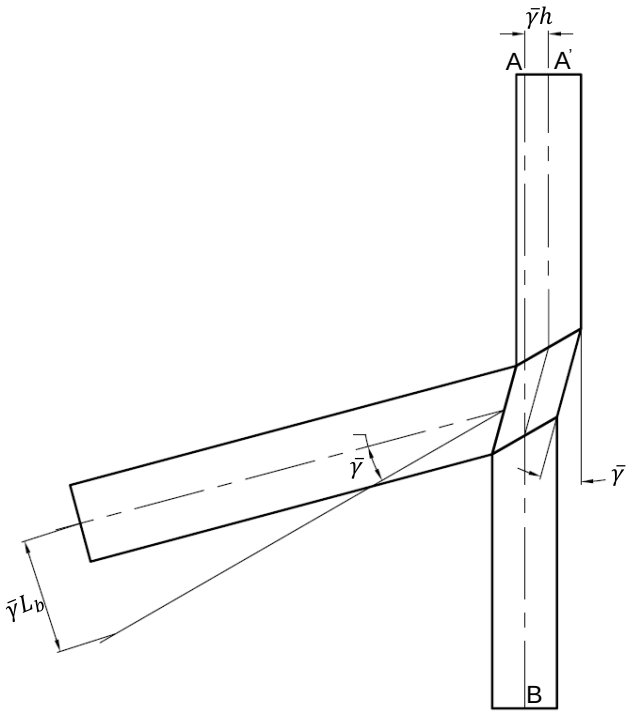

(a) before Rigid-Body Rotation

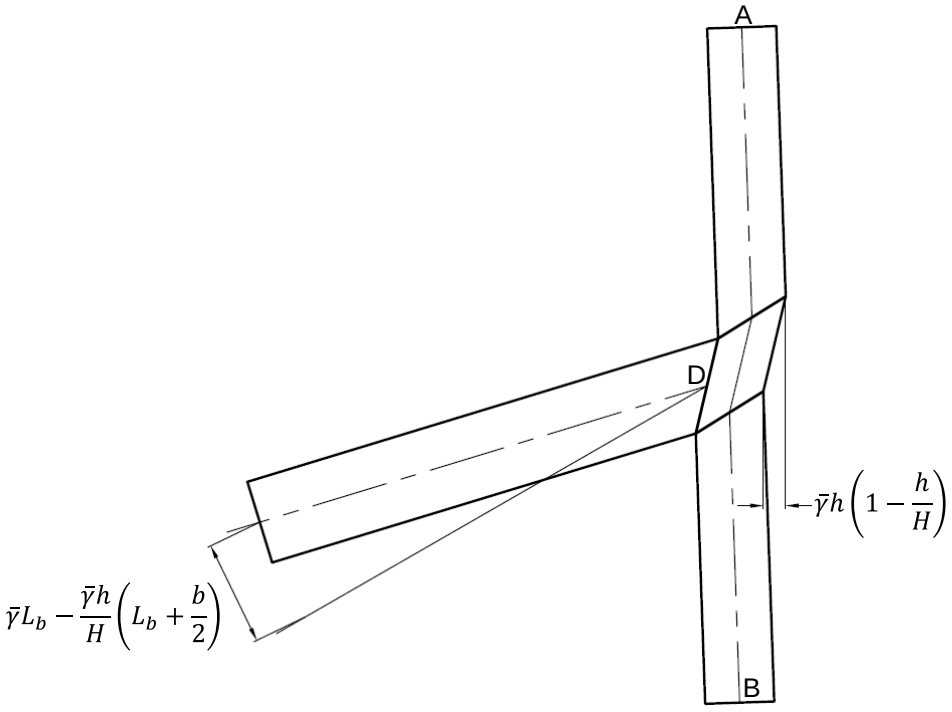

(b) after Rigid-Body Rotation (Points A and B Aligned Vertically)

Figure B.3 Effects of Panel Zone Deformation

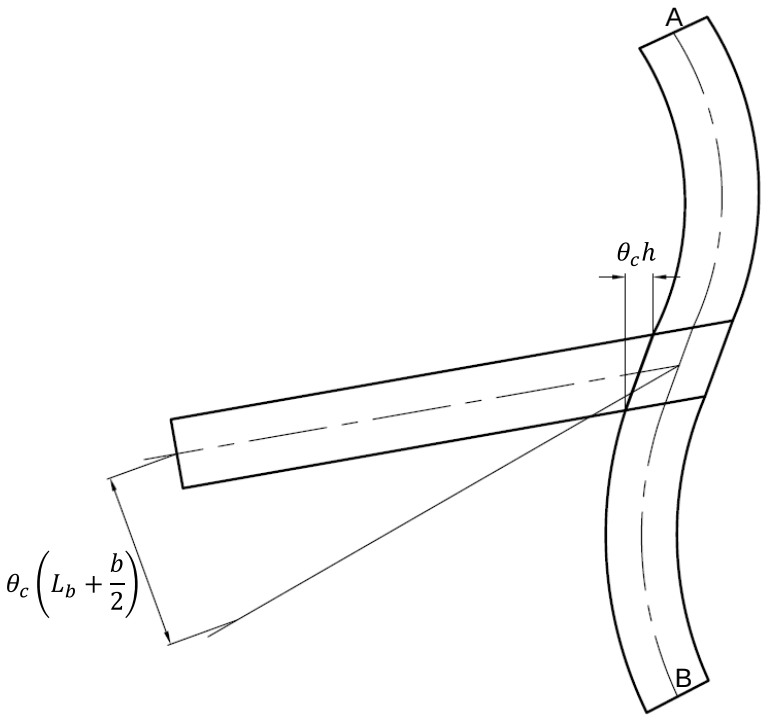

Figure B.4 Effects of Column Deformation

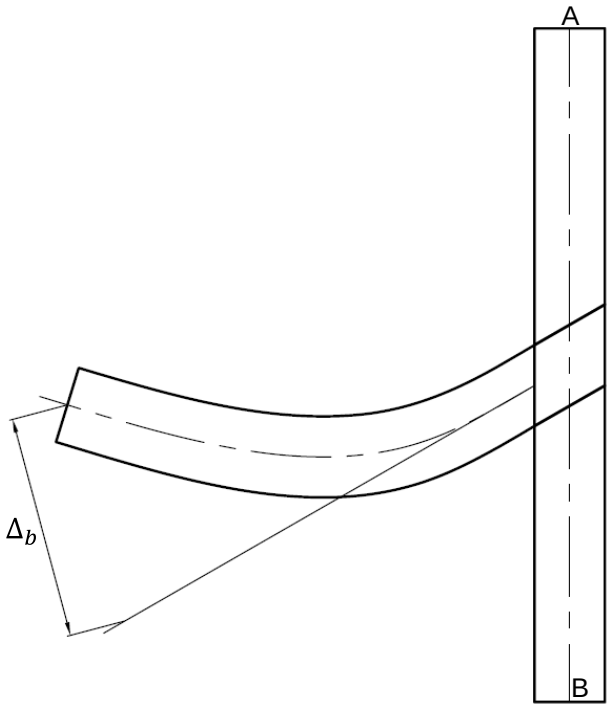

Figure B.5 Effects of Beam Deformation